

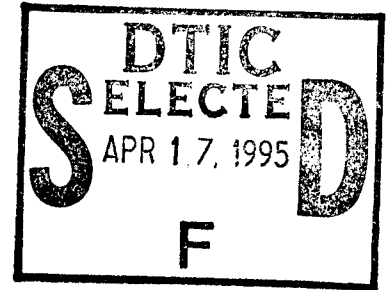
**MATERIALS FOR ADAPTIVE STRUCTURAL  
ACOUSTIC CONTROL**

Period February 1, 1994 to January 31, 1995

Annual Report

**VOLUME I**

**OFFICE OF NAVAL RESEARCH**  
Contract No.: N00014-92-J-1510



**APPROVED FOR PUBLIC RELEASE — DISTRIBUTION UNLIMITED**

Reproduction in whole or in part is permitted  
for any purpose of the United States Government

19950417 069

L. Eric Cross

**PENNSTATE**



DTIC QUALITY INSPECTED 5

**THE MATERIALS RESEARCH LABORATORY**  
UNIVERSITY PARK, PA

OMB No. 0704-0188

1. AGENCY USE ONLY (Leave blank)

2. REPORT DATE

4/6/95

3. REPORT TYPE AND DATES COVERED

**ANNUAL REPORT 02/1/94 TO 01/31/95**

#### 4. TITLE AND SUBTITLE

### 5. FUNDING NUMBERS

# MATERIALS FOR ADAPTIVE STRUCTURAL ACOUSTIC CONTROL

6. AUTHOR(S)

**L. ERIC CROSS**

7. PERFORMING ORGANIZATION NAME(S) AND ADDRESS(ES)

**MATERIALS RESEARCH LABORATORY  
THE PENNSYLVANIA STATE UNIVERSITY  
UNIVERSITY PARK, PA 16802**

8. PERFORMING ORGANIZATION REPORT NUMBER	
---	--

9. SPONSORING/MONITORING AGENCY NAME(S) AND ADDRESS(ES)

OFFICE OF NAVAL RESEARCH CODE 1513:NRJ 800 NORTH QUINCY STREET ARLINGTON, VA 22217	GERALD T. SMITH OFFICE OF NAVAL RESEARCH RES. REP. 536 SOUTH CLARK STREET, RM 286 CHICAGO, ILLINOIS 60606-1588
---	---

10. SPONSORING/MONITORING  
AGENCY REPORT NUMBER

## 11. SUPPLEMENTARY NOTES

12a. DISTRIBUTION / AVAILABILITY STATEMENT

12b. DISTRIBUTION CODE

13. ABSTRACT (Maximum 200 words)

**SEE FOLLOWING TWO PAGES**

#### 14. SUBJECT TERMS

15. NUMBER OF PAGES

16. PRICE CODE

17. SECURITY CLASSIFICATION OF REPORT

18. SECURITY CLASSIFICATION OF THIS PAGE

19. SECURITY CLASSIFICATION  
OF ABSTRACT

20. LIMITATION OF ABSTRACT

# GENERAL INSTRUCTIONS FOR COMPLETING SF 298

The Report Documentation Page (RDP) is used in announcing and cataloging reports. It is important that this information be consistent with the rest of the report, particularly the cover and title page. Instructions for filling in each block of the form follow. It is important to *stay within the lines* to meet optical scanning requirements.

**Block 1. Agency Use Only (Leave blank).**

**Block 2. Report Date.** Full publication date including day, month, and year, if available (e.g. 1 Jan 88). Must cite at least the year.

**Block 3. Type of Report and Dates Covered.** State whether report is interim, final, etc. If applicable, enter inclusive report dates (e.g. 10 Jun 87 - 30 Jun 88).

**Block 4. Title and Subtitle.** A title is taken from the part of the report that provides the most meaningful and complete information. When a report is prepared in more than one volume, repeat the primary title, add volume number, and include subtitle for the specific volume. On classified documents enter the title classification in parentheses.

**Block 5. Funding Numbers.** To include contract and grant numbers; may include program element number(s), project number(s), task number(s), and work unit number(s). Use the following labels:

C - Contract	PR - Project
G - Grant	TA - Task
PE - Program Element	WU - Work Unit Accession No.

**Block 6. Author(s).** Name(s) of person(s) responsible for writing the report, performing the research, or credited with the content of the report. If editor or compiler, this should follow the name(s).

**Block 7. Performing Organization Name(s) and Address(es).** Self-explanatory.

**Block 8. Performing Organization Report Number.** Enter the unique alphanumeric report number(s) assigned by the organization performing the report.

**Block 9. Sponsoring/Monitoring Agency Name(s) and Address(es).** Self-explanatory.

**Block 10. Sponsoring/Monitoring Agency Report Number.** (If known)

**Block 11. Supplementary Notes** Enter information not included elsewhere such as: Prepared in cooperation with...; Trans. of...; To be published in.... When a report is revised, include a statement whether the new report supercedes or supplements the older report.

**Block 12a. Distribution/Availability Statement.** Denotes public availability or limitations. Cite any availability to the public. Enter additional limitations or special markings in all capitals (e.g. NOFORN, REL, ITAR).

DOD - See DoDD 5230.24, "Distribution Statements on Technical Documents."

DOE - See authorities.

NASA - See Handbook NHB 2200.2.

NTIS - Leave blank.

**Block 12b. Distribution Code.**

DOD - Leave blank.

DOE - Enter DOE distribution categories from the Standard Distribution for Unclassified Scientific and Technical Reports.

NASA - Leave blank.

NTIS - Leave blank.

**Block 13. Abstract.** Include a brief (Maximum 200 words) factual summary of the most significant information contained in the report.

**Block 14. Subject Terms.** Keywords or phrases identifying major subjects in the report.

**Block 15. Number of Pages.** Enter the total number of pages.

**Block 16. Price Code.** Enter appropriate price code (NTIS only).

**Blocks 17. - 19. Security Classifications.** Self-explanatory. Enter U.S. Security Classification in accordance with U.S. Security Regulations (i.e., UNCLASSIFIED). If form contains classified information, stamp classification on the top and bottom of the page.

**Block 20. Limitation of Abstract.** This block must be completed to assign a limitation to the abstract. Enter either UL (unlimited) or SAR (same as report). An entry in this block is necessary if the abstract is to be limited. If blank, the abstract is assumed to be unlimited.

## ABSTRACT

The objectives of this ONR sponsored University Research Initiative (URI) entitled "Materials for Adaptive Structural Acoustic Control" concern both basic fundamental studies and highly applied development of the piezoelectric and electrostrictive ferroelectric ceramics which carry both the sensing and actuation functions for adaptive control. The report documents work over the third year of this five year program. For convenience and continuity, the activities are grouped under the headings" General Summary Papers, Materials Studies, Composite Sensors, Actuator Studies, Integration Issues, Processing Studies, Thin Film Ferroelectrics, and the Abstracts of graduating students on the program.

The first general papers illustrate the educational role undertaken by MRL faculty both in the basic understanding of ferroics, and in the philosophy of their application in 'smart' systems. It is interesting that through work pioneered on earlier ONR programs in MRL, it is now possible to measure both direct and converse electrostrictive response in simple solids, and to thus explore models to explain the signs and magnitudes of these striction constants. The relaxor ferroelectrics have been a topic of study for more than 30 years in the laboratory, but recent breakthroughs have revolutionized the level of understanding and opened a vista for further potential application of size (scale) effects in ferroics. Electrical control of shape memory has been achieved in a number of electro-ferroic solids, but full exploitation will need more complete understanding of both ferroelectric and ferroelastic/ferroelectric domain wall processes. Photostriction, the combination of photovoltaic and piezoelectric effects in ceramics promises an interesting range of new device possibilities.

In material studies, the elegant work on lanthanum modified lead titanate has now been fully written up, and the vital role of strain coupling in the onset of diffuse response underscored. New experimental methods have been applied to separating and measuring intrinsic and extrinsic components of response in PZT ceramics and to the measurement of microwave properties in these high K systems. Soft, intermediate, and hard modified lead zirconate and PZT composition have been under study for new and more interesting morphotropic phase boundaries which could be fabricated in single crystal form. Both optical birefringence and Raman studies are being used to explore domain and phase changes.

In sensing studies, the focus has been maintained upon flextensional (Moonie) structures and the enhanced performance which new end cap designs are affording. The polyvinylidene fluoride/trifluoethylene piezoelectrics are themselves an interesting composite system where the lower symmetry demands more complete characterization. The 1:3 rod and tube type composites have many performance advantages and trade-offs which will ensure wider scale application now that economical assembly techniques are at hand.



For actuation, the flexensional (Moonie) offers a number of advantages which merit further study. Both material and multilayer device related fatigue and destruction mechanisms are under study, and modes to control and alleviate microcracking and space charge degradation are examined. More detailed studies of the photostriction effects and their control by doping effects in PZTs have also been accomplished.

Integration studies have continued to explore the components which must be co-processed in the smart material or adaptive assemblage. Examples are the thick film conductors in copper or silver/palladium, the 0:3 high density piezoelectric polymer composites and the filter functions required to eliminate cross talk in the wiring system.

Processing studies are essential to the fabrication of the very wide range of materials demanded by all elements of the program. Relaxor materials have formed the focus for many processing activities but more recently the needs for high strain actuation are refocusing interest on phase switching antiferroelectric:ferroelectric compositions in the high lead zirconate PLZTs and PSnZTs with mounting evidence for multiple ferroelectric phases appearing under high fields.

Thin film papers have been selected from the extensive work in MRL on ferroelectric films because of their relevance to transduction in piezoelectric or phase switching compositions.

# MATERIALS FOR ADAPTIVE STRUCTURAL ACOUSTIC CONTROL

Period February 1, 1994 to January 31, 1995

Annual Report

VOLUME I

OFFICE OF NAVAL RESEARCH  
Contract No.: N00014-92-J-1510

APPROVED FOR PUBLIC RELEASE — DISTRIBUTION UNLIMITED

Reproduction in whole or in part is permitted  
for any purpose of the United States Government

L. Eric Cross

Accession For	
NTIS CRA&I	<input checked="" type="checkbox"/>
DTIC TAB	<input type="checkbox"/>
Unannounced	<input type="checkbox"/>
Justification	
By	
Distribution /	
Availability Codes	
Dist	Avail and/or Special
A-1	

PENNSSTATE



THE MATERIALS RESEARCH LABORATORY  
UNIVERSITY PARK, PA

## TABLE OF CONTENTS

ABSTRACT .....	8
INTRODUCTION .....	9
1.0 GENERAL SUMMARY PAPERS .....	12
2.0 MATERIALS STUDIES .....	12
3.0 COMPOSITE SENSORS .....	14
4.0 ACTUATORS STUDIES .....	14
5.0 INTEGRATION ISSUES .....	15
6.0 PROCESSING STUDIES .....	15
7.0 THIN FILM FERROELECTRICS .....	16
8.0 GRADUATING STUDENTS IN THE PROGRAM .....	16
9.0 HONORS AND AWARDS .....	17
10.0 APPRENTICE PROGRAM .....	17
11.0 PAPERS PUBLISHED IN REFEREED JOURNALS .....	18
12.0 INVITED PAPERS PRESENTATIONS AT NATIONAL AND INTERNATIONAL MEETINGS .....	21
13.0 INVITED PAPERS PRESENTED AT UNIVERSITY, INDUSTRY AND GOVERNMENT LABORATORIES .....	24
14.0 CONTRIBUTED PAPERS AT NATIONAL AND INTERNATIONAL MEETINGS .....	26
15.0 BOOKS (AND SECTIONS THEREOF) .....	33

## APPENDICES

### VOLUME I

#### *General Summary Papers*

1. Newnham, R.E., S. Trolier-McKinstry and J.R. Giniewicz, "Piezoelectric, Pyroelectric and Ferroic Crystals, *J. Mater. Educ.* **15**, 189-223 (1993).
2. Newnham R.E., "Electroceramics in the 1990s and Beyond, *Euroceramics II*, Vol. 3, Deutsche Keramische Gesellschaft Köln, Germany, 1771-1782 (1994).
3. Newnham, R.E. and V. Sundar, "Anisotropy in Electrostriction and Elasticity," *J. Mat. Sci. Lett.* **13**, 799-801, Chapman and Hall, London, England (1994).

### **General Summary Papers (continued) –Volume I**

4. Cross, L.E., "Relaxor Ferroelectrics: An Overview," *Ferroelectrics* **151**, 305-320 (1994).
5. Cross, L.E., Boundary Conditions for Shape Memory in Ceramic Material Systems, *J. Intelligent Material Systems on Structures* **6**, 55 (1994).
6. Uchino, K. and S.Y. Chu, "Photostriction and Its Applications," Proc. Amer. Ceram. Soc. Pac. Rim Conf., *Ferroic Materials*, 287-293 (1994).
7. Kumar, S., A.S. Bhalla and L.E. Cross, "Smart Ceramics for Broadband Vibration Control," *J. Intelligent Materials Systems and Structures* **5**(5), 673 (1994).
8. Kumar, S., A.S. Bhalla and L.E. Cross, "Smart Ferroelectrics for Acoustic and Vibration Control," *J. Intelligent Materials Systems and Structures* **5**(5), 678 (1994).

### **Materials Studies**

9. Rossetti, G., L.E. Cross and J.P. Cline, "Structural Aspects of the Ferroelectric Phase Transition in Lanthanum-Substituted Lead Titanate," *J. of Mat. Sci.* **30**(1), 24-34 (1995).
10. Rossetti, G.A., Jr., M.A. Rodriguez, A. Navrotsky, L.E. Cross and R.E. Newnham, "Structure of the Defect Perovskite  $[\text{Pb}_{0.85}\text{La}_{0.10}]\text{TiO}_3$  between 10 and 1023K," *J Appl. Phys.* **77**(4), 1683 (1994)
11. Zhang, Q.M., H. Wang, N. Kim and L.E. Cross, "Direct Evaluation of Domain-Wall and Intrinsic Contributions to the Dielectric and Piezoelectric Response and Their Temperature Dependence on Lead Zirconate-Titanate Ceramics," *J. Appl. Phys.* **75**(1), 454-9 (1994).
12. Li, Shaoping, A.S. Bhalla, R.E. Newnham, L.E. Cross and C.-Y. Huang, "90° Domain Reversal in  $\text{Pb}(\text{Zr}_x\text{Ti}_{1-x})\text{O}_3$  Ceramics," *J. Mater. Sci.* **29**(5), 1290-4 (1994).
13. Li, S., J. Sheen, S.-J. Jang, A.S. Bhalla, R.E. Newnham and L.E. Cross, "Modified Lumped Parameter Method for Measurements of Dielectric Susceptibility in Ferroelectrics," *Jpn. J. Appl. Phys.*, Part 1 **33**(6A), 3617-21 (1994).
14. Troilo, L.M., D. Damjanovic and R.E. Newnham, "Modified Lead Titanate Ceramics with a Relatively Large Dielectric Constant for Hydrophone Applications," *J. Am. Cer. Soc.* **77**(3), 857-59 (March 1994).
15. Subbarao, E.C., V. Srikanth, W. Cao and L.E. Cross, "Domain Switching and Microcracking During Poling of Lead Zirconate Titanate Ceramics," *Ferroelectrics* **145**, 771-781 (1993).
16. Jiang, Q.Y., E.C. Subbarao and L.E. Cross, "Dielectric Properties of Single Grain in PLZT Ferroelectric Ceramics," *Ferroelectrics Lett.* **17**, 41-46 (1994).

### **Materials Studies (continued) –Volume I**

17. Wang, J.F., J. Gineiwicz and A.S. Bhalla, "Soft Piezoelectric  $(1-x)\text{Pb}(\text{Sc}_{0.5}\text{Ta}_{0.5})\text{O}_{3-x}\text{PbTiO}_3$  Ceramics with High Coupling Factors and Low  $Q_m$ ," *Ferroelectrics Lett.* **16**, 113-118 (1993).
18. Alberta, E.F., A.S. Bhalla and T. Takenaka, "The Complex Piezoelectric, Elastic, and Dielectric Coefficients for a Lead Zirconate-Based Ceramic Under Electrical Bias," *Ferroelectrics* **154**, 11 (1994).

### **VOLUME II**

19. Alberta, E.F., A.S. Bhalla and T. Takenaka, "The Piezoelectric, Elastic and Dielectric Constants for Ceramics in the Solid Solution  $(x)\text{PbZrO}_3-(1-x-z)\text{PbZn}_{1/3}\text{Nb}_{2/3}\text{O}_3 - (z)\text{PbTiO}_3$ ," *Ferroelectrics* (in press).
20. Alberta, E.F. and A.S. Bhalla, "An Evaluation of Lead-Zirconate Based Ceramics For Use In Non-Volatile Ferroelectric Memory Devices," *Proceedings of the 9th Annual International Symposium on the Applications of Ferroelectrics* (1994).
21. Alberta, E.F. and A.S. Bhalla, "Dielectric and Piezoelectric Properties of Ceramics in the Lead Indium Niobate Lead Scandium Tantalate Solid Solution System," *Proceedings of the 9th Annual International Symposium on the Applications of Ferroelectrics* (1994).
22. Jin, B.-M., A.S. Bhalla, J.-B. Kim and J.-N. Kim, "Dielectric Response of  $\text{Li}_{0.4}\text{K}_{0.6}\text{NbO}_3$  Crystal in the Frequency Domain," *J. Mat. Sci. Mat. Electronics* **4**, 225-228 (1993).
23. Jin, B.-M., A.S. Bhalla, B.-C. Choi and J.-N. Kim, "Dielectric Anomalies in  $\text{Li}_{0.4}\text{K}_{0.6}\text{NbO}_3$  Crystals," *Physica Sta. Solidi.* **140**, 239-245 (1993).
24. Oh, K.Y., K. Uchino and L.E. Cross, "Optical Study of Domains in  $\text{Ba}(\text{Ti},\text{Sn})\text{O}_3$  Ceramics," *J. Amer. Ceram. Soc.* **77**(11), 2809-16 (1994).
25. Idink, H., V. Srikanth, W.B. White and E.C. Subbarao, "Raman Study of Low Temperature Phase Transitions in Bismuth Titanate,  $\text{Bi}_4\text{Ti}_3\text{O}_{12}$ ," *J. Appl. Phys.* **76**(3), 1819-1823 (1994).

### **Composite Sensors**

26. Newnham, R.E. and K.A. Markowski, "Composite Sensors and Actuators," Submitted for Proceedings of the Japan-U.S. Workshop on Functional Fronts in Advanced Ceramics, Tsukuba, Japan, December 6-8, 1994.
27. Dogan, A., S. Yoshikawa, K. Uchino and R.E. Newnham, "The Effect of Geometry on the Characteristics of the Moonie Transducer and Reliability Issues," *Proceedings of the IEEE Ultrasonics Symposium* **2**, 935-939 (1994).
28. Xu, Q.C., A. Dogan, J. Tressler, S. Yoshikawa and R.E. Newnham, "Ceramic-Metal Composite Actuator," *Ferroelectrics Special Issue on Piezoelectric and Electrostrictive Actuators* **160** (1994).

### ***Composite Sensors (continued) –Volume II***

29. Onitsuka, K., A. Dogan, Q.C. Xu, S. Yoshikawa and R.E. Newnham, "Design Optimization for Metal-Ceramic Composite Actuator, 'Moonie'," *Ferroelectrics* **156**, 37-42 (1994).
30. Tressler, J.F., Q.C. Xu, S. Yoshikawa, K. Uchino and R.E. Newnham, "Composite Flextensional Transducers of Sensing and Actuation," *Ferroelectrics* **156**, 67-72 (August 1994).
31. Meyer, R., H. Weitzing, Q.C. Xu, Q.M. Zhang, R.E. Newnham and J.K. Cochran, "Lead Zirconate Hollow-Sphere Transducers," *J. Am. Ceram. Soc.* **77**(6), 1669-72 (1994).
32. Wang, H., Q.M. Zhang, L.E. Cross and A.O. Sykes, "Piezoelectric, Dielectric, and Elastic Properties of Poly (Vinylidene Fluoride/Trifluoroethylene)," *J. Appl. Phys.* **74**(5), 3394-3398 (1993).
33. Wang, H., Q.M. Zhang and L.E. Cross, "Piezoelectric Relaxation of P(VDF-TrFE) Copolymer," *Ferroelectrics* **159**, 218-286 (1994).
34. Zhang, Q.M., W. Cao, H. Wang and L.E. Cross., "Characterization of the Performance of 1-3 Type Piezocomposites for Low-Frequency Applications," *J. Appl. Phys.* **73**(3), 1403-1410 (1993).
35. Zhang, Q.M., H. Wang and L.E. Cross, "Piezoelectric Tubes and 1-3 Tubular Composites as Tunable Actuators and Sensors," *Proc. SPIE-Int. Soc. Opt. Eng.* (1993), 1916 (Smart Materials), 244-54.
36. Zhang, Q.M., H. Wang and L.E. Cross, "Piezoelectric Tubes and Tubular Composites for Actuator and Sensor Applications," *J. Mater. Sci.* **28**(14), 3962-3968 (1993).

### ***Actuator Studies***

37. Newnham, R.E., A. Dogan, Q.C. Xu and S. Yoshikawa, "Flextensional 'Moonie' Actuators," *IEEE 1993 Ultrasonics Symposium Proc.*, Baltimore, Maryland, Vol. 1, 509-514 (Oct. 31-Nov. 3, 1993).
38. Dogan, A., Q. Xu, K. Onitsuka, S. Yoshikawa, K. Uchino and R.E. Newnham, "High Displacement Ceramic Metal Composite Actuators (Moonies)," *Ferroelectrics* **156**, 1 (1994).
39. Uchino, K., "Manufacturing Technology of Multilayered Transducers," *Proc. Amer. Ceram. Soc.* (in press).
40. Furuta, A. and K. Uchino, "Destruction Mechanism of Multilayer Ceramic Actuators: Case of Antiferroelectrics," *Ferroelectrics* **160**, 277-285 (1994).
41. Aburatani, H., S. Harada, K. Uchino, A. Furuta and Y. Fuda, "Destruction Mechanisms in Ceramic Multilayer Actuators," *Jpn. J. Appl. Phys.* **33**, 3091-3094 (1994).

## *Actuator Studies (continued) –Volume II*

42. Uchino, K. and H. Aburatani, "Destruction Detection Techniques for Safety Piezoelectric Actuator Systems," *Proc. 2nd Int'l Conf. Intelligent Mater.*, pp. 1248-56 (1994).

## **VOLUME III**

43. Takahashi, S., S. Hirose and K. Uchino, "Stability of PZT Piezoelectric Ceramics Under Vibration-Level Change," *J. Amer. Ceram. Soc.* **77**(9), 2429-32 (1994).
44. Jiang, Q.Y., E.C. Subbarao and L.E. Cross., "Effect of Composition and Temperature on Electric Fatigue of La-Doped Lead Zirconate Titanate Ceramics," *J. Appl. Phys.* **75**(11), 7433-7443 (1994).
45. Srikanth, V. and E.C. Subbarao, "Acoustic Emission Study of Phase Relations in Low Y<sub>2</sub>O<sub>3</sub> Portions of ZrO<sub>2</sub>-Y<sub>2</sub>O<sub>3</sub> System," *J. Mater. Sci.* **29**, 3363-3371 (1994).
46. Chu, S.Y., Z. Ye and K. Uchino, "Impurity Doping Effect on Photostriction in PLZT Ceramics," *J. Adv. Performance Mater.* **1**, 129-143 (1994)..
47. Chu, S.Y., Z. Ye and K. Uchino, "Photovoltaic Effect for the Linearly Polarized Light in (Pb,La)(Zr,Ti)O<sub>3</sub> Ceramics," *Smart Mater. Struct.* **3**, 114-117 (1994).
48. Chu, S.Y., M.L. Mulvihill, Z. Ye and K. Uchino, "Bulk Photovoltaic Effect for the Linearly Polarized Light in Pb(Zn<sub>1/3</sub>Nb<sub>2/3</sub>)O<sub>3</sub> Single Crystals," *Jpn. J. Appl. Phys.* **34** (Part 1, No. 2A) (1995).
49. Mulvihill, M.L., L.E. Cross and K. Uchino, "Low Temperature Dynamic Observation of Relaxor Ferroelectric Domain in Lead Zinc Niobate," *J. Amer. Ceram. Soc.* (in press).
50. Uchino, K., "Electrooptic Ceramics and Their Display Applications," *Ceramics International* (in press).
51. Lee, D., J. Yuk, N. Lee and K. Uchino, "Humidity-Sensitive Properties of Nb<sub>2</sub>O<sub>5</sub>-Doped Pb(Zr,Ti)O<sub>3</sub>," *Sensor and Mater.* **5**(4), 231-240 (1994).
52. Lee, N.Y., N. Usuki, H. Aburatani, Y. Ito and K. Uchino, "Pb/Ti Ratio of RF-Magnetron Sputtered PbTiO<sub>3</sub> Thin Films," *Jpn. J. Appl. Phys.* (accepted).

## *Integration Issues*

53. Dougherty, J.P. and Y. Chen, "Tailoring Materials for Smart Applications," Invited Paper, *Proc. 1994 Intl. Conf. on Intelligent Materials*, June 5-8, 1994, Williamsburg VA.
54. Hackenberger, W.S., T.R. Shrout, J.P. Dougherty and R.F. Speyer, "The Effect of Differential Shrinkage on the Sintering and Microstructural Development of Low-Temperature Co-Firable Multilayer Substrates," *Proc. SAMPE/ISHM 7th International Electronics Conference*, pp. 643-650, Parsippany, NJ, June 20-23, 1994

**Integration Issues (continued) –Volume III**

55. Wang, S.F., J.P. Dougherty, W. Huebner, and J.G. Pepin, "Silver-Palladium Thick Film Conductors," published as the feature article in *Journal of the American Ceramic Society* **77**(12), 3051-72 (December 1994).
56. Sample, D.R., P.W. Brown and J.P. Dougherty, "The Microstructural Evolution of Copper Thick Films Observed by Environmental Scanning Microscopy," *J. American Ceramic Society* (in press).

**VOLUME IV**

57. Fiallo, H.H., J.P. Dougherty, S.J. Jang, R.E. Newnham and L. Carpenter, "Transmission Properties of Metal-Semiconductor-Relaxor Microstrip Lines", *IEEE Trans. Microwave Theory & Techniques* **42**(7), 1176-1182, (July 1994).
58. Dougherty, J.P., M. Megherhi, and H.H. Fiallo, "Integrated Filters and Over Voltage Protection in Multilayer Ceramic Packaging Materials," *Proc. Eighth Cimtec World Ceramics Conference*, Florence, June 29-July 4, 1994.

**Processing Studies**

59. Miller, D.V., C.A. Randall, A.S. Bhalla, R.E. Newnham and J.H. Adair, "Electrorheological Properties of BaTiO<sub>3</sub> Suspensions," *Ferroelectrics Lett.* **15**, 141-151 (1993).
60. Fielding, J.T., Jr., T.R. Shrout and S.J. Jang, "Increased Operating Temperature Range in La-Modified Pb(Mg<sub>1/3</sub>Nb<sub>2/3</sub>O<sub>3</sub>-PbTiO<sub>3</sub> Relaxor Ferroelectric-Based Transducers," *Proc. 9th ISAF*, State College, PA (August 1994).
61. Fielding, J.T., Jr., S.J. Jang and T.R. Shrout, "Field-Induced Piezoelectric Materials for 100 kHz-10 MHz Transducer Applications," *Proc. 9th ISAF*, State College, PA (August 1994).
62. Brodeur, Russell P., Kamau wa Gachigi, Philip M. Pruna and Thomas R. Shrout, "Ultra-High Strain Ceramics with Multiple Field-Induced Phase Transitions," *J. Am. Ceram. Soc.* **77**(11), 3042 (1994).
63. Yoshikawa, S., N. Kim, T. Shrout, Q. Zhang, P. Moses and L.E. Cross, "Field-Induced Lead Zirconate Titanate Stannate Antiferroelectric-to-Ferroelectric Phase Switching Ceramics," *Proc. 9th ISAF*, State College, PA (August 1994).
64. Gururaja et al., "Electrostrictive Ultrasonic Probe Having Expanded Operating Temperature Range," United States Patent, Patent Number: 5,345,139, Date of Patent: September 6, 1994.
65. Yoon, K.H., Y.S. Cho, D.K. Kang, K. Uchino and K.Y. Oh, "Effect of Eutectic Lithium Sulphate-Sodium Sulphate Flux on the Synthesis of Lead Magnesium Niobate," *Ferroelectrics* **160**, 255-264 (1994).



***Thin Film Ferroelectrics –Volume IV***

66. Brooks, K.G., J. Chen, K.R. Udayakumar and L.E. Cross, "Electric Field Forced Phase Switching in La-Modified Lead Zirconate Titanate Stannate Thin Films," *J. Appl. Phys.* **75**(3), 1699-704 (1994).
67. Ghosh, P.K., A.S. Bhalla and L.E. Cross, "Surface Morphology of r.f. Sputtered Bismuth Titanate Thin Films," *J. Materials Science* **29**, 4659-4662 (1994).
68. Lee, N.Y., T. Sekine, Y. Ito and K. Uchino, "Deposition Profile of RF-Magnetron-Sputtered BaTiO<sub>3</sub> Thin Films," *Jpn. J. Appl. Phys.* **33** (Part 1, No. 3A), 1484-88 (1994).

***Graduating Students in the Program***

69. Dogan, Aydin. PhD Thesis (Abstract), Materials Program. Flexensional "Moonie and Cymbal" Actuators. December 1994.
70. Wang, Hong. PhD Thesis (Abstract), Materials Program. Electromechanical Effects in Polymeric Materials. August 1994.
71. Tressler, James F. Master of Science (Abstract), Ceramic Science. Smart Ceramic-Metal Composites for Active Vibration Control. December 1993.

## ABSTRACT

The objectives of this ONR sponsored University Research Initiative (URI) entitled "Materials for Adaptive Structural Acoustic Control" concern both basic fundamental studies and highly applied development of the piezoelectric and electrostrictive ferroelectric ceramics which carry both the sensing and actuation functions for adaptive control. The report documents work over the third year of this five year program. For convenience and continuity, the activities are grouped under the headings" General Summary Papers, Materials Studies, Composite Sensors, Actuator Studies, Integration Issues, Processing Studies, Thin Film Ferroelectrics, and the Abstracts of graduating students on the program.

The first general papers illustrate the educational role undertaken by MRL faculty both in the basic understanding of ferroics, and in the philosophy of their application in 'smart' systems. It is interesting that through work pioneered on earlier ONR programs in MRL, it is now possible to measure both direct and converse electrostrictive response in simple solids, and to thus explore models to explain the signs and magnitudes of these striction constants. The relaxor ferroelectrics have been a topic of study for more than 30 years in the laboratory, but recent breakthroughs have revolutionized the level of understanding and opened a vista for further potential application of size (scale) effects in ferroics. Electrical control of shape memory has been achieved in a number of electro-ferroic solids, but full exploitation will need more complete understanding of both ferroelectric and ferroelastic:ferroelectric domain wall processes. Photostriction, the combination of photovoltaic and piezoelectric effects in ceramics promises an interesting range of new device possibilities.

In material studies, the elegant work on lanthanum modified lead titanate has now been fully written up, and the vital role of strain coupling in the onset of diffuse response underscored. New experimental methods have been applied to separating and measuring intrinsic and extrinsic components of response in PZT ceramics and to the measurement of microwave properties in these high K systems. Soft, intermediate, and hard modified lead zirconate and PZT composition have been under study for new and more interesting morphotropic phase boundaries which could be fabricated in single crystal form. Both optical birefringence and Raman studies are being used to explore domain and phase changes.

In sensing studies, the focus has been maintained upon flextensional (Moonie) structures and the enhanced performance which new end cap designs are affording. The polyvinylidene fluoride/trifluoroethylene piezoelectrics are themselves an interesting composite system where the lower symmetry demands more complete characterization.

The 1:3 rod and tube type composites have many performance advantages and trade-offs which will ensure wider scale application now that economical assembly techniques are at hand.

For actuation, the flextensional (Moonie) offers a number of advantages which merit further study. Both material and multilayer device related fatigue and destruction mechanisms are under study, and modes to control and alleviate microcracking and space change degradation are examined. More detailed studies of the photostriction effects and their control by doping effects in PZTs have also been accomplished.

Integration studies have continued to explore the components which must be co-processed in the smart material or adaptive assemblage. Examples are the thick film conductors in copper or silver/palladium, the 0:3 high density piezoelectric polymer composites and the filter functions required to eliminate cross talk in the wiring system.

Processing studies are essential to the fabrication of the very wide range of materials demanded by all elements of the program. Relaxor materials have formed the focus for many processing activities but more recently the needs for high strain actuation are refocusing interest on phase switching antiferroelectric:ferroelectric compositions in the high lead zirconate PLZTs and PSnZTs with mounting evidence for multiple ferroelectric phases appearing under high fields.

Thin film papers have been selected from the extensive work in MRL on ferroelectric films because of their relevance to transduction in piezoelectric or phase switching compositions.

## INTRODUCTION

This report summarizes work carried out in the Materials Research Laboratory of The Pennsylvania State University during the third year of an ONR sponsored University Research Initiative (URI) entitled "Materials for Adaptive Structural Acoustic Control." The program has a five year duration and is being carried out largely in five sections each reporting to a senior faculty member.

These sections are:

Materials Studies	A.S. Bhalla
Composite Sensors	R.E. Newnham
Actuator Studies	K. Uchino
Integration Issues	J. Dougherty
Processing Studies	T.R. Shrout

There is certainly a necessary and highly desirable overlap between many of the topic areas, the reciprocity of the piezoelectric effect ensures that many of our most

interesting actuator concepts will find use in modified form in sensors and in integrated systems. The composite approaches for which the laboratory is justly renowned overlay strongly with the integration area and the autonomous cellular structure is almost essential for any truly 'smart' active material.

Following precedent established over more than eighteen earlier annual reports, this document presents a very brief narrative summary of the work which has been accomplished making reference for back up to the seventy one published studies from the group which are included as the technical appendices that form the bulk of the report.

It is important, however, to point out that this is not the only output from the program. The faculty, post doctorals and graduate assistants have participated in thirty three invited lectures at national and international meetings, forty-one invited presentations at university, government, and industrial laboratories all over the world and have contributed sixty four papers at national and international meetings.

Following precedent, the papers in this report are grouped under the topic headings:

1. General Summary Papers
2. Materials Studies
3. Composite Sensors
4. Actuator Studies
5. Integration Issues
6. Processing Studies
7. Thin Film Ferroelectrics.

The general summary papers illustrate rather effectively the educational role which is a major part of MRL activity. Basic symmetry arguments form an essential take-off point for understanding all ferroic phenomena, both primary and secondary, and their applications in dielectric, piezoelectric, and pyroelectric systems.

For smart materials and systems, both substance and philosophy are important. In electrostriction, the phenomenology of electro:elastic interaction has been understood since the 1890's, but it is only recently through work largely in MRL that the ultra sensitive instrumentation to measure both direct and converse effects has been developed so that it is now possible to explore possible origins for the signs and magnitudes of the polarization related striction constants. Relaxor ferroelectrics form the basis for all practical useful electrostrictors, and recent progress in understanding the phenomenon merits summary. It would appear that the superparaelectric model originally proposed in MRL is now the effective base for understanding, though interaction now leads to a whole panoply of glass like properties at lower temperatures. This evidence of the role of scale fundamentally modifying the ferroelectric behavior opens the possibility for further application of

controlled scale effects. In ferroic ceramics, electrical control of shape memory becomes possible with huge improvements of both speed and efficiency; however more work is needed to understand and control phase and domain switching. Photostriction combines the well known photovoltaic and piezoelectric effects in ferroelectrics to give most interesting possibilities for optical controlled actuation.

In material studies, the work reported earlier on the lead lanthanum titanate has been formalized and published, and gives a truly elegant and compelling evidence of the major role of elastic interaction in the break up of conventional ferroelectricity and the onset of diffuse transition behavior. Three papers on experimental methods give new insight into the separation of intrinsic (single domain) and extrinsic domain wall contributions to piezoelectric response, and a caution on the difficulty of applying microwave methods to the measurement of high permittivity dielectrics. New systems are explored with interesting morphotropic phase boundaries, and exceedingly high piezoelectric response, systems which may possibly be grown in single crystal form. Both optical birefringence and Raman spectral studies have been used to explore domain and phase changes.

In sensing studies, the flextensional (Moonie) structures continue to offer excellent scope for development, with new end cap geometries enhancing performance. A limited study in cooperation with Acoustic Associates has provided the first complete family of parameters for a well characterized commercial polyvinylidene fluoride/trifluorethylene piezoelectric. The 1:3 rod and tube type composites have been shown to offer many performance advantages for large area receptors and in actuation. New injection moulding and textile assembly techniques promise economical fabrication which will permit much wider application.

For actuation, again the flextensional (Moonie) has many unique features, and studies are continuing. For all actuators, however, reliability is a major concern. There are problems which are clearly associated with the ferroelectric material, both in piezoelectric and phase switching compositions which can be addressed. There are also a separate family of problems associated with the multilayer structure in practical co-fired actuators which we have also been addressing. In the photostrictors, there is need to control both electronic structure for the photo effect and ferroelectric microstructure for the piezoelectric capability so that doping studies are essential and have improved response remarkably.

Integration requires the assembly of a wide range of disparate solids, and we have continued to explore a wide range of the component elements. Example under study include thick film conductors in copper and silver/palladium, 0:3 high density polymer ceramic composites and the complex ferrite/ferroelectric combinations which provide most effective filter functions.

Processing is basic to all of the manifold materials needs on the program. Relaxor ferroelectric compositions have provided focus for many of the activities, with the problems of perovskite generation and pyrochlore elimination. More recently, however, new effort is being mounted on the high lead zirconate antiferroelectrics which can be phase switched to ferroelectric forms with corresponding high strains. For PLZT and PSnZT families, there is mounting evidence of ferroelectric:ferroelectric phase switching at high field levels.

The laboratory has very extensive work on ferroelectric thin films. Only three papers are presented in this report as they are relevant to the actuator use of the film systems.

## **1.0 GENERAL SUMMARY PAPERS**

In discussing piezoelectric, pyroelectric and ferroic crystals (Appendix 1), Newnham et al. take a crystallographic approach delineating the symmetry requirements and the tensorial properties. Simple model structures illustrate piezoelectricity, ferroelectricity and ferromagnetism. Secondary ferroic phenomena are briefly introduced. In his summary of electroceramics in the 1990's and beyond (Appendix 2), Newnham focuses upon evolving smart materials and systems, and the potential for microminiaturization in such electromechanical devices. Anisotropy in electrostriction and elasticity uses the modification of dielectric permittivity under uniaxial stress to measure the electrostriction constants, and looks at the electrostriction surfaces in several common cubic crystals (Appendix 3). Relaxor ferroelectrics are reviewed by Cross (Appendix 4) with emphasis upon the polarization fluctuation model to explain response in both perovskite and tungsten bronze structure relaxors. Shape memory behavior in a number of different ferroic ceramics is explored in Appendix 5 showing the possibility of electrical control with associated high speed and high efficiency. It is shown, however, that performance depends critically upon domain wall behavior in every instance. Photostriction and its application are discussed in Appendix 6. For PLZT ceramics doped with  $\text{WO}_3$  and excited with violet light, the response is large enough to permit a range of photo driven relays and small walking devices. Sensor-actuator combinations are considered in two papers (Appendices 7 and 8) for vibration control and elastic compliance control.

## **2.0 MATERIALS STUDIES**

The thesis work of Dr. G. Rossetti is summarized in the two papers (Appendices 9 and 10) dealing with structural aspects of the behavior of the lead lanthanum titanates. It is shown that the change from sharp ferroelectric, to diffuse, to relaxor ferroelectric behavior

is moderated by strain coupling through the defect fields associated with the lanthanum/vacancy population. In Appendix 11, a new method is described to separate intrinsic (single domain) and extrinsic (domain wall) contributions to piezoelectric response. The method rests on the fact that ferroelastic ferroelectric wall motion involves only shear deformations and thus cannot contribute at all to the hydrostatic response ( $d_h$ ). The importance of  $90^\circ$  wall motion in compositions near morphotropy in PZTs is confirmed in Appendix 12 by x-ray diffraction. Dangers of lumped parameter methods for microwave measurement when applied to high permittivity ceramics are highlighted in Appendix 13, and a new modified method is proposed and applied. A modified  $(\text{PbCa})\text{Ti}(\text{CoW})\text{O}_3$  composition is proposed in Appendix 14 for high hydrostatic sensor performance and low aging. In Appendix 15, acoustic emission has been used to explore the poling process in PZT and to distinguish between emission associated with domain switching and that associated with microcracking. Work on grain grown PLZTs at the 8/65/35 composition which culminated in the measurement of the properties of a single grain is discussed in Appendix 16. Soft piezoceramic compositions in the  $(1-x)\text{PbSc}_{1/2}\text{Ta}_{1/2}\text{O}_3:x\text{PbTiO}_3$  composition family are explored in Appendix 17, yielding high permittivity and high coupling ( $k_{33} \sim 0.73$ ) behavior. In Appendix 18, compositions in the lead zirconate:lead zinc niobate, lead zirconate:lead titanate near the antiferroelectric-to-ferroelectric phase boundary are explored, and the complex piezoelectric, elastic, and dielectric parameters measured. Appendix 19 extends this work, in addition exploring hysteresis and pyroelectric response. The very square loop behavior which can be achieved in these PZZN compositions is suggested as attractive to explore for thin film non volatile memory (Appendix 20). Lead indium niobate:lead scandium tantalate is a most interesting solid solution family because of the order/disorder behavior of its end members. PIN is a relaxor which orders to an antiferroelectric state; PST is a relaxor which orders to a ferroelectric. Preliminary results for some compositions in the PIN:PST system are given in Appendix 21. Dielectric studies on the single crystals  $\text{K}_{0.6}\text{Li}_{0.4}\text{NbO}_3$  are reported in Appendices 22 and 23.

$\text{Ba}(\text{Ti}_{1-x}\text{Sn}_x)\text{O}_3$  is a ceramic which can develop a core:shell structure and show unique electrostrictive properties. In Appendix 24, optical studies are used to confirm the unusual trapped domain structure and its behavior under electric field. Raman spectroscopy has been used in the study in Appendix 25 to give evidence of a subtle low temperature phase change in  $\text{Bi}_4\text{Ti}_3\text{O}_{12}$  single crystals.

### 3.0 COMPOSITE SENSORS

General considerations for piezoelectric and thermistor composites are highlighted in Appendix 26, keys to control are through connectivity, symmetry and scale. For the metal ceramic composite flextensional (Moonie), the evolution of end cap design is evident through Appendices 27, 28 and 29. It was through finite element studies that the grooved end cap and more advanced cymbal designs were evolved. Benefits from the Moonie design are also evident in the actuator:sensor vibration controlling integrated structure discussed in Appendix 30. A fascinating new type of structure evolved from very small PZT hollow shells produced by bubble blowing in a PZT slurry are explored in Appendix 31. The fired PZT shell can be poled and excited in breathing and in wall thickness vibration modes.

The PVF2:PTFE polymers are composites of high interest for sensing functions. The lower symmetry of the poled polymer, however, leads to the need for a wide family of measurements to completely characterized elastic, piezoelectric and dielectric properties, all of which are complex and strong functions of temperature. This task is taken up in Appendix 32 for the 75/25 composition over the temperature range from -100 to +65°C. In Appendix 33, a simple two phase model is proposed which accounts well for the measured parameters. Different types of 1:3 composite are discussed in Appendices 34, 35 and 36. The 1:3 rod composite is quantitatively modeled in Appendix 34, and a scheme proposed to evaluate strain profiles under hydrostatic stress. Appendices 35 and 36 deal with radially poled tubular 1:3 composites where it is shown that effective  $d_{33}$  and  $d_{31}$  may be made of the same sign, leading to very high hydrostatic sensitivity.

### 4.0 ACTUATOR STUDIES

Flextensional (Moonie) structures applied to actuation are considered in Appendices 37 and 38. End cap profile and displacements are considered for single and multiple stacked moonie structures. The high fields required for sensible displacements in piezoceramics demand multilayer structures to lower terminal voltages, and manufacturing technology for stacked, cofired and hybrid structures are discussed in Appendix 39. Reliability problems associated with cracking at field (stress) concentration in current multilayer structures are discussed in Appendices 40, 41 and 42 for piezoceramic and phase change compositions. In high AC resonant driving conditions, a new problem emerges in piezoceramics, associated with changing loss levels and associated heating. These stability problems are discussed in Appendix 43. Basic fatigue problems in PLZTs subjected to high drive polarization switching conditions are discussed in Appendix 44, and the precautions necessary to achieve long life ( $>10^9$  cycles) are delineated. Appendix 45



discusses the use of acoustic emission in exploring phase changes in the  $\text{ZrO}_2\text{:Y}_2\text{O}_3$  system. Work upon photostriction is discussed in Appendices 46 through 48. Doping studied in ceramic PZTs have led to enhanced photovoltaic performance. Clearly, the state of polarization of the exciting light will be important and this effect has been examined both in ceramic PZTs and in single crystal PZN samples. Domain structures induced by electric fields in the relaxor lead zinc niobate have been examined by optical microscopy (Appendix 49). Interesting cooperative motion of the spindle like domains which evolve under field at higher temperatures have been observed, and the freezing of a static domain structure at lower temperatures observed. Appendix 50 discusses electro-optic applications of PLZT, PZN and PMN:PT ceramics. Porous PZTs can also be used as humidity sensors making use of conduction due to adsorbed protons (Appendix 51). Sputtered PZT thin films are examined in Appendix 52 where both stoichiometry and orientation are examined for different substrates and sputtering conditions.

## **5.0 INTEGRATION ISSUES**

In this section, components necessary for effective integration are discussed. Examples of integration for compliance and vibration control have been given in Appendices 7, 8 and 30. Studies of the high sensitivity, high density 0:3 piezoceramic polymers have continued for loading up to 85 volume% ceramic, leading to excellent piezoelectric and dielectric characteristics (Appendix 53). A patent position for the fabrication method is now being established. Problems associated with cofired ceramic multilayer structures using thick film conductive inks are discussed in Appendix 54. Both silver/palladium conductors (Appendix 55) and copper conductors (Appendix 56) are of major interest for local and global interconnect in ceramic multilayer structures and both have specific problems and limitations for application which are discussed.

For dense interconnect systems, as in packaging or in smart composite structures, cross talk and electromagnetic interference are of major importance so that filter structures as discussed in Appendices 57 and 58 are of significant interest.

## **6.0 PROCESSING STUDIES**

The group maintains a continuing interest in electrophoretic and dielectrophoretic processing to produce chaining, gradient properties and patterned microstructures in polymer-ceramic composites. Appendix 59 examines the electrorheological effects associated with the onset of chaining in high K  $\text{BaTiO}_3$  suspensions under electric fields. Relaxor ferroelectrics also offer many processing challenges particularly in lead magnesium niobate:lead titanate with the need to broaden the temperature range of high

electromechanical response (Appendix 60). The large induced piezo response in these systems suggests many potential applications in agile field tunable systems, and more work to characterize both high and low field responses is being carried out (Appendix 61).

A second area of major interest is in the very high induced strains which accompany field forced antiferroelectric:ferroelectric phase switching. Current studies (Appendix 62) in the high zirconia PLZT system confirm the occurrence of more than one induced ferroelectric phase with ferroelectric:ferroelectric transitions clearly delineated in both polarization and strain behavior. Indirect evidence for additional phase change can be adduced also in the lanthanum modified PSnZT system (Appendix 62) where large continuing field induced volume change after the original anti-to ferroelectric switch cannot be explained by domain wall motion. Design for a new type of electrostrictive ultrasonic probe has been developed and a patent #5,345,139 issued for this invention. For all the perovskite type relaxor compositions, processing continues to be plagued by the alternative pyrochlore structure form. An innovative lithium sulphate:sodium sulphate eutectic flux method for processing PMN is described in Appendix 65.

## **7.0 THIN FILMS FERROELECTRICS**

With the increased interest in high strain actuator compositions, it is interesting to know if antiferroelectric:ferroelectric switching and the associated strain can be induced in a thin film system. Films of several lanthanum modified PZSnT were fabricated by sol-gel methods and shown to exhibit clear phase switching under high field (Appendix 66). This work has now continued and clear “square loop” switching with large associated strain documented. For bismuth titanate, both sputtering and evaporation methods have been used to generate thin films in Appendix 67; surface morphology associated with resputtered effects are explored. In sputter deposited BaTiO<sub>3</sub>, Appendix 68 explores the origins of preferred orientation when films are deposited onto a silica glass substrate. For these studies, the texture was examined for the as-deposited film without post deposition thermal processing.

## **8.0 GRADUATING STUDENTS ON THE PROGRAM**

The thesis work of graduating students on the program provides excellent background and summaries of major topic areas under study. For Aydin Dogan (Appendix 69), the subject was “Flexensional Moonie and Cymbal Actuators,” and the document traces in an effective clear narrative the evolution of the current end cap designs which have more than doubled the effective piezoelectric response.

The work by Hong Wang (Appendix 70) gives a full account of the detailed measurements on PVF2:TRFE composites, for the full family of elastic, dielectric, and piezoelectric parameters. The work also covers a good introduction to the new high strain urethane electrostrictive polymers.

Jim Tressler in his MS thesis (Appendix 71) designed a simple sensor/feedback/actuator system based on the flextensional moonie for the control of vibration in the range from 100 Hz to 6 kHz.

#### **Degrees Awarded to Students on the Contract**

H. Wang	PhD	Solid State Science	August 1994
A. Dogan	PhD	Materials Science	August 1994
J. Tressler	MS	Ceramic Science	December 1993

### **9.0 HONORS AND AWARDS**

<u>Name of Person Receiving Award</u>	<u>Recipient's Institution</u>	<u>Name, Sponsor and Purpose of Award</u>
A. S. Bhalla	Penn State University	IEEE, Elected General Chair for ISAF9 held at Penn State.
L. E. Cross	Penn State University	IEEE, Elected Distinguished UFFC Lecturer for 1994-95.
R. E. Newnham	Penn State University	Humboldt Senior Scientist Award from the Humboldt Society, Bonn, Germany. John F. McMahon Memorial Lecture, Alfred University, Alfred, New York. Keynote Speaker, International Meeting on Sensors, Bad Nauheim, Germany. Plenary Lecture, Norwegian Chemical Society Meeting, Trondheim, Norway. Opening Speech, U.S.-Japan Workshop on Functional Ceramics, Tsukuba, Japan.

### **10.0 APPRENTICE PROGRAM**

We expected to have three summer students join the Intercollege Materials Research Laboratory (IMRL) as part of the ONR DN Apprentice Program. Unfortunately, due to circumstances beyond our control, we only had one participant. Henry Ruffin III completed the IMRL Summer '94 DN Apprentice Program. Henry graduated from Suitland High School (5200 Silver Hill Road Forestville, Maryland 20747) where he was involved with an International Baccalaureate Program. This program was developed to set a standard for advanced placement of senior high school students in the United States and

120 other participating countries. Henry believed this program encouraged him to apply for additional opportunities of learning, including the ONR DN Apprentice Program.

During his seven week study program at the IMRL, Henry assisted on a number of projects. His primary responsibility was to make a ferroelectric ceramic composition and follow it through to completion. This hands-on approach provided Henry with the opportunity to experience the number of steps that goes into electronic ceramic materials processing and testing. According to Henry, it was not as easy as he anticipated. He discovered the reality of research, and the importance of managing not only his time, but laboratory equipment usage time as well. In addition to his laboratory responsibilities, Henry was also taking classes.

Henry will be returning to the Pennsylvania State University in the fall as a pre med student. He plans to be a surgeon. While materials research is not his first priority, he understands the impact of the technological advances made in this field on his chosen profession.

Henry's overall assessment of the DN Apprentice Program was, "I enjoyed the professional experience of being part of a team and working with others toward a common goal. Just being exposed to a facility like the IMRL was a worthwhile educational experience."

## **11.0 PAPERS PUBLISHED IN REFEREED JOURNALS**

1. Newnham, R.E., S. Trolier-McKinstry and J.R. Giniewicz, "Piezoelectric, Pyroelectric and Ferroic Crystals, *J. Mater. Educ.* **15**, 189-223 (1993).
2. Newnham R.E., "Electroceramics in the 1990s and Beyond, *Euroceramics II*, Vol. 3, Deutsche Keramische Gesellschaft Köln, Germany, 1771-1782 (1994).
3. Newnham, R.E. and V. Sundar, "Anisotropy in Electrostriction and Elasticity," *J. Mat. Sci. Lett.* **13**, 799-801, Chapman and Hall, London, England (1994).
4. Cross, L.E., "Relaxor Ferroelectrics: An Overview," *Ferroelectrics* **151**, 305-320 (1994).
5. Cross, L.E., Boundary Conditions for Shape Memory in Ceramic Material Systems, *J. Intelligent Material Systems and Structures* **6**, 55 (1994).
6. Uchino, K. and S.Y. Chu, "Photostriction and Its Applications," Proc. Amer. Ceram. Soc. Pac. Rim Conf., *Ferroic Materials*, 287-293 (1994).
7. Kumar, S., A.S. Bhalla and L.E. Cross, "Smart Ferroelectrics for Acoustic and Vibration Control," *J. Intelligent Material Systems and Structures* **5**(5), 678 (1994).
8. Kumar, S., A.S. Bhalla and L.E. Cross, "Smart Ceramics for Broadband Vibration Control," *J. Intelligent Material Systems and Structures* **5**(5), 673 (1994).

## 11.0 PAPERS PUBLISHED IN REFEREED JOURNALS (continued)

9. Rossetti, G., L.E. Cross and J.P. Cline, "Structural Aspects of the Ferroelectric Phase Transition in Lanthanum-Substituted Lead Titanate," *J. of Mat. Sci.* **30**(1), 24-34 (1995).
10. Rossetti, G.A., Jr., M.A. Rodriguez, A. Navrotsky, L.E. Cross and R.E. Newnham, "Structure of the Defect Perovskite  $[\text{Pb}_{0.85}\text{La}_{0.10}]\text{TiO}_3$  between 10 and 1023K," *J. Appl. Phys.* **77**(4), 1683 (1994)
11. Zhang, Q.M., H. Wang, N. Kim and L.E. Cross, "Direct Evaluation of Domain-Wall and Intrinsic Contributions to the Dielectric and Piezoelectric Response and Their Temperature Dependence on Lead Zirconate-Titanate Ceramics," *J. Appl. Phys.* **75**(1), 454-9 (1994).
12. Li, Shaoping, A.S. Bhalla, R.E. Newnham, L.E. Cross and C.-Y. Huang, "90° Domain Reversal in  $\text{Pb}(\text{Zr}_x\text{Ti}_{1-x})\text{O}_3$  Ceramics," *J. Mater. Sci.* **29**(5), 1290-4 (1994).
13. Li, S., J. Sheen, S.-J. Jang, A.S. Bhalla, R.E. Newnham and L.E. Cross, "Modified Lumped Parameter Method for Measurements of Dielectric Susceptibility in Ferroelectrics," *Jpn. J. Appl. Phys., Part 1* **33**(6A), 3617-21 (1994).
14. Troilo, L.M., D. Damjanovic and R.E. Newnham, "Modified Lead Titanate Ceramics with a Relatively Large Dielectric Constant for Hydrophone Applications," *J. Am. Cer. Soc.* **77**(3), 857-59 (March 1994).
15. Subbarao, E.C., V. Srikanth, W. Cao and L.E. Cross, "Domain Switching and Microcracking During Poling of Lead Zirconate Titanate Ceramics," *Ferroelectrics* **145**, 771-781 (1993).
16. Jiang, Q.Y., E.C. Subbarao and L.E. Cross, "Dielectric Properties of Single Grain in PLZT Ferroelectric Ceramics," *Ferroelectrics Lett.* **17**, 41-46 (1994).
17. Wang, J.F., J. Giniewicz and A.S. Bhalla, "Soft Piezoelectric  $(1-x)\text{Pb}(\text{Sc}_{0.5}\text{Ta}_{0.5})\text{O}_3$ - $x\text{PbTiO}_3$  Ceramics with High Coupling Factors and Low  $Q_m$ ," *Ferroelectrics Lett.* **16**, 113-118 (1993).
18. Alberta, E.F., A.S. Bhalla and T. Takenaka, "The Complex Piezoelectric, Elastic, and Dielectric Coefficients for a Lead Zirconate-Based Ceramic Under Electrical Bias," *Ferroelectrics* **154**, 11 (1994).
19. Jin, B.-M., A.S. Bhalla, J.-B. Kim and J.-N. Kim, "Dielectric Response of  $\text{Li}_{0.4}\text{K}_{0.6}\text{NbO}_3$  Crystal in the Frequency Domain," *J. Mat. Sci. Mat. Electronics* **4**, 225-228 (1993).
20. Jin, B.-M., A.S. Bhalla, B.-C. Choi and J.-N. Kim, "Dielectric Anomalies in  $\text{Li}_{0.4}\text{K}_{0.6}\text{NbO}_3$  Crystals," *Physica Sta. Solidi.* **140**, 239-245 (1993).
21. Oh, K.Y., K. Uchino and L.E. Cross, "Optical Study of Domains in  $\text{Ba}(\text{Ti},\text{Sn})\text{O}_3$  Ceramics," *J. Amer. Ceram. Soc.* **77**(11), 2809-16 (1994).

## 11.0 PAPERS PUBLISHED IN REFEREED JOURNALS (*continued*)

22. Idink, H., V. Srikanth, W.B. White and E.C. Subbarao, "Raman Study of Low Temperature Phase Transitions in Bismuth Titanate,  $\text{Bi}_4\text{Ti}_3\text{O}_{12}$ ," *J. Appl. Phys.* **76**(3), 1819-1823 (1994).
23. Xu, Q.C., A. Dogan, J. Tressler, S. Yoshikawa and R.E. Newnham, "Ceramic-Metal Composite Actuator," *Ferroelectrics Special Issue on Piezoelectric and Electrostrictive Actuators* **160** (1994).
24. Onitsuka, K., A. Dogan, Q.C. Xu, S. Yoshikawa and R.E. Newnham, "Design Optimization for Metal-Ceramic Composite Actuator, 'Moonie'," *Ferroelectrics* **156**, 37-42 (1994).
25. Tressler, J.F., Q.C. Xu, S. Yoshikawa, K. Uchino and R.E. Newnham, "Composite Flextensional Transducers for Sensing and Actuation," *Ferroelectrics* **156**, 67-72 (August 1994).
26. Meyer, R., H. Weitzing, Q.C. Xu, Q.M. Zhang, R.E. Newnham and J.K. Cochran, "PZT Hollow-Sphere Transducers," *J. Am. Ceram. Soc.* **77**(6), 1669-72 (1994).
27. Wang, H., Q.M. Zhang, L.E. Cross and A.O. Sykes, "Piezoelectric, Dielectric, and Elastic Properties of Poly (Vinylidene Fluoride/Trifluoroethylene)," *J. Appl. Phys.* **74**(5), 3394-3398 (1993).
28. Wang, H., Q.M. Zhang and L.E. Cross, "Piezoelectric Relaxation of P(VDF-TrFE) Copolymer," *Ferroelectrics* **159**, 218-286 (1994).
29. Zhang, Q.M., W. Cao, H. Wang and L.E. Cross., "Characterization of the Performance of 1-3 Type Piezocomposites for Low-Frequency Applications," *J. Appl. Phys.* **73**(3), 1403-1410 (1993).
30. Zhang, Q.M., H. Wang and L.E. Cross, "Piezoelectric Tubes and Tubular Composites for Actuator and Sensor Applications," *J. Mater. Sci.* **28**(14), 3962-3968 (1993).
31. Dogan, A., Q. Xu, K. Onitsuka, S. Yoshikawa, K. Uchino and R.E. Newnham, "High Displacement Ceramic Metal Composite Actuators (Moonies)," *Ferroelectrics* **156**, 1 (1994).
32. Aburatani, H., S. Harada, K. Uchino, A. Furuta and Y. Fuda, "Destruction Mechanisms in Ceramic Multilayer Actuators," *Jpn. J. Appl. Phys.* **33**, 3091-3094 (1994).
33. Takahashi, S., S. Hirose and K. Uchino, "Stability of PZT Piezoelectric Ceramics Under Vibration-Level Change," *J. Amer. Ceram. Soc.* **77**(9), 2429-32 (1994).
34. Jiang, Q.Y., E.C. Subbarao and L.E. Cross., "Effect of Composition and Temperature on Electric Fatigue of La-Doped Lead Zirconate Titanate Ceramics," *J. Appl. Phys.* **75**(11), 7433-7443 (1994).

## 11.0 PAPERS PUBLISHED IN REFEREED JOURNALS (continued)

35. Srikanth, S.V. and E.C. Subbarao, "Acoustic Emission Study of Phase Relations in Low  $Y_2O_3$  Portions of  $ZrO_2$ - $Y_2O_3$  System," *J. Mater. Sci.* **29**, 3363-3371 (1994).
36. Chu, S.Y., Z. Ye and K. Uchino, "Photovoltaic Effect for the Linearly Polarized Light in  $(Pb,La)(Zr,Ti)O_3$  Ceramics," *Smart Mater. Struct.* **3**, 114-117 (1994).
37. Lee, D., J. Yuk, N. Lee and K. Uchino, "Humidity-Sensitive Properties of  $Nb_2O_5$ -Doped  $Pb(Zr,Ti)O_3$ ," *Sensor and Mater.* **5**(4), 231-240 (1994).
38. Wang, S.F., J.P. Dougherty, W. Huebner, and J.G. Pepin, "Silver-Palladium Thick Film Conductors," published as the feature article in *Journal of the American Ceramic Society* **77**(12), 3051-72 (December 1994).
39. Fiallo, H.H., J.P. Dougherty, S.J. Jang, R.E. Newnham and L. Carpenter, "Transmission Properties of Metal-Semiconductor-Relaxor Microstrip Lines", *IEEE Trans. Microwave Theory & Techniques* **42**(7), 1176-1182, (July 1994).
40. Miller, D.V., C.A. Randall, A.S. Bhalla, R.E. Newnham and J.H. Adair, "Electrorheological Properties of  $BaTiO_3$  Suspensions," *Ferroelectrics Lett.* **15**, 141-151 (1993).
41. Brodeur, Russell P., Kamau wa Gachigi, Philip M. Pruna and Thomas R. Shrout, "Ultra-High Strain Ceramics with Multiple Field-Induced Phase Transitions," *J. Am. Ceram. Soc.* **77**(11), 3042 (1994).
42. Yoon, K.H., Y.S. Cho, D.K. Kang, K. Uchino and K.Y. Oh, "Effects of Eutectic Lithium Sulphate Sodium Sulphate Flux on the Synthesis of Lead Magnesium Niobate," *Ferroelectrics* **160**, 255 (1994).
43. Brooks, K.G., J. Chen, K.R. Udayakumar and L.E. Cross, "Electric Field Forced Phase Switching in La-Modified Lead Zirconate Titanate Stannate Thin Films," *J. Appl. Phys.* **75**(3), 1699-704 (1994).
44. Ghosh, P.K., A.S. Bhalla and L.E. Cross, "Surface Morphology of r.f. Sputtered Bismuth Titanate Thin Films," *J. Materials Science* **29**, 4659-4662 (1994).
45. Lee, N.Y., T. Sekine, Y. Ito and K. Uchino, "Deposition Profile of RF-Magnetron-Sputtered  $BaTiO_3$  Thin Films," *Jpn. J. Appl. Phys.* **33**, 1484-88 (1994).

## 12.0 INVITED PRESENTATIONS AT NATIONAL AND INTERNATIONAL MEETING

1. Uchino, K., "Photostriction and Its Applications," *Amer. Ceram. Soc. Pac. Rim Conf.*, Hawaii (November 7-10, 1993).
2. Takahashi, S., S. Hirose, K. Uchino and K.Y. Oh, "Electro-Mechanical Characteristics of PZT under High Vibration Level," *9th Int'l Symp. Appl. Ferroelectrics*, State College (August 7-10, 1994).

## 12.0 INVITED PRESENTATIONS AT NATIONAL AND INTERNATIONAL MEETING *(continued)*

3. Uchino, K., "Piezoelectric Actuators/Ultrasonic Motors -- Their Developments and Markets," *9th Int'l Symp. Appl. Ferroelectrics*, State College (August 7-10, 1994).
4. Uchino, K., "New Piezoelectric Devices for Smart Actuator Sensor Systems," *4th Int'l Conf. Electronic Ceram. & Appl.*, Aachen, Germany (September 5-7, 1994).
5. Takahashi, S., S. Hirose and K. Uchino, "Piezoelectric Characteristics in PZT Under High Vibration Level," *Amer. Ceram. Soc.*, Los Angeles (Fall 1994).
6. Newnham, R.E., "Resistivities of Conductive Composites," *International Symposium on Interfaces in Ionic Materials*, Schloß Ringbert, Germany (March 7-11, 1994).
7. Newnham, R.E., "Composite Sensors and Actuators," *Keynote address at International Meeting on Sensors*, VDE Meeting at Bad Nauheim, Germany (March 13-16, 1994).
8. Randall, C.A., C.P. Bowen, T.R. Shrout and R.E. Newnham, "Dielectrophoresis: A Means to Assemble Particulate-Polymer Composites," *American Ceramic Society Annual Meeting*, Indianapolis, IN (April 24-27, 1994).
9. Cann, D.P., J.P. Dougherty and R.E. Newnham, "Characterization of Ceramic Bismuth Pyrochlore Compounds," *American Ceramic Society Annual Meeting*, Indianapolis, IN (April 24-27, 1994).
10. Newnham, R.E., "Smart Ceramics and Structure-Property Relations," *Annual Meeting of Norwegian Chemical Society*, Norwegian Institute of Technology, Trondheim, Norway (May 2-3, 1994).
11. Newnham, R.E., "Composite Sensors and Actuators," *Simtec-World Ceramic Congress*, Florence, Italy (July 1-4, 1994).
12. Sundar, V. and R.E. Newnham, "Electrostriction Measurements in Diffuse Transition Materials and Perovskite Glass Ceramics," *IX-ISAF*, Penn State University, University Park, PA (August 7-10, 1994).
13. Newnham, R.E., "Composite Transducers and Actuators," *IX-ISAF*, Penn State University, University Park, PA (August 7-10, 1994).
14. Newnham, R.E., Quartz Workshop, Invited speaker on Microscopic Twinning, Naval Research Laboratory, Surface Modification Branch, Washington, DC (September 19-20, 1994).
15. Newnham, R.E., "Composite Sensors and Actuators," *Mexican Society for Instrumentation of the IXth Congress of Instrumentation*, Cancun, Mexico (September 26-30, 1994).
16. Newnham, R.E., "Composite Piezoelectric Sensors and Actuators," *Materials Research Society Meeting*, Boston, MA (November 28 - December 2, 1994).



## 12.0 INVITED PRESENTATIONS AT NATIONAL AND INTERNATIONAL MEETING *(continued)*

17. Newnham, R.E., "Composite Electroceramics," *Japan-US Workshop on Functional Fronts in Advanced Ceramics*, Tsukuba, Japan (December 6-8, 1994).
18. Cross, L.E., "The Role of Domain Walls Phase and Grain Boundaries in the Polarization Processes of Polycrystalline Ceramic Ferroelectrics," *International Symposium on Interfaces in Ionic Materials*, Schloß Ringbert (March 7-11, 1994).
19. Cross, L.E., "Applications of Ferroelectrics: Past, Present and Future (invited overview)," *ISAF'94*, State College, PA (August 8, 1994).
20. Newnham, R.E., "Size Effects in Ferroic Solids," *Gordon Research Conference on Dielectric Phenomena*, Holderness School, New Hampshire (July 31-August 5, 1994).
21. Newnham, R.E., "History and Recent Developments of Composite Piezoelectric Transducers," *Symposium on Transducteurs Piezo-Electriques Innovants: des Matériaux aux Applications*, Ecole d'Ingenieurs de Tours, France (November 7-8, 1994).
22. Cross, L.E., "Ferroelectric Materials for Electromechanical Transducer Applications," *Symposium on Transducteurs Piezo-Electriques Innovants: des Matériaux aux Applications*, Ecole d'Ingenieurs de Tours, France (November 7-8, 1994).
23. Cross, L.E., "Ferroelectric Ceramics: Materials and Applications Issues," *ACS/ISHUM Joint Fall Meeting*, Boston, MA (November 15, 1994).
24. Cross, L.E., "Sensor and Actuator Materials for Smart Systems," *MRS Meeting*, Boston, MA (November 28, 1994).
25. Cross, L.E., "Ferroelectric Materials for Electromechanical Transducer Applications," *15th Annual Meeting of IEEE Ultrasonics (Japan)*, Kyoto, Japan (November 30, 1994).
26. Cross, L.E., "Ferroelectric Ceramics for Sensor and Actuator Applications," *5th Int'l Meeting on Adaptive Structures*, Sendai, Japan (December 15, 1994).
27. Cross, L.E., "Ferroelectric Materials for Electromechanical Transducer Applications," *IUMRS/ICEM 94*, Hsinchu, Taiwan (December 19, 1994).
28. Zhang, Q.M., "Electrostrictive Materials and Piezocomposites for Transducer Applications," Schlumberger-Doll Research Center, Connecticut (December 5, 1994).
29. Dogan, A., S. Yoshikawa, K. Uchino and R.E. Newnham, "Flexensional Moonie Actuator: New Cap Design and Reliability," *IEEE International Ultrasonics Symposium*, Cannes, France (November 1-4, 1994)

## **12.0 INVITED PRESENTATIONS AT NATIONAL AND INTERNATIONAL MEETING** *(continued)*

30. Wenwu Cao, "Electron Microscopy in the Study of Domains and Domain Walls in Ferroelectrics" *52nd Annual Meeting of Microscopy Soc. Am. and 28th Annual Meeting of Microbeam Analysis Soc.*, New Orleans, Louisiana (July 31 - Aug. 5, 1994).
31. Wenwu Cao, "Modeling of Piezoelectric Ceramic-Polymer Composite Transducers", *Ultrasonic Transducer Engineering Workshop*, University Park, PA (Aug. 17-19, 1994).
32. Wenwu Cao, "Elastic and Electric Constraints in the Formation of Ferroelectric Domains", *3rd International Symposium on Domain Structure of Ferroelectrics and Related Materials*, Zakopane, Poland (September 6-9, 1994).
33. Wenwu Cao, "Coupling between primary and secondary order parameters in ferroelectric phase transitions", *European Meeting on "Kinetic Processes in Ferroelastic Materials"*, Hamburg, Germany (January 15-17, 1995).

## **13.0 INVITED PAPERS PRESENTED AT UNIVERSITY, GOVERNMENT, AND INDUSTRIAL LABORATORIES**

1. Newnham, R.E., "Piezoelectric and Electrostrictive Ceramics," Max Planck Institute, Stuttgart (March 21, 1994).
2. Newnham, R.E., "Smart Ceramics and Integrated Ceramics," Chemistry Department, University of Stuttgart, Germany (two lectures) (March 29-30, 1994).
3. Newnham, R.E., "Symmetry, Sensors and Actuators," O.N.R. Transducer Symposium at Penn State University (April 11-13, 1994).
4. Newnham, R.E., "Composite Transducers," Bosch Central Research Laboratory, Stuttgart, Germany (April 20, 1994).
5. Newnham, R.E., "Piezoelectric and Electrostrictive Ceramics," Fraunhofer Institute, Wurzburg, Germany (April 28, 1994).
6. Newnham, R.E., "Integrated Ceramics," Materials Science Dept., University Technical College of Hamburg, Germany (May 4-6, 1994).
7. Newnham, R.E., "Composite Actuators," Electrical Engineering Dept., Rhineland-Westphalen Technical Hochschule, Aachen, Germany (May 10-14, 1994).
8. Newnham, R.E., "Resistivities of Conductive Composites," Research Laboratory, Asea Brown Boveri Ltd., Baden, Switzerland (May 17, 1994).
9. Newnham, R.E., "Composite Actuators," E.T.H.L. University of Lausanne, Dept. of Materials, Lausanne, Switzerland (May 19, 1994).
10. Newnham, R.E., "Symmetry, Sensors and Actuators," Chemistry Dept., University of Münster (May 25, 1994).

**13.0 INVITED PAPERS PRESENTED AT UNIVERSITY,  
GOVERNMENT, AND INDUSTRIAL LABORATORIES** *(continued)*

11. Newnham, R.E., "Composite Sensors and Actuators," Electrotechnology Dept., University of Karlsruhe, Karlsruhe, Germany (June 2-4, 1994).
12. Newnham, R.E., "Integrated Ceramics," Harris Semiconductor Co., Dundalk, Ireland (June 8-10, 1994).
13. Newnham, R.E., "Smart Ceramics," Max-Planck Institut für Mikrostrukturphysic, Halle, Germany (June 12-13, 1994).
14. Newnham, R.E., "Size Effects in Ferroic Materials," Institute for New Materials (INM), Saarbrücken and Fraunhofer Institute for Biomedical Research, St. Ingbert (June 15-16, 1994).
15. Newnham, R.E., "Resistivity of Conducting Composites," Asea, Brown Boveri (ABB) Research Lab., Baden, Switzerland (June 19-20, 1994).
16. Newnham, R.E., "Piezoelectric and Electrostrictive Ceramics," Department of Mineralogy, University of Heidelberg, Heidelberg, Germany (June 23, 1994).
17. Newnham, R.E., "Review of European Electroceramic Research," Center for Dielectric Studies Fall Meeting, IMRL, PSU (October 4-5, 1994).
18. Newnham, R.E., "Ceramic Engineering in the Twenty-First Century: Scaling Up and Scaling Down," McMahon Memorial Lecture at Alfred, New York State College of Ceramics, Alfred, New York (October 27, 1994).
19. Newnham, R.E., "Composite Sensors and Actuators," Electrical Engineering Department Seminar, University of Trondheim, Norway.

*Cross, L.E., "Ferroelectric Materials for Electromechanical Transducer Applications," 1994/95 IEEE Distinguished Lecturer Lectures*

20. Siemens Central Research Laboratory, München, Germany (September 11-12, 1994)
21. Max-Planck Laboratories, Stuttgart, Germany (September 14, 1994).
22. Materials Research Laboratory, Carnegie Mellon University, Pittsburgh, Pennsylvania, USA (October 26, 1994).
23. Electrical Engineering School, Carnegie Mellon University, Pittsburgh, Pennsylvania, USA (October 27, 1994).
24. Laboratoire de Biophysique Medicale, Cedex, France (November 7-8, 1994).
25. Laboratoire de Chimie du Solide du CNRS, Bordeaux, France (November 9-10, 1994).
26. IEEE Ultrasonics Meeting, Kyoto, Japan (November 30, 1994).
27. Murata Manufacturing Co., Kyoto, Japan (December 1, 1994).

### **13.0 INVITED PAPERS PRESENTED AT UNIVERSITY, GOVERNMENT, AND INDUSTRIAL LABORATORIES** *(continued)*

*Cross, L.E., "Ferroelectric Materials for Electromechanical Transducer Applications,"  
1994/95 IEEE Distinguished Lecturer Lectures (continued)*

28. Mtg. Adaptive Structures ICAS, Sendai International Center, Sendai, Japan (December 5, 1994).
29. Tohoku University, Electrical Engineering Dept.(Sponsored by Tokin Corp.), Sendai, Japan (December 7, 1994).
30. Toshiba Corporation, Central Research Laboratory, Kawasaki, Japan (December 8, 1994).
31. 150th Mtg. of Japan Society for the Promotion of Science, Tokyo, Japan (December 9, 1994).
32. Tsinghua University, Beijing, China (December 12, 1994).
33. Xian Jiaotong University, Xian, China (December 14, 1994).
34. Shanghai Ceramic Society, Shanghai, China (December 16, 1994).
35. Shanghai Institute of Ceramics, Functional Ceramics Laboratory, Shanghai, China (December 16, 1994).
36. ICEM, International Materials Society Meeting, Hsincho, Taiwan (December 18, 1994).
37. IEEE Central Pennsylvania Section & Signal Processing Chapter, University Park, Pennsylvania (January 19, 1995).
38. Prairie View A&M University, College of Engineering and Architecture, Prairie View, Texas (January 30, 1995)
39. Prairie View A&M University, Center for Materials, Microdesign and Microfabrication, Prairie View, Texas (January 30, 1995).
40. Texas A&M, Dept. of Electrical Engineering, College Station, Texas (January 31, 1995).
41. Wenwu Cao, "Domains and Domain Walls in Ferroelectrics--Theory and Experiments", Swiss Federal Institute of Technology, Lausanne, Jan. 13, 1995.

### **14.0 CONTRIBUTED PAPERS AT NATIONAL AND INTERNATIONAL MEETINGS**

1. Uchino, K., "Drive/Control Techniques of Ceramic Actuators: General Review," 8th Smart Actuator Symp., State College, PA (January 20-21, 1994).
2. Uchino, K., "Control Techniques of Ultrasonics Motors," 8th Smart Actuator Symp., State College, PA (January 20-21, 1994).

#### 14.0 CONTRIBUTED PAPERS AT NATIONAL AND INTERNATIONAL MEETINGS *(continued)*

3. Uchino, K., "Active/Passive Vibration Damping," 8th Smart Actuator Symp., State College, PA (January 20-21, 1994).
4. Oh, K.Y. and K. Uchino, "Shape Memory Ceramic Actuators," 8th Smart Actuator Symp., State College, PA (January 20-21, 1994).
5. Uchino, K., S. Takahashi, S. Hirose and J. Zheng, "Drive Voltage Dependence of Electromechanical Coupling in Piezoelectric Ceramics," Mat. Res. Soc. Mtg., Boston, MA (November 28-December 2, 1994).
6. Hirose, S., S. Takahashi and K. Uchino, "Measuring Methods for High-Power Characteristics of Piezoelectric Materials," Mat. Res. Soc. Mtg., Boston, MA (November 28-December 2, 1994).
7. Oh, K.Y., H. Yamamoto, K. Uchino and L.E. Cross, "Optical Study of Domains in Antiferroelectric Ceramics," Mat. Res. Soc. Mtg., Boston, MA (November 28-December 2, 1994).
8. Chu, S.Y. and K. Uchino, "Photostrictive Effect in PLZT-Based Ceramics and Its Applications," Mat. Res. Soc. Mtg., Boston, MA (November 28-December 2, 1994).
9. Zheng, J., H. Yamamoto, P. Moses, S. Takahashi and K. Uchino, "Uniaxial Stress Dependence of Piezoestriction," Mat. Res. Soc. Mtg., Boston, MA (November 28-December 2, 1994).
10. Takahashi, S., S. Hirose and K. Uchino, "Electro-Mechanical Properties of  $\text{PbZrO}_3\text{-PbTiO}_3\text{-Pb}(\text{Mn}_{1/3}\text{Sb}_{2/3})\text{O}_3$  Under Vibration-Level Change," Mat. Res. Mtg., Boston, MA (November 28-December 2, 1994).
11. Mulvihill, M.L., L.E. Cross and K. Uchino, "Dynamic Domain Observation in Relaxor Ferroelectrics," 1994 ONR Transducer Materials and Transducers Workshop, State College, PA (April 11-13, 1994).
12. Uchino, K., S. Takahashi and Z. Ye, "Compact Piezoelectric Ultrasonic Motors," 1994 ONR Transducer Materials and Transducers Workshop, State College, PA (April 11-13, 1994).
13. Dogan, A., S. Yoshikawa, K. Uchino and R.E. Newnham, "Flexensional 'Moonie' Actuator: New Endcap Design and Reliability," 1994 ONR Transducer Materials and Transducers Workshop, State College, PA (April 11-13, 1994).
14. Oh, K.Y., K. Uchino and L.E. Cross, "Optical Study of  $\text{Ba}(\text{Ti},\text{Sn})\text{O}_3$  Ceramics," 9th Smart Actuator Symposium, State College, PA (April 20-21, 1994).
15. Mulvihill, M.L., L.E. Cross and K. Uchino, "Domain Reversal Mechanisms in Rhombohedral Relaxor Ferroelectrics," 9th Smart Actuator Symposium, State College, PA (April 20-21, 1994).
16. Aburatani, H., "Destruction Mechanisms of Multilayer Actuators," 9th Smart Actuator Symposium, State College, PA (April 20-21, 1994).

#### **14.0 CONTRIBUTED PAPERS AT NATIONAL AND INTERNATIONAL MEETINGS *(continued)***

17. Uchino, K and H. Aburatani, "Destruction Detection Techniques for Safety Piezoelectric Actuator Systems," Second International Conference on Intelligent Materials, Williamsburg, VA (June 6-8, 1994).
18. Dogan, A., K. Uchino and R.E. Newnham, "Reliability of Ceramic-Metal Composite Actuator 'Moonie'," 4th International Conference on Electronic Ceramics and Applications, Aachen, Germany (September 5-7, 1994).

#### ***American Ceramic Society 96th Annual Meeting, Indianapolis, Indiana (April 24-28, 1994).***

19. Uchino, K., "Manufacturing Technology of Multilayer Transducers."
20. Oh, K., K. Uchino, and L. E. Cross, "Observation of Domain Structures in Ba(Ti,Sn)O<sub>3</sub> Ceramics."
21. Mulvihill, M. L., L. E. Cross, and K. Uchino, "Dynamic Observation of the Domain Configuration in Pb(Mg<sub>1/3</sub>Nb<sub>2/3</sub>)O<sub>3</sub> and Pb(Zn<sub>1/3</sub>Nb<sub>2/3</sub>)O<sub>3</sub> Relaxor Ferroelectric Single Crystals."
22. Ye, Z., S. Y. Ch, K. Uchino, "Ring-Disc Type Ultrasonic Motors."
23. Randall, C. A., C. P. Bowen, T. R. Shrout, and R. E. Newnham, "Dielectrophoresis: A Means to Assemble Particulate Polymer Composites."
24. McCauley, D. E., C. A. Randall, C. P. Bowen, T. R. Shrout, and G. L. Messing, "High Dielectric Constant Particulate Materials for Electrorheological Fluids."
25. Trolier-McKinstry, S. and K. Veda, "Spectroscopic Ellipsometry as a Characterization Tool for Ceramic Materials."
26. Hackenberger, W. S., T. R. Shrout, and J. P. Dougherty, "A Novel Rate Controlled Sintering Dilatometer Using an Infrared Furnace."
27. Kirchner, J. A., J. Chen, B. Gibbons, and S. Trolier-McKinstry, "Size Effects in Sol-Gel Derived PbZrO<sub>3</sub> Thin Films."
28. Fielding, J. T., S. J. Jang, and T. R. Shrout, "Field-Induced Piezoelectric Materials for High Frequency Ultrasound Applications."
29. Aungkavattana, P. and S. Trolier-McKinstry, "Microstructure Development in Ferroelectric Thin Films by Spectroscopic Ellipsometry."

#### 14.0 CONTRIBUTED PAPERS AT NATIONAL AND INTERNATIONAL MEETINGS *(continued)*

*The Ninth International Symposium on the Applications of Ferroelectrics, The Pennsylvania State University, University Park, PA (August 7-10, 1994).*

30. Zhang, Q. M. , J. Zhao, T. Shrout, N. Kim, L. E. Cross, A. Amin\*, and B. M. Kulwicki\*, "A Tunable Piezoelectric State in Regular Ferroelectrics and Relaxor Ferroelectrics," Penn State University, Materials Research Laboratory, University Park, PA 16802, \*Texas Instruments Incorporated, Attleboro, MA 02703.
31. Fielding, J. T., Jr., T. R. Shrout, and S. J. Jang, "Increased Operating Temperature Range in La-Modified  $\text{Pb}(\text{Mg}_{1/3}\text{Nb}_{2/3})\text{O}_3\text{-PbTiO}_3$  Relaxor Ferroelectric-Based Transducers," Penn State University, Materials Research Laboratory, University Park, PA 16802.
32. Wang, H., Q. M. Zhang, L. E. Cross, R. Ting\*, C. Coughlin\*, and K. Rittenmyer\*, "The Origins of Electromechanical Responses in Polyurethane Elastomers," Penn State University, Materials Research Laboratory, University Park, PA 16802, \*Naval Research Laboratory, Underwater Sound Reference Detachment, Orlando, FL 32856.
33. Fielding, J. T., Jr., D. Smith, R. Meyer, Jr., and R. E. Newnham, "Characterization of PZT Hollow-Sphere Transducers," Penn State University, Materials Research Laboratory, University Park, PA 16802.
34. Zhao, J., Q. M. Zhang, and W. Cao, "Effects of Face Plate and Edge Strip on Piezoelectric Hydrostatic Response of 1-3 Composites," Penn State University, Materials Research Laboratory, University Park, PA 16802.
35. Bowen, C. P., T. R. Shrout, R. E. Newnham, and C. A. Randall, "Novel Processing of Ceramic/Polymer Composites Using the Dielectrophoretic Effect," Penn State University, Materials Research Laboratory, University Park, PA 16802.
36. Mathur, S. C., D. C. Dube, D. S. Rawat, H. O. Yadav, R. Kurchania, and A. S. Bhalla\*, "Studies on Oriented Domain Polystyrene - TGS Composite Films," Indian Institute of Technology, Physics Department, Hauz Khas, New Delhi 110016, India, \*Penn State University, Materials Research Laboratory, University Park, PA 16802.
37. Oh, Ki-Young, Kenji Uchino, and L. E. Cross, "Electric Properties and Domain Structures in  $\text{Ba}(\text{Ti},\text{Sn})\text{O}_3$  Ceramics," Penn State University, Materials Research Laboratory, University Park, PA 16802.

#### 14.0 CONTRIBUTED PAPERS AT NATIONAL AND INTERNATIONAL MEETINGS *(continued)*

*The Ninth International Symposium on the Applications of Ferroelectrics, The Pennsylvania State University, University Park, PA (August 7-10, 1994) (continued).*

38. Mulvihill, M. L., L. E. Cross, and K. Uchino, "Dynamic Observation of the Domain Configuration in Lead Magnesium Niobate and Lead Zinc Niobate Relaxor Ferroelectric Single Crystals," Penn State University, Materials Research Laboratory, University Park, PA 16802.
39. Trolier-McKinstry, S., "Thinned Ferroelectric Crystals and Ceramics," Penn State University, Materials Research Laboratory, University Park, PA 16802.
40. Alberta, E. F. and A. S. Bhalla, "Dielectric and Piezoelectric Properties of Ceramics in the Lead Indium Niobate-Lead Scandium Tantalate Solid Solution," Penn State University, Materials Research Laboratory, University Park, PA 16802.
41. Alberta, E. F. and A.S. Bhalla, "An Evaluation of Lead-Zirconate Based Ceramics for Use in Non-Volatile Ferroelectric Memory Devices," Penn State University, Materials Research Laboratory, University Park, PA 16802.
42. Jin, B.M., A. S. Bhalla, I. W. Kim\*, and B. C. Park\*, "Frequency Response of MgO:LiNbO<sub>3</sub> Crystals," Penn State University, Materials Research Laboratory, University Park, PA 16802, \*Ulsan University, Dept. of Physics, Ulsan, Korea.
43. Kim, I. W., B. C. Park, B. M. Jin\*, and A. S. Bhalla\*, "Growth and Characterization of MgO:LiNbO<sub>3</sub> Crystals," Ulsan University, Dept. of Physics, Ulsan, Korea, \*Penn State University, Materials Research Laboratory, University Park, PA 16802.
44. Kenji Uchino, "Piezoelectric Actuators/Ultrasonic Motors--Their Developments and Markets *(invited)*," Penn State University, Materials Research Laboratory, University Park, PA 16802.
45. Cao, Wenwu, W. K. Qi, Q. M. Zhang, and L. E. Cross, "Effects of Finite Dimensions in Piezocomposite Transducers," Penn State University, Materials Research Laboratory, University Park, PA 16802.
46. Zhang, Q. M., Y. Shui, X. Geng, Wenwu Cao, and L. E. Cross, "Piezoceramic-Polymer Composite as Thickness Resonance Mode Transducers-Dynamic Aspect and Effects of Heterogeneous Structure," Penn State University, Materials Research Laboratory, University Park, PA 16802.



#### 14.0 CONTRIBUTED PAPERS AT NATIONAL AND INTERNATIONAL MEETINGS *(continued)*

*The Ninth International Symposium on the Applications of Ferroelectrics, The Pennsylvania State University, University Park, PA (August 7-10, 1994) (continued).*

47. Sundar, V., R. E. Newnham, D. McCauley, K. wa Gachigi, and K. A. Markowski, "Electrostriction Measurements in Diffuse Phase Transition Materials and Perovskite Glass Ceramics," Penn State University, Materials Research Laboratory, University Park, PA 16802.
48. Fielding, J. T., S. J. Jang, and T. R. Shrout, "Field-Induced Piezoelectric Materials for High Frequency Transducer Applications," Penn State University, Materials Research Laboratory, University Park, PA 16802.
49. Takahashi\*<sup>+</sup>, S., S. Hirose<sup>#</sup>, K. Uchino<sup>+</sup>, and K. Y. Oh<sup>+</sup>, "Electro-Mechanical Characteristics of Lead-Zirconate-Titanate Ceramics Under Vibration-Level Change," \*NEC Corporation, Miyamae-ku, Kawasaki-shi, 216, Japan; #Yamagata University, Yonezawa-shi, Yamagata 992, Japan, +Penn State University, Materials Research Laboratory, University Park, PA 16802.
50. Gaskey, C. J., K. R. Udayakumar, H. T. Chen, L. E. Cross, "Antiferroelectric to Ferroelectric Phase Switching Thin Films in the Lead Zirconate Stannate Titanate Solid Solution System," Penn State University, Materials Research Laboratory, University Park, PA 16802.
51. Mohan Rao, G., S. B. Krupanidhi\*, "Pulsed Laser Deposition and Electrical Studies of  $(\text{Pb}_{1-x}\text{La}_x)\text{TiO}_3$  Thin Films for Electronic Applications," Indian Institute of Science, Instrumentation and Services Unit, Bangalore 560012, India, \*Penn State University, Materials Research Laboratory, University Park, PA 16802.
52. Chen, H. D., K. R. Udayakumar, L. E. Cross, J. J. Bernstein\*, and L. C. Niles\*, "Dielectric, Ferroelectric, and Piezoelectric Properties of PZT Thick Films on Si Substrates," Penn State University, Materials Research Laboratory, University Park, PA 16802, \*The Charles Stark Draper Laboratory, 555 Technology Square, Cambridge, MA 02139.
53. wa Gachigi, K., P.M. Pruna, C.A. Randall, S.J. Jang, J.P. Dougherty, "High Field Dielectric Properties of Modified Lead Zirconate Titanate Ceramics," Penn State University, Intercollege Materials Research Laboratory, University Park, PA 16802.
54. E. Furman<sup>+</sup> and L. E. Cross\*, "Dielectric Breakdown in PLZT 9.5/65/35 Ceramics," +Clemson University, The Gilbert C. Robinson Dept. of Ceramic Engr., Clemson, SC 29634-0907; \*Penn State University, Materials Research Laboratory, University Park, PA 16802.

#### 14.0 CONTRIBUTED PAPERS AT NATIONAL AND INTERNATIONAL MEETINGS *(continued)*

*The Ninth International Symposium on the Applications of Ferroelectrics, The Pennsylvania State University, University Park, PA (August 7-10, 1994) (continued).*

55. Jin, B. M., S. Erdei, and A. S. Bhalla, "Dielectric Properties and Low Temperature Relaxation Studies of Doped TGS Crystals," The Pennsylvania State University, Materials Research Laboratory, University Park, PA 16802.
56. Guo, Ruyan, A. S. Bhalla, Rustum Roy, and L. E. Cross, "Modified Ionic Polarizability Additivity Model and Its Application in Dielectric Property Studies of Ionic Materials," The Pennsylvania State University, Materials Research Laboratory, University Park, PA 16802.
57. Yu, F.T.S., A. S. Bhalla, S. Yin, F. Zhao, Z. K. Wu, and Deanna M. Salerno, "Ce:Fe LiNbO<sub>3</sub> Photorefractive Crystal: Material Properties and Applications *(invited)*," Penn State University, Department of Electrical Engineering, University Park, PA 16802, US. Army Missile Command, .
58. Chu, Sheng-Yuan, Zhou Ye and Kenji Uchino, "Photo-Acoustic Devices Using PLZT-Doped Ceramics," Penn State University, Materials Research Laboratory, University Park, PA 16802.
59. Chen, J., Q. M. Zhang, L. E. Cross, "Design of 1-3 Tubular Piezocomposite for Smart Transducer," Penn State University, Materials Research Laboratory, University Park, PA 16802.
60. Aburatani, Hideaki and Kenji Uchino, "Destruction Mechanism and Destruction Detection Technique for Multilayer Ceramic Actuators," Penn State University, Materials Research Laboratory, University Park, PA 16802.
61. Tressler, J. F., Q. C. Xu\*, S. Yoshikawa, K. Uchino, and R. E. Newnham, "Composite Flextensional Transducers for Sensing and Actuating," Penn State University, Materials Research Laboratory, University Park, PA 16802; \*Tektronix Inc., Wilsonville, OR 97070.
62. Dogan, A., S. Yoshikawa, K. Uchino, and R. E. Newnham, "Reliability of Flextensional Moonie Actuator," Penn State University, Materials Research Laboratory, University Park, PA 16802.
63. Mathur, S. C., D. C. Dube, D. P. Tewari, B.V.V.S.N. Prabhakara Rao, and A. S. Bhalla\*, "Hyperpolarizabilities and Dipole Moment Calculations for Various Nitroalkene Molecules and the Effect of Methyl Group Orientation," Indian Institute of Technology, Physics Department, Hauz Khas, New Delhi-110016, India, \* Penn State University, Materials Research Laboratory, University Park, PA 16802.

#### 14.0 CONTRIBUTED PAPERS AT NATIONAL AND INTERNATIONAL MEETINGS *(continued)*

*The Ninth International Symposium on the Applications of Ferroelectrics, The Pennsylvania State University, University Park, PA (August 7-10, 1994) (continued).*

64. Guo, Ruyan, J. F. Wang\*, J. M. Pova\*\*\*, and A. S. Bhalla, "Temperature Dependent Electrooptic Properties of Lead Barium Niobate Single Crystals," The Pennsylvania State University, Materials Research Laboratory, University Park, PA 16802; \*visiting scientist, Shandong Univ., Department of Physics, Jinan, China, \*\*\*visiting scientist, Department of Physics, Universidade Federal De Sao Carlos, Sao Carlos, SP Brazil.

#### 15.0 BOOKS (AND SECTIONS THEREOF)

1. Uchino, K., Applied Solid State Chemistry (Partial Charge: Section 3.3 Pyroelectric and Piezoelectric Materials), Asakura Pub. Co., Tokyo (1994).
2. Uchino, K., New Actuator Handbook for Precision Control, Editor in Chief and Partial Author (Introduction, Piezoelectric and Electrostrictive Effects, Shape Memory Ceramics, Photostrictive Actuators etc.), Fuji Technosystem, Tokyo (1994).
3. Uchino, K., Encyclopedia of Science & Technology (Partial Charge: Inchworm), Maruzen, Tokyo (1995).
4. Newnham, R. E. and M. I. Samoilovich. An Overview of Materials for Electronics and Optics, Chapter 7. Advanced Mineralogy, Vol. 1 (A. Marfunin, editor), MacMillan India Ltd., 514-528 (1994).

# **GENERAL SUMMARY PAPERS**

# APPENDIX 1

## PIEZOELECTRIC, PYROELECTRIC AND FERROIC CRYSTALS

R. E. Newnham, S. Trolier-McKinstry and J. R. Giniewicz  
Materials Research Laboratory  
The Pennsylvania State University  
University Park, PA 16802

### INTRODUCTION

A classification scheme for the thirty-two crystallographic point groups with respect to the electrical phenomena associated with a particular crystal class is pictured in Figure 1. Twenty-one point group symmetries are acentric and all but one of these are piezoelectric, developing an electric polarity under an applied stress. There are among the twenty piezoelectric classes ten polar or pyroelectric point groups which possess a unique polar axis, a vector direction unrelated by symmetry to any other direction in the crystal. Such crystals contain a "built-in" spontaneous polarization  $P(s)$ . Ferroelectric crystals are pyroelectric crystals with a reorientable spontaneous polarization. This switching process is accomplished by the movement of domain walls and is characterized by a hysteresis loop between the polarization and the electric field.

Many of the physical properties of crystals can be formulated in tensor notation. Tensors are defined in terms of transformations from one orthogonal axial system to another. Letting  $x_1, x_2, x_3$  be the old axes and  $x'_1, x'_2, x'_3$  be the new set, then  $a_{ij}$  ( $i, j=1, 2, 3$ ) is a set of nine numbers representing the cosines of the angles between the new axes  $x'_i$  and the old axes  $x_j$ . The axes transform according to the equations  $x'_i = a_{ij}x_j$  where

# Piezoelectric, Pyroelectric and Ferroic Crystals

summation applies for repeated subscripts. A zero-rank tensor is unchanged by the transformation from old to new axes. Scalar properties, such as density, are zero-rank tensors. The transformation law for a first-rank tensor is the same as that for the coordinates. Force, electric field, and other vector quantities are first-rank tensors. The transformation law for a second-rank tensor is the same as that for the product of two coordinates. A tensor of rank  $n$ , therefore, has  $n$  subscripts and transforms as the product of  $n$  coordinates (Nye, 1985).

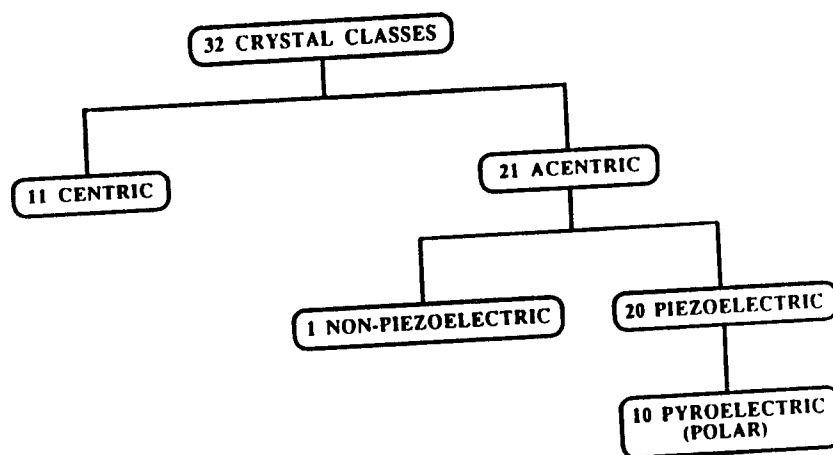


FIG. 1

A classification scheme for the 32 crystallographic point groups.

The tensors just described are polar tensors. The transformation law for a polar tensor is unaffected by handedness. It is the same regardless of whether the old and new axes are both of the same handedness or not. For an axial tensor, a change in handedness introduces a minus sign to the transformation law. Magnetic field is an axial first-rank tensor whose components transform as  $H'_i = \pm a_{ij} H_j$ . The positive sign applies if the old and new axial systems are both right-handed or both left-handed. If the transformation is from right to left, or from left to right, the negative sign is required.

The number of independent coefficients of a tensor property increases rapidly with rank. Crystallographic symmetry reduces the number of independent coefficients in keeping with Neumann's Principle: the symmetry elements of any physical property of a crystal must include the

## Piezoelectric, Pyroelectric and Ferroic Crystals

symmetry elements of the point group of the crystal. Magnetic symmetry and magnetic properties require special consideration (Birss, 1964).

Defining relations for the tensor properties considered in the following sections are summarized in Table 1. A more detailed treatment of these properties and the various ferroic phenomena will be presented next with selected mineral and mineral-related examples.

TABLE 1  
The rank of some tensor properties.

PROPERTY	POLAR TENSOR	AXIAL TENSOR	TENSOR RANK
Density [ $\rho$ ] Specific Heat [ $C$ ] Optical Rotatory Power [ $\beta$ ]	$M = \rho V$ $\delta q = C_p \delta T$	$\beta = \pi / \lambda_0 (n_l - n_r)$	Zero
Pyroelectricity [ $\pi_i$ ] Pyromagnetism [ $Q_i$ ]	$P_i = \pi_i \Delta T$	$M = Q_i \Delta T$	First
Electric Susceptibility [ $\kappa_{ij}$ ] Magnetic Susceptibility [ $\chi_{ij}$ ] Magnetoelectric Effect [ $\alpha_{ij}$ ]	$P_i = \kappa_{ij} E_j$ $M_i = \chi_{ij} H_j$	$M_i = \alpha_{ij} E_j$	Second
Piezoelectric Effect [ $d_{ijk}$ ] Magnetoelastic Effect [ $Q_{ijk}$ ]	$P_i = d_{ijk} \sigma_{jk}$	$M_i = Q_{ijk} \sigma_{jk}$	Third
Elastic Compliance [ $s_{ijkl}$ ]	$\epsilon_{ij} = s_{ijkl} \sigma_{jk}$		Fourth

## PIEZOELECTRICITY

The direct piezoelectric effect is manifested for an acentric crystal in the development of an electric charge or polarization under an applied stress. The linear relationship between the induced polarization and the applied stress is expressed in tensor form as:

$$P_i = d_{ijk} \sigma_{jk} \quad [i, j, k = 1, 2, 3]$$

where  $P_i$  is induced polarization,  $\sigma_{jk}$  is the second-rank stress tensor, and  $d_{ijk}$  is the third-rank tensor quantity relating the two, identified as the piezoelectric coefficient with units of [pC/N]. It is evident in this



## Piezoelectric, Pyroelectric and Ferroic Crystals

relationship that the directions of the induced polarization under equal tensile and compressive stresses will be opposite in sense.

The converse piezoelectric effect is observed when an applied electric field  $[E_i]$  produces a strain  $[\epsilon_{jk}]$ , expressed as:

$$\epsilon_{jk} = d_{jki} E_i \quad [i, j, k = 1, 2, 3]$$

where the units for  $d_{ijk}$  in this case are  $[m/V]$ . The piezoelectric coefficients defined for both effects are numerically equivalent and the units associated with one are readily converted to that of the other by simple arithmetic manipulation.

Both the direct and the converse piezoelectric coefficients are often expressed in a compressed matrix notation  $d_{ij}$ , where  $i$  describes the polarization direction and  $j$  the stress. In this notation,  $j$  ranges from 1 to 6, so that  $\sigma_1, \sigma_2$ , and  $\sigma_3$  correspond to stresses directed along the  $x_1, x_2$ , and  $x_3$  axes, and  $\sigma_4, \sigma_5$ , and  $\sigma_6$  to shear around the same axes. It is important to note that while the piezoelectric effect can be expressed as,

$$P_i = d_{ij} \sigma_j \quad [i = 1, 2, 3; j = 1, 2, \dots, 6]$$

$d_{ij}$  does not transform as a second rank tensor (Nye, 1985).

The electromechanical coupling factor,  $k^2$ , which is defined as the ratio of the output energy to input energy is typically used to evaluate the strength of the piezoelectric response of a crystal. It is determined for the material in terms of the pertinent resonant frequencies of a particular vibrational mode. The  $k^2$  values for a variety of piezoelectric materials are shown in Table 2.

TABLE 2  
Electromechanical coupling coefficients for commercially  
useful piezoelectric materials (from Jaffe et al., 1971).

MATERIAL	$k^2$
Quartz	0.01
Barium Titanate ceramics	0.16
Lead Zirconate Titanate ceramics	0.25 - 0.49
Rochelle Salt	0.81

## Piezoelectric, Pyroelectric and Ferroic Crystals

Crystals made up of acentric molecular groups have a greater probability of being piezoelectric than those containing centric groups. Consequently, many materials composed of tetrahedrally coordinated cations, including  $\alpha$ -quartz and zincblende are piezoelectric. The symmetry of the regular tetrahedron is  $\bar{4}3m$ , which is not centrosymmetric. Most piezoelectric crystals have rather complicated structures, but zincblende (cubic ZnS) is relatively simple. Zincblende belongs to crystal class  $\bar{4}3m$ , which has just one independent piezoelectric coefficient,  $P_1 = d_{14}\sigma_4$ , in matrix notation.  $P_1$  represents an electric polarization along [100] and  $\sigma_4$  is a shearing stress about [100]. Jaffe (Jaffe, 1944) described a model showing how the sign and magnitude of the piezoelectric coefficient  $d_{14}$  is related to structure. When subjected to a shearing stress  $\sigma_4$ , the crystal shears about  $x$ , changing the angle between  $y$  and  $z$  by an amount  $\epsilon_4 = s_{44}\sigma_4$ . The effect on a single tetrahedron in the zincblende structure is shown in Figure 2. When sheared about a cube axis, the two upper zinc atoms move closer to the sulfur, while the lower two move further away. To maintain four equal bonds, the sulfur atom moves down in the  $-x$  direction, toward the more distant zinc neighbors. From the geometry, the dipole moment per molecule developed along  $x$  is  $-qa\epsilon_4/4$ , where  $q$  is the charge of the sulfur ion and  $a$  is the unit cell dimension. Since there are four molecules per cell, and all tetrahedra behave alike under the shearing stress, the resultant polarization is  $P_1 = qs_{44}\sigma_4/a^2$ , giving  $d_{14} = qs_{44}/a^2$ . Substituting experimental values for  $a$ ,  $s_{44}$ , and  $d_{14}$ , Jaffe obtained  $q = 0.25e$ , a reasonable value for the charge, since the bonding is largely covalent.

By far, the most commercially important piezoelectric crystal is  $\alpha$ -quartz. When an alternating electric field is applied to an electroded crystal, it is forced into mechanical vibration via the piezoelectric effect. As the frequency of the oscillating field is varied, the crystal undergoes a series of resonances which depend on both the device geometry and the stiffness and density of the material. For a thickness shear mode, the resonant frequency is given by

$$f = \frac{1}{2t} \sqrt{\frac{c}{\rho}}$$

where  $t$  is the thickness of the crystal plate,  $\rho$  is the density, and  $c$  is the shear stiffness coefficient. Although the piezoelectric effect in quartz is comparatively small, its great utility lies in the fact that for some crystallographic cuts, the resonance frequency can be made independent of temperature. As a result, the resonance frequency is stable enough to be used in timing and frequency control standards such as tuning forks in quartz watches and crystal-controlled oscillators.

## Piezoelectric, Pyroelectric and Ferroic Crystals

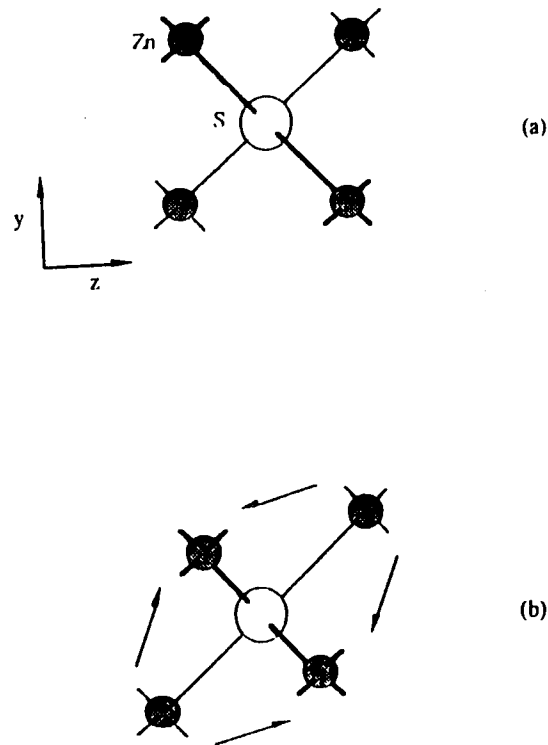


FIG. 2

A single tetrahedron of the zincblende structure, unstressed (a), and under shear stress (b). Piezoelectric coefficient  $d_{14}$  relates polarization along  $x$  to the shear stress in the  $y$ - $z$  plane (after Jaffe, 1944).

The structural origin of piezoelectricity in quartz has been discussed by Karasawa (1974). In the quartz structure, tetrahedrally coordinated silicons are connected through oxygens to form spirals around the  $z$  axis. The atomic motions accompanying the  $\alpha$ - $\beta$  transition (Young and Post, 1962) at 573°C provide the key to understanding the piezoelectric effect. On cooling through the transition, the tetrahedra rotate about the two-fold axes, with alternate tetrahedra rotating clockwise and counterclockwise, lowering the symmetry from hexagonal to trigonal. At the same time the tetrahedra expand slightly around  $z$ , causing two oxygens to move away from the center of each tetrahedron. To maintain four equal bond lengths, the silicons move laterally along the  $x$ -axis, creating the electric dipoles

## Piezoelectric, Pyroelectric and Ferroic Crystals

shown in Figure 3. In the absence of applied stress, the dipole moments of neighboring tetrahedra cancel, so that there is no net spontaneous polarization. However, when the structure is deformed by an external stress, the dipole balance is destroyed, producing a piezoelectric polarization. The principal change is in the Si-O-Si bond angle at the point of contact between neighboring tetrahedra. Figure 3 illustrates the piezoelectric effect accompanying stress along the x-axis, with dipoles combining to produce a polarization along x. The origin of other piezoelectric effects in quartz can be explained in a similar way (Karasawa, 1974).

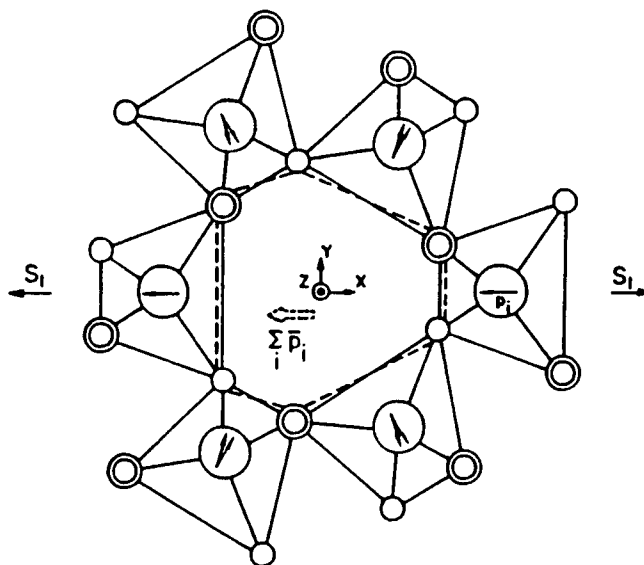


FIG. 3

Atomistic origin of the longitudinal piezoelectric effect in quartz. Dotted lines indicate the deformation resulting from a tensile stress along x. Dipole moments which cancel in the undeformed structure tilt slightly under stress to produce a piezoelectric polarization along x (after Karasawa, 1974).

Many applications of piezoelectric materials as actuators or transducers, however, require a much larger piezoelectric effect and a more efficient conversion from electrical to mechanical energy than is provided in quartz. In applications such as sonar and ultrasonic imaging,  $\text{Pb}(\text{Zr,Ti})\text{O}_3$  ceramics with a distorted perovskite structure are most frequently utilized.

## Piezoelectric, Pyroelectric and Ferroic Crystals

The piezoelectric coefficient matrix of a poled  $\text{PbZr}_{0.52}\text{Ti}_{0.48}\text{O}_3$  ceramic takes the form:

$$\begin{bmatrix} 0 & 0 & 0 & 0 & 494 & 0 \\ 0 & 0 & 0 & 494 & 0 & 0 \\ -93.5 & -93.5 & 223 & 0 & 0 & 0 \end{bmatrix}$$

where each of the numbers is in pC/N. A schematic representing the physical origin of each of the non-zero coefficients is shown in Figure 4 for the case of tetragonal  $\text{PbTiO}_3$ .

The prototype (high temperature) structure for  $\text{Pb}(\text{Zr,Ti})\text{O}_3$  is pictured in Figure 5. Below the Curie temperature, the titanium ion displaces either along the z-axis or along one of the cube body diagonals, leading to tetragonal or rhombohedral distortions, depending on the Zr:Ti ratio. A phase diagram for the solid solution is given in Figure 6. The morphotropic phase boundary marking the transition between the two regions is of especial practical interest, as it marks the composition at which the free energies of the two phases are nearly identical. In order to utilize a ceramic as a piezoelectric element, it is essential to align the polarization directions in each grain to induce a net polarization in an initially isotropic material. The more potential directions the spontaneous polarization can assume, the more likely that one will be oriented favorably with respect to the applied field in any grain of a random polycrystalline material. This, in turn, leads to a better alignment of the individual polar directions and large net piezoelectric coefficients. Near the morphotropic phase boundary, there are 14 directions (6 from the  $\langle 001 \rangle$  family in the tetragonal phase and 8 from the  $\langle 111 \rangle$  family in the rhombohedral phase) which are nearly equivalent in free energy. As a result, a very high degree of poling can be achieved in the ceramic.

Table 3 provides a set of piezoelectric coefficients for several oxide materials used in active devices. It can be seen there that while several minerals, including quartz and tourmaline have appreciable and useful piezoelectric constants, the largest  $d_{ij}$  values are demonstrated by some ferroelectric ceramics.

## Piezoelectric, Pyroelectric and Ferroic Crystals

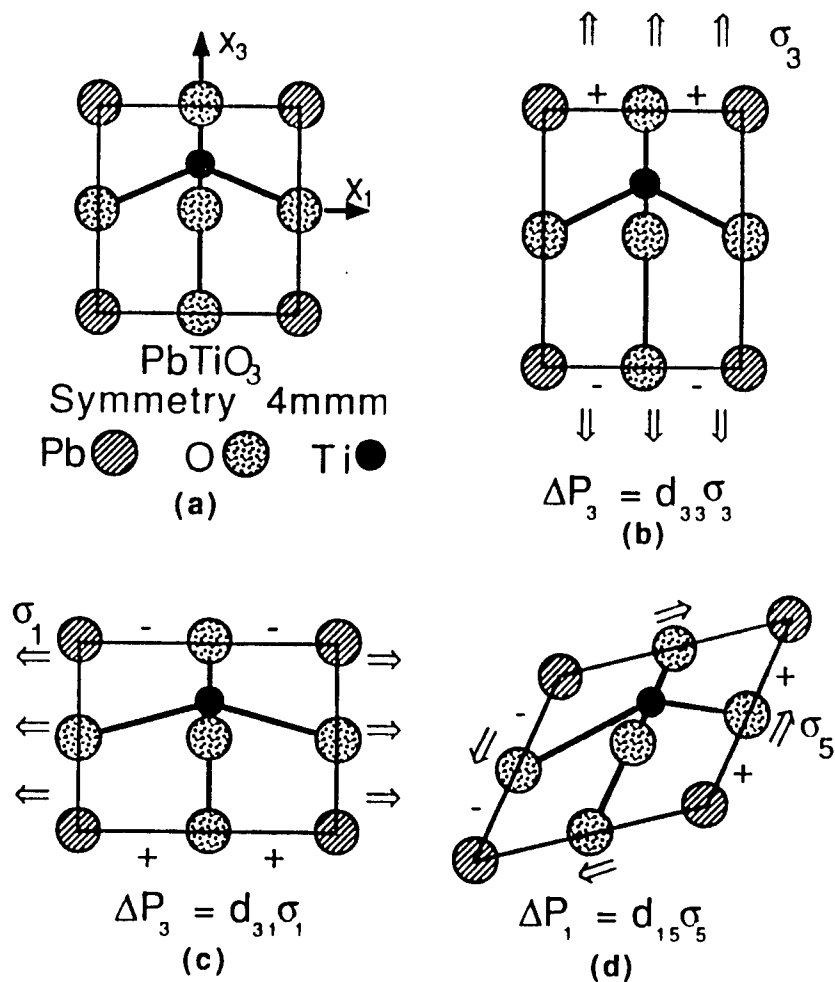


FIG. 4

Atomistic origin of the piezoelectric coefficients for tetragonal  $\text{PbTiO}_3$ . (a) Tetragonal  $\text{PbTiO}_3$  is acentric, with the titanium ion displaced from the center of the unit cell. When a tensile stress is applied to  $x_3$  as shown in (b), the  $\text{Ti}^{4+}$  ion displaces further in its off-center position, creating a positive polarization in the same direction:  $P_3 = d_{33}\sigma_3$ . If the stress is applied along  $x_1$  (c), the dipole moment of the unit cell is diminished, and a negative polarization appears. Hence  $d_{31}$  is negative while  $d_{33}$  is positive. For a shear stress about  $x_2$  (d), the dipole moment is tipped, producing polarization in the  $x_1$  direction:  $P_1 = d_{15}\sigma_5$ .

## Piezoelectric, Pyroelectric and Ferroic Crystals

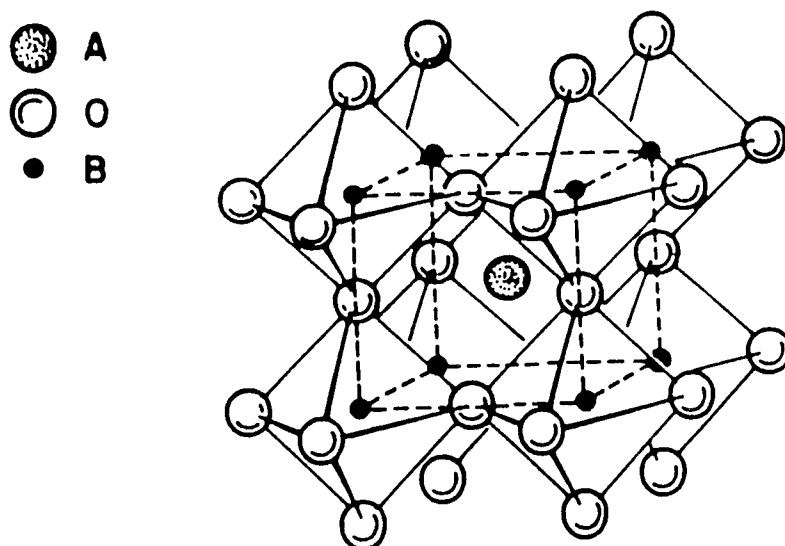


FIG. 5

A schematic of the prototype perovskite structure.

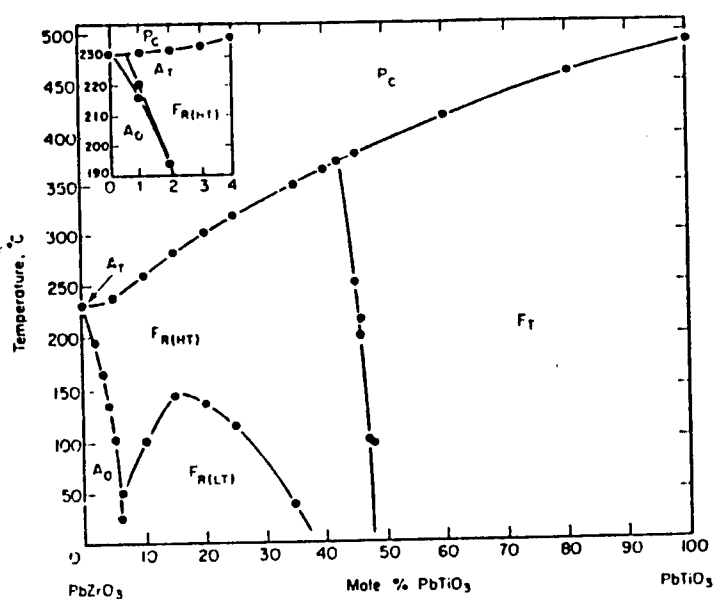


FIG. 6

The  $\text{PbTiO}_3$ - $\text{PbZrO}_3$  sub-solidus phase diagram (after Jaffe et al., 1971).

## Piezoelectric, Pyroelectric and Ferroic Crystals

TABLE 3

Piezoelectric coefficients for selected oxide materials.

MATERIAL	$d_{ij}$ (pC/N)
Quartz <sup>a</sup>	$d_{11} = -2.3$
Tourmaline <sup>b</sup>	$d_{33} = 1.9$
BaTiO <sub>3</sub> <sup>c</sup>	$d_{33} = 85.6$
PbZr <sub>0.52</sub> Ti <sub>0.48</sub> O <sub>3</sub> <sup>c</sup>	$d_{33} = 223$
Pb <sub>0.988</sub> (Zr <sub>0.52</sub> Ti <sub>0.48</sub> ) <sub>0.976</sub> Nb <sub>0.024</sub> O <sub>3</sub> <sup>c</sup>	$d_{33} = 374$

<sup>a</sup> from Nye, 1985

<sup>b</sup> from Dietrich, 1985

<sup>c</sup> From Jaffe et al., 1971

## PYROELECTRICITY

Pyroelectric crystals contain a unique polar axis, a vector direction unrelated by symmetry to any other direction in the crystal. These are, hence, regarded as "polar" crystals which possess a spontaneous polarization, the magnitude of which varies with changing temperature. The pyroelectric effect is thus defined as the change in polarization  $[\Delta P(s)_i]$  induced by a change in temperature  $[\Delta T]$  and is expressed in tensor form as:

$$\Delta P(s)_i = \pi_i \Delta T \quad [i=1,2,3]$$

Since  $\Delta P(s)_i$  is a vector (first-rank tensor) quantity and  $\Delta T$  is a zero-rank tensor, the pyroelectric coefficient  $[\pi_i]$  is also a first-rank tensor with units [C/m<sup>2</sup>K]. The sign of the polarization change is reversed when the crystal is heated or cooled.

Only ten of the twenty piezoelectric point groups are polar and in all but two of these (1 and m) the polarization vector is oriented parallel to a rotation axis. The polarization direction is along the c-axis in crystal classes 6mm6, 4mm, 4, 3mm, 3, and mm2, and along the b-axis for that with point group symmetry 2.

The pyroelectric effect actually observed for a particular crystal is generally comprised of two distinct effects commonly referred to as Primary



## Piezoelectric, Pyroelectric and Ferroic Crystals

and Secondary Pyroelectricity. If the shape and size of the specimen are held constant under "clamped" conditions on heating, the Primary or "True" pyroelectric effect is observed. An additional contribution to the total pyroelectricity arises through the secondary pyroelectric effect when the specimen is free to deform. In this case, the strain generated in the sample due to thermal expansion results in a polarization via the piezoelectric effect. The secondary effect is typically significantly larger than the primary effect so that for most crystals measurement of the pyroelectric effect under free conditions reflects essentially that associated with the piezoelectric response of the material. Consequently, for many materials, the pyroelectric coefficients can be estimated from a knowledge of the thermal expansion, the elastic and the piezoelectric coefficients. i.e.

$$\left(\frac{\delta P}{\delta T}\right)_{\sigma} = \left(\frac{\delta P}{\delta T}\right)_{\epsilon} + \left(\frac{\delta P}{\delta \sigma}\right)_T \left(\frac{\delta \sigma}{\delta \epsilon}\right)_T \left(\frac{\delta \epsilon}{\delta T}\right)_{\sigma}$$

where the first term on the right hand side corresponds to the primary pyroelectric effect and the other to the secondary effect. When the first term is negligible,

$$\pi_i \approx \frac{d_{ijk} \alpha_{ln}}{s_{lnjk}}$$

Pyroelectricity was first observed in gem-quality tourmaline crystals. Tourmaline has a variable composition, most often described as  $XY_3Z_6B_3Si_6O_{27}(O,OH,F)_4$  where X is a large cation with 9-10 coordination, Y and Z are octahedral cations, and B is triangularly coordinated. It crystallizes into a complex structure in the rhombohedral system and is pyroelectric along the unique c axis. This property has earned it the name "aschentrekker" or "ash-drawer," for its ability to attract ash particles when the crystal is heated (Dietrich, 1985).

One of the simplest pyroelectric crystals is wurtzite, the hexagonal form of ZnS (see Fig. 7). Zincite, or hexagonal ZnO, also has the wurtzite structure and is pyroelectric. The crystal class is 6mm, for which the polar axis and  $P_s$  are parallel to c, the six-fold symmetry axis. The sign and magnitude of the spontaneous polarization in wurtzite can be estimated from the structure (Newnham, 1975). The wurtzite structure can be visualized as alternating layers of positive (zinc) and negative (sulfur) ions with equal numbers in each layer stacked perpendicular to c. Since each layer contains all positive or all negative ions, the polar chains in Figure 7b can be used to calculate  $P_s$ . In computing  $P_s$ , a neutral portion of the

## Piezoelectric, Pyroelectric and Ferroic Crystals

crystal is chosen, and  $p$ , the dipole moment per molecule is calculated from  $p = 1/n \sum_i q_i r_i$ . Here  $n$  is the number of molecules, and  $q_i$  and  $r_i$  are the charge and position vector for the  $i^{\text{th}}$  ion, respectively. While the choice of origin is unimportant for a neutral collection of charges ( $\sum_i q_i = 0$ ),  $p$  does depend on the crystal boundary. If the specimen is terminated as in Figure 7b, as would seem most likely,  $p = +Q(1/2 - u) c$ .

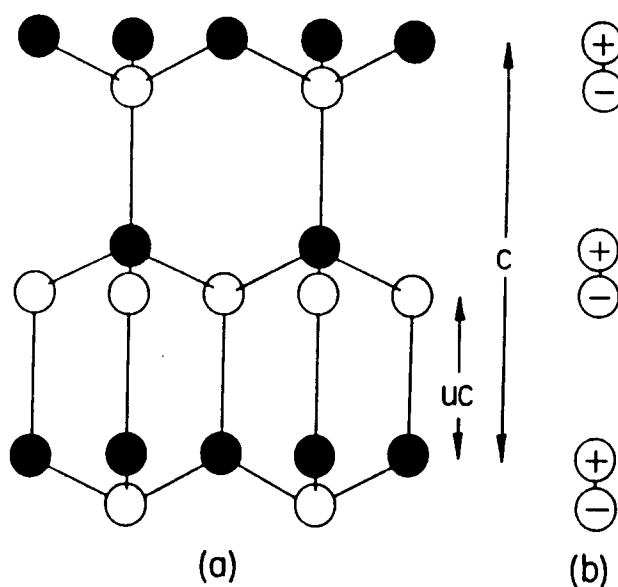


FIG. 7

A projection of the wurtzite structure along (010) and the equivalent polar chain.

The spontaneous polarization is related to the dipole moment per molecule by  $P_s = N p$ ,  $N$  being the number of molecules per unit volume. Since there are two molecules in a cell of volume  $\sqrt{3}(a^2 c/2)$  the spontaneous polarization is

$$\frac{4Q(1/2-u)}{\sqrt{3} a^2}$$

While the magnitude of the spontaneous polarization is difficult to measure directly, changes in  $P_s$  with temperature, i.e. the pyroelectric effect, are more readily detectable.

Large pyroelectric coefficients are often tied to the approach of a phase transition in the material. This is not surprising as near the phase

## Piezoelectric, Pyroelectric and Ferroic Crystals

transformation significant structure changes (and hence in some cases, polarization changes) occur over a small temperature interval. Such behavior is characteristic of many of the displacive perovskite ferroelectrics, where the ferroelectric-paraelectric transition corresponds to the reversion of a polar low temperature phase to a centric prototype phase. Figure 8 shows a typical curve of spontaneous polarization versus temperature for a normal ferroelectric with a first-order phase transition. The pyroelectric coefficient is the derivative of this curve. Near the transition temperature, where the polarization is changing most rapidly, the pyroelectric coefficient is large. Well below the transition temperature, although the polarization itself is larger, the change in polarization with temperature is smaller, and the pyroelectric coefficient drops off. A collection of pyroelectric coefficients for several mineral and commercial pyroelectric materials is given in Table 4.

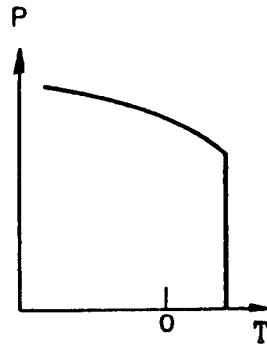


FIG. 8

Spontaneous polarization versus temperature for a normal ferroelectric with a first-order phase transition.

## FERROIC PHENOMENA

A ferroic crystal contains two or more possible orientation states or domains; under a suitably chosen driving force the domain walls move, switching the crystal from one orientation state to another. Switching may be accomplished by applying a mechanical stress [ $s_{ij}$ ], an electric field [ $E_j$ ], a magnetic field [ $H_j$ ], or some combination of the three.

Twinned crystals may be classified on the basis of the tensor properties of the twin domain, considering the relationship between the free-energy and the twin structure. This classification scheme is outlined in Table 5.

## Piezoelectric, Pyroelectric and Ferroic Crystals

Two main categories are defined: the Primary and Secondary Ferroics. The three primary ferroic phenomena are ferroelectricity, ferromagnetism, and ferroelasticity in which the orientation states differ respectively in spontaneous polarization  $[P(s)_i]$ , spontaneous magnetization  $[M(s)_i]$ , and spontaneous strain  $[\epsilon(s)_{ij}]$ . The remaining secondary ferroic phenomena listed in Table 5 are characterized by orientation states which are distinguished by terms other than the primary quantities  $P(s)_i$ ,  $M(s)_i$ , and  $\epsilon(s)_{ij}$ . It becomes readily apparent, in regarding a twinned system in this light, which forces and fields will be effective in moving twin (domain) walls, where each type of domain reorientation arises from a particular term in the free-energy function.

TABLE 4  
Pyroelectric coefficients for selected materials.

MATERIAL	$\pi_i$ (C/m <sup>2</sup> • K)
Tourmaline	$4.0 \times 10^{-6}$ a
Triglycine Sulfate	$300 \times 10^{-6}$ b
LiTaO <sub>3</sub>	$190 \times 10^{-6}$ b
Sr <sub>0.5</sub> Ba <sub>0.5</sub> Nb <sub>2</sub> O <sub>6</sub>	$600 \times 10^{-6}$ b
BaTiO <sub>3</sub>	$200 \times 10^{-6}$ b

a From Nye, 1985

b From Lines and Glass, 1977

The stability of an orientation state is governed by the free energy. The differential form of the Gibb's free energy  $[dG]$  is comprised of thermal energy and various work terms:

$$dG = SdT - \epsilon_{ij}d\sigma_{ij} - P_i dE_i - M_i dH_i \quad [i,j=1,2,3] \quad (1)$$

where  $S$  is the entropy,  $T$  the temperature,  $\epsilon_{ij}$  the strain,  $\sigma_{ij}$  the stress,  $P_i$  the polarization,  $E_i$  the electric field,  $M_i$  the magnetization, and  $H_i$  the magnetic field, all generally expressed in rationalized MKS units. Assuming that the experiments are performed under isothermal conditions, the entropy term may be neglected.

## Piezoelectric, Pyroelectric and Ferroic Crystals

TABLE 5

The classifications of primary and secondary ferroics.

FERROIC CLASS	DOMAINS DIFFER BY	SWITCHING FORCE
<b>PRIMARY</b>		
<b>Ferroelectric</b>	Spontaneous Polarization $\{P(s)_i\}$	Electric Field $\{E_j\}$
<b>Ferromagnetic</b>	Spontaneous Magnetization $\{M(s)_i\}$	Magnetic Field $\{H_j\}$
<b>Ferroelastic</b>	Spontaneous Strain $\{\epsilon(s)_{ij}\}$	Mechanical Stress $\{\sigma_{kl}\}$
<b>SECONDARY</b>		
<b>Ferroelectric</b>	Dielectric Susceptibility $\{\kappa_{ij}\}$	Electric Field $\{E_j\}$
<b>Ferroimagnetic</b>	Magnetic Susceptibility $\{\chi_{ij}\}$	Magnetic Field $\{H_j\}$
<b>Ferroelastic</b>	Elastic Compliance $\{s_{ijkl}\}$	Mechanical Stress $\{\sigma_{kl}\}$
<b>Ferroelastoelectric</b>	Piezoelectric Coefficients $\{d_{ijk}\}$	Electric Field $\{E_k\}$ Mechanical Stress $\{\sigma_{kl}\}$
<b>Ferromagnetoelastic</b>	Piezomagnetic Coefficients $\{Q_{ijk}\}$	Magnetic Field $\{H_k\}$ Mechanical Stress $\{\sigma_{kl}\}$
<b>Ferromagnetoelctric</b>	Magnetoelectric Coefficients $\{\alpha_{ij}\}$	Magnetic Field $\{H_k\}$ Electric Field $\{E_k\}$

Considering now the primary quantities appearing in the free energy function, it is generally found that each is comprised of a spontaneous component plus an induced contribution. The electric polarization can thus be expanded with contributions from a spontaneous polarization  $P(s)_i$  and several induced effects:

$$P_i = P(s)_i + \kappa_{ij}E_j + d_{ijk}\sigma_{jk} + \alpha_{ij}H_j \quad [i,j,k=1,2,3]$$

## Piezoelectric, Pyroelectric and Ferroic Crystals

where  $\kappa_{ij}$  is the electric susceptibility tensor,  $d_{ijk}$  the piezoelectric coefficients, and  $\alpha_{ij}$  the magnetoelectric tensor. In addition to the spontaneous polarization, present for any of the ten polar crystal classes, an electrically-induced polarization is always present since all materials have finite electric susceptibility coefficients. Magnetoelectricity is found only in solids with certain types of magnetic symmetry.

Similarly, the magnetization  $[M_i]$  can be expanded in terms of the spontaneous magnetization  $M(s)_i$  and induced effects arising from electric and magnetic fields and mechanical stress:

$$M_i = M(s)_i + \chi_{ij}H_j + Q_{ijk}\sigma_{jk} + \alpha_{ij}E_j \quad [i,j,k=1,2,3]$$

where  $\chi_{ij}$  is the magnetic susceptibility,  $Q_{ijk}$  the piezomagnetic coefficients, and  $\alpha_{ij}$  the magnetoelectric coefficients. Only ferromagnetic and ferrimagnetic crystals have non-zero  $M(s)_i$ . All materials possess non-zero magnetic susceptibility coefficients  $[\chi_{ij}]$ , but the induced magnetization is often very small.

Finally, the strain is measured relative to the prototype structure and can be written as a spontaneous strain plus an induced strain:

$$\epsilon_{ij} = \epsilon(s)_{ij} + s_{ijkl}\sigma_{kl} + d_{kij}E_k + Q_{kij}H_k \quad [i,j,k,l=1,2,3]$$

where  $s_{ijkl}$  is the fourth-rank elastic compliance tensor,  $d_{kij}$  is the piezoelectric coefficient tensor, and  $Q_{kij}$  are the piezomagnetic coefficients. Only the second term in this expression is always present. Piezoelectricity and piezomagnetism are null properties which disappear for certain symmetry groups, but all groups have non-zero elastic constants.

Substituting the expressions for  $P_i$ ,  $M_i$  and  $\epsilon_{ij}$  into Equation (1), combining terms, and integrating gives the thermodynamic potential  $G$ , which applies to all orientation states. The driving potential for a state shift is then:

$$\Delta G = {}^1G - {}^2G$$

where  ${}^1G$  and  ${}^2G$  represent the free energy for the first and second orientation states respectively. In the absence of external fields the energy of all orientation states is equal and  $\Delta G = 0$ . When external forces and fields are applied, the difference in free-energy for the two orientation states is:

## Piezoelectric, Pyroelectric and Ferroic Crystals

$$\begin{aligned} \Delta G = & \Delta P(s)_i E_i + \Delta M(s)_i H_i + \Delta \epsilon(s)_{ij} \sigma_{ij} + 1/2 \Delta \kappa_{ij} E_i E_j \\ & + 1/2 \Delta \chi_{ij} H_i H_j + 1/2 \Delta s_{ijkl} \sigma_{ij} \sigma_{kl} + \Delta d_{ijk} E_i \sigma_{jk} \\ & + \Delta Q_{ijk} H_i \sigma_{jk} + \alpha_{ij} H_i H_j \quad [i,j,k,l=1,2,3] \end{aligned}$$

where each term of the free-energy function is represented as the difference in the property with respect to the 1 and 2 orientation states.

A wide variety of ferroic phenomena is possible depending on which terms in  $\Delta G$  are important. Ferroic phenomena are not mutually exclusive; for example, in  $\text{BaTiO}_3$ ,  $90^\circ$  domains are both ferroelectric and ferroelastic. Almost all types of mimetic twins belong to one or more of the ferroic classes.

## PRIMARY FERROICS

A more detailed discussion of primary ferroic phenomena including ferroelectricity follows. Specific mineral examples are described for each.

## FERROELECTRICITY

A ferroelectric is a pyroelectric material possessing a reversible polarization which is manifested in a dielectric hysteresis loop. Domains in a ferroelectric differ in spontaneous polarization  $P(s)$  and can be switched by an electric field. Ferroelectric crystals become paraelectric above a temperature known as the Curie temperature (or Curie point)  $T_C$ , transforming to a non-polar parent [prototype] phase. A selection of both mineralogical and commercially important ferroelectric materials, along with their values for  $P(s)$  and  $T_C$  is given in Table 6.

The ferroelectric mineral colemanite  $[\text{CaB}_3\text{O}_4(\text{OH})_3 \cdot \text{H}_2\text{O}]$  was initially investigated by Goldsmith (1956). The paraelectric  $[2/m] \rightarrow$  ferroelectric  $[2]$  transition occurs for natural specimens in a range  $-7^\circ$  to  $0^\circ\text{C}$  depending on the concentration of impurities. Spontaneous polarization develops along the monoclinic  $b$ -axis, accompanied by the formation of  $180^\circ$  domains. A structural description of the ferroelectric effect in colemanite has been presented by Hainsworth and Petch (1966). A state of dynamic disorder involving one of the hydrogen atoms of the water molecule and one from an adjacent hydroxyl group exists above  $T_C$ . Ordering of these atoms occurs as the temperature is decreased through the transition, accompanied by small displacements of other atoms from their centric positions resulting in the generation of an acentric structure and ferroelectricity.

TABLE 6  
Some standard ferroelectric materials. Data from Lines and Glass, 1977.

MATERIAL	$T_c$ ( $^{\circ}\text{C}$ )	$P$ ( $\mu\text{C}/\text{cm}^2$ )	MEASUREMENT $T$ ( $^{\circ}\text{C}$ )	SYMMETRY
$\text{BaTiO}_3$	135	26	23	$m\bar{3}m$ F 4mm
$\text{PbTiO}_3$	490	>50	23	$m\bar{3}m$ F 4mm
$\text{LiNbO}_3$	1210	71	23	$\bar{3}m$ F 3m
$\text{Bi}_4\text{Ti}_3\text{O}_{12}$	675	>30		$4/m\bar{m}m$ F m
$\beta\text{-Gd}_2(\text{MoO}_4)_3$	163	0.185	25	$\bar{4}2m$ F mm2
$\text{CaB}_3\text{O}_4(\text{OH})_3 \cdot \text{H}_2\text{O}$	-7	0.65	-70	$2/m$ F 2
$\text{KH}_2\text{PO}_4$	-150	4.75	-177	$\bar{4}2m$ F mm2
$(\text{NH}_2\text{CH}_2\text{COOH})_3 \cdot \text{H}_2\text{SO}_4$	49	2.8	20	$2/m$ F 2



## Piezoelectric, Pyroelectric and Ferroic Crystals

Ferroelectric oxides with the perovskite, tungsten-bronze, pyrochlore, and bismuth titanate layer structures all have high dielectric constants and high refractive indices, and all contain corner-linked octahedral networks of  $\text{Ti}^{4+}$ ,  $\text{Nb}^{5+}$ , or other  $d^0$  ions. In most commercial electroceramics used as capacitors or transducers, these transition metal elements are the highly polarizable "active" ions which promote ferroelectricity.

Two major groups of active ions may be identified with respect to the periodic system as shown in Figure 9; both are near electronic "cross-over" points where different types of atomic orbitals are comparable in energy and where hybrid bond formation is prevalent. The first group, typified by  $\text{Ti}^{4+}$ ,  $\text{Nb}^{5+}$ , and  $\text{W}^{6+}$ , are  $d^0$  ions octahedrally coordinated to oxygen. The electronic cross-over for  $\text{Ti}^{4+}$  involves the mixing of 3d, 4s, and 4p orbitals which combine with the  $\sigma$ - and  $\pi$ -orbitals of its six  $\text{O}^{2-}$  neighbors to form a number of molecular orbitals for the  $(\text{TiO}_6)^{8-}$  complex. The bond energy of the complex can be lowered by distorting the octahedron to a lower symmetry. This leads to dipole moments, ferroelectricity, and large dielectric constants. The second group of active elements contributing to polar distortions are the lone-pair ions (see Fig. 9). Lone-pair ions have

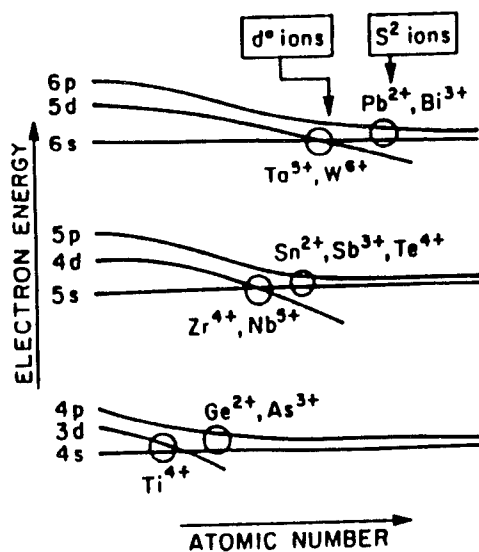


FIG. 9

Active ions promoting ferroelectricity and high dielectric constants in oxides fall into two categories: the  $d^0$  ions, typified by  $\text{Ti}^{4+}$  and  $\text{Nb}^{5+}$ , and the lone pair  $s^2$  ions such as  $\text{Pb}^{2+}$  and  $\text{Bi}^{3+}$ . Both groups lie near energy level crossovers, giving rise to hybrid bond formation and asymmetric structures.

## Piezoelectric, Pyroelectric and Ferroic Crystals

two electrons outside a closed shell in an asymmetric sp hybrid orbital. Among the oxides, the most important of these lone-pair ions are  $\text{Pb}^{2+}$  and  $\text{Bi}^{3+}$  which are constituents in a number of ferroelectric materials [ $\text{PbTiO}_3$ ,  $\text{Bi}_4\text{Ti}_3\text{O}_{12}$ ,  $\text{PbNb}_2\text{O}_6$ ] with high Curie temperatures. In many of these compounds,  $\text{Pb}^{2+}$  and  $\text{Bi}^{3+}$  are in pyramidal coordination with oxygen and therefore contribute to the spontaneous polarization.

The perovskite ferroelectrics are among the most numerous and the most popular for a variety of applications due in large part to the many types of substitutions the structure can so readily accommodate. The classic example of a perovskite ferroelectric is  $\text{BaTiO}_3$ , which has been extensively investigated and utilized in a number of applications. The crystal structure of  $\text{BaTiO}_3$  undergoes three ferroelectric phase transitions upon cooling from its cubic parent phase as shown in Figure 10 with the generation of the spontaneous polarization occurring as indicated. Due to

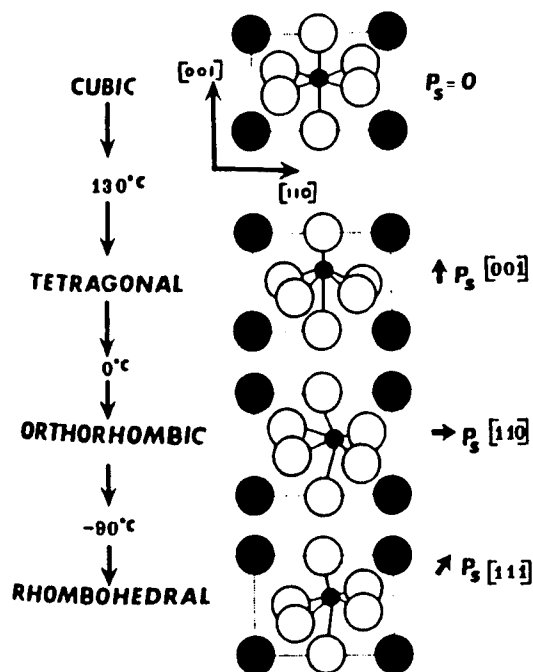


FIG. 10

A schematic of the  $\text{TiO}_6$  octahedra in  $\text{BaTiO}_3$  demonstrating the distortions that occur during the ferroelectric phase transitions.

## Piezoelectric, Pyroelectric and Ferroic Crystals

the presence of the highly polarizable Ti ion,  $\text{BaTiO}_3$  has a very large dielectric constant ( $\kappa \sim 1000$ , in contrast to most other oxides, for which  $\kappa \sim 5-15$ ). This makes it particularly useful in charge storage devices, and as a result most multilayer capacitor formulations are based on modified  $\text{BaTiO}_3$  compositions. Substitutions at either the A-site or B-site or both sites of the perovskite lattice effect many interesting and useful changes in the material.

The substitution of smaller divalent cations for barium in  $\text{BaTiO}_3$  modifies the transition temperatures; the three most commonly used "Curie Point Shifters" are  $\text{Pb}^{2+}$ ,  $\text{Sr}^{2+}$ , and  $\text{Ca}^{2+}$ . A modest concentration of  $\text{Pb}^{2+}$  raises  $T_c$ ,  $\text{Sr}^{2+}$  lowers it, while  $\text{Ca}^{2+}$  has a much smaller effect as shown in Figure 11. Divalent Pb is one of the very few modifiers which increases the transition temperature; the tetragonal pyramidal coordination favored by  $\text{Pb}^{2+}$  stabilizes the tetragonal phase with respect to the adjacent cubic and orthorhombic phases. The effect of all three of the Curie point shifters is to destabilize the orthorhombic and rhombohedral phases of  $\text{BaTiO}_3$  and the lower two transition temperatures (see Fig. 11) are seen to decrease with increasing concentrations of  $\text{Pb}^{2+}$ ,  $\text{Sr}^{2+}$ , or  $\text{Ca}^{2+}$ . The opposite effect is achieved by replacing titanium with larger tetravalent ions. Substitution of  $\text{Zr}^{4+}$  or  $\text{Sn}^{4+}$  for  $\text{Ti}^{4+}$  causes a convergence of the three transition temperatures.

A number of different types of domain walls are found in  $\text{BaTiO}_3$ . The tetragonal phase has  $180^\circ$  and  $90^\circ$  walls. Orthorhombic domain walls separate regions differing in spontaneous polarization by  $60^\circ$ ,  $90^\circ$ , and  $180^\circ$ , while, for the rhombohedral phase, there are  $180^\circ$  and  $70.5^\circ$  walls. Donor and acceptor dopants have a pronounced effect on the mobility of domain walls. Acceptor doping enhances domain wall motion whereas donor-doping tends to impede it. Acceptor-dopants such as  $\text{K}^+$  or  $\text{Fe}^{3+}$  create oxygen vacancies in  $\text{BaTiO}_3$  [ $(\text{Ba}_{1-x}\text{K}_x)\text{Ti}(\text{O}_{3-x/2}\square_{x/2})$  and  $\text{Ba}(\text{Ti}_{1-x}\text{Fe}_x)(\text{O}_{3-x/2}\square_{x/2})$ ] which, compared with cation vacancies, diffuse much faster due to the proximity of oxygen sites. Defect dipoles in acceptor-doped  $\text{BaTiO}_3$ , consisting of paired iron atoms and oxygen vacancies, realign more easily than do the corresponding dipoles in the donor-doped material. Thus the defect dipoles in acceptor-doped  $\text{BaTiO}_3$  align with the spontaneous polarization of the domain structure to pin domain walls.

Ordered perovskite structures also occur with the substitution of cations of the appropriate size and valence on the A- or B-sites of the lattice. The  $\text{Ba}(\text{Bi}_{0.5}\text{Nb}_{0.5})\text{O}_3$  structure, for example, has a cubic unit cell with doubled lattice parameters consisting of eight perovskite-like cells (see Fig. 12). Bismuth and niobium ions occupy alternate octahedral sites

## Piezoelectric, Pyroelectric and Ferroic Crystals

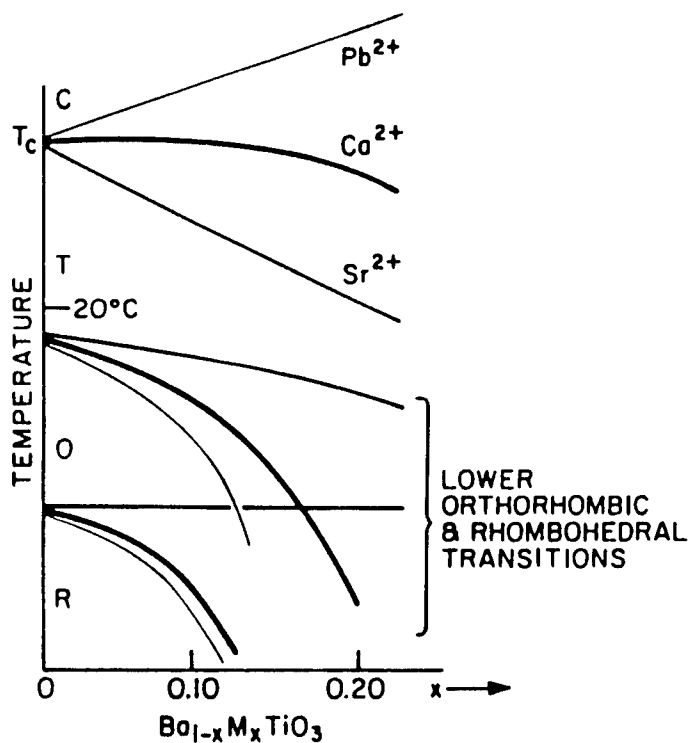


FIG. 11

Additions of  $\text{Pb}^{2+}$ ,  $\text{Sr}^{2+}$  and  $\text{Ca}^{2+}$  affect the Curie temperature of  $\text{BaTiO}_3$  in different ways, although all three lower the transitions to the orthorhombic and rhombohedral phases.

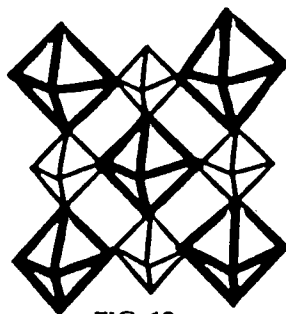


FIG. 12

Alternating large and small octahedra in the ordered perovskite.

## Piezoelectric, Pyroelectric and Ferroic Crystals

such that every (NbO<sub>6</sub>)-octahedron shares corners with six (BiO<sub>6</sub>)-octahedra, and vice versa. Although Bi<sup>3+</sup> has a much larger ionic radius and longer bond lengths than Nb<sup>5+</sup>, the octahedra pack very efficiently when alternated in this manner. The compound Pb(Sc<sub>0.5</sub>Ta<sub>0.5</sub>)O<sub>3</sub> is a complex lead perovskite ferroelectric for which the radii of the cations sharing the B-site are similar. The relatively small difference in ionic radii of the B ions and the charge difference between the two are, in fact, sufficient to allow for an ordered structure and Pb(Sc<sub>0.5</sub>Ta<sub>0.5</sub>)O<sub>3</sub> may exist in states of order ranging from a completely random distribution of B ions to nearly perfect ordering of B' and B'' in alternating planes along <111>. The unit cell of the superstructure is face-centered with space group Fm3m in the cubic (paraelectric) phase. The ordered low temperature (ferroelectric) phase has been determined to be rhombohedral with a subcell lattice parameter of 4.072 Å and  $\alpha=89.82^\circ$ . The dipole displacement in the ferroelectric phase is along the <111> directions. It has been demonstrated for this material that normal ferroelectric behavior occurs for highly ordered specimens while more relaxor-type ferroelectric behavior is observed for partially ordered samples (Setter, 1980; Stenger and Burggraaf, 1980).

Relaxor ferroelectrics are characterized by a diffuse and dispersive paraelectric  $\rightarrow$  ferroelectric phase transition, as monitored by means of the dielectric response as a function of temperature and frequency, and optical and x-ray isotropy to temperatures well below the transition range. Relaxor ferroelectric materials are typically of the perovskite or tungsten-bronze structure-type, incorporating multiple ionic species on a particular crystallographic site. It has been determined for the Pb-based perovskite relaxors (Randall and Bhalla, 1990) that partial ordering of cations at the B-site results in the formation of temperature-sensitive polar microregions on the order of 20-800 Å which interact in a complex manner that depends, in part, on the size and arrangement of the polar regions and which ultimately leads to the observed relaxor phenomena. Among the most thoroughly studied Pb-based perovskites are Pb(Mg<sub>1/3</sub>Nb<sub>2/3</sub>)O<sub>3</sub>-PbTiO<sub>3</sub>, Pb(Zn<sub>1/3</sub>Nb<sub>2/3</sub>)O<sub>3</sub>-PbTiO<sub>3</sub>, and partially ordered Pb(Sc<sub>0.5</sub>Ta<sub>0.5</sub>)O<sub>3</sub>.

Relaxor ferroelectrics are now under investigation for a variety of commercial applications, including capacitors and electromechanical transducers. Due to the diffuse phase transition, the dielectric constant of many relaxor ferroelectrics has a broad maxima with respect to temperature. This, combined with the large absolute magnitude of the dielectric constant makes these materials attractive for capacitor applications. In addition, some relaxor ferroelectrics are also useful in electrostrictive transducers. In electrostrictive materials, induced strain is related to the square of the applied electric field, rather than the first

## Piezoelectric, Pyroelectric and Ferroic Crystals

power, as is the case for piezoelectric crystals. This is advantageous in micropositioning applications as significant strains can still be achieved, while many of the hysteretic effects associated with normal ferroelectric transducers are eliminated.

## FERROMAGNETISM

The orientation states of a ferromagnet differ in spontaneous magnetization and can be switched by a magnetic field. This broad definition encompasses ferrimagnets [magnetite] and weak ferromagnets [hematite], as well as ordinary ferromagnets [iron]. It does not include antiferromagnetic, paramagnetic, and diamagnetic substances which have no spontaneous magnetization. Such materials are not ferromagnetic but may be ferrobimagnetic.

Domains in transparent ferromagnetic and ferrimagnetic crystals are visible in polarized light because of the Faraday Effect, which involves a rotation of the plane of polarization described by:

$$\theta = \rho t \cos \theta$$

where  $\theta$  is the angle of rotation,  $\rho$  the rotation per unit thickness,  $t$  the specimen thickness, and  $\theta$  the angle between the propagation direction and the magnetization vector.

The dominant mechanism for magnetic ordering in oxides (and hence, most minerals), is the superexchange interaction. Direct exchange seldom occurs in such materials because the transition-metal ions are not in direct contact, but interact via an intermediate oxygen anion. In FeO, for example, two iron ions,  $M_1$  and  $M_2$ , on opposite sides of an oxygen ion interact through a p-orbital of oxygen (see Fig. 13). Since the oxygen ion is not fully ionized, its outer electrons spend time on the neighboring transition-metal ions. When it enters the d-shell of one of the  $Fe^{2+}$ , in which the d-orbitals of the cation are more than half full, the oxygen electron spin is antiparallel to those of the metal ion, in accordance with Hund's rule. Meanwhile the other electron in the same oxygen p-orbital is on the opposite side of the oxygen ion because of the coulomb repulsion between two electrons in the same p-orbital. While there, the second electron (whose spin is antiparallel to the first electron because of the Pauli exclusion principle) also interacts with transition metal ions and its spin will again be antiparallel to that of the metal ion. The antiferromagnetic superexchange thus arises from the alignment as shown below: the first metal atom accepts an electron with antiparallel spin from an oxygen neighbor. The spins of the two electrons in the same oxygen p-orbital are

antiparallel, and the second electron spends part of its time in parallel alignment with the d-electrons of the second metal ion. A similar situation occurs when the d-electron shell of the transition metal ion is less than half full, again resulting in antiferromagnetic superexchange. The oxygen electrons enter the metal atom d-shell parallel to the net spin, but since the same thing happens to the other electron, the interaction remains antiferromagnetic. Superexchange is strongest when the angle  $M_1-O-M_2$  is  $180^\circ$ , allowing maximum overlap of the p-orbital with the two metal ions. The interaction weakens as the angle approaches  $90^\circ$ , even though the metal-metal distance may be shorter.

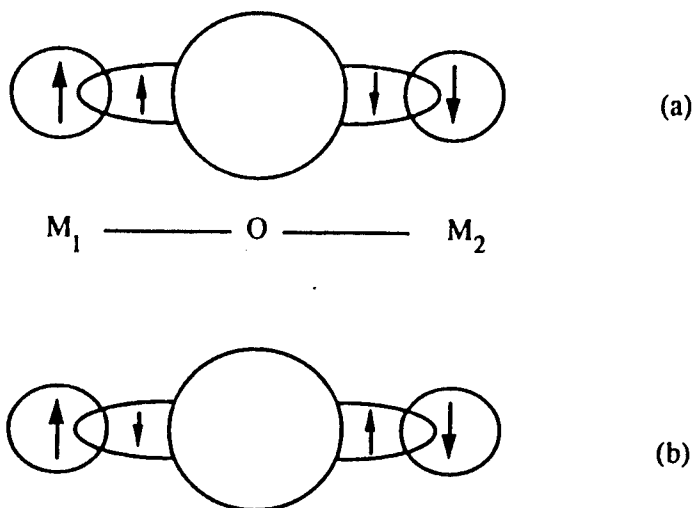


FIG. 13

The  $180^\circ$  superexchange interaction when the transition metal shell is  
(a) less than half full and (b) more than half full.

Among oxides, antiferromagnetism is much more common than ferromagnetism or ferrimagnetism. Superexchange is a strong interaction, leading to magnetic transition temperatures comparable to metals. Ferromagnetic ordering in Fe occurs at 1040 K, antiferromagnetism in hematite ( $\alpha\text{-Fe}_2\text{O}_3$ ) at 950 K, and ferrimagnetism in magnetite ( $\text{Fe}_3\text{O}_4$ ) at 860 K.

$\text{Fe}_3\text{O}_4$  has the spinel structure, in which the oxygen ions are tetrahedrally coordinated, as are 1/3 of the cations. The remaining cations

### Piezoelectric, Pyroelectric and Ferroic Crystals

are octahedrally coordinated. The coordination for a single oxygen is shown in Figure 14. If the tetrahedral cation is oriented with spin up, then the superexchange interaction through the oxygen forces all of the octahedral cations to be spin down. The net imbalance between the tetrahedral and octahedral ions ( $1/3$  vs.  $2/3$ ), leads to the net ferrimagnetism at temperatures below  $\sim 860\text{K}$ .

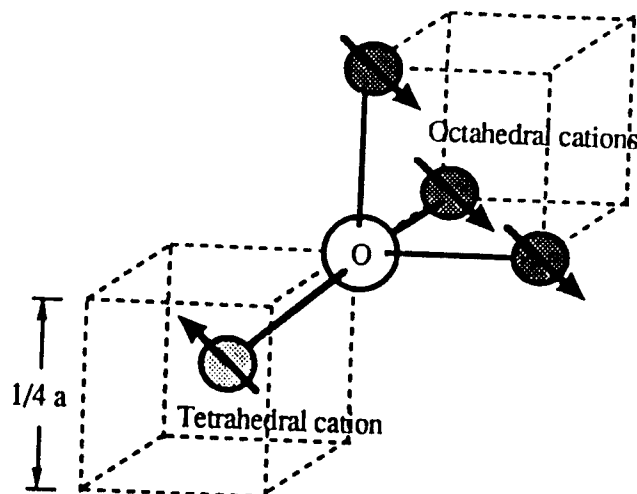


FIG. 14

The coordination of one oxygen in the spinel structure showing the superexchange interaction between the tetrahedral cation and the octahedral cations.

Hematite,  $\alpha\text{-Fe}_2\text{O}_3$ , is similar to FeO in that the dominant magnetic ordering is antiferromagnetic. There is, however, a small ferromagnetic component along (111). Mineralogists generally assign hematite to trigonal class  $\bar{3}m$ , but the magnetic point symmetry is  $2/m$  at room temperature. Antiferromagnetic crystals often exhibit weak (parasitic) ferromagnetism when the ferromagnetic component does not violate the symmetry elements of the antiferromagnetic spin array (Birss, 1964). In hematite, weak spontaneous magnetization appears along the monoclinic two-fold axis, corresponding to one of the three diad axes in  $\bar{3}m$ . At 250K, the spin direction changes to the rhombohedral axis [111], and the weak ferromagnetic effect disappears. Below the spin-flop transition, the magnetic point group is  $\bar{3}m$ .



## FERROELASTICITY

Ferroelasticity is a type of mechanical twinning in which the lattice reorients rapidly in response to a mechanical stress. There is no diffusion or breaking of chemical bonds, only small rearrangements with atomic displacements on the order of  $[0.1\text{\AA}]$ . Ferroelastic twinning is accompanied by a change in form associated with the reorientation of the spontaneous strain.

Spontaneous strain is measured relative to the prototype structure. In the ferroelastic state, the crystal symmetry is reduced to a subgroup of a higher symmetry class by a small distortion, typically on the order of parts per thousand, which is a measure of the spontaneous strain  $\epsilon(s)_{ij}$ . When measured relative to the prototype structure, the  $\epsilon(s)_{ij}$  values of all orientation states are equal in magnitude. The prototype state, containing all the pseudosymmetry elements is, therefore, the zero reference for spontaneous strain. It is seen in this case then that, analogous with ferroelectricity, just as  $P(s)_i$  can be redirected by an electric field, so is it possible to reorient  $\epsilon(s)_{ij}$  with a mechanical stress.

The triclinic feldspars have been shown to twin in response to stress (Mugge and Heide, 1931; Laves, 1952; Borg and Heard, 1969) and are considered a good mineral example of ferroelasticity. The basic structural unit of the feldspar structure is the aluminosilicate framework shown in Figure 15. Two alkali or alkaline earth cations fill each of the large cavities. At high temperatures, thermal vibration enables even moderately-sized cations such as  $\text{Na}^+$  and  $\text{Ca}^{2+}$  to fill the cavities and hold the framework in a symmetric configuration. As the temperature is decreased, however, the large cavity is no longer completely "filled," and the aluminosilicate framework slumps around the stuffing cations as shown in Figure 15b. This lowers the symmetry of the low temperature phase, and gives rise to the ferroelastic spontaneous strain. The two possibilities shown in the figure constitute the two stable domain states. Under stress, conversion between the two states is possible when one has a more favorable strain. Consequently, associated with the domain wall motion is a reorientation in the spontaneous strain which leads to a net shape change for the material.

Pressure-twinning in feldspars is easier in "high-temperature" varieties, indicating that the Al-Si ordering tends to freeze-in the twin states, raising the coercive stress. Ordered albite will not twin in response to pressure because strong chemical bonds have to be broken during twinning. The Al-Si distribution in low albite has triclinic symmetry, so that Al-Si

# Piezoelectric, Pyroelectric and Ferroic Crystals

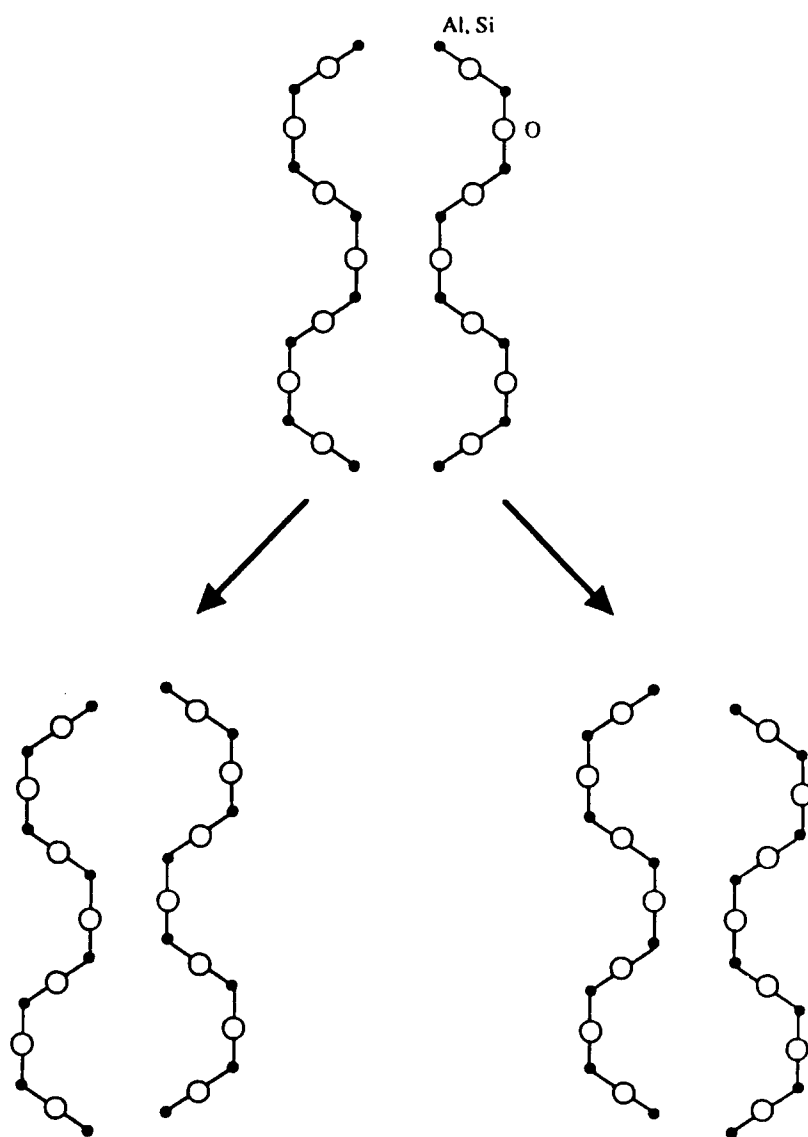


FIG. 15

The aluminosilicate framework of the feldspar structure. (a) The symmetric arrangements and (b) the two slumped domain states in the triclinic phase.

## Piezoelectric, Pyroelectric and Ferroic Crystals

interchange is required during switching from one orientation state to the other. No interchange is required in ordered anorthite where Al and Si occupy alternate tetrahedral sites. Therefore, glide twinning is easier in ordered Ca-rich plagioclases. The relation between structural state and ease of formation of pericline-albite twins by gliding has been discussed by Starkey (1967).

## SECONDARY FERROICS

The secondary ferroic phenomena are also variously represented in the mineral realm. Brief descriptions of each of these ferroic classes are presented in conclusion to this general review and important mineral and mineral-related examples of each are cited.

### FERROBIELECTRICITY

Ferrobielectricity arises from field-induced electric polarization, rather than spontaneous polarization as in a ferroelectric. Switching occurs between orientation states because of differences in the dielectric permittivity tensor. Permittivity is a second-rank tensor, like strain or magnetic susceptibility and hence any orientation states that differ in spontaneous strain will also differ in both electric and magnetic susceptibility. All ferroelastics are, therefore, potentially ferrobielectric and ferrobimagnetic. Ferrobielectricity can be expected in non-polar crystals with mimetic twinning and substantial dielectric anisotropy such as  $\text{SrTiO}_3$ , which is also ferroelastic, and  $\text{NaNbO}_3$  (Newnham, 1974).

### FERROBIMAGNETISM

Anisotropic magnetic susceptibility may lead to ferrobimagnetism. Magnetic susceptibility is a polar second-rank tensor like strain and electric permittivity; therefore, ferrobimagnetism has the same symmetry requirements as ferroelasticity and ferrobielectricity. Materials which possess a spontaneous magnetization will exhibit a ferromagnetic effect; this much stronger effect typically dominates and ultimately masks any ferrobimagnetism present in the crystal. Ferrobimagnetism is most likely to occur in antiferromagnetic crystals since the  $\chi_{ij}$  is relatively small and isotropic in paramagnetic and diamagnetic solids. An important mineral example of this ferroic class is bunsenite  $[\text{NiO}]$  which is also a ferroelastic (Roth, 1960).

## FERROBIELASTICITY

The orientation states in a ferrobielastic differ in elastic compliance. It is a second-order effect in which the strain difference between orientation states is induced by applied stress. When the stress is removed, the induced strain and the difference in free energy disappear also. Domain changes under stress can be observed optically because of differences in the photoelastic tensor for the two twin segments. Photoelasticity, the change in refractive index with stress, is a fourth-rank tensor like elasticity. Orientation states differing in elastic constants will also differ in photoelastic coefficients.

A classic ferrobielastic crystal is  $\alpha$ -quartz (Aizu, 1973; Laughner, 1982). Dauphiné or electrical twins are induced in quartz with the application of a stress. When referred to the same axes, the Dauphiné twin orientations differ with respect to the component of the elastic compliance  $s_{1123}$ ; therefore a uniaxial stress applied  $45^\circ$  to  $x_2$  and  $x_3$  is effective in switching the ferrobielastic domains. Atomic movements are small and do not involve the breaking of Si-O bonds; in shifting from one orientation state to the other, silicon atoms are displaced by  $0.3\text{\AA}$  while the oxygen atoms move about twice that amount. The shape of the induced twins, which typically take the form of long-thin stripes or somewhat thicker wedges running parallel to  $x_3$  or large volume diffuse twins, depends upon the experimental conditions and the stress history of the specimen. It has been shown (Laughner, 1982) that with repeated cycling, heating of the sample, and slow stress rates the coercive stress decreases and a corresponding variation in the twin shape is observed. Striped twins induced under the highest coercive stress conditions are the lowest volume twins appearing on the  $x_1$  face of the sample. Intermediate coercive stresses produce the wedge-shaped twins which occupy a higher volume than the striped twin, while the diffuse twins, generated under the lowest coercive stress conditions, are of the greatest size, tending to occupy the entire crystal volume with increasing applied stress.

The motion of ferrobielastic twin walls in quartz is evidently thermally-activated (Laughner, 1982) whereby the movement of atoms during a twinning event occurs as a result of the ferrobielastic response coupled with thermal vibration such that the thermal energy supplements that associated with the bias so as to more effectively drive twin wall motion. An important contribution to twin nucleation has also been identified in the lattice distortions associated with the presence of defects (Laughner, 1982).

## Piezoelectric, Pyroelectric and Ferroic Crystals

## FERROELASTOELECTRICITY

The domain states of a true ferroelastoelectric differ in the piezoelectric tensor, when referred to a common set of axes. The crystal can be switched from one state to another when an electric field and a mechanical stress are applied simultaneously. Both forces are required to switch a true ferroelastoelectric, as it is neither ferroelectric nor ferroelastic. Since all polar classes are potentially ferroelectric, a likely source of ferroelastoelectrics are the ten non-polar piezoelectric classes:  $222$ ,  $32$ ,  $4$ ,  $\bar{4}2m$ ,  $6$ ,  $\bar{6}m2$ ,  $622$ ,  $23$ , and  $\bar{4}3m$ . Minerals such as quartz and sal ammonium  $[\text{NH}_4\text{Cl}]$  are excellent examples of potentially ferroelastoelectric crystals (Newnham, 1974).

## FERROMAGNETOELASTICITY

The domains of a ferromagnetoelastic material differ in piezomagnetic coefficients which are switched by simultaneously applying a mechanical stress and a magnetic field. Crystals with magnetic symmetry  $3m$  are potentially piezomagnetic (Birss, 1964). Siderite  $[\text{FeCO}_3]$  (Pickart, 1960) is an important example of a ferromagnetoelastic which is of magnetic point group  $3m$  and is antiferromagnetic below 30 K. Switching of the  $180^\circ$ -type domains in this material occurs when a magnetic field is directed along  $x_1$  and a shearing stress is imposed about  $x_1$  (Borovik-Ramanov et al., 1962).

## FERROMAGNETOELECTRICITY

The orientation states in a ferromagnetoelectric crystal differ in magnetoelectric coefficients. The coupling between the electric and magnetic variables of a material is called the magnetoelectric effect; an induced magnetization linearly proportional to an applied electric field. The existence of the magnetoelectric effect may be predicted by symmetry arguments (Landau and Lifshitz, 1958) which also serve to demonstrate that long-range magnetic order is a necessary, although not sufficient, requirement. Magnetoelectricity is permissible in 58 of the 90 magnetic point groups (Birss, 1964) and has been studied in several materials including eskolaite  $[\text{Cr}_2\text{O}_3]$ , triphylite  $[\text{LiFePO}_4]$  (Bertraut and Mercier, 1971; Santoro and Newnham, 1967), and lithiophilite  $[\text{LiMnPO}_4]$ .

## SUMMARY

Pyroelectricity and piezoelectricity are odd-ranked tensor properties which disappear in centrosymmetric crystals. Zincite and tourmaline have modest pyroelectric effects which develop along the [001] polar axes. Larger pyroelectric coefficients are observed in ferroelectric crystals such as triglycine sulfate.

Synthetic quartz crystals have maintained a strong position in the transducer market despite their rather small piezoelectric coefficients. The large mechanical  $Q$  coefficients of quartz give rise to extremely sharp electromechanical resonances which are useful in controlling oscillator frequencies and timing devices. Thermal stability is obtained for special orientations in which the resonant frequency is independent of temperature.

For power applications, however, quartz has been replaced by poled piezoelectric ceramics made of PZT (lead zirconate titanate). These ferroelectric ceramics have much larger piezoelectric coefficients because of the polar displacements accompanying the paraelectric-ferroelectric phase transformation, and the extrinsic effects caused by domain wall motion. PZT ceramics are used in low-frequency applications such as spark generators and sonar systems, and as high-frequency transducers for biomedical and non-destructive-evaluation systems. The electromechanical energy conversion approaches 50% for PZT and PMN (lead magnesium niobate).

As pointed out, the very best piezoelectric and pyroelectric materials are ferroelectric in nature. Ferroelectrics are part of a very large family of ferroic materials characterized by moveable domain walls. These walls contribute strongly to the high dielectric constant of capacitor dielectrics and to the high magnetic susceptibility of the soft ferrites used as memory elements and transformers. In addition to ferroelectric and ferromagnetic solids, there is a third class of primary ferroics characterized by reversible mechanical twinning. Examples of such ferroelastic materials include the triclinic feldspars, zirconia, and the  $90^\circ$  walls in barium titanate. The various types of primary and secondary ferroic phenomena were derived from a free energy difference between domain states. Based on such a scheme, it becomes immediately apparent what orientation and combination of fields and forces will be effective in moving domain walls. Examples of these more unusual and underutilized ferroic effects were presented.

## Piezoelectric, Pyroelectric and Ferroic Crystals

## REFERENCES

- Aizu, K. (1973) Second-order ferroic state shifts. *J. Phys. Soc. Japan* 34, 121-128.
- Bertraut, E. F. and Mercier, M. (1971) Magnetoelectricity in theory and experiment. *Mat. Res. Bull.* 6, 907-922.
- Birss, R. S. (1964) *Symmetry and Magnetism*. North-Holland Publishing Co., Amsterdam, 252.
- Borg, I. Y. and Heard, H. C. (1969) Mechanical twinning and slip in elastically deformed plagioclases. *Contrib. Mineral Petrol.* 23, 128-135.
- Borovik-Romanov, A. S., Aleksanjan, G. G., and Rudashevskij, E. G. (1962) *Int. Conf. on Magnetism and Crystallography, Kyoto, Japan, Pap.* 155.
- Dietrich, R. V., (1985) *The Tourmaline Group*. Van Nostrand Reinhold Company, New York. p. 166.
- Goldsmith, G. J. (1956) Ferroelectricity in colemanite. *Bull. Am. Phys. Soc.* 1, 322.
- Hainsworth, F. N. and Petch, H. E. (1966) The structural basis of ferroelectricity in colemanite. *Can. J. Phys.* 44, 3083-3107.
- Jaffe, B., Cook, W. R., and Jaffe, H. (1971) *Piezoelectric Ceramics* Academic Press Ltd., India.
- Jaffe, H. (1944) Calculation of the piezoelectric effect in ionic lattices of the zinc blende type. *Phys. Rev.* 66, 357-358.
- Karasawa, S. (1974) Origin of piezoelectricity in an  $\alpha$ -quartz. *Jpn. J. Appl. Phys.* 13, 799-803.
- Landau, L. D. and Lifshitz, E. M. (1960) *Electrodynamics of Continuous Media*. Addison-Wesley Publishing Co., Reading, Massachusetts, p. 119.
- Laves, F. (1952) Mechanische Zwillungsbildung in Feldspaten in Abhängigkeit von Ordnung/unordnung der Si/Al-Verteilung innerhalb des  $(\text{Si,Al})_4\text{O}_8$ -Gerüsts. *Naturwissenschaften* 39, 546-547.
- Laughner, James W. (1982) Induced dauphiné twinning in quartz. Ph.D. Thesis, The Pennsylvania State University.
- Lines, M. E. and Glass, A. M. (1977) *Principles and Applications of Ferroelectrics and Related Materials*. Clarendon Press, Oxford.
- Mugge, O. and Peterson, S. W. (1931) Einfache schiebungen am anorthit. *Neues Jahrb. Mineral. Abt. A* 64, 163-169.
- Newnham, R. E. (1975) *Structure-Property Relations*. Springer-Verlag, New York 80-82.
- Newnham, R. E. (1974) Domains in Minerals. *Am. Mineral.* 59, 906-918.
- Nye, J. F. (1985) *Physical Properties of Crystals: Their representation by tensors and matrices*. Clarendon Press, Oxford.

## Piezoelectric, Pyroelectric and Ferroic Crystals

- Pickart, S. J. (1960) Antiferromagnetic ordering in  $\text{FeCO}_3$ . *Bull. Am. Phys. Soc.* 5, 357.
- Randall, C. A. and Bhalla, A. S. (1990) Nanostructural-property relations in complex lead perovskites. *Jap. J. Appl. Phys.* 29, 327.
- Roth, W. L. (1960) Neutron and optical studies of domains in  $\text{NiO}$ . *J. Appl. Phys.* 31, 2000-2011.
- Santoro, R. P. and Newnham, R. E. (1967) Antiferromagnetism in  $\text{LiFePO}_4$ . *Acta Cryst.* 22, 344-347.
- Setter, N. (1980) The role of positional disorder in ferroelectric relaxors. Ph.D. Thesis, The Pennsylvania State University.
- Starkey, J. (1967) On the relationship of pericline and albite twinning to the composition and structural state of plagioclase feldspar. *Schweiz. Mineral. Petrogr. Mitt.* 47, 257-268.
- Stenger, C. G. F. and Burggraaf, A. J. (1980) Order-disorder reactions in the ferroelectric perovskites  $\text{Pb}(\text{Sc}_{0.5}\text{Nb}_{0.5})\text{O}_3$  and  $\text{Pb}(\text{Sc}_{0.5}\text{Ta}_{0.5})\text{O}_3$ . I: Kinetics of the ordering process. *phys. stat. sol. (a)* 61, 275.
- Stenger, C. G. F. and Burggraaf, A. J. (1980) Order-disorder reactions in the ferroelectric perovskites  $\text{Pb}(\text{Sc}_{0.5}\text{Nb}_{0.5})\text{O}_3$  and  $\text{Pb}(\text{Sc}_{0.5}\text{Ta}_{0.5})\text{O}_3$ . II: Relation between ordering and properties. *phys. stat. sol. (a)* 61, 653.
- Young, R. A. and Post, B. (1962) Electron density and thermal effects in alpha quartz. *Acta Cryst.* 15, 337-346.



# APPENDIX 2

# ELECTROCERAMICS IN THE 1990s AND BEYOND

R.E. Newnham

Materials Research Laboratory, Pennsylvania State University, University Park,  
PA 16802 USA

## ABSTRACT

Following a brief survey of the current electroceramic markets, a few predictions are made for the coming decades. Emphasis is placed on "smart" ceramics that perform both sensing and actuating functions. Passively smart materials respond to external change like a reflex response, whereas actively smart materials have a feedback circuit and function more like a cognitive response. The ideas are illustrated with vibration-control systems for automobiles and other engineering transducers designed to function like the lateral line and swim bladders of fish.

## INTRODUCTION

In this paper, we briefly review the world market and a few predictions for the next few decades, and then focus on the subject of smart materials and their application to vibration control and in underwater communication systems.

### Electroceramics Today

The world market for electroceramics exceeds 10<sup>11</sup> units per year with a net value of approximately \$10 billion dollars (1). Japanese suppliers dominate the market and maintain very strong positions globally. Alumina packages, barium titanate capacitors, magnetic ferrites, and PZT transducers are the four principal electroceramic products. Collectively, they account for about 90% of worldwide sales. Other products with significant sales are resistors, thermistors, and varistors. Annual growth rates are about 5%.

## PEACE, POPULATION AND PROSPERITY

### The Future

It is no accident that soothsayers, palm readers, and fortune tellers are generally old people, for one of the few advantages of growing old is that one can make bold predictions of the future, safe in the knowledge that you will be firmly ensconced in your ground state by the time the future arrives.

Two facts give me hope for a world at peace: (i) throughout history, no wars have been fought between independent freely elected governments, and (ii) the number of democracies is growing, despite occasional setbacks. Before 1800 there was only one freely elected government, but there were five by 1850, 15 by 1900, and 43 by 1950, with about half the world's population. And the rest may soon follow -- time is on our side. Given the choice, most people do not want war (2).

To understand some of the changing demands made of electroceramists in the coming century, we need a vision of what the world might be like. A few of my predictions and those of the World Future Society are listed in Tables 1 and 2. Several involve the development of inexpensive sensor-actuator systems, often called "smart materials." In the discussion which follows, we describe the application of electroceramic materials to vibration control and underseas systems.

Table 1. Technological developments of the next century.

War and Peace. There has never been a major war between democracies.

Philosophy and Religion. Immortality by the year 2030 with computerized after-life.

Medicine and Disease. Cures for cancer, AIDS, aging, and the human cold.

Overpopulation and the Third World. More than 40,000 children die of hunger everyday. A solution must be found.

Farming the Ocean. Organized fish farming and extensive desalination programs.

Engineering Megaworks. Major irrigation and energy projects to compensate for shortages in water and petroleum.

Engineering Microworks. Sensors, actuators and signal processing: there is plenty of room at the bottom for building intelligence into materials. Expert systems for many everyday activities.

Biology and Psychology. Complete analysis of the human genome and the thought processes of the human brain.

*Table 2. Ten forecasts by the World Future Society for the 1990s.*

Cash will become illegal.  
Electronic immigration.  
Intelligent robotic systems.  
Prisons replaced by implants.  
Voice-driven furniture.  
Population shifts north.  
Defective gene replacement.  
Collision avoidance systems.  
Older generation families.  
Automated foods and gardens.

#### SMART MATERIALS

Modern materials bear little resemblance to those of the past; miniature integrated devices are tailored to perform complex functions in response to changing conditions in the surrounding environment. An important class of these increasingly sophisticated materials incorporates functions of sensing, actuating, control, and even a degree of intelligence. These "smart" materials possess a certain ability to sense and respond to stimuli and are used in a variety of engineering applications. Smart material technology, for example, is the basis for muscle implants made from rubbery gels that respond to electric fields, and dental braces made from shape memory alloys; electrochromic windows that control the flow of heat and light in response to weather changes and human activity; airplane wings that achieve greater fuel efficiency by altering their shape in response to air pressure and flying speed, and water purification systems that sense and remove noxious pollutants. In a number of instances, the application of smart materials has become commonplace in today's living.

## PASSIVE SMARTNESS

Smart materials are of two basic types: passively smart and actively smart (3). A passively smart material has the ability to respond to environmental conditions in a useful manner. It differs from an actively smart material in that there are no external fields or forces or feedback systems used to enhance its behavior. Depending on circumstances, these materials can demonstrate: selectivity, self-diagnosis, self-tuning, sensitivity, shapeability, self-recovery, self-repair, stability and multistability, standby phenomena, survivability, and switchability (4).

Ceramic varistors (devices whose electrical resistance decreases rapidly under high voltage) and ceramic thermistors (resistors whose electrical resistance depends on temperature) are passively smart materials. When struck by lightning, a zinc oxide varistor loses most of its electrical resistance and the current is by-passed to ground. This resistance change is reversible and acts as a stand-by protection phenomenon. Varistors also have a self-repair mechanism in which the highly nonlinear I-V relationship can be restored by repeated application of voltage pulses.

## ACTIVE SMARTNESS

An actively smart ceramic senses a change in the environment and, using a feedback system, makes a useful response. It is both a sensor and an actuator. Examples include vibration damping systems for outer space platforms and electronically controlled automobile suspension systems using piezoelectric ceramic sensors and actuators.

The piezoelectric Pachinko machine, a pinball machine popular in Japan, illustrates the principle of an actively smart material. The piezoelectric Pachinko game, constructed by engineers at Nippon Denso, is made from PZT multilayer stacks which act as both sensors and actuators. When a ball falls on the stack, the force of impact generates a piezoelectric voltage. Acting through a feedback system, the voltage pulse triggers a response from the actuator stack, which responds rapidly, throwing the ball out of the hole. During a sequence of such events, the ball moves up a spiral ramp and eventually falls into a hole, and begins the spiral climb all over again.

The video tape head positioner developed by Piezoelectric Products, Inc., operates on a similar

principle, Fig. 1. A bilaminate bender made from tape-cast PZT ceramic has a segmented electrode pattern dividing the sensing and actuating functions of the positioner. The voltage across the sensing electrode is processed through the feedback system, resulting in a voltage across the positioning electrodes. This causes the cantilevered bilaminate bender to bend, following the video tape track path. Articulated sensing and positioning electrodes near the tape head help keep the head perpendicular to the track. The automatic scan tracking system operates at 450 Hz.

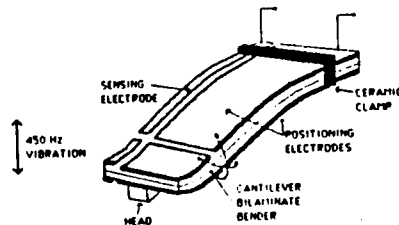


Fig. 1. Video tape head positioner made from PZT bimorph with sensor and actuator-divided electrodes.

#### VIBRATION CONTROL

A smart sensor-actuator system can mimic a very stiff solid or a very compliant rubber. This can be done while retaining great strength under static loading, making the smart material especially attractive for vibration control. If the phase of the feedback voltage is adjusted to cause the responder to contract in length rather than expand, the smart material mimics a very soft compliant substance, reducing the force on the sensors and partially eliminating the reflected signal. The reduction in output signal of the sensor is a measure of the effectiveness of the feedback system. The stiffness of the actuator-sensor composite can be reduced by a factor of ten compared to rubber.

The automobile industry is a very large market in which sensors and actuators are already widely used. More than 50 electroceramic components can be found in today's high-tech autos, ranging from the air-fuel oxygen sensors used in most cars to the more exotic piezoelectric raindrop sensor that automatically senses

the amount of water falling on the windshield and adjusts the wipers to the optimum speed (5).

Controlled compliance with piezoelectric ceramics is utilized in Toyota's piezoTEMS (Toyota Electronic Modulated Suspension), a system which has been developed to improve the drivability and stability of the automobile and at the same time enhance passenger comfort (6). The TEMS is basically a road stability sensor and shock adjustor that detects bumps, dips, rough pavement and sudden lurches by the vehicle, then rapidly adjusts the shock absorbers to apply a softer or firmer damping force, depending on what is necessary to minimize discomfort while maintaining control of the vehicle. The shock absorbers are continuously readjusted as the road conditions change so that rocking or wobbling on soft shocks is eliminated.

A cross-sectional view of the shock absorber is shown in Fig. 2. The road surface sensor consists of the five-layer piezoelectric ceramic sensor mounted on the piston rod of the shock absorber. When a bump in the road is encountered, the resulting stress applied to the sensor produces a voltage which is fed into an electronic control unit that amplifies the signal, changes the phase, and supplies a high voltage to the piezoelectric actuator. The 88-layer PZT actuator produces a 50  $\mu\text{m}$  displacement on the oil system which is hydraulically enlarged to two millimeters, enough to change the damping force from firm to soft. The entire process takes only about 20 milliseconds -- not even enough time to slam on the brakes. Also figured into the actuator output are the vehicle speed and driver's preference for a generally softer (American) or firmer (European) ride.

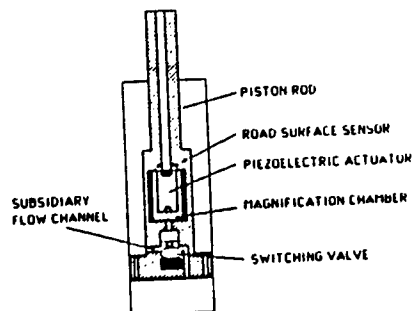


Fig. 2. Cross section of the principal portion of the TEMS shock absorber (6).

In designing a smart system for vibration control, it is necessary to properly position the actuator. Since action is followed by reaction, the control force must act between the controlled object and a reacting object. Three types of active damping systems can be identified according to the reaction mechanism.

Type I uses a fixed base as the reacting object.

Type II uses an auxiliary mass as the reacting object.

Type III uses a support structure as the reacting object.

Studies are underway to incorporate electroceramic actuators and reaction structures into functional composite damping materials which perform in both passive and active modes (7). In addition to automobiles and other vehicles, active control systems have been developed for trains, airplanes, bridges, flexible arms and rotors, forging hammers, cantilevered pipes, conveying fluids, off-shore rigs, space structures and radio antennae.

#### OCEANOGRAPHIC COMMUNICATION

It has been estimated that 74% of the earth's crust is covered by water, and the other 26% by mortgages! With increasing population pressures, it is inevitable that greater use will be of the world's oceans, and one of the great engineering challenges is long-distance underwater communication. Subsonic acoustic signals have been transmitted halfway around the world in the SOFAR experiments reported in the last decade (8). The oceans have an efficient waveguide centered at a depth of approximately 1 km where the acoustic velocities reach a minimum. Sound travels faster near the surface where temperatures are higher, and at great depths where pressures are higher. As in multimode, optical waveguides, the acoustic waveguide transmits a number of modes simultaneously, presenting a number signal processing opportunities for sonar engineers. The design and construction of inexpensive transceiver arrays is a central challenge for these experiments. Electroceramic transducers, capable of functioning at depths of 1-2 km, are a requirement.

#### IMITATING UNDERWATER BIOLOGICAL SYSTEMS

Biomimetics is a rapidly expanding field of research in materials. The word, from the Greek *bios*, life, and *mimetikos*, to imitate, indicates the use of



the biological world as inspiration for new technologies.

Fish and other underwater inhabitants have some interesting ways of communicating and listening that have been copied in the hydrophones used as sonar systems for submarines, geophysical prospecting equipment, and as fish finders. In most fish, the principal sensors are the inner ear, coupled to the swim bladder, and the lateral line that runs from the head to tail of the fish, resembling a towed array with sensing organs (stitches) spaced at intervals along the nerve fiber (9). Each stitch contains several neuromasts made up of gelatinous cupulae that contain fibers which vibrate as the fish swims through water and act as sensors for flow noise. Hydrophones made of a 1-3 composite are patterned after the hair-filled cupulae of a fish's lateral line. Thin PZT fibers embedded in polymer mimic the hairs and provide excellent electromechanical coupling to a liquid medium. The piezocomposites can be used as both sensors and actuators and are very sensitive to pressure waves in water (10).

The primary function of the fish's gas-filled swim bladder is to provide buoyancy but it is also used for sound and pressure reception and in some species is equipped with drumming muscles for sound propagation. The flexible swim bladder responds to hydrostatic pressure waves by changing volume, and fish with swim bladders can perceive relative pressure changes equivalent to less than 0.5% of the ambient hydrostatic pressure. These features are mimicked by another piezoelectric hydrophone composite (Fig. 3) which redirects applied stresses using flexensional transducers that mimic the motions of the swim bladder. These composites are known as "moonies" because of the internal crescent-shaped cavities. Under the hydrostatic stress of waves, the thick metallic electrodes convert a portion of the z-direction stress into large radial stresses of opposite sign (11). Composite sensors and actuators made with this geometry possess electromechanical coupling coefficients an order of magnitude larger than that of conventional PZT multilayer stacks.

#### Future Developments

Intelligent systems for hostile environments such as the deep ocean, are an area of considerable importance, and many new developments can be expected in the coming decade. There is a need for sensor and actuator systems that can operate at high temperatures

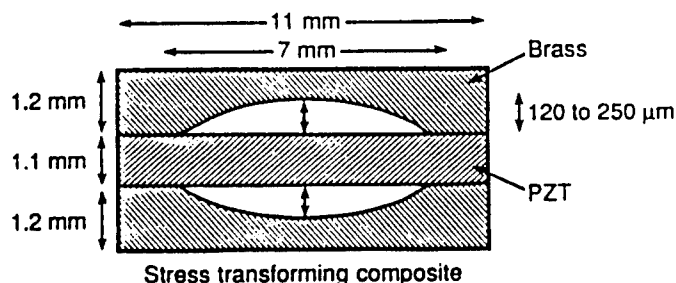


Fig. 3. Geometry of the "moonie" composite, designed to redirect applied stresses. Design is fashioned after the fish swim bladder and functions in a flextensional mode.

inside engines or furnaces to monitor combustion and to provide pollution control, and intelligent systems are required for oceanographic studies and oil exploration that can withstand high pressures and salinity conditions. Radioactive and chemical waste sensors are yet another field for fruitful research. In these and other areas, electroceramics can play a vital role in the intelligent systems of the future.

Many of these sensors and actuators can be fabricated in the form of multilayer ceramic packages. Until recently multilayer packages consisted of low-permittivity dielectric layers with metal circuitry printed on each layer and interconnected via holes between layers. Buried capacitors and resistors have now been added to the three-dimensional packages, and other components will follow. Smart sensors, adaptive actuators, and display panels with thermistors to guard against current and voltage overload are next in line for development.

#### CONCLUSION

I would like to close with a few personal thoughts concerning the age of smart materials and biomimetic engineering. The prospects of future developments in the next century both fascinate and frighten me. I am troubled by the fact that much of the hardware and software research is being undertaken for military systems -- weapons that may one day kill us all. I also have a vague fear of the unknown power of these electronic and optical systems -- a fear personified by the computer Hal in the movie "2001," and by the repressive society described in the book, "1984."

But I am, by nature, an optimist, and these fears are overridden by the thrill of scientific and technological achievements. My father and grandfathers were both carpenters and builders who took great pride in their work. I, too, love to build things with my hands -- wooden ship and airplane models, atomic models of crystal structures and phase transformations, multifunction composite materials, and polyphasic ceramic bodies. I love to see little things carefully designed, beautifully made, and serving a useful purpose. The craftsmanship delights me, and as Richard Feynman said, "There is plenty of room at the bottom" to construct engineering devices and systems on the submicron scale where biosystems operate. It makes me glad to be alive and taking part in this great adventure as we learn what we can from the structures nature has shown us, and then do our best to improve upon the designs using engineering materials.

#### REFERENCES

1. Kline & Company, Inc. "Survey of Electronic Ceramics" 330 Passaic Avenue, Fairfield, N.J. 07006, U.S.A.
2. D. V. Babst, "A Force for Peace" Ind. Res. 4 55-58 (1972).
3. R. E. Newnham and G. R. Ruschau, "Smart Electroceramics", J. Amer. Ceram. Soc. 74 463-480 (1991).
4. T. Takagi, "The Concept of Intelligent Materials and the Guideline for R & D Promotion" Japan Science and Technology Agency Report, Tsukuba Science City, Japan, 1989.
5. M. Taguchi, "Applications of High-Technology Ceramics in Japanese Automobiles," Adv. Ceram. Mater. 2 754-762 (1987).
6. H. Tsuka, J. Nakamo, and Y. Yokoya, "A New Electronic Controlled Suspension Using Piezoelectric Ceramics" IEEE Workshop on Electronic Applications in Transportation, 1990.
7. K. Seto, "Active Damping Systems," J. Japan Soc. Mech. Eng. 89 635-638 (1986).
8. R. C. Shockley, J. Northrup, P. G. Hansen and C. Hartdegen, "SOFAR Propagation Paths from Australia to Bermuda," J. Acoust. Soc. Amer. 71 51-60 (1982).

9. P. B. Moyle and J. J. Cech, Jr., "Fishes: An Introduction to Ichthyology" Prentice Hall, Englewood Cliffs, N.J., 1988.
10. K. A. Klicker, J. V. Biggers and R. E. Newnham, "Composites of PZT and Epoxy for Hydrostatic Transducer Applications," J. Amer. Ceram. Soc. 64 5-9 (1981).
11. Q. C. Xu, J. Belsick, S. Yoshikawa, T. T. Srinivasan and R. E. Newnham, "Piezoelectric Composites with High Sensitivity and High Capacitance for Use at High Pressures" Proc. IEEE, in press.

# APPENDIX 3

## Anisotropy in electrostriction and elasticity

V. SUNDAR, R. E. NEWNHAM

Intercollege Materials Research Laboratory, Pennsylvania State University, University Park, PA 16802, USA

Electrostriction is the basis of electromechanical coupling in all non-piezoelectric insulators. From the Devonshire formalism of the thermodynamic phenomenology that describes the coupling between dielectric and elastic properties of solids, two equivalent forms of the electrostrictive effect, the "direct" and the "converse" effects, may be derived [1].

From such an approach, the strain  $x_{ij}$  in a material may be derived from expressions for the Gibbs free energy and the elastic Gibbs function as:

$$x_{ij} = s_{ijkl}^E X_{kl} + M_{mnij} E_m E_n$$

and

$$x_{ij} = s_{ijkl}^P X_{kl} + Q_{mnij} P_m P_n$$

where  $s_{ijkl}$  is the elastic compliance tensor under appropriate boundary conditions and  $X_{kl}$  the elastic stress. From these relations the "direct" effect  $Q$  and  $M$  coefficients are defined as:

$$M_{mnij} = \frac{1}{2} (d^2 x_{ij} / dE_m dE_n)_X$$

and

$$Q_{mnij} = \frac{1}{2} (d^2 x_{ij} / dP_m dP_n)_X$$

To be completely formal, partial derivatives are to be used in these and the following equations. Alternatively, the "converse" effect  $Q$  and  $M$  coefficients may be derived as:

$$M_{mnij} = \frac{1}{2} (d\eta_{ij} / dX_{mn})_P$$

and

$$Q_{mnij} = \frac{1}{2} (d\chi_{ij} / dX_{mn})_P$$

where the dielectric susceptibility  $\chi_{ij} = 1/\eta_{ij} = 1/[\epsilon_0(\epsilon_{ij} - 1)]$ .

Thus, we may rewrite the coefficients in terms of the dielectric permittivities  $\epsilon_{ij}$  of the material, as:

$$M_{mnij} = (\epsilon_0/2)(d\epsilon_{ij}/dX_{mn})_P$$

and

$$Q_{mnij} = [1/2\epsilon_0(\epsilon - 1)^2][(d\epsilon_{ij}/dX_{mn})_P]$$

The direct and converse electrostriction effects are of importance in that they offer two independent and equivalent techniques of measuring the electrostriction in a material: (i) by measuring the strains induced in materials in response to applied fields or induced polarizations, by the direct effect, and (ii) by measuring the change in permittivity (the change in capacitance for suitably shaped samples) under an appropriate stress by the converse effect.

Reliable and accurate measurements of the separated electrostriction coefficients of a material then offer us a way to understand better the physical origin of electromechanical coupling in insulating solids.

Electrostriction is an electromechanical coupling. Both the dielectric and elastic properties of the material are expected to affect the electrostrictive phenomenon. It is of interest to investigate the nature of the correlations between these properties, in terms of the anisotropy in single crystals.

A modified compressometer (Fig. 1) was used to measure the separated electrostriction coefficients of fluorite and fluoride perovskite single crystals. Details of this method are presented in [2].

Well-characterized  $\text{CaF}_2$ ,  $\text{BaF}_2$ ,  $\text{SrF}_2$  and  $\text{KMnF}_3$  single crystals, in  $\langle 100 \rangle$ ,  $\langle 110 \rangle$ , and  $\langle 111 \rangle$  orientations were used for this study. These were prepared in the form of thin discs with plane parallel faces. The crystals were polished to near optical finishes and electroded with sputtered gold. Since the capacitance changes measured are very small, guard ring electrodes were scribed on to the samples.

Small static loads of up to 4 kg mass were applied in steps of 0.5 kg on the samples. The pressure dependence of the capacitance was measured for each orientation of the material. This, along with elastic constant values from the literature [3, 4], was used as input in calculating the separated electrostriction coefficients of the materials. The results are shown in Table I. These results agree to within  $\pm 5\%$  with prior measurements by both direct and converse methods on these materials [2, 4-6].

All four materials evaluated are cubic materials, and have no dielectric anisotropy. The anisotropy surfaces for the dielectric constants of these materials are, therefore, spheres. It is, then, expected that the anisotropy in elastic properties would be the

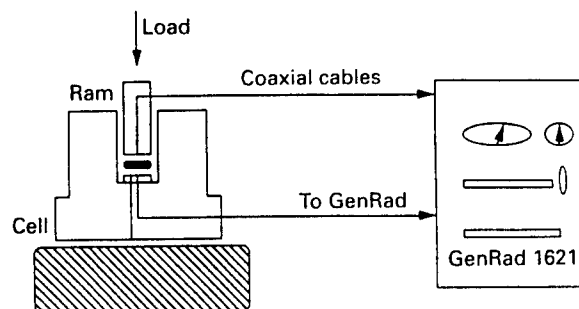


Figure 1 Schematic diagram of the modified compressometer.

TABLE I Electrostriction and elastic coefficient values

Material	$Q_{11}^a$	$Q_{12}^a$	$Q_{44}^a$	$s_{11}^b$	$s_{12}^b$	$s_{44}^b$
CaF <sub>2</sub>	-0.49	-0.48	2.01	0.69	-0.15	2.99
SrF <sub>2</sub>	-0.33	-0.39	1.90	0.97	-0.26	3.02
BaF <sub>2</sub>	-0.31	-0.29	1.48	1.53	-0.47	4.06
KMnF <sub>3</sub>	0.49	-0.10	1.15	1.21	-0.35	3.75

<sup>a</sup> $Q_{ij}$  values in m<sup>4</sup>/C<sup>2</sup>, this work.

<sup>b</sup> $s_{ij}$  values in 10<sup>-11</sup> Pa<sup>-1</sup> [3, 4].

main contribution to the anisotropy in electrostrictive properties.

To verify this, the elastic compliance coefficients  $s_{ij}$  of the materials were used as input to plot the projections of the elastic anisotropy surfaces on the (110) plane. This plane contains the principal directions  $\langle 110 \rangle$ ,  $\langle 111 \rangle$  and  $\langle 001 \rangle$  of the cubic unit cell. A projection on this plane thus enables us to observe the variation of anisotropic properties in the three main symmetry directions.

Using the Voigt notation, the longitudinal compliance coefficient  $s'_{11}$  was calculated as a function of the angle  $\theta$  from the  $\langle 001 \rangle$  axis for all four materials. The variation of  $s'_{11}$  is quite similar for the three fluorites, as may be expected. At no point does  $s'_{11}$  go to zero. The materials are seen to be most compliant in the  $\langle 111 \rangle$  directions, and stiffest in the  $\langle 001 \rangle$  directions (Fig. 2).

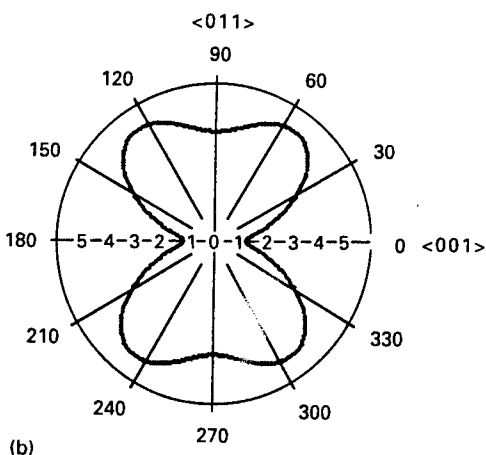
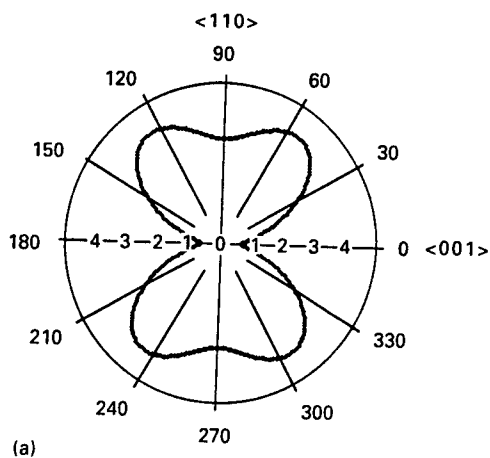


Figure 2 Anisotropy in compliance for (a) CaF<sub>2</sub> and (b) KMnF<sub>3</sub>.

Using the  $Q_{11}$ ,  $Q_{12}$  and  $Q_{44}$  coefficients measured, the anisotropy in electrostriction was plotted in a similar manner. A significant resemblance is noted in the shapes of the anisotropy plots of both  $s'_{11}$  and  $Q'_{11}$ , especially for KMnF<sub>3</sub> (Figs 2 and 3). This indicates that the anisotropy in electrostriction does indeed correlate with the anisotropy in compliance.

For the fluorites, both  $Q_{11}$  and  $Q_{12}$  are negative. This gives rise to a very interesting effect. The longitudinal electrostriction coefficient  $Q'_{11}$  goes to zero in directions angled at  $\sim 13.4^\circ$  to the  $\langle 001 \rangle$  axes, for CaF<sub>2</sub>,  $\sim 10.6^\circ$  for SrF<sub>2</sub> and  $\sim 16.3^\circ$  for BaF<sub>2</sub>. The maximum value of the coefficient  $Q'_{11}$  is observed along the  $\langle 111 \rangle$  directions, which are the most compliant directions in the fluorites (Figs 2a, 3a).

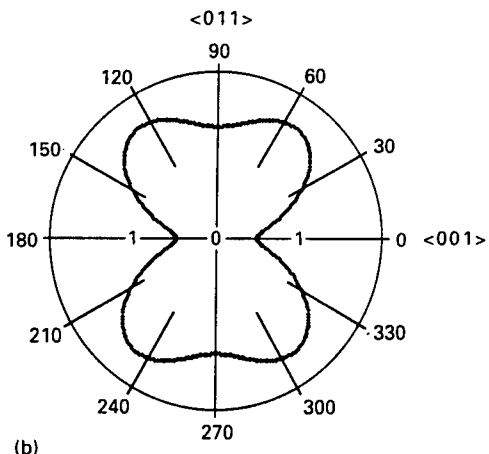
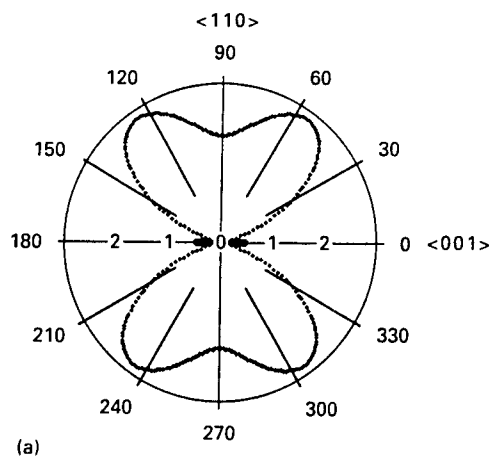


Figure 3 Anisotropy in electrostriction for (a) CaF<sub>2</sub> and (b) KMnF<sub>3</sub>.

Viewing both electrostriction and elasticity as primarily distortive effects, an explanation may be sought for these observations. The Ca-F bonding direction in the fluorite structures is along the  $\langle 111 \rangle$  directions (Fig. 4). There are empty cavities in the fluorite structure which interrupt the bonds along  $[111]$ . Along the  $\langle 100 \rangle$  directions,  $F^-$  ions are arranged in a continuous linear chain. The distance between  $F^-$  ions is very small, and this makes distortion along this direction more difficult than along other directions.

For  $KMnF_3$ , only the  $Q_{12}$  coefficient is negative. No zero electrostriction directions exist, and the electrostriction anisotropy closely parallels the compliance anisotropy (Figs 2b, 3b). The principal bonds in the perovskite structure are along the  $\langle 100 \rangle$

directions, and are continuous. These materials are elastically and electrically stiffest in these directions.

In conclusion, compressometry is seen to be a reliable method to evaluate separated electrostriction coefficients in materials. The anisotropic variation of electrostriction in these materials is seen to be significantly affected by the compliance coefficient. Since these materials are isotropic in terms of dielectric properties, it is reasonable to assume that elastic effects are the main contributions to the anisotropy. An analysis of materials with strong dielectric anisotropy could possibly yield more interesting correlations between the dielectric, elastic and electrostrictive effects.

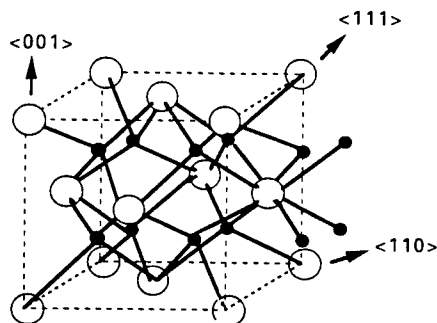


Figure 4 The fluorite structure: (●), F: (○), Ca.

## References

1. A. F. DEVONSHIRE, *Adv. Phys.* **3** (1954) 94.
2. Z. Y. MENG and L. E. CROSS, *J. Appl. Phys.* **57** (1985) 488.
3. Y. SUN, W. W. CAO, W. Y. PAN, Z. P. CHANG and L. E. CROSS, *J. Mater. Sci. Lett.* **7** (1988) 327.
4. K. S. ALEXANDROV and T. V. RHYZHOVA, *Sov. Phys. Cryst.* **6** (1961) 252.
5. K. RITTENMEYER, Ph.D. thesis, Pennsylvania State University (1985).
6. Q. M. ZHANG, W. Y. PAN and L. E. CROSS, *J. Appl. Phys.* **63** (1988) 2492.

Received 19 October  
and accepted 10 November 1993



# APPENDIX 4

## RELAXOR FERROELECTRICS: AN OVERVIEW

L. ERIC CROSS

Materials Research Laboratory, The Pennsylvania State University, University  
Park, PA 16802-4800 USA.

(Received August 9, 1993)

**Abstract** The paper will trace the evolution of understanding related to the modification of sharp ferroelectric phase transition behavior that occurs in composition systems which exhibit diffuse and relaxor ferroelectric properties. The focus will be primarily upon the perovskite structure families where cations of different valence occupying similar crystallographic sites in the structure appear to play an important role. Limited ordering in the  $\text{Pb}(\text{B}_1\text{B}_2)\text{O}_3$  systems will be discussed and possible mechanisms for self limiting to nanometer scales in some systems explored. New studies of the break up of the simple ferroelectric behavior in lanthanum modified lead zirconate titanate (PLZT) and in lead titanate (PLT) systems will be discussed and the relevance to the general problem of relaxor behavior examined. Evidence for enhanced polarization fluctuations and super paraelectric behavior at high temperatures will be discussed and random field and spin glass models for the lower temperature state considered.

In the tungsten bronze structure relaxors barium strontium niobate (SBN) and lead barium niobate (PBN) the behavior is more complex suggesting the possibility for relaxor behavior in directions orthogonal to existing polarization systems.

## INTRODUCTION

It is perhaps useful to begin the discussion of the interesting sub group of relaxor ferroelectrics by considering in a more general way the nature of the Curie point transition which heralds the onset of proper ferroelectric behavior. In figure 1a is illustrated first the behavior in a rather perfect single crystal which goes through an abrupt second order phase transition into the ferroelectric phase. Above  $T_c$ , the permittivity follows a Curie Weiss law  $\epsilon^1 = C(T - T_c)^{-1}$ , at  $T_c$  there is an abrupt but continuous onset of spontaneous polarization which evolves into the domain structure of the ferroelectric form. In some crystals the transition at  $T_c$  is first order, there is a finite maximum of  $\epsilon$  at  $T_c$  and the Curie Weiss temperature  $\theta$  in the relation  $\epsilon = C(T - \theta)^{-1}$  occurs some degrees below  $T_c$  e.g.  $11^\circ\text{C}$  in  $\text{BaTiO}_3$ . Again there is an abrupt loss of

polarization at  $T_c$  now in a discontinuous step but  $\epsilon_{\max}$  and  $P_s \rightarrow 0$  occur at the same temperature  $T_c$ .

For many practical applications it is desired to use the very large property maxima in the vicinity of the ferroelectric phase transition, to move the transition into the temperature range of interest and to broaden and diffuse the very large sharp peak values. In solid solution systems this is accomplished by trimming the mean composition to move the Curie point and at the same time making the sample (often a ceramic) deliberately inhomogeneous. In these diffuse transition systems the dielectric maximum is now much 'rounder' and polarization persists for a short range of temperature above  $T_m$  (figure 1b). Almost all practical Z5U and Y5V capacitor dielectrics use such diffuse transitions.

In the relaxor ferroelectrics, three features of the dielectric response are qualitatively different. The transition is clearly diffuse and rounded, but the response is now markedly dispersive below  $T_m$  and  $T_m$  is a function of frequency (figure 1c). The response at weak fields above  $T_m$  is no longer Curie Weiss. In the polarization the RMS value persists to a temperature ( $T_D$ ) 200 to 300°C above  $T_m$  but the mean polarization  $\bar{P}$  decays to zero at a temperature  $T_F$  which is well below  $T_m$ .

The weak field dielectric behavior for a typical relaxor ferroelectric in the perovskite structure family lead magnesium niobate is shown in more detail in figure 2a, taken from the pioneer work of Smolensky,<sup>1</sup> the dispersion over the frequency range 10 Hz to  $10^7$  Hz is clearly evident. That the material is ferroelectric is evident from figure 2b which traces the evolution of dielectric hysteresis under high field as a function of temperature. Unlike the sharp transition materials there are not abrupt changes and non linearity persists to temperature well above  $T_m$ . Perhaps the most puzzling feature is the absence of evidence for any macroscopic phase change below  $T_m$  either in the X-rays spectra, or the optical birefringence (figure 2c), yet clearly spontaneous polarization is impossible in cubic symmetry.

The original explanation offered by Bokov and Mylnikova<sup>2</sup> for this behavior was that the diffuseness was again due to heterogeneity, giving a range of Curie points, but that now the scale was very small and therefore below the resolution of X-ray and optical probes. Considering this model of nano-scale polar regions, it appeared probable to us that since the energy barriers to reorientation in any ferroelectric are linearly related to the volume, at these very fine scales the electrocrystalline

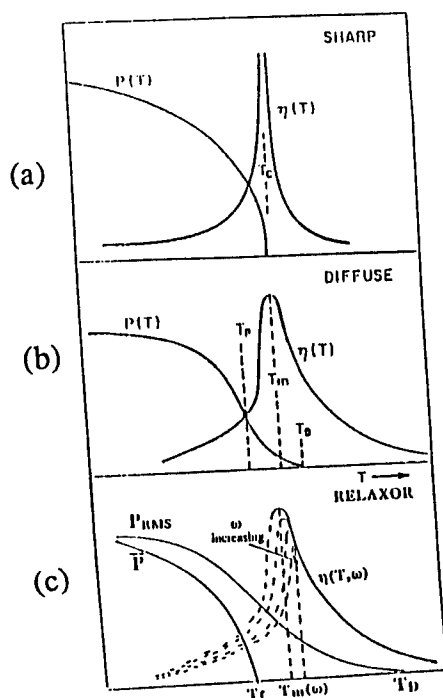


FIGURE 1 Types of Ferroelectric Phase Transitions.

- (a) Simple proper ferroelectric: sharp second order phase change in highly perfect single crystal.  
 (b) Diffuse phase transition associated with macroscopic heterogeneity as in practical capacitor dielectrics.  
 (c) Relaxor ferroelectric defining  $T_m(\omega)$ ,  $T_D$ ,  $T_F$ .

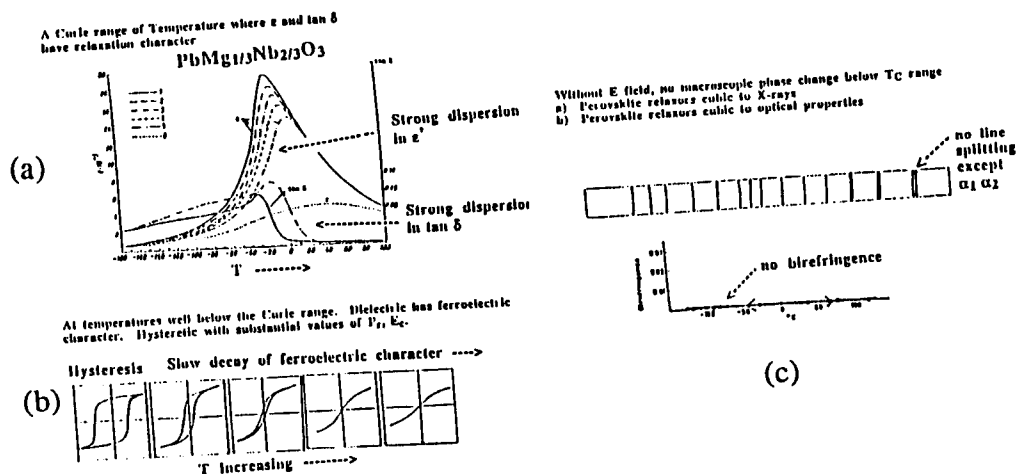


FIGURE 2 (a) Dispersion around  $T_m$  is Lead Magnesium niobate PMN, a typical relaxor ferroelectric.  
 (b) Slow decay of polarization with temperature.  
 (c) Absence of a macroscopic symmetry change.

anisotropy energy  $\Delta H_r$  might become comparable to  $kT$  leading to super-paraelectric behavior at higher temperature.

A range of perovskite structure compounds with complex composition and a number of Tungsten bronze structure materials (Table I) show relaxor ferroelectric behavior. In perovskites the behavior occurs dominantly in lead based compositions and in both perovskites and bronzes there is always more than one type of ion occupying crystallographically equivalent sites.

For this brief review we will discuss first the origin of the symmetry breaking which occurs in the pre-cursors chemistry of these systems. It is reasonably well understood in  $A(B_1B_2)O_3$  compositions but is less clear in the PLZTs and bronze family materials. Then the detail of the dielectric response which points towards a spin glass model for the freeze out of polar fluctuations as the origin of the dispersion will be considered. We then touch on some new evidence for unusual relaxor behavior in the low temperature polar phase of the tungsten bronze systems.

TABLE I Systems Which Exhibit Relaxor Ferroelectric Behavior

PEROVSKITES OF COMPLEX COMPOSITIONS

B-site complex	Lead magnesium niobate (PMN)	$PbMg_{1/3}Nb_{2/3}O_3$
	Lead scandium tantalate (PST)	$PbSc_{1/2}Ta_{1/2}O_3$
	Lead zinc niobate (PZN)	$PbZn_{1/2}Nb_{1/2}O_3$
	Lead indium niobate (PIN)	$PbIn_{1/2}Nb_{1/2}O_3$
A-site	Lead lanthanum zirconate titanate (PLZT)	$Pb_{1-x}La_{2x/3}TiO_3$
	Lead lanthanum titanate (PLT)	$Pb_{1-x}La_{2x/3}TiO_3$
Both sites complex	Potassium lead zinc niobate	$K_{1/3}Pb_{2/3}Zn_{2/9}Nb_{7/9}O_3$

TUNGSTEN BRONZE STRUCTURE COMPOSITIONS

Strontium barium niobate (SBN)	$Sr_{1-x}Ba_xNb_2O_6$
Lead barium niobate (PBN)	$Pb_{1-x}Ba_xNb_2O_6$

PERCURSON CHEMISTRY

In the lead based perovskite  $A(B_1B_2)O_3$  relaxors it is clear from very extensive TEM studies<sup>3,4,5</sup> that in  $Pb(Mg_{1/3}Nb_{2/3})O_3$  the origin of the nanoscale heterogeneity is in a strictly limited 1:1 non stoichiometric ordering of the Mg and Nb. A crude two dimensional picture is given in figure 3a showing the scale of the region's which are of

the order 5 nm. The dark field TEM image confirming the ordering and the scale is shown in figure 3b.

This 1:1 ordering must give rise to a significant charge imbalance and it has been suggested<sup>6</sup> that the developing electric field limits the scale. In  $\text{PbSc}_{1/2}\text{Ta}_{1/2}\text{O}_3$  the ordering which is again 1:1 may be carried through to a highly ordered form by controlled thermal annealing, recovering full translational symmetry.<sup>7</sup> It is important to note that the nano scale ordered PST exhibits relaxor behavior whilst the highly ordered crystal shows a first order ferroelectric phase change.

Our picture of relaxor behavior in the  $\text{A}(\text{B}_1\text{B}_2)\text{O}_3$  systems is suggested schematically in figure 4. Either complete disorder, or full long range order appears to give rise to normal ferroelectric behavior. It is the limited nano-scale ordering which appears to favor the development of small scale polar regions. The fascinating feature in the PMN type compounds is that the local non stoichiometry inherent in the ordering process appears to make it a self limiting nano-composite which cannot be changed by annealing. It should be emphasized that this is a most unusual nano-composite as the oxygen lattice is continuous and coherent through both ordered and disordered regions.

In the mixed A site relaxors such as the PLZTs with compositions along the 65:35 Zr:Ti mole ratio and Lanthanum concentration of more than 2 mole% the dielectric response is similar in many respects to the PMN system, however the symmetry breaking nanostructure is not so clear. Very careful TEM studies have revealed direct evidence of nano scale polar regions at low temperature<sup>8</sup> but the precursor chemistry which forces their formation is not yet clear. Very recently Rossetti<sup>9</sup> has explored the Lead lanthanum titanate system with high resolution X-ray techniques. It is clear that quite low levels of Lanthanum concentration rapidly reduce the strongly first order nature of the pure  $\text{PbTiO}_3$  Curie point transition and begin to lead to a sub domain modulation of the magnitude of  $P_s$  in the domain, although there is no strong evidence for ordering of the lanthanum or the associated lead site vacancies at the higher concentrations. The necessary high defect concentration in the PLZT does however lead to an aging phenomenon<sup>10</sup> which modifies the relaxation response markedly making longer time measurements of response impossible to interpret unequivocally.

In the tungsten bronze family, Barium strontium niobate  $\text{Ba}_x\text{Sr}_{1-x}\text{Nb}_2\text{O}_6$  is a prototypic relaxor here the structure is much more complex than the perovskite and more open. Again it is built on corner linked oxygen octahedra, but the sheet normal to the c

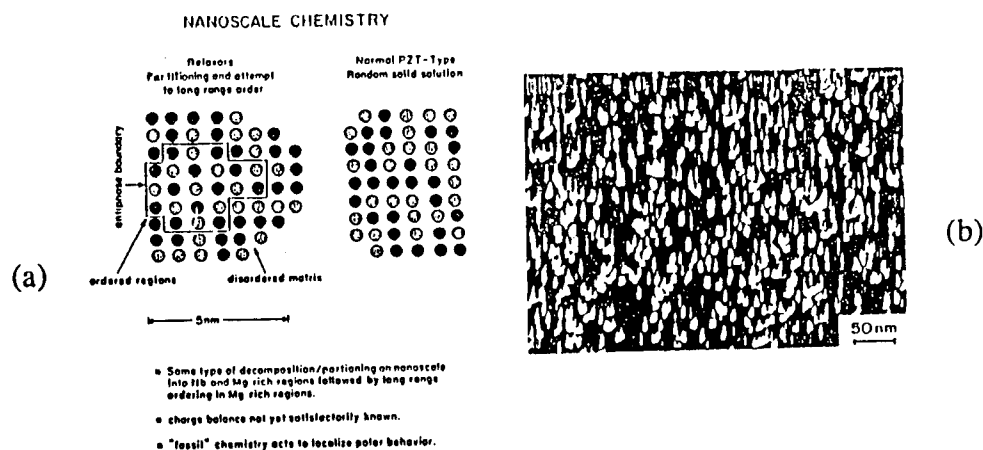


FIGURE 3 (a) Two dimensional sketch of observed 1:1 ordering of Mg:Nb cations in PMN.  
(b) Dark field TEM and PMN showing the scale of the ordered regions.

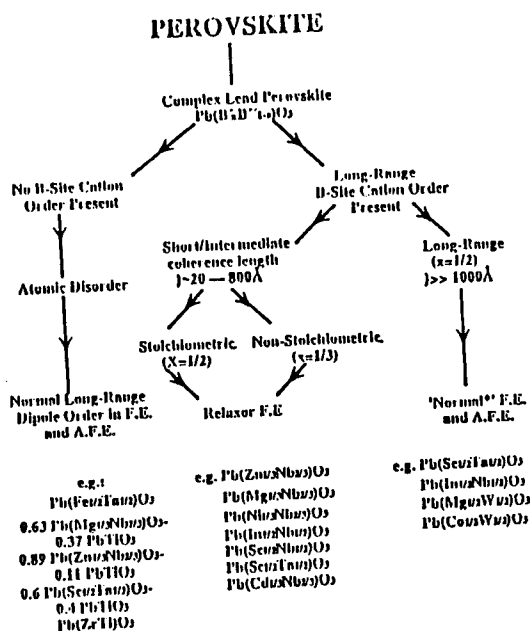


FIGURE 4 Suggested dependence of relaxor behavior in perovskite  $Pb(B_1B_2)O_3$  compositions on limited  $B_1:B_2$  ordering.

axis of the tetragonal paraelectric form figure 5 is markedly crumpled. Here Nb ions occupy the centers of the oxygen octahedra, Ba ions the larger 5 fold channels and strontium are distributed between 4 fold and 5 fold channels. X-ray studies using the Rietveld method<sup>11</sup> suggest that Ba is always in the 5 fold channel but that annealing can

Ferroelectric Tungsten Bronze Crystallographic Structure

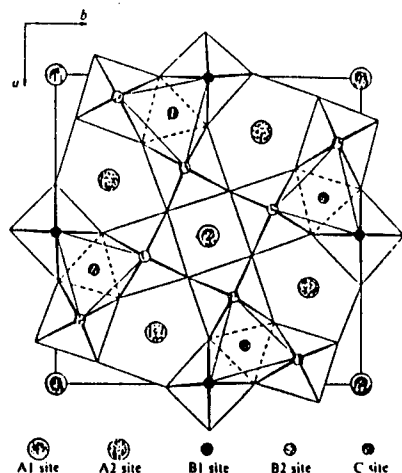
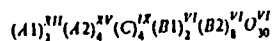


FIGURE 5 Projection of the Tungsten Bronze ferroelectric structure normal to the 4 fold c axis showing the sites for cation occupancy.



change the Sr occupancy between 4 fold and 5 fold sites. Changing Sr occupancy has a marked effect upon the dielectric peak position  $T_m$  and it is suggested that variations in distribution throughout the crystal may be responsible for a wide distribution of local Curie points. It is interesting to note that the relaxation phenomenon becomes steadily stronger with increasing Sr concentration.

Much more work is however needed to pin down the symmetry breaking nanostructures in both the PLZTs and the bronze compositions.

### ELASTO-DIELECTRIC RESPONSE

Earlier studies have shown that the relaxor ferroelectric retain large values of RMS polarization to temperature some 100s of degrees above the dielectric maximum. In PMN, PLZT and SBN types measurement of lattice strain (thermal expansion) and optical refractive index<sup>12,13,14</sup> show very good agreement in the prediction of the decay of RMS polarization. The question as to whether the residual polarization is static or dynamic has been more difficult to decide. Measurement of electrostriction in SBN above  $T_m$  strongly suggested the dynamical model,<sup>15</sup> but it is only very recently that careful neutron spectroscopy has completely confirmed the super-paraelectric behavior at higher temperature in PMN.

A key feature of the dielectric response is the strong dispersion in the weak field permittivity. Studies by Viehland et al<sup>16</sup> have shown that the frequency/temperature



characteristics are nicely described by the Vogel:Fulcher relation (figure 6a) and that the freezing temperature  $T_f$  deduced from this relation agrees closely with the thawing temperature where remanent polarization is lost on heating a field cooled sample (figure 6b). Vogel:Fulcher suggests a slowing down and freezing into a glass like ensemble of nano-domains, such a behavior would also suggest that the weakly cooperating nano-polar regions should begin to depart markedly from Debye like response towards a very long flat tail upon an  $\epsilon''$  corresponding to the freezing process and this is indeed observed.<sup>17</sup>

For any precise dielectric studies it is essential to recognize and eliminate the aging process. As discussed earlier it is impossible to eliminate defects which couple to the polarization system in PLZT, since the  $\text{La}^{3+}$  doping necessitates that the sample have equivalent lead vacancies. In  $\text{Pb}(\text{Mg}_{1/3}\text{Nb}_{2/3})\text{O}_3$  however the crystal is a compound, and if it is made with care from very high purity starting materials, macroscopic stoichiometry can be preserved in a fully stuffed structure. For this type of material aging can be eliminated, and the phenomenon can be reintroduced by a low level  $\text{MnO}$  doping. A full explanation is given in references 18 and 19 but is beyond the scope of this review. The data are emphasized however as it is clearly essential to 'uncouple' aging if time dependent properties of the relaxor are to be studied without gross perturbation.

To explore the high field response it is necessary to turn to the PLZTs and to take care to always study freshly de-aged samples. For an 8:2:70:30 PLZT composition Randall<sup>20</sup> has imaged using TEM the nano domain structure at low temperature (figure 7a) and by using charging from the beam current the evolution of nano-domains towards more normal continuous ferroelectric domains (figure 7b). Consequences of the application of static fields to PLZT samples which have been cooled in the zero field state have been explored by Yao Xi et al.<sup>21</sup> If the system behaves as a spin glass the

## PMN-10PT AGE FREE

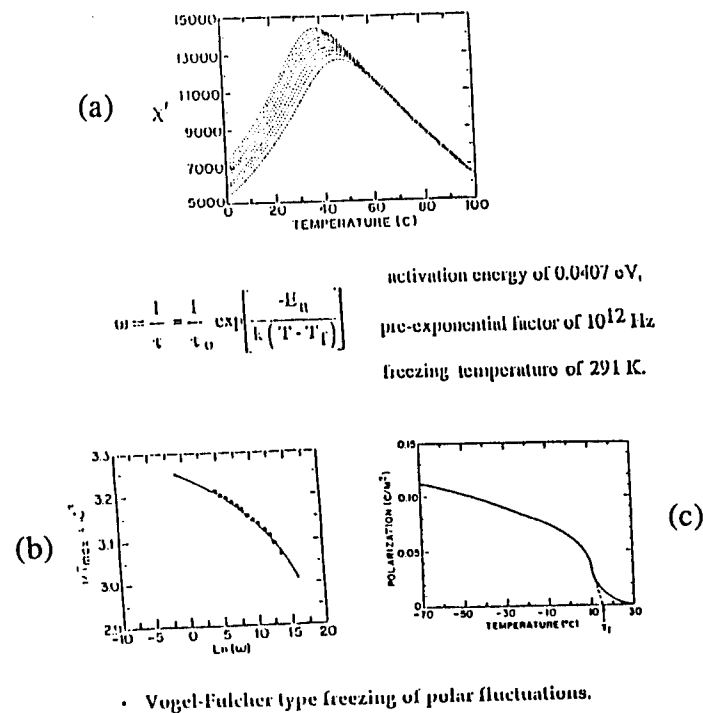


FIGURE 6 (a, b) Evidence for a glass like freezing of the dielectric response in PMN:PT solid solution lead in to Vogel:Fulcher type behavior with freezing temperature  $T_F$ .  
(c) Field cooled poled sample show "thawing" temperature  $T_F$ .

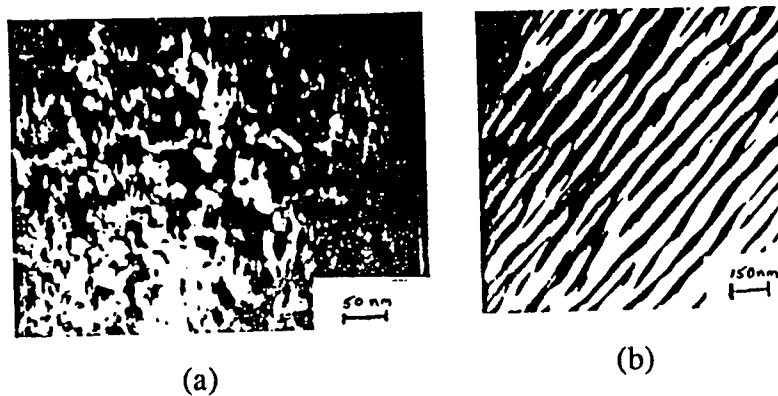


FIGURE 7 (a) Structure of nano-scale polar domains revealed in PLZT at the 8.2:65:35 composition by dark field TEM.  
(b) Modification to the domain pattern by beam charging showing the induction of larger macro-domain stripes.

switch over should be modeled by the deAlmeida-Thouless relation<sup>22</sup> and data taken from the measurements of Yao Xi et al are modeled in this manner in figures 8.<sup>23</sup>

In deducing the RMS polarization it was tacitly assumed that the polarization related electrostriction constants  $Q_{11}$ ,  $Q_{12}$  are independent of temperature in fact this has been proven by direct measurement.<sup>24</sup> Clearly then in this circumstance one must expect that all the dielectric (Polarization) behavior will be reflected into the elastic response. The close relation between elastic and dielectric responses is evident in figure 9. For the high field response, it is to be expected that the high polarization values which can be induced anhyserically near  $T_m$  will give rise to large elastic strains values of  $x_{33}$  the strain in the field direction for a PMN:PT solid solution are shown in figure 10. The slope of this curve at any point is the effective d constant ( $d_{33}$ ) which goes to very large values at relatively modest E fields.<sup>25</sup>

$$E = \Lambda \left[ \frac{T_f(0) - T_{zfc}(E)}{T_f(0)} \right]^{\frac{3}{2}}$$

deAlmeida-Thouless relationship

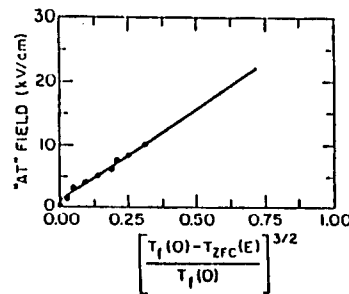
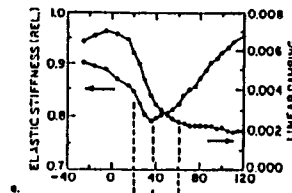


FIGURE 8 Similar studies at different field levels fitted to the de Almeida-Thouless relation.

Elastic Response



Dielectric Response

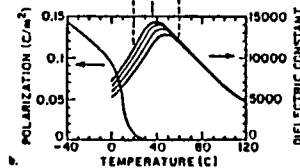


FIGURE 9  
(a) Elastic stiffness and damping in ceramic PMN:10PT.  
(b) Comparison to dielectric softening associated with micro-polar behavior.

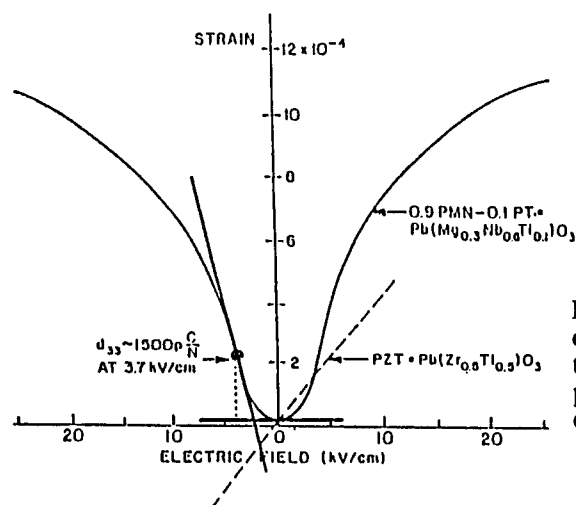


FIGURE 10 Strain vs Field curve for PMN:10PT illustrating the large values of induced piezoelectric  $d_{33}$  under DC field control.

#### TUNGSTEN BRONZE STRUCTURE RELAXOR FERROELECTRICS

In the solid solution system  $\text{Sr Nb}_2\text{O}_6\text{:BaNb}_2\text{O}_6$  the end member compositions are not in the bronze structure, however in the range between  $\text{Sr}_{0.8}\text{Ba}_{0.2}\text{Nb}_2\text{O}_6$  and  $\text{Sr}_{0.3}\text{Ba}_{0.7}\text{Nb}_2\text{O}_6$  stable SBN bronzes form.<sup>26</sup> Across this range the prototypic structure is tetragonal and for fields in the 001 (c) axis direction the characteristics are these of a relaxor ferroelectric with polarization along (001). Both optical<sup>27</sup> and elastic<sup>28</sup> studies confirm that large values of RMS polarization persist to temperatures well above  $T_m$  and there is clear evidence of ferroelectric behavior at low temperature.<sup>29</sup> Dispersion near  $T_m$  becomes steadily more pronounced in compositions with increasing Strontium content.<sup>30</sup> For the congruently melting  $\text{Sr}_{0.6}\text{Ba}_{0.4}\text{Nb}_2\text{O}_6$  excellent quality single crystals have been grown<sup>31</sup> and the crystal is widely used in photorefractive applications.<sup>32</sup>

The bronze system Lead barium niobate  $\text{Pb}_{1-x}\text{Ba}_x\text{Nb}_2\text{O}_6$  (PBN) is of special interest as in the vicinity of the  $\text{Pb}_{0.6}\text{Ba}_{0.4}\text{Nb}_2\text{O}_6$  composition there is a pseudo morphotropic phase boundary between orthorhombic and tetragonal ferroelectric forms (figure 11).<sup>33</sup> For the tetragonal form at the 57:43 composition the permittivity for

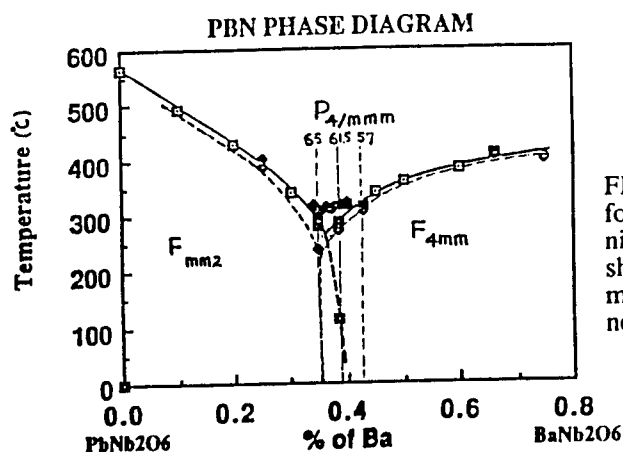


FIGURE 11 Phase diagram for the lead niobate:barium niobate system (PBN) showing the pseudo-morphotropic phase boundary near the 60:40 composition.

fields along (001) shows a transition with only very weak dispersion and large thermal hysteresis (figure 12a), however for fields along (100) there is now a pronounced dispersion at lower temperature (figure 12b).

In compositions on the orthorhombic side of the MPB again the upper transition exhibited for fields along 100 is reasonably sharp, however, now there is a lower temperature relaxation for field in the 001 (c) axis direction. There are no evidences of phase transitions in either crystal in the region of the dispersion, but cooling the crystal under a poling field orthogonal to the main polarization direction produces a clear remanence of order less than  $1/20^{\text{th}}$  of the major polarization.<sup>34</sup> It is interesting to note that for compositions close to the MPB large orthogonal electric fields will switch the major component of  $P$  changing the symmetry from tetragonal to orthorhombic or vice versa. With symmetry change the lower frequency dispersion also changes axial direction always appearing normal to the major component of  $P$ .

Clearly at low temperature, the field forced symmetry must be truly monoclinic in each case, as the  $P_s$  is tilted away from the primary axis (4 fold or 2 fold). Our suggestion is that in each case the micro polar regions which make up the mean

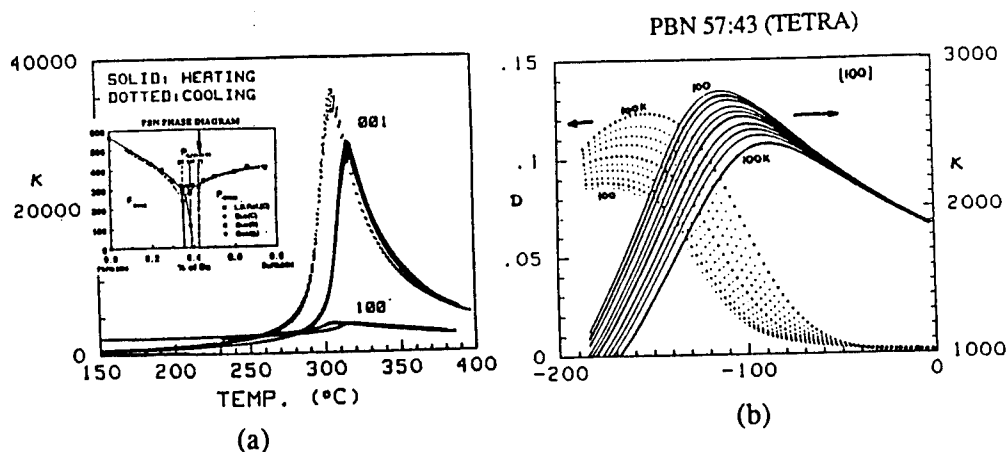


FIGURE 12 (a) Dielectric response for fields along 001 and 100 directions for a composition in the tetragonal ferroelectric phase field (57:43) of PBN.  
 (b) Low temperature dispersive dielectric response for fields orthogonal to the major polar direction.

polarization have  $P_s$  vectors which are slightly tilted away from the major axis. At the higher temperature transitions the energy barriers against polarization inversion are large and the dispersion weak, however the tilts perpendicular to  $P$  are random and dynamical, freezing out at the lower temperature dispersion. The situation could be envisaged as that of a spin glass with two freezing temperatures for the orthogonal components of  $P$ . Magnetic systems which exhibit such phenomena have been studied.<sup>35</sup>

### THEORETICAL UNDERSTANDING

The relaxor ferroelectrics in the oxygen octahedron families are very complex solids so that it is certainly not surprising that in spite of some thirty years of continuous effort there is no comprehensive quantitative theory. It does appear that there is reasonably general agreement of the superparaelectric character at temperatures well above  $T_m$  but the detail of the kinetics of these regions and their mutual interaction as the temperature decreases is not clear.

An appealing simple model from A. Bell at EPFL<sup>36</sup> treats the micro region as a simple Devonshire ferroelectric, to calculate the activation energy  $\Delta H$  as a function of

size (assuming a simple spherical region). The distribution of activation energies then comes from a specific distribution of sizes, however to get good agreement with experiment it is still necessary to put in weak interaction between regions.

In a more general vein, Viehland<sup>37</sup> has pointed up the many behavior features of the relaxors which suggest spin glass like features.

An alternative model which can again explain qualitatively most features of the relaxor appeals to random electric fields associated with the composition fluctuations as the origin of the break up of normal domain structure and the tremendous slowing down of the dynamics in PMN. For large non zero electric fields, it becomes difficult to explain the aging phenomena which occur in PLZT and in suitably doped PMN. For such crystals aging under a field as little as 3KV/cm is sufficient to wipe out the relaxation at room temperature and to lead to a poled ferroelectric structure on cooling under short circuit conditions. Evidently the kinetics is very sensitive to small fields generated by defect dipole systems. Perhaps a way out of this dilemma would be the suggestion that the random field is of elastic rather than electric origin.

Recent measurements of the poling of zero field cooled PMN does suggest<sup>38</sup> the presence of barkhausen pulses which could occur from the switching of ferroelectric micro-domains in concert with the random field model however it is not clear whether these measurements were carried out on aging free material.

In summary, many features of the chemo-elasto-dielectric behavior of relaxors are becoming more clear, even though there is not yet a comprehensive qualitative theory to explain the responses.

## REFERENCES

1. G. S. Smolensky, A. Agronovskaya, Soviet Physics Solid State, **1**, 1429 (1960).
2. V. Bokov and I. Mylnikova, Soviet Physics Solid State, **3**, 3 (1960).
3. C. Randall and A. Bhalla, J. Mat. Sci., **29**, 5 (1990).
4. J. Chen and M. Harmer, J. Am. Ceram. Soc., **72**, 593 (1989).
5. C. Randall, PhD Thesis, University of Essex, Colchester, England (1987).
6. A. Katchaturyan, Privat Communication.
7. N. Setter, PhD Thesis, Pennsylvania State University (1980).
8. C. Randall, D. J. Barber, and R. W. Whatmore, Journal of Microscopy **145** (3), 275 (1984).
9. G. Rossetti, PhD Thesis, Pennsylvania State University (1993).
10. W. A. Schulze, J. V. Biggers, and L. E. Cross, J. Am. Ceram. Soc., **61**, 749 (1980).
11. M. P. Leffler, MS Thesis, Pennsylvania State University (1989).
12. G. Burns and F. Dracol, Solid State Commun., **48**, 853 (1983).
13. P. Asadipour, U. Kumar, S. J. Jang, A. S. Bhalla, and L. E. Cross, Ign. J. Appl. Phys., **24** (2), 742 (1985).
14. A. S. Bhalla, R. Guo, L. E. Cross, and G. Burns, Phys. Rev. B., **36** (4), 2030 (1987).
15. P. Asadipour, MS Thesis, Pennsylvania State University (1986).
16. D. Viehland, S. J. Jang, L. E. Cross, and M. Wuttig, J. Appl. Phys., **66**, 2916 (1990).
17. D. Viehland, M. Wuttig, and L. E. Cross, Ferroelectrics, **120**, 71 (1991).
18. W. Pan, E. Furman, G. O. Dayton, and L. E. Cross, J. Mat. Sci. Letters, **5**, 647 (1986).
19. W. Pan, Q. Zhang, and L. E. Cross, J. Am. Ceram. Soc., **71**, C17 (1988).
20. C. Randall, D. Barbes, and P. Groves, J. Mat. Sci., **21**, 4456 (1986).
21. Y. Xi, C. Zhilli, and L. E. Cross, J. Appl. Phys., **54**, 3399 (1983).
22. J. deAlmedia and D. Thouless, J. Phys A, **11**, 983 (1978).



23. R. Chamberlin, M. Hardiman, L. Turkevich, and R. Orbach, Phys. Rev. B, **25**, 6720 (1982).
24. W. Pan and L. E. Cross, ONR Annual Report for 1985 on contract N00014-82-K0339 (July 1986).
25. W. Pay, W. Y. Gu, D. J. Taylor, and L. E. Cross, Jpn. J. Appl. Phys., **28** (4), 653 (1989).
26. A. M. Glass, J. Appl. Phys., **40**, 4699 (1981).
27. G. Burns and F. H. Dacol, Ferroelectrics, **104**, 25 (1990).
28. G. Burns, Phase Transitions, **5**, 261 (1985).
29. T. Cline, PhD Thesis, Pennsylvania State University (1979).
30. M. E. Lines and A. M. Glass, Principles and Applications of Ferroelectrics and related materials, Clarendon, Oxford (1977).
31. R. R. Neurgaonkar and W. K. Kory, J. Opt. Soc. Am., **3(B)**, 274 (1986).
32. E. J. Sharp, W. W. Clark III, M. Miller, G. L. Wood, B. Monson, and G. J. Salamo, Applied Optics, **29** (6), 743 (1990).
33. M. H. Francombe, Acta. Cryst., **13**, 131 (1960).
34. R. Guo, A. S. Bhalla, C. Randall, and L. E. Cross, J. Appl. Phys., **67** (10), 6405 (1990).
35. A. Schröder, J. Fisher, H. von Lohneysen, W. Bauhofer, and U. Steigenberger, J. Phys (Paris) Colloq (to be published).
36. A. Bell, J. of Physics: Condensed Matter (submitted).
37. D. Viehland, PhD Thesis, Pennsylvania State University (May 1991).
38. V. Westphal, W. Kleemann, and M. D. Glinchuk, Phys. Rev. Letters, **(68** (6), 847 (1992).

# APPENDIX 5

# Boundary Conditions for Shape Memory in Ceramic Material Systems

L. ERIC CROSS

*Evan Pugh Professor of Electrical Engineering, Intercollege Materials Research Laboratory,  
The Pennsylvania State University, University Park, PA 16802-4800*

**ABSTRACT:** Piezoelectric ceramics have excellent transduction capability in elastoelectric conversion and are widely used as both sensors and actuators for smart materials and systems. The very high authority in actuation (tons/in<sup>2</sup>) is limited in application by the very short throw (strains  $\approx 10^{-3}$ ) and there is urgent need to improve this strain capability. Since the polarization related piezoelectric and electrostriction constants in perovskites have a very limited range, to improve strain it is necessary to switch larger values of polarization. In this paper, phase change and domain switching systems which mimic the high strain of the metallic martensite shape memory alloys will be reviewed. Characteristic features necessary to ensure electrical control of the shape will be discussed and illustrated by three different families of perovskites. It is speculated that at very high switching speeds the electrostrictive domain strain may become 'uncoupled' from the polarization and evidence that this occurs in bismuth titanate is presented.

## INTRODUCTION

**I**N the hierarchy of systems which can be used for mechanical actuation, the traditional electromagnetic hydraulic or pneumatic systems (Table 1) have strong advantages in the large throw (strain) and very high overall efficiency, but are markedly deficient in speed of actuation and in simplicity and maintainability. For the available solid state actuator families the shape memory alloys provide massive actuation stress, tolerable strain but very low efficiency and speed. The piezoelectric, electrostrictive and magnetostrictive systems are capable of large stresses, high speeds and reasonable efficiency but are very strongly limited in strain capability. Muscle as we are all aware is an excellent actuator, but is proving very difficult to mimic in polymeric systems and the contractile polymers are still at an early stage of development.

Clearly, there could be a very useful advantage if some of the higher force and strain capability of the ferroelastic shape memory alloy could be engineered to have the speed and efficiency of the piezoelectric/electrostrictive actuator.

The actuation mechanism of the alloy system is illustrated in cartoon form in Figure 1 (Saburi, 1992). In the low temperature martensitic phase, the metal is twinned and soft, and can be readily deformed to a new state by stress induced reconfiguration of the twin system. To recover the original shape requires that the metal be heated to pass through the phase change to the Austenitic form which is untwinned and which can then be cooled to recover the original shape after which the cycle can be repeated. It is this need for heating and cooling in the shape recovery cycle which leads to the long time constant and low actuation efficiency of the metal system.

For perovskite structure ferroelectrics in the PZT and PLZT systems there are necessarily twin (domain) states which are both ferroelectric and ferroelastic and martensitic like phase changes to other symmetry states, however unlike the metal, the ferroelectric domains carry a polarization and can be reoriented by electric field. Also in suitable compositions, there are phase changes from non polar to ferroelectric states which can be induced by electric field and do not require that the system be heated or cooled to drive the phase change.

It is the purpose of this paper to explore the necessary boundary conditions on the different systems which can give rise to analogous domain controlled shape change to those in the shape memory alloys but where the phenomena can be electric field controller rather than requiring the heating and cooling which is so very expensive both in energy and in time in the metal alloys.

## POTENTIAL FERROELECTRIC SHAPE MEMORY MATERIALS

### Antiferroelectric to Ferroelectric Switching Systems

Perhaps the closest analog to the shape memory alloy in the ceramic systems occur for zirconia rich composition in the ternary  $\text{PbZrO}_3$ ;  $\text{PbSnO}_3$ : $\text{PbTiO}_3$  compositions family. Suitable compositions in this family have a stable orthorhombic or tetragonal antiferroelectric structure in the base state (Figure 2) but can be driven by high electric field to a rhombohedral ferroelectric state. For composition which are some distance away from the antiferroelectric ferroelectric phase boundary both this forward switching A  $\rightarrow$  F

**Table 1. Mechanical actuators.**

Traditional Technologies			
	Stress (MPa)	Strain	Efficiency
Electromechanical	0.02	0.5	90%
Hydraulic	20	0.5	80%
Pneumatic	0.7	0.5	90%
Solid State Actuators			
Shape memory alloys	200	0.1	3%
Piezoelectric	35	0.001	50%
Electrostrictive	50	0.002	50%
Magnetostrictive	35	0.002	80%
Contractile polymeric	0.3	0.5	30%
Muscle	0.35	0.2	30%

under increasing field, and the backward switching  $F \rightarrow A$  under decreasing field can be very rapid as shown by the studies of Wuyi Pan et al. (Figure 3,4) (Pan et al. 1989). Since the  $A \rightleftharpoons F$  transition is necessarily first order by symmetry (Shuvalov, 1970) there is a finite region in the phase diagram where the two phase  $A + F$  can coexist (Figure 5). If compositions are chosen in this region then it is possible because of the energy barriers between states to leave a

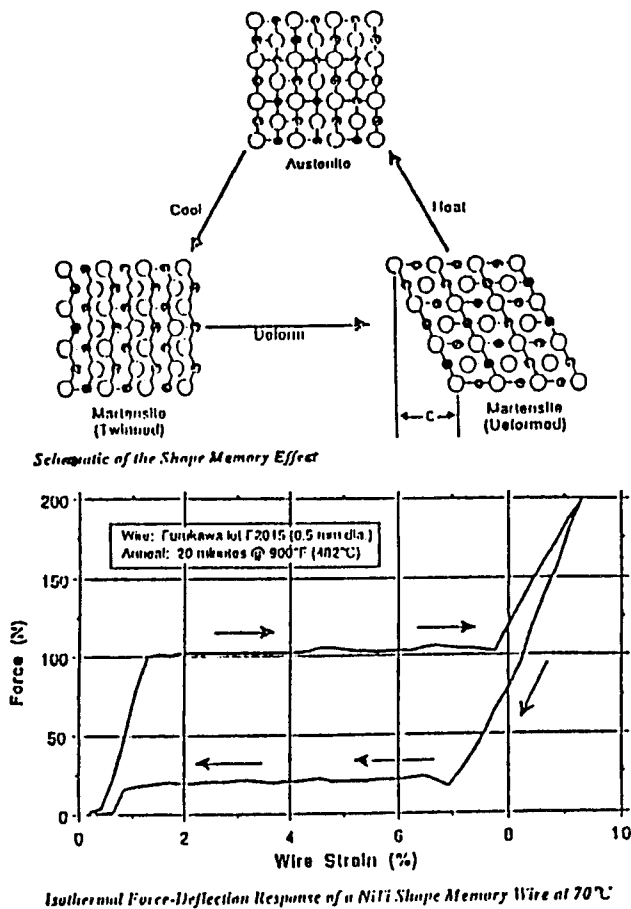


**Figure 1.** Cartoon illustrating the Working of a NiTi Shape Memory Alloy.

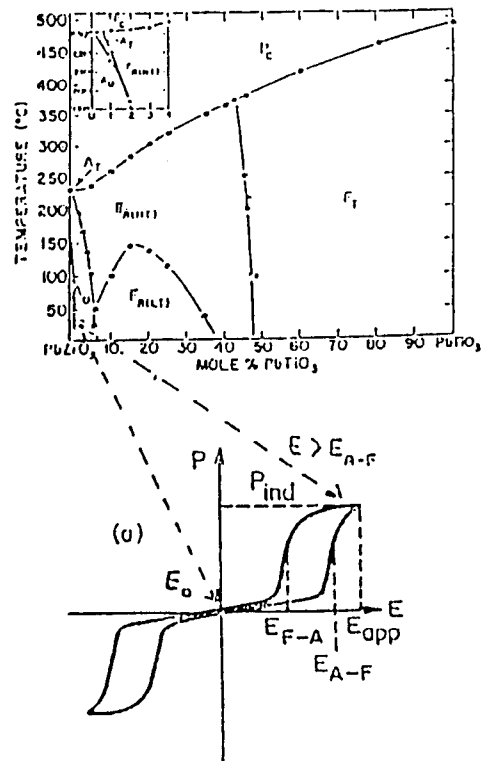


**Figure 2.** Lead zirconate titanate phase diagram showing location of the  $\text{PbZrO}_3$  rich antiferroelectric phase and of the induction of a ferroelectric phase in this region by a high electric field.

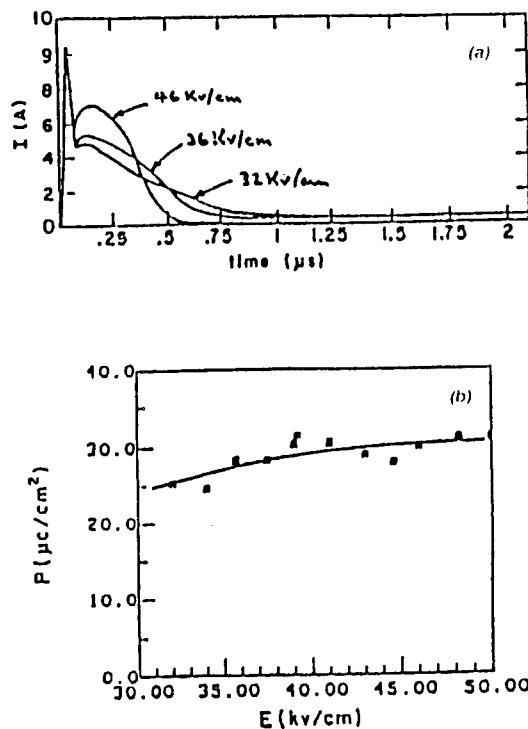


**Figure 3.** (a) Forward switching  $AF \rightarrow F$  speed as a function of applied field; (b) Switched charge as a function of driving field.

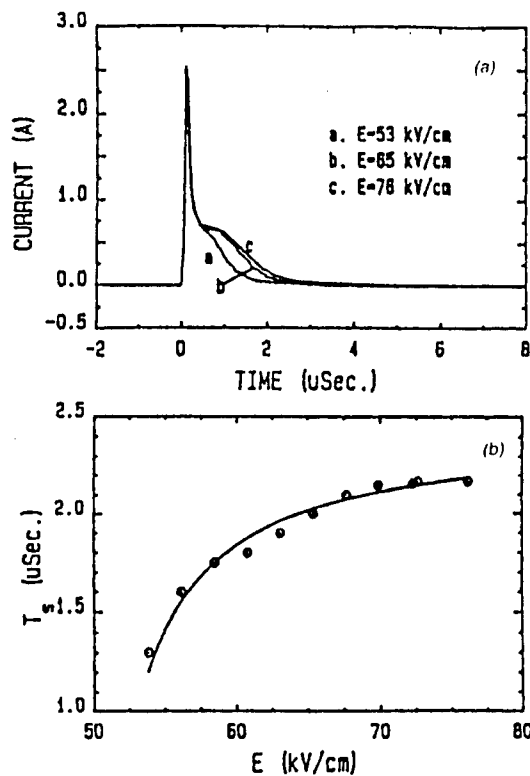


Figure 4. Backward Switching F-AF as a Function of Ferroelectric inducing field.

suitable crystal or ceramic "hug up" in a mixed phase state. It is this co-existence region in the phase diagram of Figure 5 which gives the possibility of a sequence of remanent states which are of different dimensions to the original antiferroelectric form. For simple electrical control of shape recovery a critical problem is outlined in cartoon form in Figure 6. If on increasing the reverse field the system first drops back into the antiferroelectric form [Figure 6(a)] the original shape is recovered. There is however an alternative path which would be direct polarization inversion by  $180^\circ$  domain wall motion shown in cartoon form in Figure 6(b).

In the practical systems, it is clear from studies by Payne (Yang and Payne, 1992) and Uchino (Uchino, 1985) that either alternative can be realized in different composition

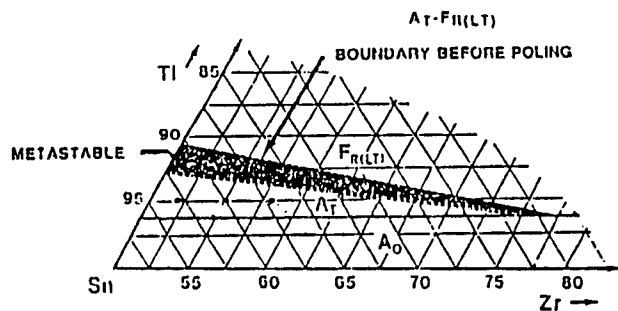


Figure 5. Coexistence region between AF and F phases which makes Shape Memory Possible in this system.

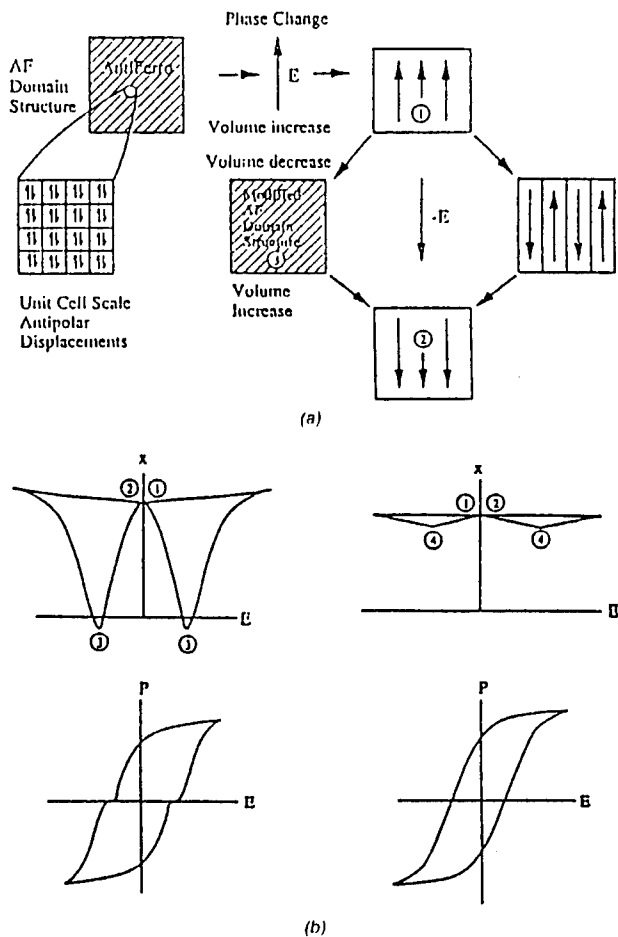


Figure 6. Cartoon illustrating the induction of the ferroelectric phase under high field and the possible evolution of polarization and strain. (a) If antiferroelectric switch back is preferred; (b) If simple  $180^\circ$  domain inversion takes place.

ranges in the modified PSnZT family. The study by Uchino (Uchino, 1985) shows that even in the same system, there may be only a very limited range over which the simple field inversion control of shape memory may be realized (Figures 7,8).

For all compositions in the two phase region it is clear that thermal shape recovery will be possible in direct analog to the metal systems. Since however the ceramics are brittle and the domain strains are smaller, these compositions would be significantly inferior to their metallic counterparts.

### Relaxor Ferroelectric Spin Glass to Ferroelectric Switching

An alternative family of compositions in the perovskite structure which have interesting electrical characteristics are in the lead lanthanum zirconate titanate family (PLZTs). The phase diagram for the PLZTs after Haertling and Land [Haertling and Land, (1971)] is shown in Figure 9. The compositions which are of interest here are close to the pseudo

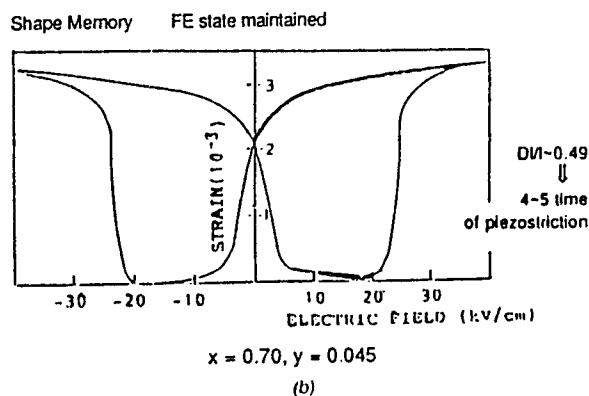
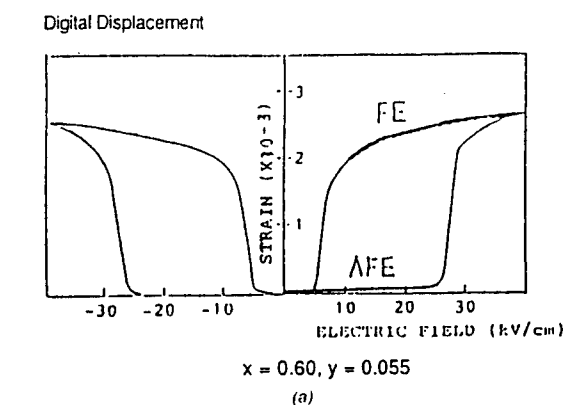


Figure 7. Illustration of the strain behavior for AF-F Switching (Uchino et al.). (a) without shape memory; (b) with shape memory which can be electrically erased.

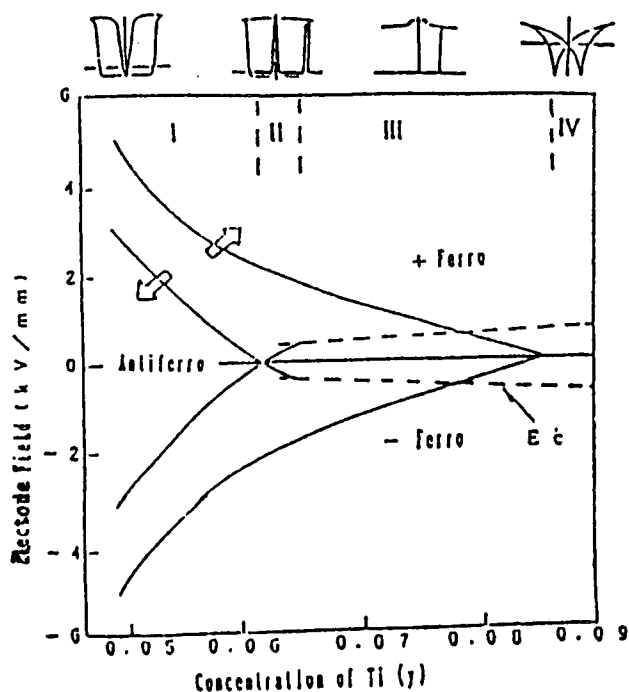


Figure 8. Illustration of the limited window in the composition field where electrically erasable shape memory is possible (Uchino et al.).

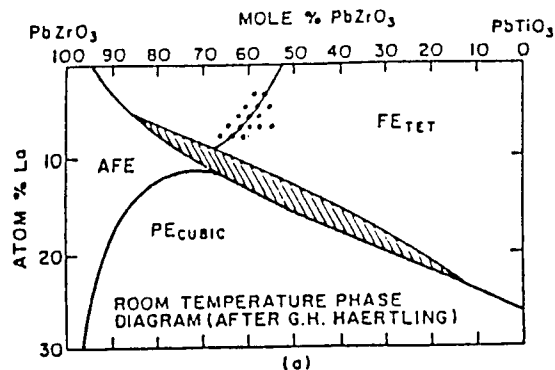


Figure 9. Lead lanthanum zirconate titanate phase diagram after Haertling and Land illustration the compositions close to the MPB which have been explored for shape memory.

morphotropic boundary between tetragonal and rhombohedral phases and in the higher  $\text{La}_2\text{O}_3$  region marked in Figure 9. A characteristic of the dielectric response is that unlike that of the normal ferroelectric the temperature of the dielectric maximum observed on heating or cooling is very strongly frequency dependent. This behavior has been shown (Viehland et al. 1991) to stem from a set of micropolar regions at high temperature which freeze in on cooling to a glass like ensemble.

In this case, the glass like ensemble may be reconstructed under electric field into a polar ferroelectric form. The polarization and associated shape changes in these composition are suggested in a highly simplified cartoon form in Figure 10.

Again switch forward and switch back involve crossing a finite energy barrier so that the system may be left in a remanent distorted state. For switch back to the glass like state it is essential that under reverse field this process [Figure 10(a)] take place before the possible inversion of the polar direction by  $180^\circ$  domain wall motion as envisaged in Figure 10(b). Extensive studies by Meng et al. (Meng, Kumar and Cross, 1985) have explored both the electrical polarization and the elastic strain for compositions in this family (Figures 11,12). Here it would appear that the glass like switch back is rather strongly preferred over the  $180^\circ$  type switching so that electric field recovery of the unstrained state is preferred.

### Simple Proper Ferroelastic: Ferroelectric Domain Switching

In studied by Meng which extended farther into the "normal" ferroelectric region of the PLZT system, but again with compositions just on the rhombohedral side of the MPB, it becomes clear that large remanent domain strains can be left in these systems at zero field, but can be recovered on reversing the field. The process requires that the ferroelastic reorientation process occur before simple ferroelectric inversion (Figure 13).

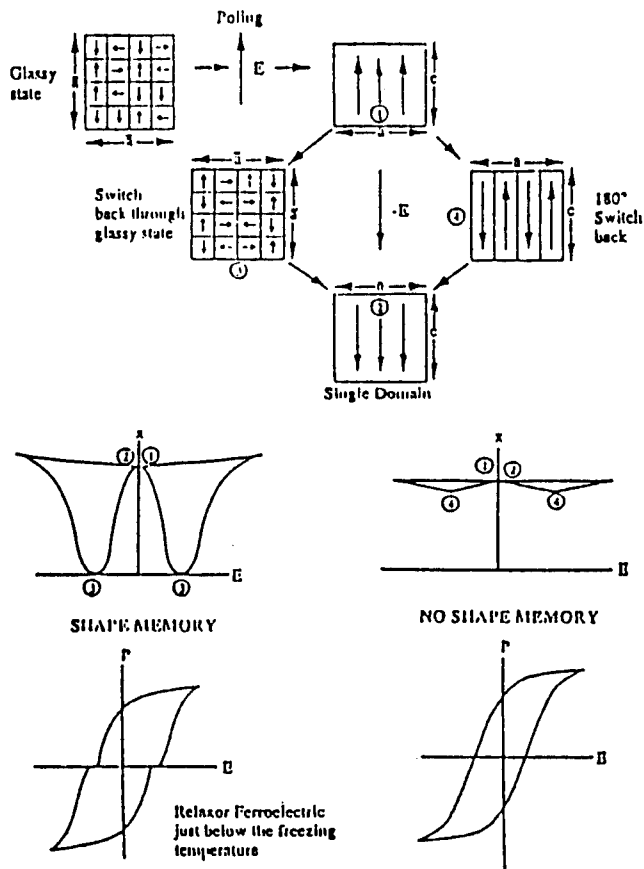


Figure 10. Cartoon of the possible electrically erasable shape memory in the relaxor ferroelectric PLZT composition. Competition between switch back to the spin glass state and direct 180° main inversion is illustrated.

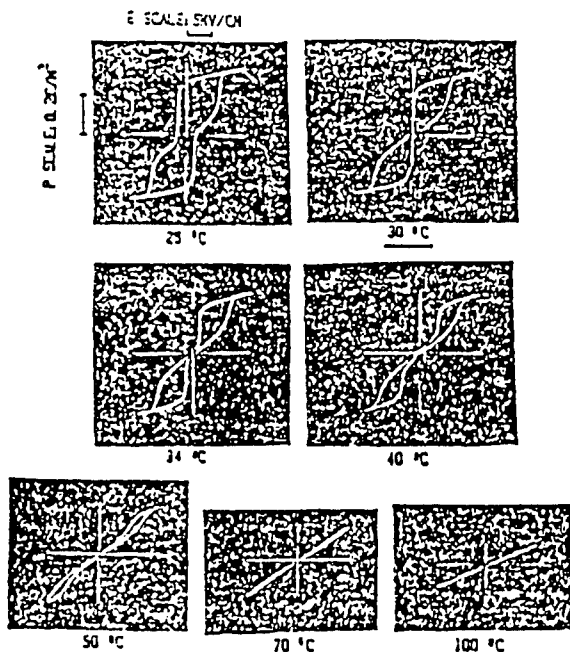


Figure 11. Electrical behavior of an 8:70:30 PLZT composition in the relaxor region.

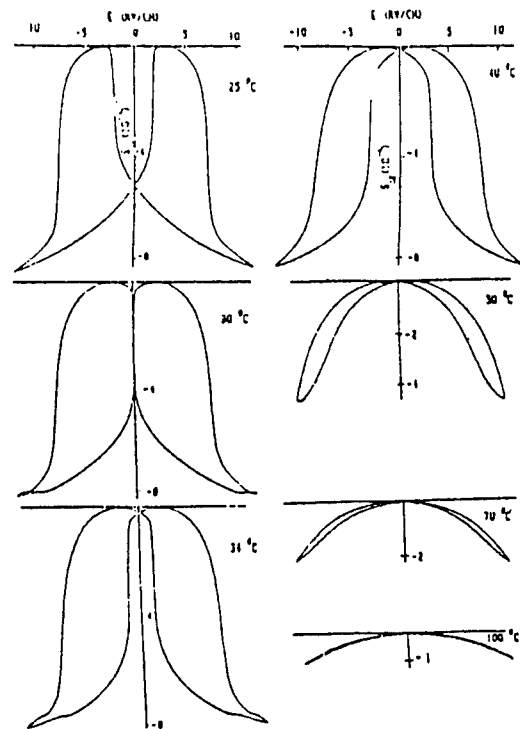


Figure 12. Strain behavior of the relaxor ferroelectric under high cyclic field showing electrically erasable shape memory for the composition at 25 and 30 °C.

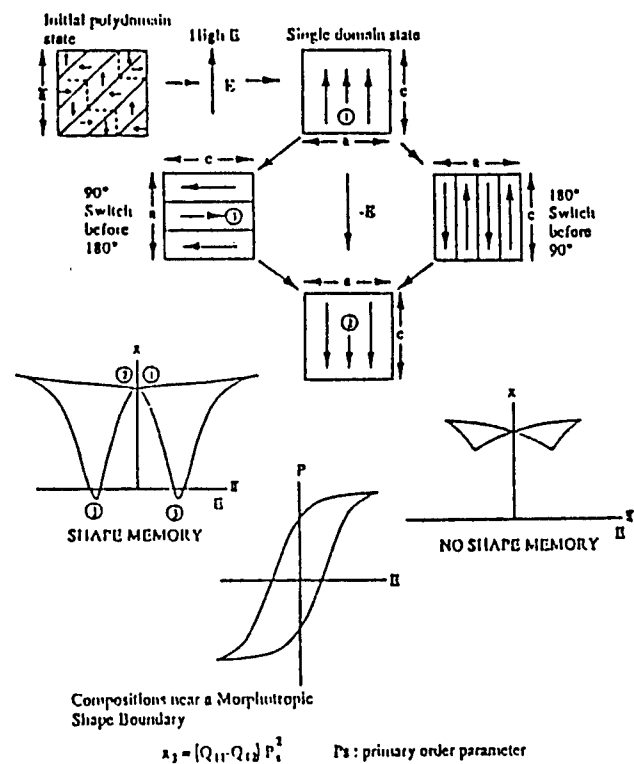


Figure 13. Possible shape memory behavior in a normal ferroelectric perovskite in which 90° switching is strongly preferred over 180° inversion. Behavior which is likely in compositions close to the morphotropic boundary (MPB).

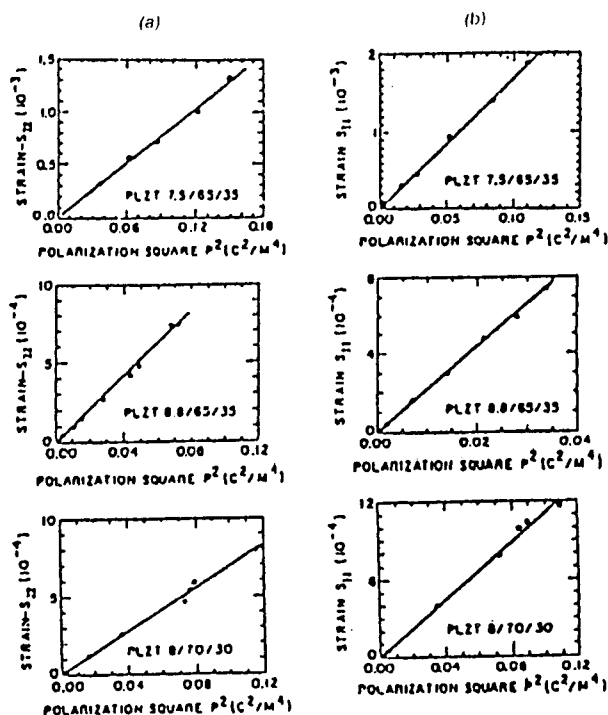


Figure 14. Confirmation of the electrostrictive character of the deformation on the PLZT relaxor compositions.

In all the PLZT compositions explored the induced elastic strain is dominantly electrostrictive as evidenced by the linearity of the plots of strain vs (polarization)<sup>2</sup> (Figure 14). It is most interesting to note that with decreasing La<sub>2</sub>O<sub>3</sub> content near the bound of the onset of proper ferroelectric behavior the intercept of the  $x$  vs  $P^2$  line rises above the origin on the strain axis. We believe that this offset is due to the non zero ferroelectric polarization in the domain structure which is at the coercive field folded out orthogonal to the poling direction. Now the origin of the strain measurement is at a lower thickness dimension due to the predominance of the shorter 'a' axis leading to this offset. One may note that the slope of the lines does not change, confirming again the basic electrostrictive origin. Clearly in this system at compositions close to the MPB ferroelastic-ferroelectric switching is strongly preferred over simple 180° inversion so that these compositions are very favorable for electrically controlled shape memory.

## SWITCHING SPEED CONSIDERATIONS

In the antiferroelectric: ferroelastic switching compositions which exhibit shape memory the response speeds have not been explored at short switching times.

Earlier work by Pan at compositions outside the two phase co-existence region has shown sub microsecond switching speeds in both forward and backward directions. Since the transition is displacive and diffusionless this ap-

pears entirely consistent. For the domain driven changes one may note that the polarization process depends upon an optic mode of ionic motion, but that the elastic response through the coupling by electrostriction is essentially an acoustic mode.

A question which we have speculated about is whether at very high switching speeds (under high fields) the polarization could be uncoupled from the strain, switched to a metastable minimum under high field, then left for the strain to catch up. Such behavior in the perovskites could give rise to a sort of high speed latching type actuator, but we know of no experimental data to support such a speculation.

For the bismuth titanate (Bi<sub>4</sub>Ti<sub>3</sub>O<sub>12</sub>) single crystal system, Cummins et. al., (Cummins and Luke) have shown that the single domain symmetry is monoclinic ( $m$ ) with the polar axis tilted slightly out of the ( $a$ ) plane and switchable between the two alternative tilt positions. In this case, the tilt of polarization is coupled to a very weak shear which switches sign on polarization inversion.

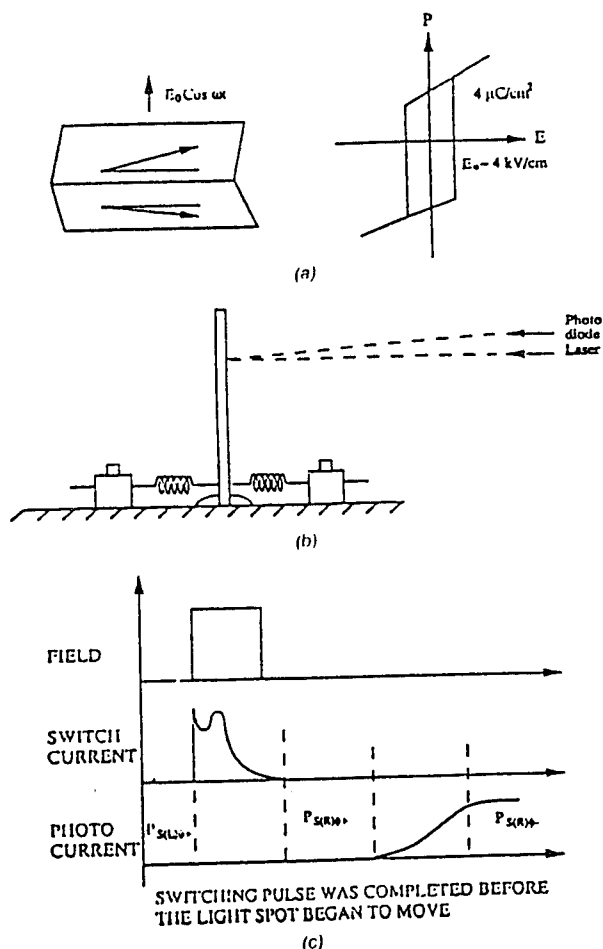


Figure 15. (a) Illustration of the polarization situation in a Bi<sub>4</sub>Ti<sub>3</sub>O<sub>12</sub> crystal, the shear which accompanies the small tilt of the  $P_s$  vector is grossly exaggerated; (b) Experimental setup for exhibiting the polarization switching and associated strain behavior; (c) Conformation of the separation of polarization and strain switching in the Bi<sub>4</sub>Ti<sub>3</sub>O<sub>12</sub> crystal.



For a lath like crystal polarized to a single domain state and rigidly mounted at one end (Figure 15) polarization switching tilts the crystal and the tilt angle may be monitored by a simple optical lever. Using fast pulse switching in this arrangement Cummins and Cross were able to demonstrate that the whole polarization switch could be accomplished before the crystal began to move, and thus that in this system polarization and strain can in fact be decoupled.

## CONCLUSIONS

Conventional thermally driven shape memory may occur in a number of ferroelastic: ferroelectric perovskites which go through martensitic like phase changes. For the more useful shape memory which can be driven by a simple electric field configuration, it is essential that in the composition of interest ferroelastic domain or phase switching take place at lower field strength than simple pure ferroelectric switching. In the antiferroelectric:ferroelectric systems the compositions "window" where this may occur appears quite narrow. For relaxor ferroelectric PLZTs at compositions close to morphotropy the requirement is again similar, however now because of the closeness to the MPB ferroelastic switching appears to be strongly preferred.

Since polarization is a very much faster process than elastic strain we speculate that electrostriction may become "uncoupled" at very high switching speeds and show evidence

that such an uncoupling has been observed in  $\text{Bi}_4\text{Ti}_3\text{O}_{12}$  single crystals.

## REFERENCES

- Cummins, S. E. and T. Luke. Private Communications.
- Haertling, G. H. and C. E. Land. 1971. "Transparent Ceramics in the Lead Lanthanum Zirconate Titanate Composition Family", *J. Am. Ceram. Soc.* 54(1).
- Meng, Z., U. Kumar and L. E. Cross. 1985. "Electrostriction in Lead Lanthanum Zirconate Titanate Ceramics", *J. Am. Ceram. Soc.*, 68(8):335.
- Pan, W., Q. Zhang, A. Bhalla and L. E. Cross. 1989. "Antiferroelectric to Ferroelectric Switching in Modified Lead Zirconate Titanate Stannate Ceramics", *J. Am. Ceram. Soc.*, 72(4):571.
- Saburi, T. 1992. "Ti-Ni Shape Memory Alloys and Martensitic Transformation", *Proc. Int. Conf. on Martensitic*, 20-24. C. M. Wyman and J. Perkins, eds., p. 857.
- Shuvalov, L. A. 1970. "Symmetry Aspects of Ferroelectricity", *J. Phys. Soc. Japan* 28 (Supplement):38.
- Uchino, K. 1985. "Digital Displacement Transducer Using Antiferroelectrics", *Japan J. Appl. Phys.*, 24:460.
- Viehland, D., M. Wuttig and L. E. Cross. 1991. "The Glassy Behavior of Relaxor Ferroelectrics", *Ferroelectrics*, 120:71.
- Viehland, D., S. J. Jang, L. E. Cross and M. Wuttig. 1991. "Local Polar Configuration in Lead Magnesium Niobate Relaxors", *J. Appl. Phys.*, 69:1.
- Viehland, D., S. J. Jang, L. E. Cross and M. Wuttig. 1991. "The Dielectric Relaxation of Lead Magnesium Niobate Relaxor Ferroelectric", *Phil. Mag. B*, 64(3):335.
- Yang, P. and D. A. Payne. 1992. "Thermal Stability of Field Forced and Field Assisted Antiferroelectric to Ferroelectric Phase Transitions in  $\text{Pb}(\text{Zr}, \text{Sn}, \text{Ti})\text{O}_3$ ", *J. Appl. Phys.*, 71(3):1361.

# APPENDIX 6

# PHOTOSTRICTION AND ITS APPLICATIONS

Kenji Uchino and Sheng-Yuan Chu  
International Center for Actuators and Transducers  
Materials Research Laboratory, The Pennsylvania State University  
University Park, PA 16802

## Abstract

The photostrictive effect is the superimposing of photovoltaic and piezoelectric effects.  $(\text{Pb},\text{La})(\text{Zr},\text{Ti})\text{O}_3$  ceramics doped with  $\text{WO}_3$  exhibit large photostriction under irradiation of purple-color light, and are applicable as remote control actuators. Photo-driven relays and micro walking devices which have been developed, are designed to start moving as a result from the irradiation, having neither electric lead wires nor electric circuit.

## INTRODUCTION

Photostrictive effect is a phenomenon in which strain is induced in the sample when it is illuminated. This effect is focused especially in the fields of micromechanism and optical communication.

With decreasing the size of miniature robots/actuators, the weight of the electric lead wire connecting the power supply becomes significant, and remote control will definitely be required for sub-millimeter devices. A photo-driven actuator is a very promising candidate for micro-robots. On the other hand, the key components in optical communication are solid state lasers as a light source, optical fibers as a transfer line, and displays/ telephones as a visual/audible interface with the human. The former two components have been developed fairly successfully, and the photo-acoustic device (i. e. optical telephone or "photophone") will be eagerly anticipated in the next century.

Photostrictive devices which function when they receive the energy of light will be particularly suitable for use in the above-mentioned fields. In principle, the photostrictive effect is the superimposing of a photovoltaic effect, where a large voltage is generated in ferroelectrics through the irradiation of light,<sup>1)</sup> and a piezoelectric effect, where the material expands or contracts from the voltage applied. The photovoltaic effect mentioned here generates a greater-than-band-gap voltage, and is quite different from that based on the p-n junction of semiconductors (i. e. solar battery). It is generated when electrons excited by light move in a certain direction of the ferroelectric crystal due to the spontaneous polarization (i. e. crystallographic anisotropy).

---

To the extent authorized under the laws of the United States of America, all copyright interests in this publication are the property of The American Ceramic Society. Any duplication, reproduction, or republication of this publication or any part thereof, without the express written consent of The American Ceramic Society or fee paid to the Copyright Clearance Center, is prohibited.

This paper describes the details of the fundamental photostrictive effect in  $(\text{Pb},\text{La})(\text{Zr},\text{Ti})\text{O}_3$  ceramics first, then introduces its applications to a photo-driven relay and a micro walking machine, which are designed to move as a result of irradiation, having neither lead wires nor electric circuit.

## PHOTOSTRICTIVE PROPERTIES

### Materials Research

PLZT (x/y/z) samples were prepared in accordance with the following composition formula:  $\text{Pb}_{1-x}\text{La}_x(\text{Zr}_y\text{Ti}_z)_{1-x/4}\text{O}_3$ . The interrelation of photovoltaic current with remanent polarization is plotted for the PLZT family in Fig. 1. The average remanent polarization exhibiting the same magnitude of photo-current differs by 1.7 times between the tetragonal and rhombohedral phases; this suggests the photo-induced electron excitation is related to the (0 0 1) axis-oriented orbit, i. e. the hybridized orbit of p-orbit of oxygen and d-orbit of Ti/Zr. The photostrictive figure of merit is evaluated by the product of the photovoltaic voltage and the piezoelectric coefficient. Therefore, PLZT (3/52/48) was selected because the largest figure of merit is obtained with this composition.<sup>2,3)</sup>

Impurity doping on PLZT also affects the photovoltaic response significantly.<sup>4)</sup> Figure 2 shows the photovoltaic response for various dopants with the same concentration of 1 atomic % under an illumination intensity of  $4 \text{ mW/cm}^2$  at 366 nm. The dashed line in Fig. 2 represents the constant power curve corresponding to the non-doped PLZT. Regarding the photostriction effect, it is known that as the photovoltaic voltage increases, the strain value increases, and with increasing photo-current, there is an increase in the overall response. The photovoltaic response is enhanced by donor doping onto the B-site ( $\text{Nb}^{5+}$ ,  $\text{Ti}^{5+}$ ,  $\text{W}^{6+}$ ). On the other hand, impurity ions substituting at the A-site and/or acceptor ions substituting at the B-site, whose ionic valences are small (1 to 4), have no effect on the response. Figure 3 shows the photovoltaic response plotted as a function of atm % of  $\text{WO}_3$  doping concentration. Note that the maximum power is obtained at 0.4 % of the dopant.

Even when the composition is fixed, the photostriction still depends on the sintering condition or the grain size.<sup>5)</sup> Figure 4 shows the dependence of the photostrictive characteristics on the grain size. The smaller grain sample is preferable, if it is sintered to a high density.

### Effect of Light Polarization Direction

Effect of the light polarization direction on the photovoltaic phenomenon was investigated on the polycrystalline PLZT, using an experimental setup shown in Fig. 5 (a). This experiment is important when the photostriction is employed to "photophones", where the sample is illuminated with the polarized light traveling through an optical fiber. The rotation angle  $\theta$  was taken from the vertical spontaneous polarization direction, as shown in Fig. 5 (b). Both the photovoltaic voltage and current provided the maximum at  $\theta = 0$  and  $180^\circ$  and the minimum at  $\theta = 90^\circ$ ; this also indicates that the contributing electron orbit may be the p-d hybridized orbit mentioned above.

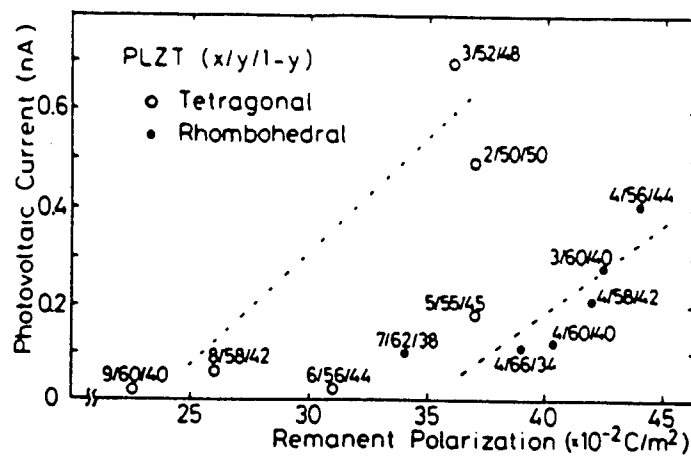


Fig.1. Interrelation of photovoltaic current with remanent polarization in PLZT family.

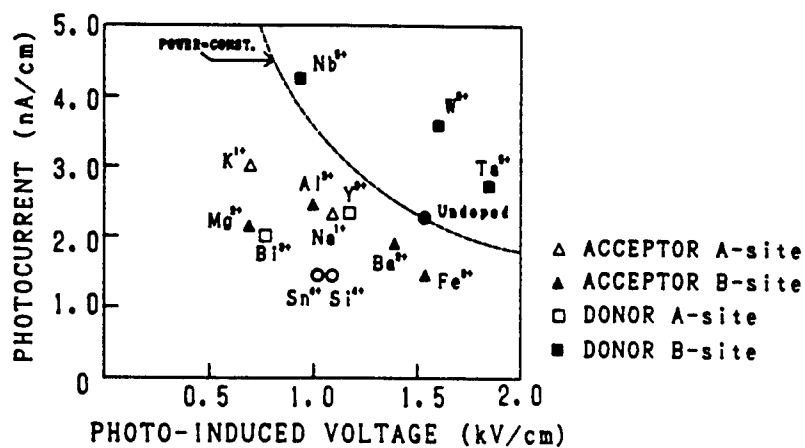


Fig.2. Photovoltaic response as a function of impurity doping.

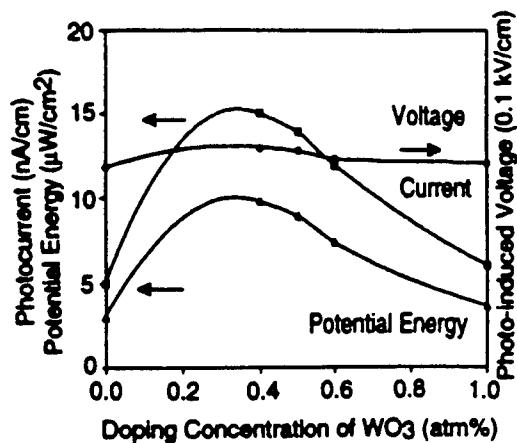


Fig.3. Photovoltaic current and voltage as a function of dopant concentration in  $\text{WO}_3$  doped PLZT.

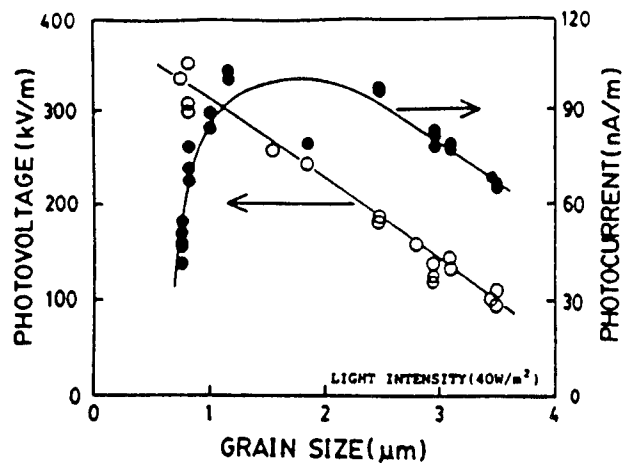


Fig.4. Grain size dependence of photostrictive characteristics in PLZT(3/52/48).

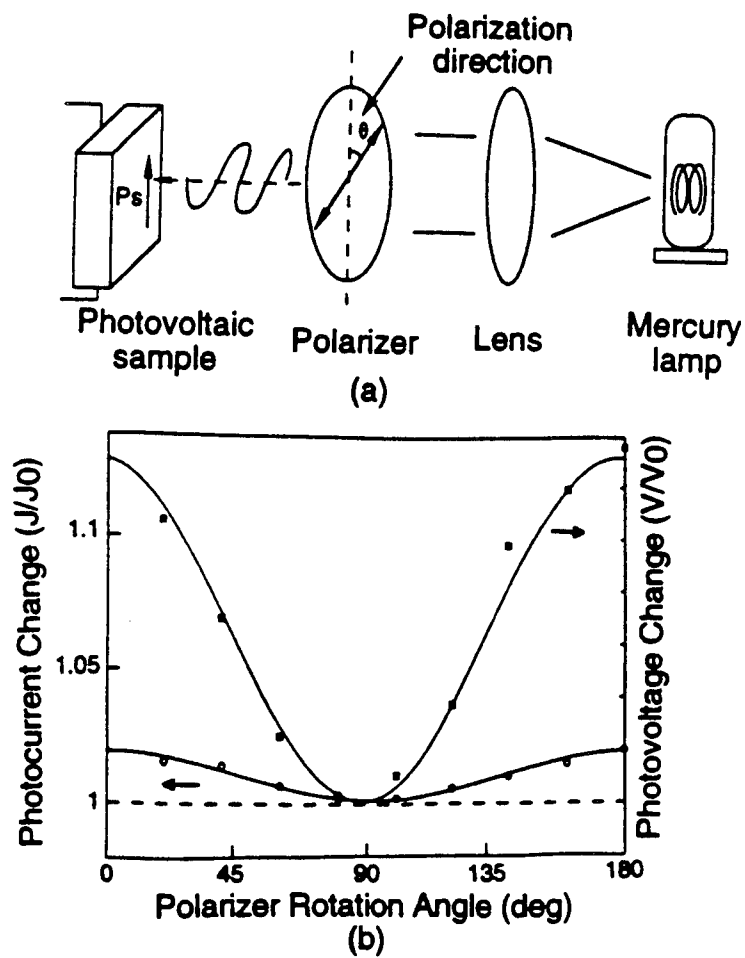


Fig.5. (a) Measuring system of the dependence of photovoltaic effect on light polarization direction, and (b) photovoltaic voltage and current as a function of the rotation angle.

# PHOTOSTRICTIVE ACTUATORS

## Photo-Driven Relay

A photo-driven relay was constructed using a photostrictor as the driver (Fig. 6).<sup>4)</sup> The driving part was a bimorph which consisted of two ceramic plates (5mmx20mmx0.16mm in size) joined so that their polarization directions were opposing. A dummy plate was positioned adjacent to the bimorph to cancel the photovoltaic voltage generated on the bimorph. Utilizing a dual beam method, switching was controlled by alternately irradiating the bimorph and the dummy. The time delay of the bimorph that ordinarily occurs in the off process due to a low dark conductivity could be avoided, making use of this dual beam method. Figure 7 shows the response of a photostrictive bimorph made from PLZT doped with 0.5 at%  $\text{WO}_3$  under an illumination intensity of  $10 \text{ mW/cm}^2$ . The amount of displacement observed at a tip of the bimorph (2 cm long and 0.32 mm thick) was  $150 \mu\text{m}$ . A snap action switch was used for the relay. Switching by a displacement of several tens of micron was possible with this device.<sup>6)</sup> The On/Off response of the photo-driven relay showed a typical delay time of 1 - 2 sec.

## Micro Walking Device

A photo-driven micro walking machine has also been developed using the photostrictive bimorphs.<sup>7)</sup> It was simple in structure, having only two ceramic legs (5mmx20mmx0.35mm) fixed to a plastic board (Fig.8). When the two legs were irradiated with purple light alternately, the device moved like an inchworm. The photostrictive bimorph as a whole was caused to bend by  $150 \mu\text{m}$  as if it averted the radiation of light. The inchworm built on a trial basis exhibited rather slow walking speed (several  $\mu\text{m/min}$ ) as shown in Fig. 9, since slip occurred between the contacting surface of its leg and the floor.

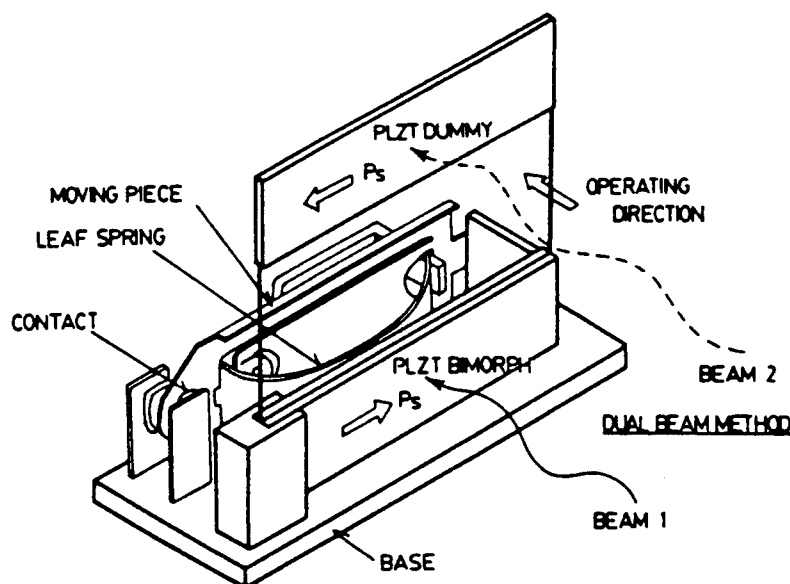


Fig.6. Structure of the photo-driven relay.

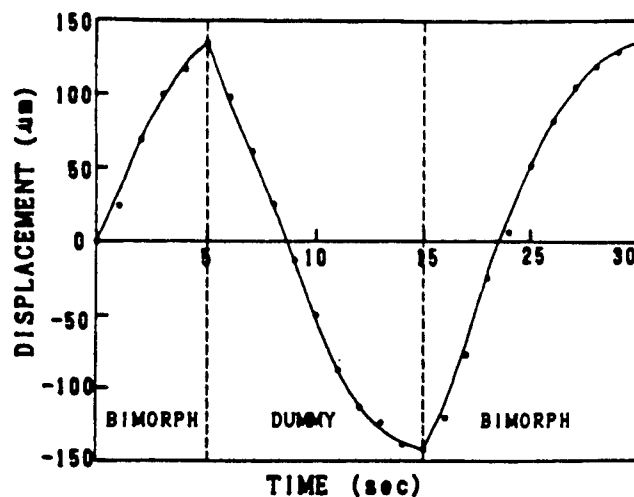


Fig.7. Bimorph deflection of the device made from  $\text{WO}_3$  0.5 atm% doped PLZT.

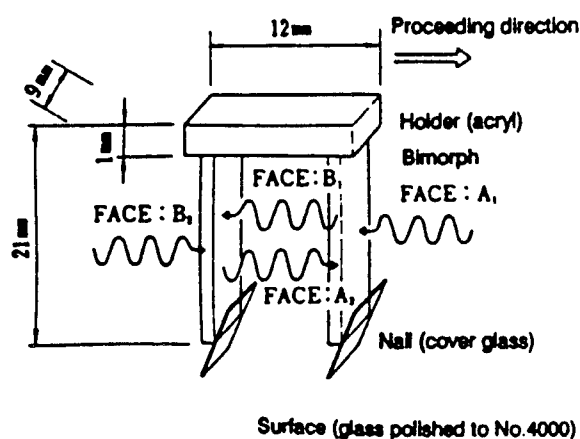


Fig.8. Structure of the photo-driven micro walking machine, and the direction of irradiation.

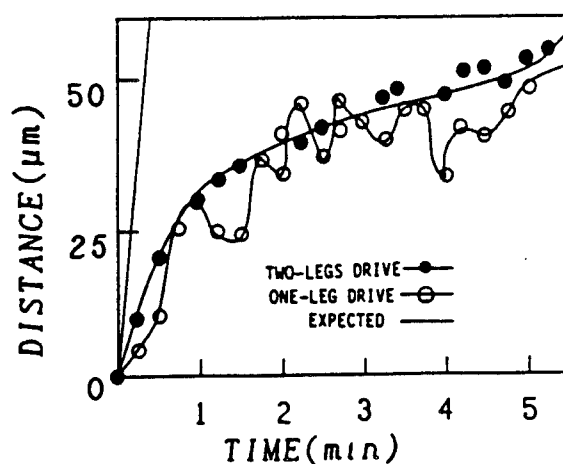


Fig.9. Position change of the photo-driven micro walking machine with time.



## CONCLUSION

The photostrictive actuators can be driven by the irradiation of light alone, so that they will be suitable for use in actuators, to which lead wires can hardly be connected because of their ultra-small size or of their employed conditions such as ultra-high vacuum. New actuators of this type have considerable effects upon the future micro-mechatronics.

This work was supported by US Army Research Office through Contract No. DAAL 03-92-G-0244.

## References

- 1) V. M. Fridkin, Photo-ferroelectrics, Solid-State Sciences 9, Springer-Verlag (1979).
- 2) K. Uchino, Y. Miyazawa and Late S. Nomura, "Photovoltaic Effect in Ferroelectric Ceramics and Its Applications," Jpn. J. Appl. Phys. **22**, Suppl. 22-2, 102 (1983).
- 3) K. Uchino, M. Aizawa and Late S. Nomura, "Photostrictive Effect in  $(\text{Pb},\text{La})(\text{Zr},\text{Ti})\text{O}_3$ ," Ferroelectrics **64**, 199 (1985).
- 4) M. Tanimura and K. Uchino, "Effect of Impurity Doping on Photostriction in Ferroelectric Ceramics," Sensors & Mater. **1**, 47 (1988).
- 5) T. Sada, M. Inoue and K. Uchino, "Photostrictive Effect in PLZT Ceramics," J. Ceram. Soc. Jpn. **5**, 545 (1987).
- 6) R. Sato, T. Taniguchi and M. Oba, "Piezoelectric Relays," OMRON Technics, No. 70, 52 (1983).
- 7) K. Uchino, "Micro Walking Machines Using Piezoelectric Actuators," J. Rob. Mech. **1**, 124 (1989).

# APPENDIX 7

# Smart Ceramics for Broadband Vibration Control

S. KUMAR,\* A. S. BHALLA AND L. E. CROSS

*Materials Research Laboratory, The Pennsylvania State University, University Park, PA 16802*

**ABSTRACT:** The broadband control of compliance coefficient  $S_{33}$  of a hard ceramic has direct applications in active vibration control. A collocated smart system consisting of ceramic sensor, actuator and a feedback amplifier is developed with 3.5 kHz bandwidth of compliance control without using filter in the feedback circuit. It is found that modified lead titanate with very low planar coupling coefficient  $k_p$  is most suited as a sensor material for this type of system. The requirements of the feedback amplifier for such a system are discussed and an amplifier design presented. The bandwidth of compliance control is experimentally determined by bench tests using a B and K shaker.

## INTRODUCTION

THE dynamic compliance coefficient  $S_{33}$  of a hard ceramic can be controlled over a narrowband rather easily by incorporating ceramic sensor and actuator in a collocated structure and placing a high  $Q$  bandpass filter in the feedback circuit [1]. The disadvantage of such a system is that the frequency of the incident pressure field on the smart structure should be known beforehand so that the bandpass filter can be tuned to that frequency. Obviously this severely restricts the application of such systems to active vibration control and other fields. For practical applications, the smart material/system should have a reasonable bandwidth of vibration control. This is where "smartness" of material may come in. The dynamic compliance  $S_{33}$  of this smart material should be controllable over a broad frequency range and with a simple control algorithm. A broadband control technique which does not require microprocessors and needs few electronic components would also enhance the smartness and the applicability of the system in vibration control. This smart material would then sense and react to any pressure fluctuation within the frequency band and contribute to active vibration control. In this paper we present a technique which can be used to achieve broadband control of compliance coefficient  $S_{33}$ .

## DESIGN CONSIDERATIONS

The system in which the sensor is mounted on top of the actuator will be investigated since it provides the most effective response to the pressure fluctuations. This system is shown in Figure 1. It is obvious that a 180 degree phase shift

between the sensor voltage and voltage applied to the actuator should be maintained over the frequency band of interest. A good broadband system therefore should have constant 180 degree phase shift and gain over the frequency band. Maintaining 180 degree phase shift (or close to it) is more crucial for the system than keeping the gain flat over the frequency band because if the gain drops with frequency in the frequency band, the effectiveness of the smart material would be reduced but if phase shift is not close to 180 degrees then the system may not work at all. Now since the amplifier is receiving the signal from the sensor and sending it to the actuator, the requirements of phase and gain become the requirements of the feedback amplifier. It should be noted that a 180 degree phase shift can be obtained by just interchanging positive and ground leads of the sensor. In that case, the feedback amplifier should have zero degree phase shift and constant gain over the frequency band. The basic requirements of the feedback amplifier are then stated as,

1. It is essential to maintain phase within the frequency band.
2. A reasonable gain flatness within the frequency band.
3. The amplifier must have gain and phase margins for stability.
4. It should be a low noise amplification.

Along with these requirements, there are also some constraints placed on the feedback amplifier. For example, to obtain a reasonable bandwidth of compliance control in the low frequency range, compensated operational amplifier cannot be used in the feedback circuit. This is because in compensated operational amplifiers, a pole is deliberately placed at some low frequency typically 1 Hz to 20 Hz. The effect of this is to have a 90 degrees phase shift over the passband for stability reasons. Because of this pole, a gradual phase change is introduced at the low frequency end which is not desired. Also, since the sensor is mounted on top of the actuator, there is a direct field coupling between

Associate Editor: D. Inman.

\*Author to whom correspondence should be addressed.

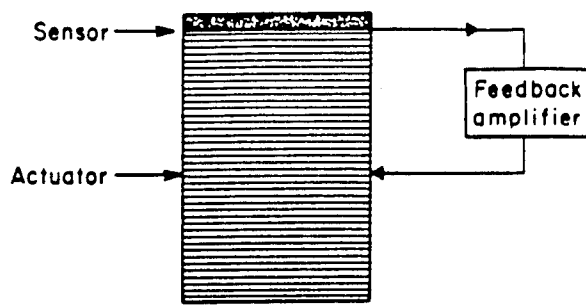


Figure 1. Mechanically coupled system. The sensor is mounted directly on top of the actuator.

sensor and actuator and oscillations are very likely to occur at one of the resonance frequencies of the system (including actuator and sensor resonance frequencies) if there is positive feedback at these frequencies. Precautions are required in designing of the smart system and electronic component layout to avoid oscillations.

The broadband control of the compliance coefficient was obtained by using a wideband feedback amplifier with high gain in the feedback circuit. This suppresses resonant modes of the actuator and eliminates use of lowpass filter in the feedback circuit. If the gain of the negative feedback is high and has wide bandwidth, i.e., gain and phase start to drop only at very high frequency and no filter is used in the circuit then for any disturbance in the actuator there is negative feedback. The disturbance will be picked up by the sensor, amplified and fed to actuator in opposite phase. Therefore actuator resonance will be heavily damped and the system will not oscillate at that frequency. Figure 2

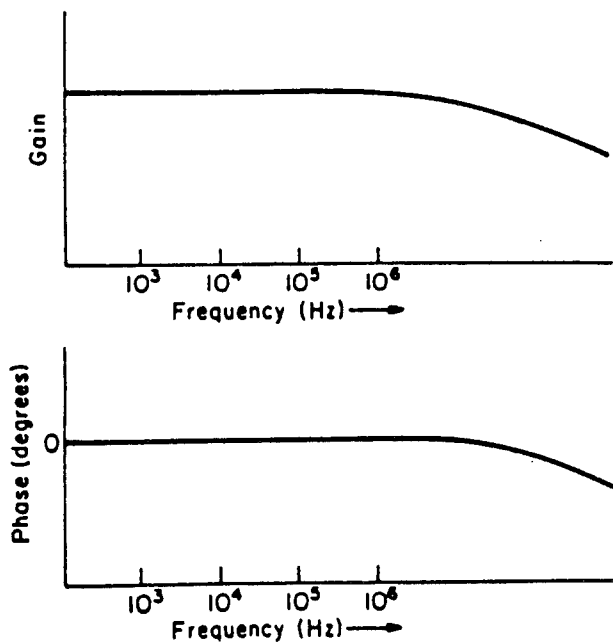


Figure 2. Desired frequency response of the feedback amplifier.

shows the desired frequency response of such a feedback amplifier. For a sensor, there is no negative feedback and therefore the system may oscillate at the sensor resonance frequencies. Therefore it is important to consider sensor characteristics carefully. Some of the desired characteristics of the sensor used in a smart material system for broadband response are:

1. Low  $Q_m$  (required for broadband response)
2. High resonance frequency
3. Low  $k_p$
4. High  $k_t$  and  $k_{32}$

It is clear that PZT would not be a good material to be used as sensor because of high  $k_p$  ( $\sim 0.6$ ). The radial modes will come into play and provide additional problems. Modified lead titanate, because of its very low  $k_p$  ( $\sim 0.02$ ), is a good sensor material to be used in smart system designs. The extremely low value of planar coupling coefficient  $k_p$  for calcium and samarium modified lead titanate ceramic is due to temperature dependence of  $d'_{31}$  which passes through zero near room temperature [2,3].

The  $d'_{31}$  is the real part of the  $d_{31}$  and  $k_p$  is related to the transverse coupling coefficient  $k_{31}$  and the material constants given by the following equation,

$$k_p = k_{31} [2/(1 - \sigma^E)]^{1/2} = \frac{d_{31} [2/(1 - \sigma^E)]^{1/2}}{(s_{11}^E \epsilon_{33}^T)^{1/2}}$$

where  $\sigma^E$  is the Poisson's ratio,  $s_{11}^E$  is the elastic compliance and  $\epsilon_{33}^T$  is the dielectric permittivity.

The lead titanate is a perovskite type ferroelectric belonging to the tetragonal 4 mm point group but unlike  $\text{BaTiO}_3$ , it does not undergo low temperature phase transition. The dielectric permittivity of the lead titanate shows low anisotropy. Turik et al. [4] have shown that by averaging single crystal properties in modified lead titanate ceramic, low anisotropy of dielectric permittivity of lead titanate gives large anisotropy of the piezoelectric coefficients (large  $d_{33}$  and small  $d_{31}$ ).

The actuator should have a linear response with respect to the applied voltage. Also a low capacitance actuator is preferred because of two reasons. First from circuit design considerations, driving a high capacitive load creates a pole at relatively low frequency influencing phase characteristics and second, high capacitance reduces the slew rate. The linearity of the NEC actuator was checked by placing a sensor on top of the actuator and driving the actuator. The sensor voltage was found to increase linearly with the voltage applied to the actuator up to a few volts.

The feedback circuit is designed for this system with the following considerations: a) Input impedance: Since the impedance of the sensor is very high, the input impedance of the first stage of the amplifier should be very high. FET input op-amp may be used for the first stage; b) AC coupling: The first stage of the amplifier should be AC coupled to prevent DC voltage amplification. This would make the system

## FEEDBACK CIRCUIT

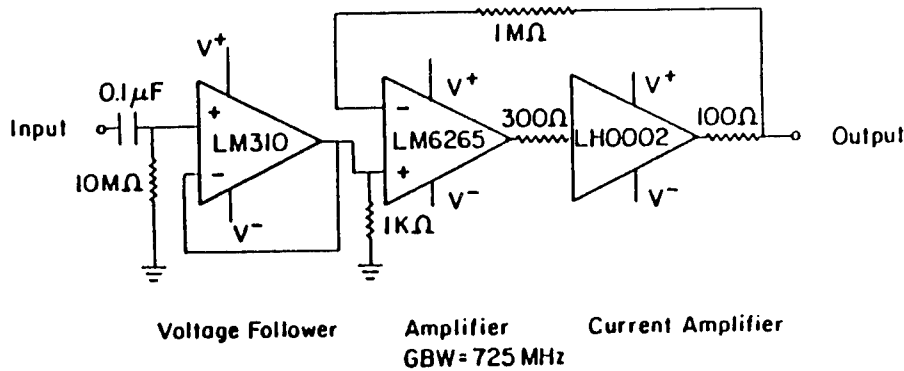


Figure 3. Circuit diagram of the feedback amplifier.

independent of static pressures. The other stages should be DC coupled otherwise coupling capacitors would form high pass filter with the resistances and introduce phase shift at lower frequencies; c) Slew rate: High speed electronic components should be used. When driving a capacitive load, slew rate is limited by available peak output current  $dV/dt = I_{pk}/C_L$  where  $C_L$  is the load capacitance (capacitance of the actuator); d) Output resistance: Driver output stage resistance should be very low because this resistance and capacitance of the actuator forms a low pass filter. Low load capacitance implies high 3 dB frequency of RC filter which is preferred. Low 3 dB frequency will influence the phase characteristics at low frequencies; e) The number of components: The total number of components in the feed-

back circuit should be kept as low as possible in order that the system can be miniaturized. Figure 3 shows the circuit diagram of the feedback circuit used in the smart system. A 5 to 10 pF capacitor is put across the feedback resistor.

Figure 4 shows the experimental set up. A shaker (B and K Type 4810) was used to provide pressure fluctuations and sensor voltage was monitored with and without feedback. Figure 5 shows the dimensions of the NEC actuator and modified lead titanate sensor. The frequency of the shaker was changed and at each frequency, the sensor voltage with and without feedback was recorded. The voltage applied to the shaker was kept constant therefore displacement was constant and the force exerted by the shaker could change. If the experiment is done with shaker current constant, then the force provided by the shaker is constant but stress on the sensor will change due to feedback because the actuator force is proportional to the strain. There was no filter in the feedback circuit. Both Spectrum Analyzer HP 3585A (20 Hz–40 MHz) and Dynamic Signal Analyzer HP 3562 were used to monitor the sensor voltage. Since Dynamic Signal Analyzer has upper frequency range of only 100 kHz, the

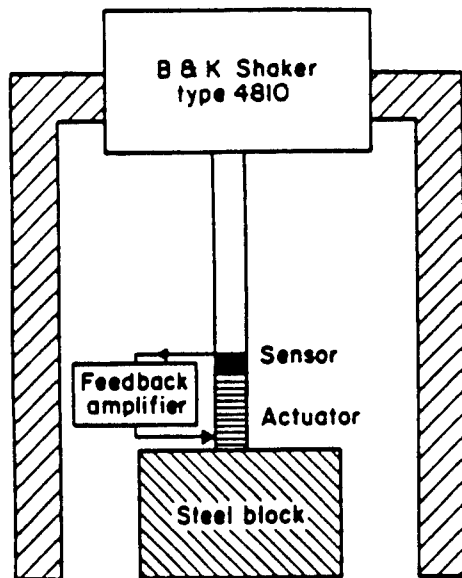


Figure 4. Experimental setup for the broadband response of the smart system.

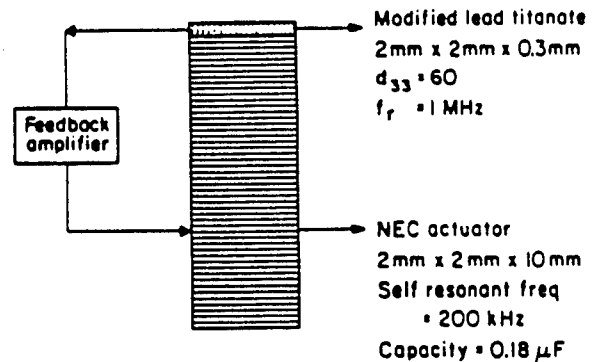


Figure 5. Sensor-actuator combination for the miniaturized smart system.

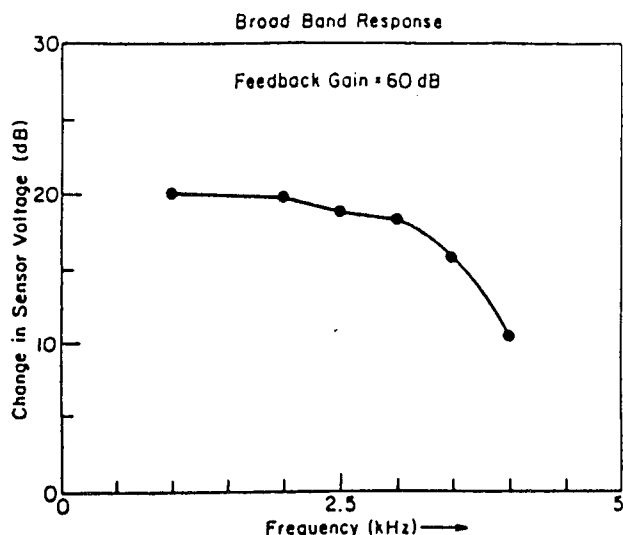


Figure 6. Broadband response of the miniaturized smart system.

Spectrum Analyzer was used to observe the resonance peaks of the system.

## RESULTS AND DISCUSSION

Figure 6 shows the broadband response of the smart system. The bandwidth of this system is about 3.5 kHz. For this system a resonance peak was observed at 23.8 MHz in the frequency spectrum and it did not affect the performance of the system. The reason for 3.5 kHz bandwidth of the

broadband system is because the impedance of the output stage and the actuator capacitance forms a pole at low frequency, Figure 7 shows the frequency response of the amplifier when there is no capacitive loading. In Figure 7, the top and bottom displays show the magnitude and the phase response of the feedback amplifier. The displays show no variation of magnitude and phase with frequencies up to 10 kHz. The frequency and the magnitude of the marker for the top display is shown by  $X$  and  $Y_u$  ( $X = 5.038$  kHz,  $Y_u = 60.12$  dB). The phase of the marker for the bottom display is shown by  $Y_b$  ( $Y_b = -1.63$  degrees). The frequency of the bottom display marker is same as that of top marker and is not shown here. When a  $0.18 \mu\text{F}$  capacitor is connected to the output, the frequency response of the amplifier becomes as shown in the Figure 8 indicating a pole at about 10 kHz. The reason for connecting a  $0.18 \mu\text{F}$  capacitance as that of actuator as a load to the feedback amplifier is to find the effect of actuator capacitance loading on the system. The output resistance of the current amplifier LH0002 is 6 ohms and there is a series resistance of 100 ohms for short circuit protection. The 3 dB frequency of this pole ( $R = 106$  ohms,  $C = 0.18 \mu\text{F}$ ) is given by

$$f_{3\text{dB}} = 1/(2\pi RC) = 9 \text{ kHz}$$

the phase therefore starts to drop at low frequency.

It is shown that bandwidth of about 3.5 kHz is obtained for the control of the compliance of the sensor-actuator system. This implies that this system is effective in active vibration control and partially neutralizes pressure fluctuations up to 3.5 kHz. The fact that the smart system has band-

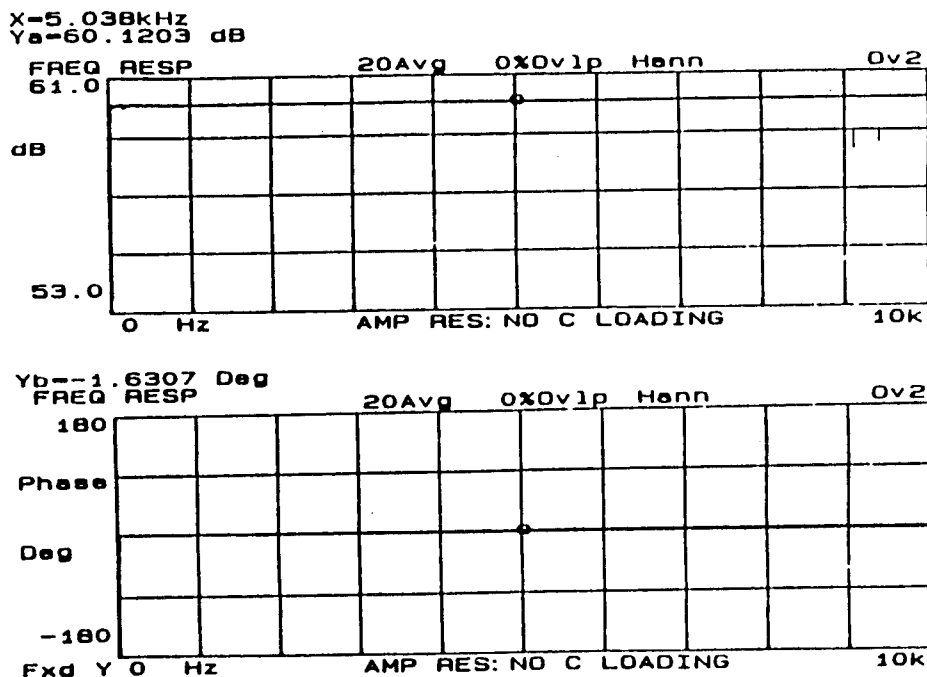


Figure 7. Frequency response of the feedback amplifier without capacitive loading.

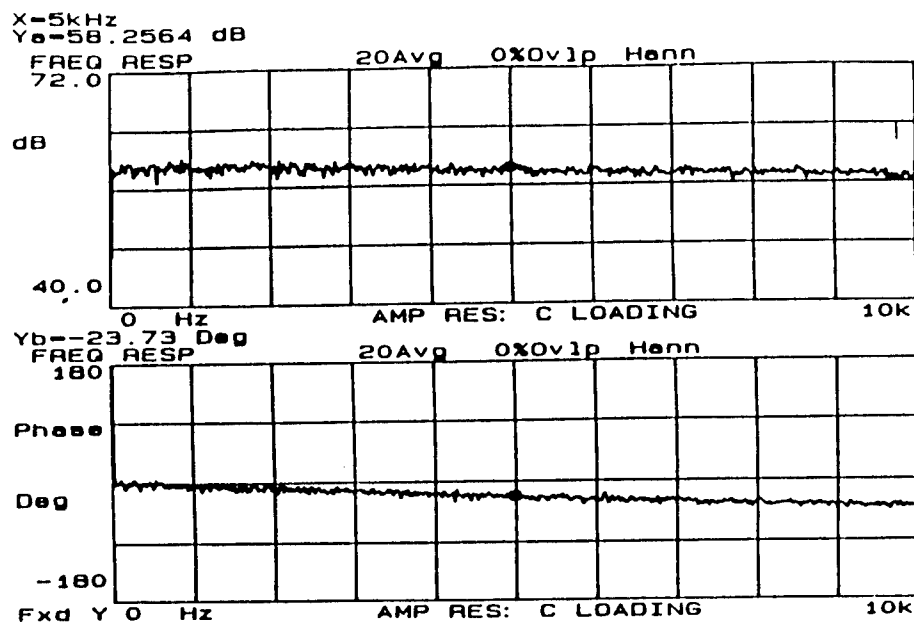


Figure 8. Frequency response of the feedback amplifier with capacitive loading.

width in kiloHertz range at low frequencies may be quite useful for underwater acoustic applications where low frequencies are often used.

It is clear that with this approach in which negative feedback with high gain is maintained over a wide frequency band is the right approach in the sense that there is no higher order filter requirement, actuator resonant frequencies are damped and the system can have large bandwidth. It should be pointed out that no higher order filter requirement is a major success for the system. Not only this makes miniaturization possible (fewer electronic components) but also allows no drop in phase over a wide frequency band. Gain of the feedback should be high so as to damp the actuator resonant frequencies. However, one cannot have very high gain in single operational amplifier because then the phase will start to drop early due to low 3 dB frequency of the op-amp. Using two or more stages in the amplifier gives problems of coupling capacitors and thermal drift of d.c. offset voltage. It is important to have a low capacitance actuator. But this may mean larger thickness of each layer of the actuator resulting in increase in size of the actuator and will lower its resonant frequency. The layout and shielding of the components is quite important to prevent oscillations due to use of uncompensated operational amplifiers.

It is important to note that compliance control does not depend on the nature of the incident pressure fluctuations. The system will be effective for both sinusoidal and pulsed

incident pressure fluctuations. In case of multiple frequency component field, the system will respond most effectively for highest amplitude frequency component.

## SUMMARY

It is shown that a collocated smart broadband system (bandwidth 3.5 kHz) can be developed using modified lead titanate as sensor material and designing the feedback circuit so that the resonance frequencies of the system are suppressed and do not affect the performance of the system. This system would be quite useful in active vibration control or acoustic absorption where small displacements are sufficient for controlling the field.

## REFERENCES

1. Kumar, S. 1991. "Smart Materials for Acoustic and Vibration Control," Ph.D. thesis, The Pennsylvania State University.
2. Damjanovic, D., T. R. Gururaja, S. J. Jang and L. E. Cross. 1986. *Materials Letters*, 4(10):414.
3. Damjanovic, D., T. R. Gururaja and L. E. Cross. 1987. *Am. Ceram. Soc. Bull.*, 66(4):699-703.
4. Turik, A. V., E. G. Fesenko, V. G. Gavrilachenko and G. I. Khasabov. 1975. *Soviet Physics*, 19(5):677-678.

# APPENDIX 8



# Smart Ferroelectrics for Acoustic and Vibration Control

S. KUMAR,\* A. S. BHALLA AND L. E. CROSS

*Materials Research Laboratory, The Pennsylvania State University, University Park, PA 16802*

**ABSTRACT:** The dynamic compliance coefficient  $S_{33}$  of hard ceramic structures can be changed by incorporating them as sensor-actuator combinations and applying electronic feedback in proper phase. These smart ceramic structures can sense and react to pressure fluctuations by changing their compliance so that energy can be removed from the stimulus. Some basic geometries of smart structures in which there is negligible field coupling between the sensor and the actuator and a basic smart structure with very high field coupling are developed and their applications in active vibration control investigated. Results for narrowband vibration control are presented which clearly show that ceramic structures can be made harder or softer depending on the phase of the feedback signal.

## INTRODUCTION

DEVELOPMENT of smart structures and systems are gaining considerable attention due to their potential applications [1-11]. Various geometries of sensor-actuator combinations are possible. In general, these configurations can be classified into two groups: 1) structures where there is negligible or zero field coupling between the sensor and the actuator and 2) structures where there is a strong field coupling. Figures 1 and 2 show some examples of the two categories. The second group of smart structures are most suitable to control or modify the field since sensing and actuating takes place at the same point. However they are more difficult to incorporate into smart systems compared to the group in which there is very little field coupling. This is due to stability aspects of the system. For narrowband systems, the stability problem is easily handled by placing a high Q bandpass filter in the system.

In this paper, we present several examples of smart structures in which there is negligible field coupling and a basic smart structure with a very strong coupling between sensor and actuator. They are incorporated in systems to show that the dynamic compliance coefficient  $S_{33}$  of the structure can be controlled by application of electronic feedback in proper phase. Immediate application of such systems is in active vibration control and acoustic absorption since such systems can remove energy from the incident field.

As shown in Figures 1 and 2, the compliance of an active or adaptive material can be changed in several ways depending on the geometry of the structure. The reason for classifying systems into two categories is primarily based on the stability considerations of the systems. If the acoustic coupling between the sensor and the actuator is below a certain level then it is relatively easy to design the system so that the

sensor-actuator combination would not oscillate. It should be pointed out that if the feedback gain is very high, the geometry of the combination will not matter and with very little field coupling, the system will oscillate irrespective of the phase. The highest feedback gain before the oscillations start depends on the field coupling which depends on the geometry of the combination.

## Structures with Negligible Field Coupling

Some examples are discussed to illustrate these systems. In an optics table, such a system is used to isolate/suppress vibration from the floor. A sensor is mounted at the side of the each leg of the table and an air pressure mount is placed underneath the leg. The sensor converts any vibration coming from the floor to voltage which is amplified and feedback in opposite phase to the air pressure controller of the mount to adjust the air pressure so that vibration amplitude is neutralized. Another example would be that of a smart skin over a submerged object surface. This skin would have actuators only. The whole object surface area could be divided into smaller areas and a sensor could be placed in front of each smaller surface areas. The sensor should be very small in size so that the incident acoustic field on the object is not affected by the sensor. The phase delay in the system because of the separation between sensor and actuator could be corrected electronically in the feedback control.

In the case of a sensor within the actuator, advantage is taken of the geometrical design. Figure 1 shows some designs in detail. Depending on the application, the sensor surface could be flush with the actuator surface or the sensor could be mounted on the bottom plate. In the case where the sensor surface is flush with the actuator surface, the sensor directly senses the vibration or the acoustic field. In the other case where sensor is put on the bottom plate, the sensor may sense the vibration transmitted through the actuator [Figure 1(c)].

Associate Editor: D. Inman.

\*Author to whom correspondence should be addressed.

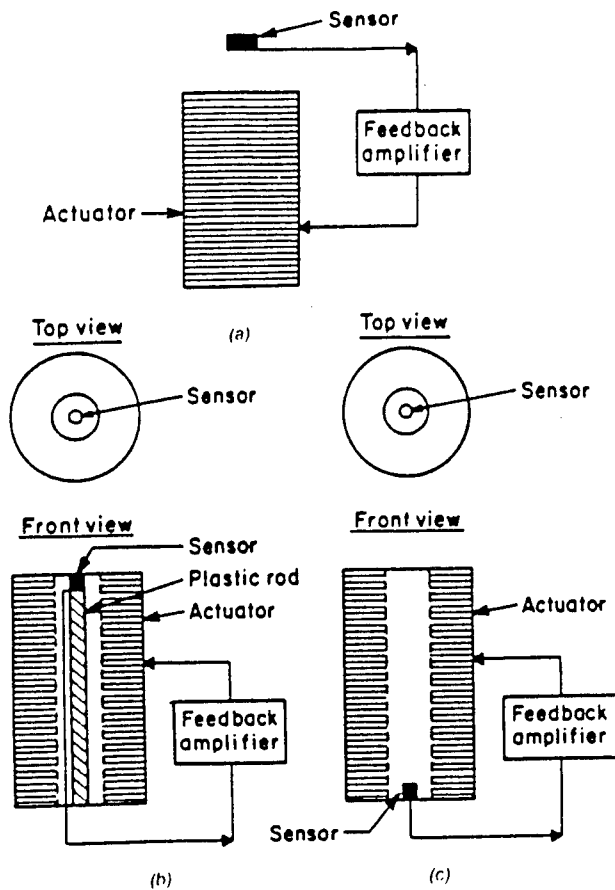


Figure 1. Mechanically decoupled systems. In each geometry, the sensor is mechanically isolated from the actuator.

In all the above examples, the sensor is mechanically decoupled from the actuator. This makes the design of such systems easier because the sensor does not respond directly to the actuator and oscillations are less likely to occur. Oscillations will occur in a feedback system if for any frequency there is positive feedback.

### Structure with Strong Field Coupling

Consider a system as shown in Figure 2. The sensor is mounted directly on top of the actuator (mechanically coupled to the actuator). In this configuration, there is very strong field coupling between the sensor and the actuator. This is also a better system because sensing and actuating take place at the same point. This system provides more effective control over the stimulus. From Figure 2, it is also easy to see the effect of feedback on the sensor-actuator combination. If the feedback electronics is such that the sensor voltage is amplified, inverted in phase and fed to the actuator, then for an incident sinusoidal pressure wave, the top sensor surface will move back and forth because of the actuator action. When the pressure is increasing at the sensor surface, the actuator contracts thereby moving the

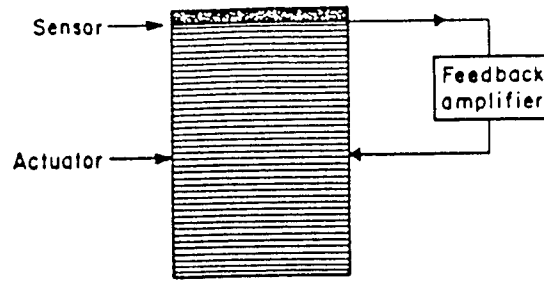


Figure 2. Mechanically coupled system. The sensor is mounted directly on the top of the actuator.

sensor away from the original position. Similarly, when pressure is reducing at the sensor surface, the actuator expands thereby moving the sensor ahead from the original position.

The effect of moving the sensor surface in this manner is to increase the time interval  $dt$  over which momentum is transferred to the sensor surface resulting in less force seen by the surface. The material in effect has become more compliant. There are two possible mechanisms which are involved in the removal of the energy from the incident pressure fluctuations. First, the energy from the pressure fluctuations can be absorbed by the material in the form of heat due to the loss factor of the material. For a perfectly elastic solid, no energy is absorbed in the deformation processes, i.e., energy stored in the solid on compaction is recovered from the solid when it recovers original dimensions. Similarly, in tension on the rarefaction cycle energy is stored which is recovered at the zero of the deformation. Second, the energy can go to the source which is driving the actuator. This can be understood in the following way: Consider the sensor-actuator combination with negative feedback as shown in Figure 3. When there is no incident pressure fluctuation, the amplifier is driving the actuator

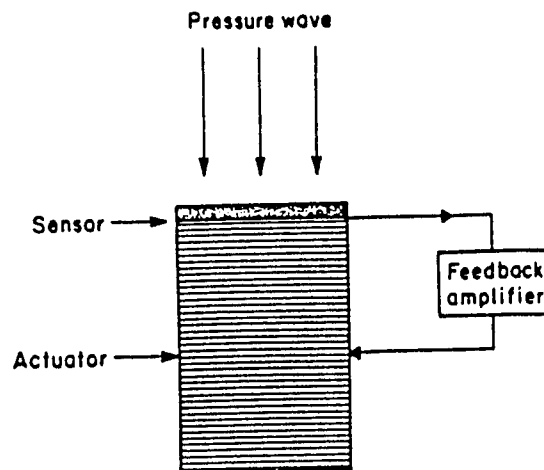


Figure 3. Energy absorption by a smart material.

and some current  $I_0$  is flowing in the feedback circuit. If there is an incident pressure fluctuation, because of the phase in the feedback system, the incident pressure fluctuation will help the amplifier drive the actuator. The current flowing in the feedback circuit will be less than  $I_0$ . This implies that energy of the incident pressure fluctuation is going to the source driving the amplifier. It is easy to see the effect of the same phase voltage feedback on the compliance of the sensor-actuator combination. The system will become less compliant and will not remove energy from the incident field.

## EXPERIMENTAL AND RESULTS

### Sensor-Actuator Geometry 1

Figure 4 shows the details of the experimental set-up. A piezoelectric actuator (PZT, EDO Western Corporation) was used as a driver to generate pressure fluctuations. This sensor-actuator geometry can be used to isolate the floor from heavy machinery and equipment producing vibrations. This system would reduce the vibration level at the bottom plate which is on the ground. The driver in this experiment could be a heavy machine.

Although the driver (actuator) was not clamped on the top side, it does provide some coupling of stress to the steel plate ( $3" \times 4" \times 0.5"$ ) underneath it. A low level source like this was acceptable in this experiment because the aim of the experiment was to check the feasibility of this sensor-actuator geometry. These pressure fluctuations pass through the actuator of the smart material and are picked up by a PZT sensor (2 mm dia., 5 mm long). The signal is amplified by a preamplifier, filtered by selective amplifier (band-pass filter,  $Q = 100$ , Model 189 Princeton Applied Research), adjusted in phase (821 phase shifter, Keithley Instruments) and then sent to actuator (1.25" dia., 1.75" long, 0.25" dia. hole along the axis). The sensor voltage is monitored after preamplification by HP3562 Dynamic Signal Analyzer. The driver frequency was 1.06 kHz and the driver

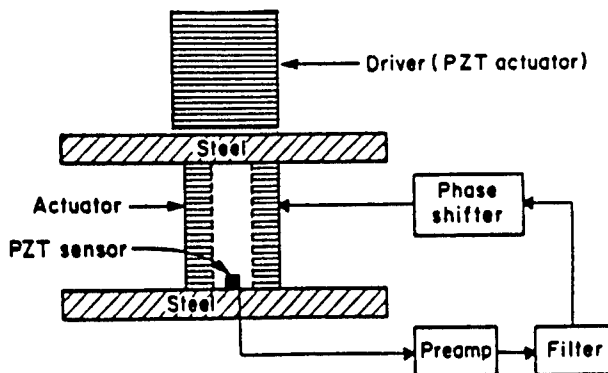


Figure 4. Experimental set-up for testing the effectiveness of the sensor-actuator geometry 1 for vibration control.

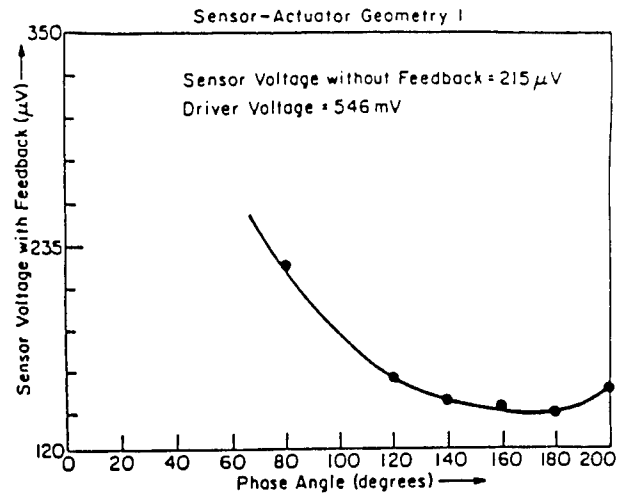


Figure 5. Variation of the sensor voltage with phase for the sensor-actuator geometry 1.

(actuator) was driven by a 546 nV signal (F47 Interstate Sweep Generator). Without feedback, the sensor voltage was measured to be 215 nV. Feedback gain was kept constant and phase was changed by a phase shifter in the circuit. Figure 5 shows the variation of sensor voltage with phase. This clearly shows that vibration amplitude can be increased or decreased depending on the value of the phase. The system is found to be unstable for the other phase angles because the feedback becomes positive.

### Sensor-Actuator Geometry 2

In this experiment, the geometry of the sensor-actuator combination is slightly different as shown in Figure 6. This sensor-actuator geometry can also be used to isolate equipment and heavy machines. In this geometry, the vibration field is reduced at the top steel plate. The pressure fluctuations do not pass through the actuator to reach the PZT sensor. As before, the pressure fluctuations are picked up by the PZT sensor. The signal is amplified by a preamplifier, filtered by selective amplifier (band-pass filter,  $Q = 100$ ),

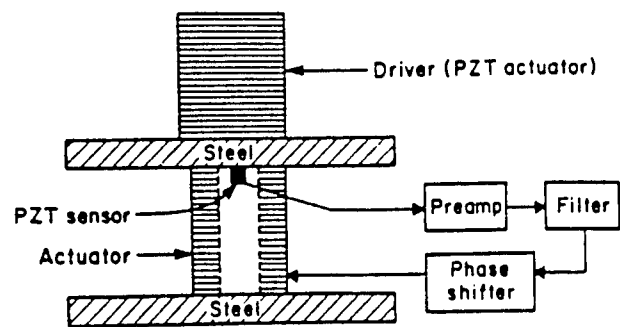


Figure 6. Experimental set-up for testing the effectiveness of the sensor-actuator geometry 2 for vibration control.

adjusted in phase by phase shifter and then sent to the actuator. The sensor voltage is again monitored after preamplification by Dynamic Signal Analyzer HP3562. Two different values of driver voltage were chosen to see the effect of larger amplitude pressure fluctuations. In the first case, driver voltage was taken to be 1.49 V and in second case 13.75 V. The driver frequency in each case was 1.015 kHz. Without feedback, the sensor voltage was 5.331 mV in the first case (driver voltage = 1.49 V) and was 37.417 mV for the second case (driver voltage = 13.75 V). Figures 7(a) and 7(b) show the variation of sensor voltage with phase at different driving voltages. In these cases also the systems are found to be unstable at other phase angles because the feedback becomes positive.

To study the feasibility of compliance control of a smart structure with strong field coupling as shown in Figure 2, a bench experiment was done. The experimental set-up is shown in Figure 8. The driver was a PZT actuator which

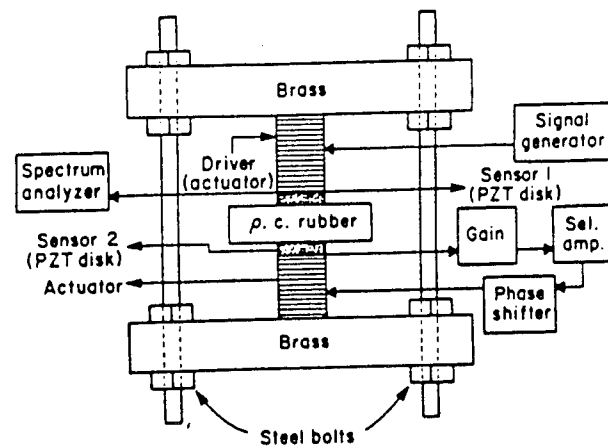


Figure 8. Experimental set-up to study the feasibility of the compliance control of a strongly coupled structure.

sends pressure fluctuations through sensor 1 and qc rubber to the sensor 2-actuator 2 combination which is the smart material. Sensor 1 and sensor 2 are PZT discs (0.5" dia., 1 mm thick). Driver and actuator 2 are PZT actuators (0.5" dia., 0.25" long, EDO Western Corporation). One side of both driver and actuator 2 are clamped to heavy brass plates (3" x 1" x 0.5"). These two brass plates are bolted together so as to adjust the static pressure on sensor 2-actuator 2. Some ground planes (thin aluminum foil) were introduced between driver and sensor 2 to avoid direct electrical pickup.

The feedback components between sensor 2 and actuator 2 consisted of a preamplifier (built by the author), selective amplifier (high Q filter, Model 189 Princeton Applied Research) and a phase shifter (821 phase shifter, Keithley Instruments). Sensor 1 was connected to another preamplifier and then to a Spectrum Analyzer. The driver was driven by a sinusoidal voltage source (F47 Interstate Sweep Generator) of low frequency. Although the driver is sending the pressure wave at single frequency to the rubber, other modes of vibration can develop in the rubber and will be picked up by sensor 2. To avoid these other modes in the feedback circuit, a selective amplifier was used.

Suppose there is no feedback between sensor 2 and actuator 2. Then a low frequency pressure wave passing through the rubber will strike sensor 2 and will be partially reflected back. Sensor 1 will develop some voltage (at that frequency) depending on the relative pressure on its sides. That voltage of sensor 1 is measured and recorded. If feedback between sensor 2 and actuator 2 is allowed in the opposite phase, then the pressure wave passing through the rubber will see a compliant surface at sensor 2. The reflection will be less in this case and sensor 1 should develop lesser voltage compared to without feedback. Sensor 1 voltage therefore is a measure of the effectiveness of the smart material. Figure 9 shows the result of the experiment. The driver frequency was changed from 10 Hz to 150 Hz and at each frequency the selective amplifier was tuned. Figure 9 therefore repre-

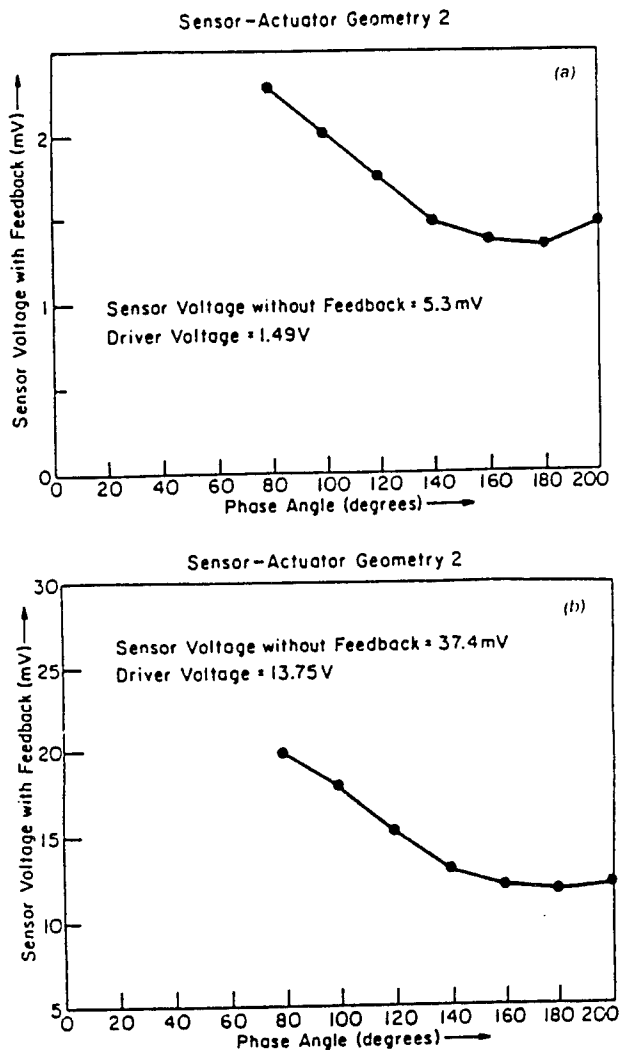
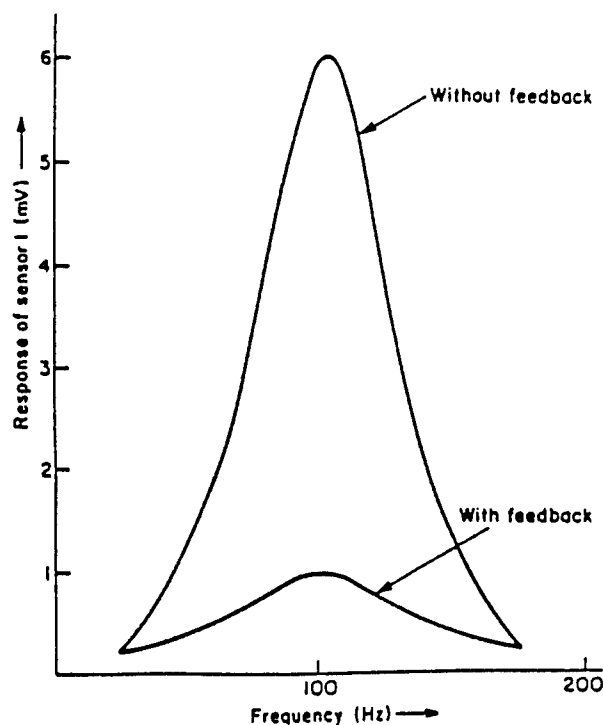


Figure 7. Variation of the sensor voltage with phase for the sensor-actuator geometry 2. (a) driver voltage = 1.49 V, (b) (driver voltage = 13.75 V).

sents a narrow band response. The reduction by factor of six in the sensor 1 voltage was observed up to 150 Hz. This result is quite significant. The softest material between the driver and the smart material is the rubber. If one is able to influence the stress in the system as this experiment shows, then the compliance of the ceramic (smart material) is of the same order as that of a rubber.

It should be noted that for low driving frequencies, the acoustic wavelengths are very large compared to the structure and therefore the structure can be considered as a lumped system. This means that at any given instant the stress is the same in all elements in the rigid frame. From the experimental point of view, it would not make a difference if sensor 1 and sensor 2 leads are interchanged.



**Figure 9.** Response of sensor 1 with and without feedback. This response indicates the relative compliance of the sensor-actuator combination with respect to the compliance of the rubber.

## SUMMARY

The control of compliance coefficient  $S_{33}$  of the various smart structures clearly show that the acoustic or vibration field can be influenced by such structures with proper electronic feedback. These systems are most suited for the applications where the frequency of the acoustic or vibration field to be controlled is known beforehand so that the systems can be tuned to that particular frequency. For fields of unknown frequency, these narrowband systems will not be useful and therefore development and design of systems with broadband response is required. The design of one broadband smart structure incorporated in a system will be presented in another paper. It should also be pointed out that in all the experiments described in this paper, the actuator displacement is small (microns) due to use of piezoelectric actuators. This may reduce the overall effectiveness of these systems in some applications where large displacement of the actuator is required for effective control of the field.

## REFERENCES

1. Newnham, R. E., Q. C. Xu, S. Kumar and L. E. Cross. 1988. *ARO Smart Materials, Structures and Mathematical Issues Workshop Proceedings*, Virginia Polytechnic and State Univ., Blacksburg, VA.
2. Newnham, R. E. and G. R. Ruschau. 1991. *J. Am. Ceramic Soc.*, 74(3):463-480.
3. Newnham, R. E., L. J. Bowen, K. A. Klicker and L. E. Cross. 1980. *Materials in Engineering*, 2:93-106.
4. Crawley, E. F. and E. H. Anderson. 1990. *J. Intell. Mater. Syst. Struct.*, 1:4-25.
5. Crawley, E. F. and J. DeLuis. 1989. *AIAA Journal*, 25(10).
6. Hagood, N. W., E. F. Crawley, J. DeLuis and E. H. Anderson. 1989. *Smart Materials, Structures, and Mathematical Issues*. Lancaster, PA: Technomic Publishing Co., Inc.
7. Hanagud, S., M. W. Obal and A. G. Calise. 1989. *Smart Materials, Structures, and Mathematical Issues*. Lancaster, PA: Technomic Publishing Co.
8. Poh, S. and A. Baz. 1990. *J. Intell. Mater. Syst. Struct.*, 1:273-288.
9. Egusa, S. and N. Iwasawa. 1993. *J. Mater. Sci.*, 28:1667-1672.
10. Case, S. W. and G. P. Carman. 1994. *J. Intell. Mater. Syst. Struct.*, 5:4-11.
11. Liang, F. P. and C. A. Rogers. 1994. *J. Intell. Mater. Syst. Struct.*, 5:12-20.

# **MATERIALS STUDIES**

# APPENDIX 9

# Structural aspects of the ferroelectric phase transition in lanthanum-substituted lead titanate

G. A. ROSSETTI Jr\*, L. E. CROSS

*Materials Research Laboratory, The Pennsylvania State University, University Park, Pennsylvania 16802, USA*

J. P. CLINE

*Ceramics Division, The National Institute of Standards and Technology, Gaithersburg, Maryland 20899, USA*

The structural characteristics and ferroelectric phase transition behaviour of chemically derived lanthanum-substituted lead titanate powders have been investigated by high-temperature X-ray diffraction and differential scanning calorimetry. Using X-ray line profile analyses and precise lattice parameter determinations, the important influence of strain coupling through lanthanum/vacancy-induced defect fields on the first-order character of the ferroelectric phase transition was demonstrated. The relaxation of the lattice to the defects as observed in the X-ray measurements was correlated with the onset of diffuse phase transition behaviour revealed by the calorimetry experiments. The lattice relaxation mechanism was connected with the appearance of mesoscopic modulations of the ferroelectric domain structure, and with anomalies in the dielectric behaviour near the transition.

## 1. Introduction

Lead titanate is generally regarded as one of the best-behaved ferroelectric perovskites. Of the seven proper ferroelectric phases allowed by the symmetry of the Pm3m prototype, it exhibits only one confirmed transition at 763 K to a tetragonal P4mm phase [1]. The transition is strongly discontinuous, with a latent heat of at least  $1.5 \text{ kJ mol}^{-1}$  [2]. Raman spectra show sharp, well-defined modes that all correctly obey the selection rules and disappear abruptly at  $T_c$  [3]. Based on inelastic neutron scattering data,  $\text{PbTiO}_3$  has been seen as a textbook example of a purely displacive ferroelectric [4], although some evidence for a component of order–disorder behaviour has more recently been reported [5]. Nevertheless, the transition behaviour appears to be well described [6–9] by the phenomenological theory of ferroelectricity [10].

At room temperature the tetragonal distortion of lead titanate is large, with lattice constants  $a = 0.3899 \text{ nm}$  and  $c = 0.4154 \text{ nm}$  [11]. This translates into a spontaneous strain, relative to the prototype at the same temperature, of nearly 5.0% [8]. The tetragonal crystal structure involves only minimal distortion of the oxygen octahedra, and has atomic displacements along the polar axis of  $dz_{\text{Ti}} = 0.017 \text{ nm}$  and  $dz_{\text{O(II)}} = dz_{\text{O(III)}} = 0.047 \text{ nm}$  relative to Pb at the origin. These displacements give rise to a spontaneous

polarization that is unusually large ( $\sim 0.75 \text{ C m}^{-2}$ ) [13, 14].

The break in translational periodicity caused by the introduction of lattice defects leads to rather dramatic changes in the structural properties and ferroelectric phase transition behaviour of lead titanate [15, 16]. An understanding of the role of these defects is important, since doping with aliovalent impurities is commonly used to control the electrical, optical and elastodielectric properties of lead titanate and its technologically important solid solution with lead zirconate.

In this connection, compositions in the system  $\text{PbO-TiO}_2\text{-La}_2\text{O}_3$  (Fig. 1) are of particular interest. The tetragonal distortion ( $(c/a) - 1$ ) of lead titanate is strongly affected by the substitution of lanthanum, and the lattice constants suffer deviations from Vegard's law over a compositional interval extending from approximately 2.5 to 10 at% [18]. This deviation reduces the initial slope of the tetragonal distortion–composition curve by a factor of about four. The behaviour of the cell constants is reminiscent of that observed for lead titanate single crystals subjected to hydrostatic compressive stress [19], where it is found that at room temperature, the transition passes in proximity to a Curie critical point at a critical stress of 1.75 GPa [20]. Indeed, the characteristic first-order discontinuity of the reciprocal permittivity at the

\* Present address: Department of Geological and Geophysical and Princeton Materials Institute, Princeton University, Princeton, New Jersey 08544, USA.



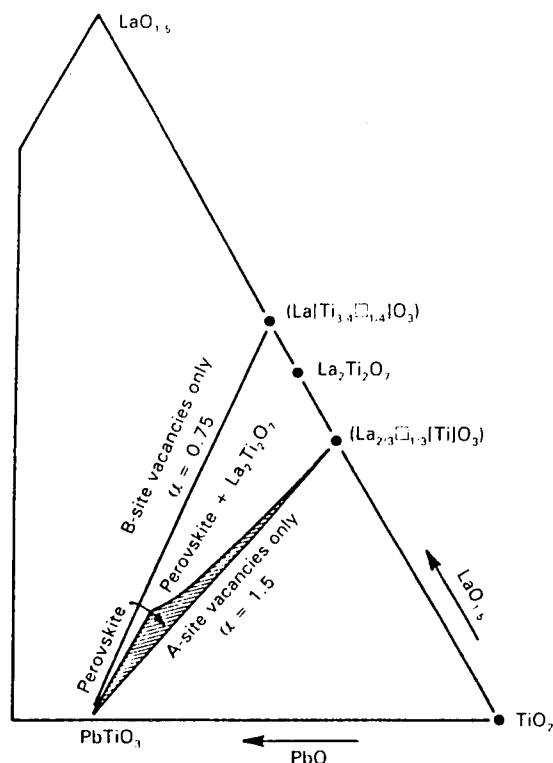


Figure 1 Partial isothermal section at 1603 K for the  $\text{PbO-La}_2\text{O}_3\text{-TiO}_2$  system referring to compositions of general formula  $\text{Pb}_{1-2x}\text{La}_x[\text{Ti}] \text{O}_3$  (after Hennings [17]).

transition is greatly diminished by the introduction of as little as 0.2 at% lanthanum [21].

In addition to reducing the first-order character of the transition, the substitution of lanthanum induces anomalous or "diffuse" phase transition behaviour characterized by a pronounced smearing of the dielectric susceptibility-temperature curve. Studies of the dielectric properties of ceramic specimens with different grain sizes and lead stoichiometries have demonstrated that a change from conventional to diffuse ferroelectric phase transition behaviour occurs at lanthanum concentrations above about 5 at% [22]. For lanthanum concentrations higher than about 10 at%, the values of the permittivity near the transition are some 100% larger than would be predicted by the generalized Lydanne-Sachs-Teller relationship [23], suggesting that the relaxation of the structural disorder introduced by the lanthanum in some way provides additional contributions to the dielectric response above what is expected from the soft mode theory [24]. This structural disorder appears in the Raman spectra as an additional mode that does not obey the selection rules [25].

The present investigation was undertaken in order to gain a better understanding of the structural factors influencing the breakdown of conventional ferroelectric phase transition behaviour as observed in lanthanum-substituted lead titanate. A series of well-crystallized powder specimens were prepared according to the A-site vacancy formula [17] ( $\text{Pb}_{1-1.5y}\text{La}_y[\text{Ti}] \text{O}_3$ ) using a chemical method based on a modifica-

tion [26] of the solution-gelation (sol-gel) technique developed for lead titanate [27]. The phase transition behaviour of these materials was examined directly by differential scanning calorimetry and by high-temperature X-ray diffraction. The diffractometer employed was specially configured to yield high-quality data on line profile shape. This allowed the temperature evolution of both the macroscopic and microscopic lattice strain to be studied. These data were preferred over data such as might be obtained from ceramic specimens, because they are not likely to be strongly compromised by the effects of elastic boundary conditions, which can be uncertain in densely sintered polycrystalline bodies, and which can influence the phase transition behaviour and ferroelectric properties.

## 2. Experimental procedure

### 2.1. Sol-gel powder synthesis

Powders for calorimetric and X-ray studies were prepared from lead acetate trihydrate, lanthanum isopropoxide and titanium isopropoxide dissolved in 2-methoxyethanol according to a modification of a previously developed procedure [26, 27]. All manipulations of the starting chemicals and reaction mixtures were carried out under anhydrous conditions in a Braun glove box fitted with a recirculating dry nitrogen purge and liquid nitrogen cooled vapour trapping system. The box atmosphere was sufficiently dry ( $\leq 5$  p.p.m.  $\text{H}_2\text{O}$ ) that no fuming was visually detectable on exposure to diethyl zinc.

In each case, the preparation was based on 16.8 mmol of titanium isopropoxide, which was measured out volumetrically using a microlitre pipet. The corresponding amounts of lead acetate trihydrate and lanthanum isopropoxide required to make samples with  $y = 0, 0.005, 0.01, 0.02, 0.035, 0.05$  and  $0.15$  according to the formula  $\text{Pb}_{1-1.5y}\text{La}_y[\text{Ti}] \text{O}_3$  were weighed out on an electronic balance precise to 1 mg. The required distillation and refluxing operations of the starting solutions were conducted under dry argon purge in a standard glass distillation apparatus utilizing ground-glass joints. The refluxing was continued until the temperature of the vapours condensing in the still head reached that of the boiling point of the pure solvent.

The water for hydrolysis (4 mol per mol alkoxide) was introduced to the reaction mixture at  $< 250$  K as a solution in 2-methoxyethanol. Transparent amber-coloured gels were obtained on warming this mixture to room temperature. After volatilizing the entrapped solvent, the gel products were gently powdered in a mortar and were calcined on platinum foil within a closed, virgin, alumina crucible. The maximum calcining temperature was 1323 K (1 h) with intermediate holds on heating at 623 K (1 h) and 1073 K (3 h). The resultant light yellow powders were examined by transmission electron microscopy and showed no evidence of second phases, amorphous material, or incomplete or inhomogeneous reaction. The nominal compositions of the powders were checked by comparing the tetragonal distortion determined by X-ray diffraction against the previously reported values [18].

## 2.2. X-ray measurements

X-ray powder diffraction data were collected on a Siemens D500 diffractometer equipped with an incident-beam monochromator and scanning linear position-sensitive detector (PSD). The monochromator consisted of a focusing crystal of germanium that virtually eliminated the peaks associated with the  $K_{\alpha 2}$  component of the Cu radiation. The near elimination of the bremsstrahlung resulted in reduced intensity in the tail region of the diffraction peaks and increased the peak to background ratio. The use of the PSD resulted in dramatic increases in the diffraction signal. Although this gave rise to some small increase in the peak width, as an overall indication of the resolution of the system, the typical full width at half maximum for the Bragg peaks of a lanthanum hexaboride reference standard (Standard Reference Material No. 660) was approximately  $0.06^\circ$  in  $2\theta$ . Ambient temperature data were collected using zero-background quartz plates on to which the specimens were uniformly deposited from an isopropanol suspension. The scan ranges were from  $18$  to  $98^\circ 2\theta$  with a step increment of  $0.01^\circ$  and a scan rate for the PSD of  $0.6^\circ \text{ min}^{-1}$ . With a PSD window of  $4.67^\circ$ , this translated into a count time of  $7.78 \text{ min}$  per step.

High-temperature data were collected on the same diffractometer fitted with a Bühler hot stage utilizing two platinum heaters. The first of these was a strip heater on which the specimen resided during analysis. A second heater surrounded the first and was positioned to reduce temperature gradients. The temperature was measured with a type S thermocouple welded to the underside of the heating strip. The scan range and step increment were the same as those used in the collection of the room-temperature data, but the scan rate was increased to  $1.25^\circ \text{ min}^{-1}$  (count time =  $3.86 \text{ min}$  per step). The data were collected in  $5 \text{ K}$  increments straddling the anticipated cubic  $\rightarrow$  tetragonal transition temperature by  $20 \text{ K}$ , and in  $10 \text{ K}$  increments straddling this temperature by  $40 \text{ K}$ . All data were collected on cooling, with additional data collected at  $100 \text{ K}$  increments as the specimen cooled to the final temperature of  $373 \text{ K}$ . The data were collected in an air atmosphere.

All data analysis was performed using the Siemens DIFFRAC 5000 software. Lattice parameters were determined by the least-squares refinement method using 15–20 of the tetragonal reflections and all of the cubic reflections appearing in the scan range. The peak positions were determined using a variable tip-width peak-locating algorithm based on a second-derivative test. The results of the algorithm were visually inspected by expanding each peak region on a monitor, and manual corrections to the peak positions were made when necessary.

The peak positions so determined were corrected by applying a calibration curve generated by fitting a second-order polynomial to the known peak positions for the lanthanum hexaboride (SRM 660) external reference standard. Using this procedure, the absolute angular precisions of the least-squares fits for pure lead titanate at room temperature seldom exceeded  $0.005^\circ 2\theta$ . For reasons that will become evident, the

precision of the fits for the lanthanum-modified specimens varied somewhat, but were almost always better than  $0.025^\circ 2\theta$ . A comparable precision was achieved in the fits of high-temperature data. Because of the smaller tetragonal distortion and more pronounced broadening of the diffraction profiles observed for the specimen with  $y = 0.05$ , this procedure proved impractical in analysing the high-temperature data. Instead, the peak positions of the 213/312/321 reflections for this specimen were determined by deconvolution and these were then used to calculate the lattice parameters. More scatter in the data for this sample was therefore observed.

Line profile analyses were conducted by fitting the diffraction profiles to split Pearson distributions. Pearson type VII distributions are of the form [28]

$$y(x) = y_0 \left( 1 + \frac{(x - \bar{x})^2}{ma^2} \right)^{-m} \quad (1)$$

with  $y_0 = y(\bar{x})$ . The full width  $\beta$  at the  $(1/p)$ th maximum is

$$\beta \left( \frac{y_0}{p} \right) = 2a[m(p^{1/m} - 1)]^{1/2} \quad (2)$$

The function varies from Lorentzian when  $m = 1$  to Gaussian in the limit  $m = \infty$ . The split distributions allowed the profile shape on the low and high angle sides of  $\bar{x}$  to be fitted with separate exponents,  $m^L$  and  $m^H$ . These distributions gave two values for the corresponding equivalent full width at half maximum (FWHM),  $\beta^L$  and  $\beta^H$ , and so permitted the investigation and quantification of the profile symmetry.

## 2.3. Calorimetry

Differential scanning calorimetry (DSC) was performed using two calorimeters. Estimates of the phase transition temperatures were made using a Perkin Elmer DSC-2C calorimeter calibrated to a zinc foil reference standard. The samples (40 to 60 mg in size) were weighed out on an electronic microbalance that was precise to  $0.01 \text{ mg}$  and were sealed in aluminium capsules. The measurements were made in heating runs performed under a dry nitrogen purge using a scan rate of  $2.5 \text{ K min}^{-1}$ . Transition temperatures were estimated directly from the calorimeter power versus temperature curves using the Perkin Elmer software. Prior to the experiments, the operational controls of the instrument were carefully adjusted to achieve a degree of baseline flatness sufficient for these estimations to be readily made without applying baseline slope or curvature corrections. Although enthalpies of transition could also be estimated from these data, the signal from the higher lanthanum content materials was weak, and not suitable for analysis.

Consequently, the enthalpies of transition of selected samples were measured using a Setaram TG-DSC 111 calorimeter operated in the horizontal configuration. The Setaram DSC is a microcalorimeter of the twin Calvet design. The temperature of the instrument was calibrated to the melting points of high-purity ( $99.999 + \%$ ) In, Pb, Zn and Al. Power calibration was performed electrically using a Joule effect

device. Again, the samples were weighed out on an electronic balance that was precise to 0.01 mg and were sealed in aluminium crucibles. The measurements were made in heating runs in a static air atmosphere at scan rates of  $1.5 \text{ K min}^{-1}$ .

For the purposes of comparing the transition behaviour of the various specimens, enthalpies of transition were estimated directly from the power versus temperature curves using a thermal analysis software package (Astra Scientific International). The procedure adopted for carrying out the integration of these curves was tested by measuring the enthalpy of the  $\alpha \rightarrow \beta$  transition for a high-purity synthetic quartz sample. The transition enthalpy so obtained was  $0.610 \text{ kJ mol}^{-1}$  and was reproducible to within  $\sim 0.03 \text{ kJ mol}^{-1}$ . This result was in good agreement with the recent literature value of  $0.625 \text{ kJ mol}^{-1}$  [29]. However, it must be emphasized that, although useful for comparative purposes, the transition enthalpies obtained in this way should be regarded as estimates. A more detailed analysis of precise heat capacity data would be required to accurately determine these values.

### 3. Results and analysis

#### 3.1. Structural studies

An X-ray powder diffraction pattern collected on the sol-gel derived lead titanate at room temperature is shown in Fig. 2. The high degree of crystallinity evident in the pattern is representative of that observed for all of the specimens examined. The peak intensity on the 100% peak varied from 1500 to 3000 c.p.s. depending on the lanthanum concentration, while the background signal seldom exceeded 20 c.p.s. Consequently, no background subtraction, smoothing or other data corrections were required. Careful inspection and fitting of the background around a variety of  $hkl$  reflections across the entire scan range revealed no reflections associated with secondary phases, and no anomalous background scattering could be detected.

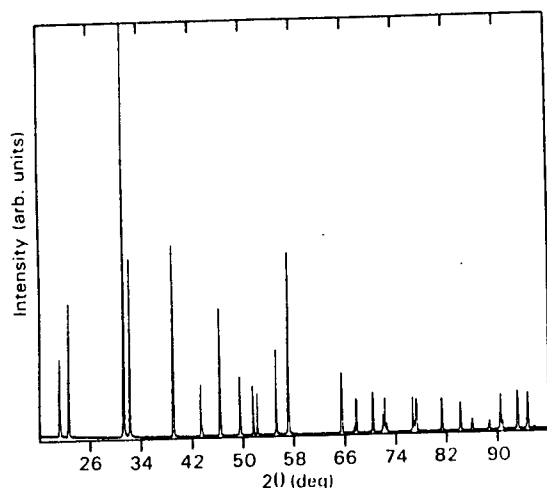


Figure 2 X-ray powder diffraction pattern for lead titanate at room temperature ( $\text{CuK}_{\alpha}$  radiation).

In order to gain some insight into the effect of lanthanum substitution on the intrinsic shapes and breadths ( $\beta$ ) of the diffraction profiles, a split Pearson analysis of the 300 reflection was conducted at a temperature above the expected Curie point at  $T \sim T_c + 35 \text{ K}$ . The results of the analysis are shown in Table I. The shapes of the diffraction profiles for all specimens were found to be nearly symmetric and were predominantly Lorentzian in shape. For the samples with lanthanum concentrations  $y < 0.020$ , no significant broadening of the diffraction profiles relative to the profile for unmodified lead titanate was observed, and the full width at half maximum was approximately 1.5–2 times that of the expected resolution of the instrument. For  $y > 0.020$ , some additional broadening of the diffraction profiles became apparent.

The room-temperature FWHM values for selected reflections of samples with different lanthanum concentrations are collected in Table II. Several important trends in these values were observed. First, for all reflections and compositions investigated, a significant increase in line breadth over that observed for unmodified lead titanate was evident. For each reflection, the composition dependence of the FWHM value was qualitatively similar, with the magnitude of the broadening increasing between  $y = 0$  and  $y = 0.05$  but then decreasing when the lanthanum concentration was further increased to  $y = 0.15$ . The broadening of the diffraction profiles was most pronounced in the peaks that had high  $l$ -component indices, such as the 002, 012 or 222 reflections. For all of the lanthanum-substituted materials, the ratio  $\beta_{00l}/\beta_{h00} \sim 2.0$  was significantly greater than the corresponding value ( $\sim 1.2$ ) observed for lead titanate. Although this result implies that the incorporation of lanthanum induces a structural distortion associated primarily with a variance in the  $c$  lattice parameter, the significant broadening of the  $h00$  reflections suggests that some variance in the  $a$  lattice parameter also occurred.

Marked changes in the shape of the diffraction profiles relative to unmodified lead titanate were also observed. Table III shows that the diffraction profiles for the lanthanum-modified materials exhibited a significantly greater degree of asymmetry than those for the pure compound. As with the FWHM value, the degree of the asymmetry was most obvious in the peaks having high  $l$ -component indices. This can be visually ascertained from Fig. 3, where the shapes of the 002 and 200 profiles for lead titanate and a lanthanum-modified sample are compared. In this figure the crosses represent the raw data points, and the solid lines represent the best approximation of the profile shape obtained by the split Pearson fitting. The fitted curves are plotted less background in order that the shapes of the profiles may be more easily appreciated. The horizontal line in the centre of each figure represents the difference curve between the measured data points and the fitted values. The quality of the fits as determined by the reliability index

$$R = \left( \frac{\sum [I(\text{obs}) - I(\text{calc})]^2}{\sum [I(\text{obs})]^2} \right)^{1/2} \quad (3)$$

TABLE I Split Pearson analysis of the 300 reflection of  $\text{Pb}_{1-1.5y}\text{La}_y[\text{Ti}]\text{O}_3$  at  $T \approx T_c + 35 \text{ K}$ 

La content, $y$	$\beta^L$ (deg 2 $\theta$ )	$\beta^H$ (deg 2 $\theta$ )	$\beta$ (deg 2 $\theta$ )	$m^L$	$m^H$
0	0.081(2)	0.096(2)	0.089(2)	0.75(3)	0.90(4)
0.005	0.112(2)	0.103(2)	0.108(2)	1.7(1)	1.3(0.9)
0.010	0.098(2)	0.091(2)	0.095(2)	1.1(0.6)	1.0(0.5)
0.020	0.132(4)	0.121(4)	0.127(4)	1.1(0.7)	1.1(0.9)
0.035	0.155(5)	0.133(5)	0.144(5)	0.90(6)	0.89(7)
0.050	0.208(9)	0.208(9)	0.208(9)	0.73(6)	0.92(9)

The numbers in parentheses represent the standard deviation in the least significant digit.

TABLE II FWHM for various reflections of  $\text{Pb}_{1-1.5y}\text{La}_y[\text{Ti}]\text{O}_3$  at room temperature

Reflection $hkl$	FWHM(deg. 2 $\theta$ )						
	$y = 0$	$y = 0.005$	$y = 0.010$	$y = 0.020$	$y = 0.035$	$y = 0.050$	$y = 0.150$
001	0.116(2)	0.178(2)	0.278(6)	0.280(6)	0.272(6)	0.299(7)	0.219(8)
100	0.099(0.9)	0.131(0.9)	0.164(1)	0.163(1)	0.162(1)	0.174(2)	0.150(2)
101	0.092(0.3)	0.130(0.5)	0.190(1)	0.202(1)	0.195(1)	0.214(1)	0.163(0.8)
110	0.091(0.9)	0.129(1)	0.174(3)	0.179(2)	0.178(2)	0.196(3)	0.175(2)
111	0.085(0.4)	0.116(1)	0.163(1)	0.183(1)	0.173(1)	0.191(1)	0.150(1)
002	0.105(1)	0.252(7)	0.486(13)	0.492(17)	0.478(14)	0.494(17)	0.342(12)
200	0.086(0.4)	0.134(1)	0.205(2)	0.213(2)	0.209(2)	0.229(2)	0.168(2)
012	0.099(1)	0.226(4)	0.425(10)	0.465(11)	0.415(11)	0.455(13)	0.341(18)
201	0.084(1)	0.134(3)	0.200(6)	0.223(6)	0.224(7)	0.254(11)	0.196(13)
210	0.085(1)	0.143(3)	0.217(7)	0.227(7)	0.235(8)	0.267(14)	0.192(15)
222	0.103(2)	0.192(4)	0.324(10)	0.378(12)	0.368(13)	0.406(12)	0.320(10)

The numbers in parentheses represent the standard deviation in the least significant digit.

TABLE III Split Pearson analysis for various reflections of  $\text{Pb}_{1-1.5y}\text{La}_y[\text{Ti}]\text{O}_3$  at room temperature

Reflection $hkl$	$y = 0$		$y = 0.01$	
	$\beta^L$	$\beta^H$	$\beta^L$	$\beta^H$
001	0.145	0.087	0.209	0.347
100	0.120	0.078	0.197	0.129
101	0.109	0.075	0.154	0.225
110	0.107	0.074	0.214	0.132
111	0.094	0.076	0.155	0.171
002	0.107	0.102	0.223	0.748
200	0.099	0.071	0.261	0.149
012	0.099	0.100	0.237	0.612
201	0.084	0.085	0.202	0.196
210	0.094	0.076	0.285	0.149
222	0.093	0.113	0.267	0.379

The standard deviations in the least significant digit are similar to those reported in Table II.

depended to some extent on the lanthanum concentration, but the  $R$  value typically increased from as low as  $R \approx 0.015$  for the 001 reflection to  $R \approx 0.065$  for the 222 peak.

As an overall indication of the profile asymmetry, the composition dependencies of the ratio  $\beta^H/\beta^L$  for the 002 and 200 reflections are compared in Fig. 4. As seen in the figure, the behaviour of  $\beta^H/\beta^L$  for the 002 reflection is the mirror image of that for the 200 peak, with both ratios having sharp extrema centred near the composition  $y = 0.01$ . The strong coupled asymmetry for these reflections combined with the increase

in overall peak breadth suggests that a distortion associated with a non-uniform variance in the crystal tetragonality ( $c/a$ ) existed in all of the lanthanum-modified compositions investigated. The degree of the non-uniformity decreased sharply between  $y = 0.01$  and  $y = 0.05$  but did not change significantly on further increasing the lanthanum content to  $y = 0.15$ .

Lattice parameters for the samples investigated are listed in Table IV. As expected from previously reported data, the lattice distortion along the tetragonal  $c$  axis was much more strongly affected by the incorporation of lanthanum than was the distortion along the  $a$  axis. The crystal tetragonality  $c/a = 1.0649$  determined for unmodified lead titanate powder compares favourably with the single-crystal value 1.0653 determined using the Debye-Scherrer camera method [11]. It is interesting to note that the standard errors of the refinements appeared to pass through a maximum centred near the composition  $y = 0.02$ . This was most likely a result of the marked peak asymmetry near this composition, which made the assignment of the peak positions somewhat more uncertain. Nevertheless, the standard errors for all specimens were of similar magnitude and were quite small ( $10^{-5} \text{ nm}$ ).

The values of  $a$  and  $c$  listed in Table IV are plotted in Fig. 5. As previously observed for mixed oxide specimens [18], pronounced deviations from Vegard's law are apparent for both the  $a$  and  $c$  lattice parameters. Based on the changes in diffraction profile symmetry (Fig. 4), and on the fact that all of the specimens were prepared according to the A-site va-

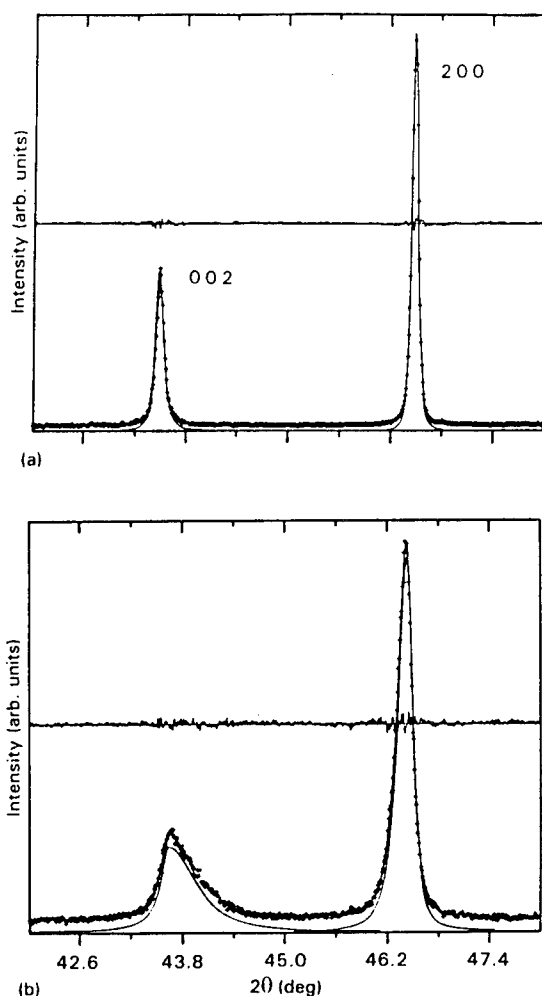


Figure 3 Split Pearson fitting of the 002/200 reflections of  $\text{Pb}_{1-1.5y}\text{La}_y[\text{Ti}]\text{O}_3$  for (a)  $y = 0$  and (b)  $y = 0.01$ . (Cu  $K\alpha_1$  radiation).

cancy formula, it is proposed that this deviation results from a lattice relaxation mechanism as opposed to a change in the vacancy site distribution as suggested earlier [18].

To better understand the nature of this relaxation mechanism, the temperature dependence of both spontaneous and lattice strains was examined. The spontaneous strain is related to the tetragonal distortion  $((c/a) - 1)$  and so may be determined from the lattice constants. The results for specimens with  $y = 0.0-0.05$  are shown in Fig. 6. The relative degree of lattice strain as a function of composition and temperature was qualitatively assessed from a measurement of the FWHM of the 222 reflection. The 222 reflection is not split by the tetragonal symmetry, and so the temperature dependence of the FWHM can be conveniently compared both above and below the transition temperature. Based on the data in Table II, this reflection also showed a marked broadening related to the lanthanum concentration.

Representative results for a specimen of composition  $y = 0.01$  are shown in Fig. 7a. On cooling through the transition a large change in lattice strain occurred,

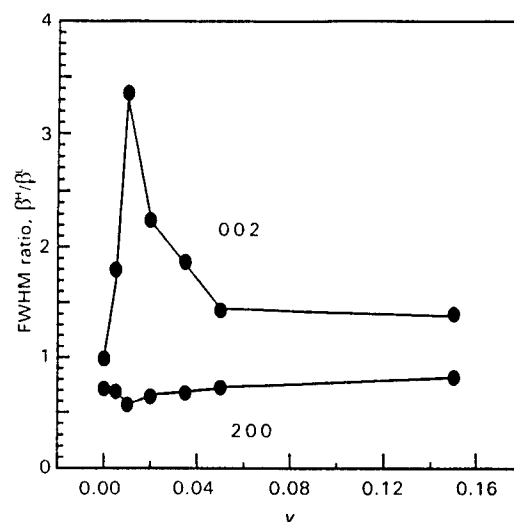


Figure 4 Peak asymmetry of the 002/200 reflections of  $\text{Pb}_{1-1.5y}\text{La}_y[\text{Ti}]\text{O}_3$ .

TABLE IV Lattice parameters of  $\text{Pb}_{1-1.5y}\text{La}_y[\text{Ti}]\text{O}_3$  at room temperature

La content, $y$	$a$ (nm)	$c$ (nm)	$c/a$
0	0.38997(0.5)	0.41529(1)	1.0649
0.005	0.39014(0.8)	0.41444(2)	1.0623
0.010	0.39032(2)	0.41367(5)	1.0598
0.020	0.39055(3)	0.41156(6)	1.0538
0.035	0.39082(2)	0.40961(4)	1.0481
0.050	0.39098(2)	0.40734(4)	1.0418
0.150	0.39166(2)	0.39867(3)	1.0179

The numbers in parentheses represent the standard errors obtained from least-squares refinement.

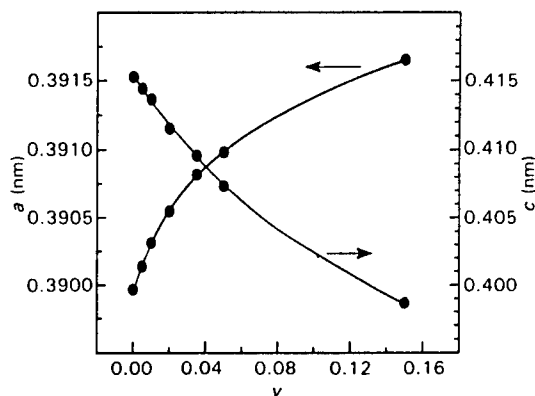


Figure 5 Lattice parameters of  $\text{Pb}_{1-1.5y}\text{La}_y[\text{Ti}]\text{O}_3$  at room temperature.

as indicated by the abrupt discontinuity in the FWHM value near  $T_c$ . Despite this, as shown in Fig. 7b, no unusual or anomalous behaviour could be detected in the temperature dependence of the lattice constants near the transition. It should be recalled, however, that in the vicinity of a first-order transition,

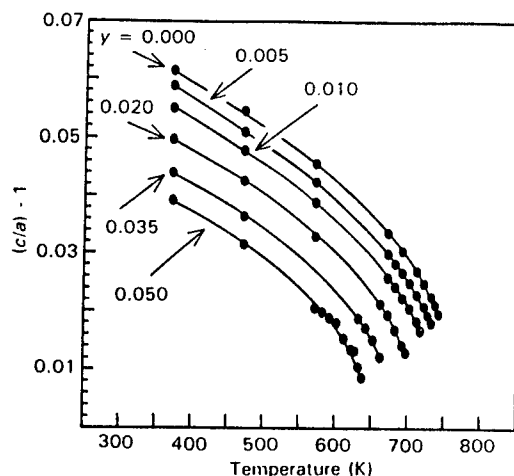


Figure 6 Temperature dependence of the tetragonal distortion  $(c/a) - 1$  for  $\text{Pb}_{1-1.5}\text{La}_y [\text{Ti}]\text{O}_3$ .

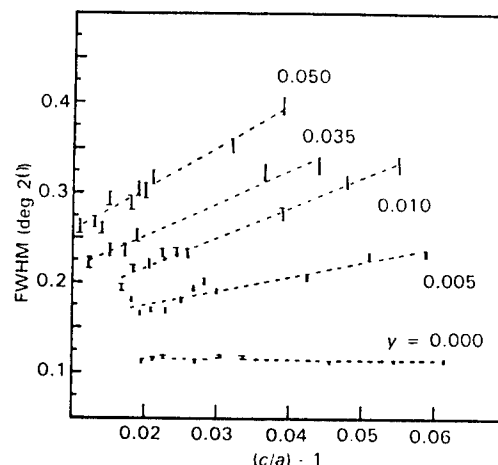


Figure 8 Influence of tetragonal distortion  $(c/a) - 1$  on the FWHM of the 222 reflection for  $\text{Pb}_{1-1.5}\text{La}_y [\text{Ti}]\text{O}_3$ .

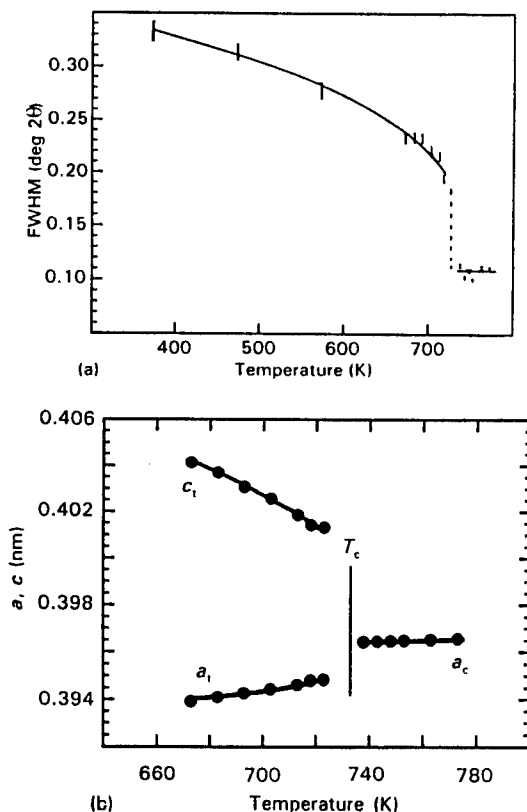


Figure 7 Temperature dependence of the FWHM of the 222 reflection of  $\text{Pb}_{1-1.5}\text{La}_y [\text{Ti}]\text{O}_3$  ( $y = 0.01$ ) (a). The associated variation in the lattice parameters (b).

some discontinuity in peak breadth is expected due to the overlap of tetragonal and cubic reflections occurring in the coexistence region of the two phases. The data for such profiles are not shown in the figure and were readily identified because considerably poorer fitting, as indicated by a sharp increase in the reliability index, was observed when peaks from both phases were present.

The temperature dependence of the line breadth data in Fig. 7 suggested that the increased FWHM values relative to the pure specimen as observed at room temperature were directly related to the degree of tetragonal distortion. As shown in Fig. 8, the tetragonal distortion  $(c/a) - 1$  when plotted against the FWHM for the 222 reflection did in fact yield a family of approximately straight lines with slopes and intercepts dependent on the lanthanum concentration. The large change in slope occurring between  $y = 0.0$  and  $y = 0.01$  is indicative of the strong initial relaxation of the lattice due to the effects of the dopant. The observed  $c/a$  dependence of the peak breadth combined with the marked profile asymmetry in the 002/200 reflections suggests that the primary contribution to the broadening as observed in the diffraction data at room temperature results from the relaxation of the uniform tetragonal distortion due to the incorporation of the lanthanum.

In fact, recent *in situ* transmission electron microscopy studies [30] of lanthanum-substituted lead titanate ceramics have revealed the presence of sub-domain modulations oriented primarily along the tetragonal  $c$  axis, which is mechanically the softest [19]. The modulated textures occurred on a scale of  $\sim 10$  nm within well-defined ferroelectric domains, in which there must exist an average, but spatially varying, polarization  $\vec{P}$ . Such microstructures are not unique to ferroelectrics, and are commonly observed in ferroelastic minerals and materials formed via kinetic processes, that is, under conditions where cation-ordering reactions have occurred incompletely or inhomogeneously or in crystals that are otherwise not at equilibrium [31]. As seen in Fig. 9, these modulations first became obvious at a lanthanum concentration of  $y \approx 0.05$  and developed into a cross-hatched or "tweed" texture on reaching  $y \approx 0.25$ . These textures were found to disappear on heating above the transition temperature, and so could not be associated with exsolution lamellae. As can be appreciated from the data in Table II and Fig. 4, the appearance and extent of the sub-domain texture correlates well with the

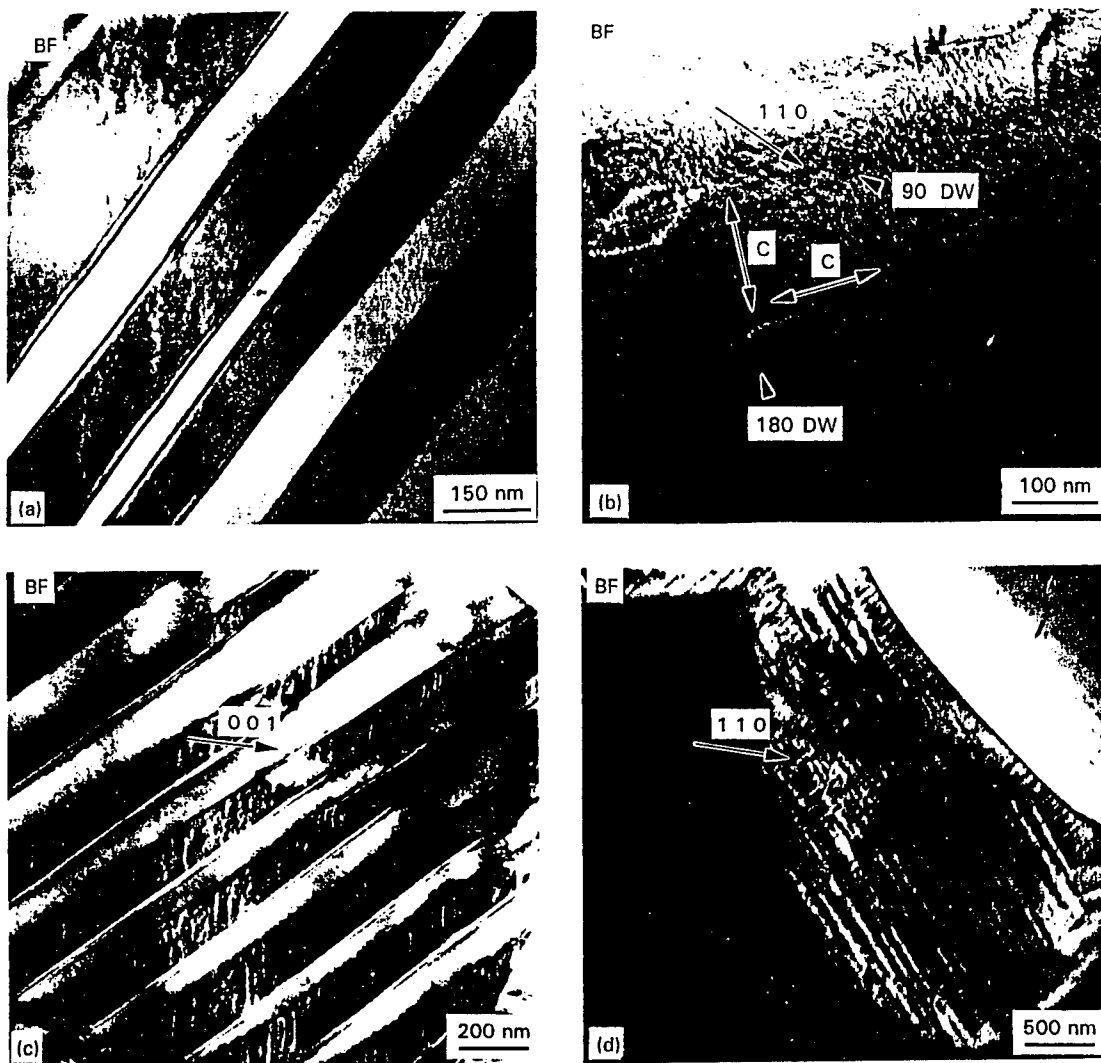


Figure 9 Transmission electron micrographs showing the modulated ferroelectric domain structure as observed for  $\text{Pb}_{1-x}\text{La}_x\text{TiO}_3$ : (a)  $x = 0.01$ , (b)  $x = 0.05$ , (c)  $x = 0.10$ , (d)  $x = 0.25$  (after Randall *et al.* [30]).

changes in profile breadth and symmetry found in the diffraction experiments.

It should be noted that the data presented here are consistent neither with particle size effects nor with the existence of macroscopic inhomogeneities in the chemical composition. Observations arguing against the influence of these two effects are (i) the temperature dependence of the profile broadening below the Curie point; (ii) the inherent homogeneity achievable with the sol-gel process; (iii) the pronounced asymmetry of the diffraction profiles for all of the  $hkl$  reflections investigated (composition fluctuations should give a random distribution in  $c/a$ ); and (iv) that the profile breadth decreased when the dopant level was increased above  $\sim 5$  at%.

### 3.2. Phase transition behaviour

In investigating the influence of these structural changes on the phase transition behaviour, it proved informative to analyse the scalar strain data (Fig. 6) as

though all of the specimens were close to a Curie critical transition. At a Curie critical instability, the order of the transition changes, and the temperature dependence of the order parameter (i.e. the spontaneous polarization) is given by

$$P(T) \propto [(c/a) - 1]^{1/2} \propto (T_c - T)^{1/4} \quad (4)$$

Consequently, plots of  $[(c/a) - 1]^2$  versus  $T$  should give a good indication of any changes in the nature of the phase transition as the lanthanum content is increased. The results of this analysis are shown in Fig. 10a, where it is seen that Equation 4 holds approximately for all of the specimens investigated. However, as shown in Fig 10b, the absolute values of the slopes of the lines so obtained decreased with increasing dopant concentration, with the rate of decrease in slope with composition changing to a smaller value for samples with  $x \geq 0.02$ . This decrease in slope reflects the more continuous nature of the transition.

Additional insight into the meaning of this observation was gained from the calorimetry data. Normalized

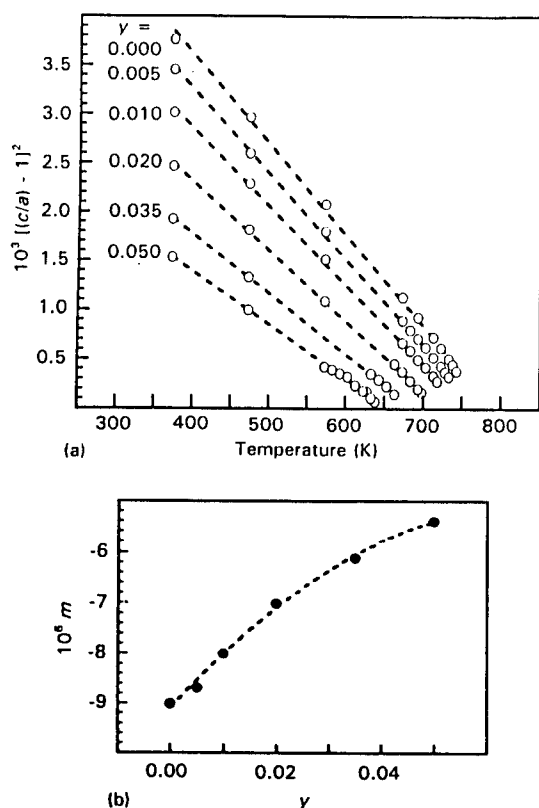


Figure 10 Plots of  $[(c/a) - 1]^2$  versus  $T$  for  $\text{Pb}_{1-1.5\gamma}\text{La}_{\gamma}[\text{Ti}]\text{O}_3$  (a). The composition dependence of the slope  $m$  of the curves (b).

power versus temperature curves for the various specimens investigated are shown in Fig. 11a. The transition enthalpies obtained by the direct integration of these curves are shown in Fig. 12. It was found that the transition enthalpy dropped substantially between  $y = 0.00$  and  $y = 0.01$ , but after the initial drop did not change significantly with subsequent increases in lanthanum concentration. Despite the rather dramatic changes in the nature of the phase transition, the shift in transition temperature with composition was nearly linear, with a slope  $dT_c/dy = -20.9$  K per at% La. This value is in good agreement with the value of  $-19.9$  K per at% obtained from dielectric measurements made on dense ceramic specimens over a much wider range of composition extending from  $y = 0.04$  to  $y = 0.30$  [22].

Corresponding to the initial drop in the transition enthalpy, a small anomaly in the DSC curves was detected. As shown in Fig. 11b, even at scan rates as low as  $1 \text{ K min}^{-1}$  this anomaly was not resolved into separate enthalpic events. The anomaly was observed both on heating and cooling, and showed a reproducible thermal hysteresis that occurred after repeated cycling through the transition. This behaviour was detected in both the Perkin Elmer and Setaram calorimeters, and so was not an artefact of the measurement technique. Furthermore, it was evident only in the samples with  $y = 0.005$  and  $0.01$ , and could not be detected for unmodified lead titanate or for samples

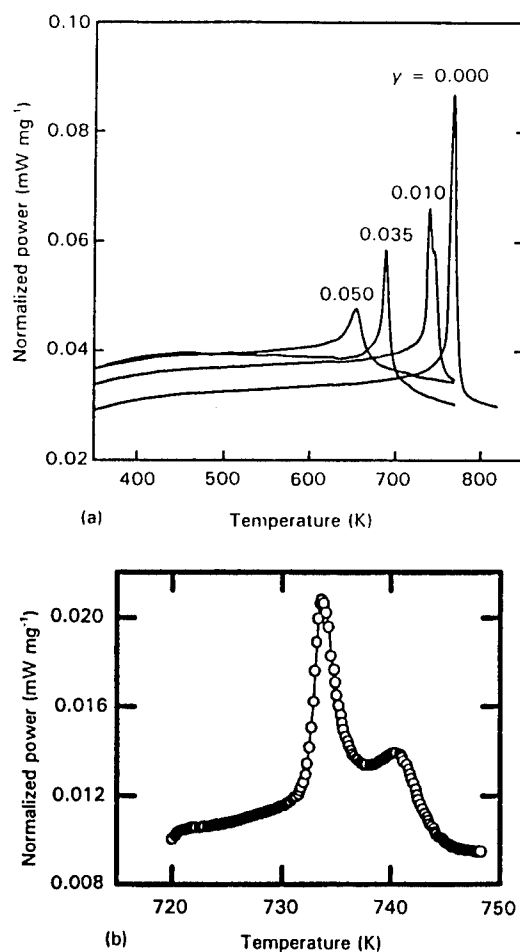


Figure 11 DSC curves for  $\text{Pb}_{1-1.5\gamma}\text{La}_{\gamma}[\text{Ti}]\text{O}_3$  obtained in heating runs at  $5 \text{ K min}^{-1}$  (a). The anomalous behaviour observed for the specimen with  $y = 0.01$  as obtained at a slower heating rate of  $1 \text{ K min}^{-1}$  (b).

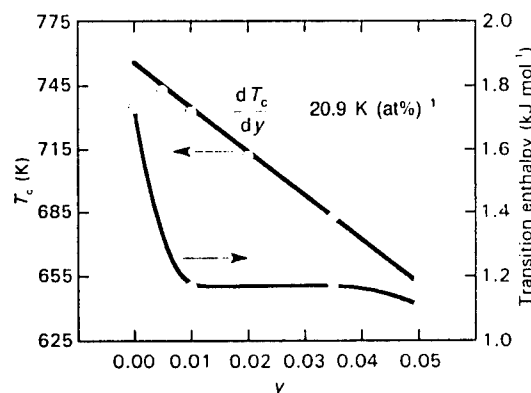


Figure 12 Estimated transition temperatures and enthalpies of  $\text{Pb}_{1-1.5\gamma}\text{La}_{\gamma}[\text{Ti}]\text{O}_3$ .

with lanthanum contents higher than  $y = 0.01$ . Based on the diffraction profile data presented in Figs 4 and 8, it is proposed that this anomalous behaviour reflects the breakdown of conventional first-order ferroelectric



phase transition behaviour as the lattice relaxes to the defects and long-range order is disrupted.

Specimens with higher lanthanum concentrations did not exhibit the anomalous transition behaviour, but instead exhibited broadened DSC peaks indicative of a smeared phase transition. Consequently, for specimens with  $0.02 \leq y \leq 0.05$ , the apparent changes in the nature of the transition as revealed in the diffraction data of Fig. 10 can be associated with the change-over from conventional to diffuse transition behaviour. For the specimen with  $y = 0.05$ , the transition was very diffuse and took place over a temperature interval that was estimated to be as much as 150 K. Indeed, as shown in Fig. 13, local distortions of the structure connected with the smearing of the transition could be detected as a temperature-dependent X-ray profile broadening that continued above the expected transition temperature. Fig. 14 shows that as a result of this smearing, the signature of the first-order discontinuity of the transition was obscured, and the transition appeared to take place in a continuous manner. Similar behaviour has also been observed in synchrotron studies of lightly doped barium titanate [32].

#### 4. Discussion

For specimens prepared according to the A-site vacancy formula, the introduction of lanthanum to lead titanate produces one lead vacancy for every two La (III) ions. These defects locally break the translational periodicity of the lattice and produce elastic and electric fields that fall off slowly as a function of distance from the defect cores [33]. The role of these defects may be mediated during the phase transition by direct coupling to the primary order parameter (spontaneous polarization), and/or by indirect coupling through the elastic strain. Because of the large tetragonal distortion of lead titanate, it seems likely that the latter interaction is the dominant one. Phenomena due to strain coupling through defects has

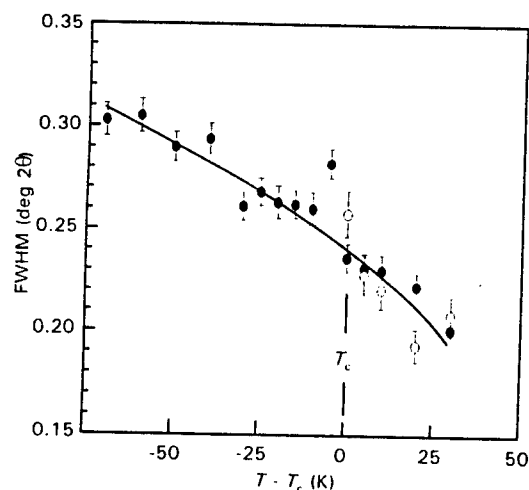


Figure 13 Temperature dependence of the FWHM of (●) 222 and (○) 300 reflections of  $\text{Pb}_{1-x}\text{La}_x[\text{Ti}]\text{O}_3$  ( $y = 0.05$ ).

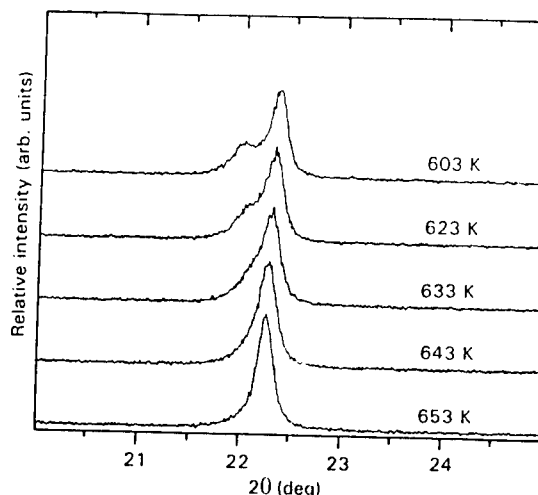


Figure 14 Temperature dependence of 001/100 reflections of  $\text{Pb}_{1-x}\text{La}_x[\text{Ti}]\text{O}_3$  ( $y = 0.05$ ). ( $\text{Cu K}\alpha$  radiation).

been identified as important in a wide variety of structural phase transitions [34].

When small amounts ( $y \leq 0.01$ ) of lanthanum are first introduced into the lattice, the defects are widely separated. The degree of interaction between the defects will be primarily determined by the strength of the defect fields, by the characteristic range of interaction, and by the temperature relative to  $T_c$  [35, 36]. The fact that no "plateau" effect (a range of composition over which the transition temperature does not renormalize) was observed for lanthanum concentrations as low as 0.5 at% indicates that the defects interact strongly with the lattice [35].

For these specimens, a strong asymmetry and temperature-dependent broadening was observed in the X-ray diffraction profiles. The associated changes in the elastic properties of the lattice appeared to be connected with the sharp decrease in the transition enthalpy. These observations are consistent with an analysis [37] of the Devonshire energy function [10] for lead titanate [8], which predicts a strong decrease in the first-order character of the transition resulting from even subtle changes in elastic or electrostructure behaviour. The initial loss in the first-order character of the transition observed in the calorimetry data has also been reported for lanthanum-doped single-crystal specimens [21], as well as for lead titanate specimens into which lattice defects have been deliberately introduced by processing [15, 16].

At higher dopant levels ( $y \geq 0.02$ ), a clear change in the mode by which the lanthanum or vacancies were accommodated was observed. This behaviour was signalled by the abrupt increase in the symmetry of the diffraction profiles (Fig. 4) and by the onset of the departure of the lattice parameters from Vegard's law (Fig. 5). Transmission electron microscopy confirmed that the lattice relaxation mechanism involved a non-uniform distribution of the crystal tetragonality that manifested itself in a progressive complication of the ferroelectric domain structure. As the extent of the sub-domain texture increased, the character of the

transition became more diffuse. Indeed, the changes in domain texture as seen in Fig. 9 have been recently shown [38] to correlate well with the degree of deviation of the dielectric response from the expected Curie-Weiss behaviour [22]. Similar microstructures are also observed in lanthanum-substituted lead zirconate-titanate compositions having diffuse transitions [39]. The implications of these modulated domain structures with respect to the crystal symmetry and phase transition behaviour have been recently discussed in more detail.

## 5. Summary

The phase transition behaviour and structural characteristics of lanthanum-substituted lead titanate ferroelectrics were investigated by high-temperature X-ray diffraction and differential scanning calorimetry. Interconnections between the phase transition behaviour, the ferroelectric domain structure and the dielectric properties were identified. The results demonstrated the important influence of elastic strain coupling through lanthanum/vacancy-induced defect fields on the first-order character of the transition. The initial relaxation of the lattice to these fields manifested itself in a substantial decrease in the signature first-order discontinuity of the phase transition. Associated with this relaxation process was the development of a modulated ferroelectric domain structure, the appearance of which correlated well with the onset of the diffuse phase transition behaviour. It was suggested that further degeneration of the domain structure into tweed textures is responsible for the anomalous dielectric response near the phase transition.

## Acknowledgements

The authors are indebted to the Office of Naval Research for providing financial support for this research. The transition enthalpy measurements were carried out in the Calorimetry Laboratory of Professor A. Navrotsky at Princeton University and were supported by the NSF grant DMR 92-15802.

## References

1. A. M. GLAZER and S. A. MABUD, *Acta Crystallogr.* **B34** (1978) 1065.
2. G. A. SAMARA, *Ferroelectrics* **2** (1972) 277.
3. G. BURNS and B. A. SCOTT, *Phys. Rev. Lett.* **25** (1970) 1191.
4. M. E. LINES and A. M. GLASS, "Principles and Applications of Ferroelectrics and Related Materials" (Clarendon, Oxford, 1977) p. 248.
5. R. J. NELMES, R. O. PILTZ, W. F. KUHS, Z. TUN and R. RESTORI, *Ferroelectrics* **108** (1990) 165.
6. E. G. FESENKO, V. G. GAVRILYACHENKO and E. V. ZAROCHENTSEV, *Izv. Akad. Nauk SSSR Ser. Fiz.* **34** (1970) 2541.

7. *Idem*, *Bull. Acad. Sci. USSR* **34** (1970) 2262.
8. M. J. HAUN, E. FURMAN, S. J. JANG, H. A. MCKINSTRY and L. E. CROSS, *J. Appl. Phys.* **62** (1987) 3331.
9. G. A. ROSSETTI Jr, K. R. UDAYAKUMAR, M. J. HAUN and L. E. CROSS, *J. Amer. Ceram. Soc.* **73** (1990) 3334.
10. A. F. DEVONSHIRE, *Adv. Phys.* **3** (1954) 85.
11. S. A. MABUD and A. M. GLAZER, *J. Appl. Crystallogr.* **12** (1979) 49.
12. G. SHIRANE, R. PEPINSKY and B. C. FRAZER, *Acta Crystallogr.* **9** (1956) 131.
13. S. C. ABRAHAMS, S. K. KURTZ and P. B. JAMIESON, *Phys. Rev.* **172** (1968) 551.
14. V. G. GAVRILYACHENKO, R. I. SPINKO, M. A. MARTYNENKO and E. G. FESENKO, *Sov. Phys. - Solid State* **12** (1970) 1203.
15. S. SHIRASAKI, *Solid State Commun.* **9** (1971) 1217.
16. S. SHIRASAKI, K. TAKAHASHI and K. KAKEGAWA, *J. Amer. Ceram. Soc.* **56** (1973) 430.
17. D. HENNINGS, *Mater. Res. Bull.* **6** (1971) 329.
18. D. HENNINGS and K. H. HÄRDTL, *Phys. Status Solidi (a)* **3** (1970) 465.
19. R. J. NELMES and A. KATRUSIAK, *J. Phys. C: Solid State Phys.* **19** (1986) L725.
20. R. RAMIREZ, M. F. LAPENA and J. A. GONZALO, *Phys. Rev.* **B42** (1990) 2604.
21. K. WOJCIK, *Ferroelectrics* **99** (1989) 5.
22. K. KEIZER, G. J. LANSINK and A. J. BURGGRAAF, *J. Phys. Chem. Solids* **39** (1978) 59.
23. G. BURNS and B. A. SCOTT, *Solid State Commun.* **13** (1973) 417.
24. G. BURNS, *Phys. Rev.* **B13** (1976) 215.
25. R. MERLIN, J. A. SANJURJO and A. PINCZUK, *Solid State Commun.* **16** (1975) 931.
26. T. W. DEKLEVA, J. M. HAYES, L. E. CROSS and G. L. GEOFFROY, *J. Amer. Ceram. Soc.* **71** (1988) C280.
27. J. B. BLUM and S. R. GURKOVICH, *J. Mater. Sci.* **20** (1985) 4479.
28. M. M. HALL Jr, V. G. VEERARGHAVAN, H. RUBIN and P. G. WINCHELL, *J. Appl. Cryst.* **10** (1977) 66.
29. B. HEMINGWAY, *Amer. Mineralogist* **72** (1987) 273.
30. C. A. RANDALL, G. A. ROSSETTI Jr and W. CAO, *Ferroelectrics* in press.
31. E. SALJE, *Phase Transitions* **34** (1991) 25.
32. C. N. W. DARLINGTON and R. J. CERNIK, *J. Phys: Condens. Matter* **3** (1992) 4387.
33. A. P. LEVANYUK and A. S. SIGOV, "Defects and Structural Phase Transitions" (Gordon and Breach, New York, 1986) p. 172.
34. S. MARAIS, V. HEINE, C. NEX and E. SALJE, *Phys. Rev. Lett.* **66** (1991) 2480.
35. E. SALJE, U. BISMAYER, B. WRUCK and J. HENSLE, *Phase Transitions* **35** (1991) 61.
36. W. CAO and J. A. KRUMHANS, *Phys. Rev.* **B42** (1990) 4334.
37. G. A. ROSSETTI Jr, *Ferroelectrics* **133** (1992) 103.
38. G. A. ROSSETTI Jr, W. CAO and C. A. RANDALL, *ibid.* in press.
39. C. A. RANDALL, D. J. BARBER and R. W. WHATMORE, *J. Microsc.* **145** (1987) 275.

Received 11 April  
and accepted 10 May 1994

# APPENDIX 10

# Structure of the defect perovskite $[\text{Pb}_{0.85}\text{La}_{0.10}]_{\square}\text{TiO}_3$ between 10 and 1023 K

George A. Rossetti, Jr., Mark A. Rodriguez, and Alexandra Navrotsky  
*Department of Geological and Geophysical Sciences and Princeton Materials Institute,  
 Princeton University, Princeton, New Jersey 08544*

L. Eric Cross and Robert E. Newnham  
*Materials Research Laboratory, The Pennsylvania State University, University Park, Pennsylvania 16802*

(Received 2 August 1994; accepted for publication 25 October 1994)

The structure of the defect perovskite  $[\text{Pb}_{0.85}\square_{0.05}\text{La}_{0.10}]\text{TiO}_3$  was investigated by powder neutron and x-ray diffraction and by specific heat measurements made at various temperatures. Refinement of the structure by the Rietveld technique at 10, 200, and 300 K from time-of-flight powder neutron diffraction data revealed no low temperature transitions from the ferroelectric tetragonal ( $4mm$ ) phase. On average, the oxygen octahedral framework of the parent compound was not distorted by the incorporation of lanthanum and vacancies, and the ratio of cation displacements along the polar axis was comparable to that observed for pure  $\text{PbTiO}_3$ . However, the material showed a large nonuniform strain that increased with decreasing temperature. As a result, the effective coupling between the uniform tetragonal deformation and cation displacement was reduced. X-ray diffraction and specific heat measurements at 298–1023 K indicated that the ferroelectric  $m3m \rightarrow 4mm$  transition was nearly tricritical and took place at 565 K. The diffuse nature of the transition was reflected in a temperature-dependent x-ray profile broadening and anomalous excess specific heat that persisted to  $\approx 775$  K, close to the phase transition temperature of pure lead titanate. © 1995 American Institute of Physics.

## I. INTRODUCTION

One of the most studied aspects of ferroelectric phase transitions concerns the extreme broadening of the transition anomalies observed in complex compounds or solid solutions in which foreign ions occupy crystallographically equivalent lattice sites. The break in translational invariance caused by the foreign ions/lattice imperfections leads to the observation of "diffuse" phase transition (DPT)<sup>1</sup> behavior that is characterized by a pronounced smearing of such properties as the spontaneous polarization, the specific heat anomaly, the refractive index, etc., that would normally exhibit abrupt changes at a ferroelectric instability.<sup>2</sup>

The perovskite-structured solid solution in the system  $\text{PbO-La}_2\text{O}_3\text{-TiO}_2$  provides an interesting example of a compositional series for which a changeover from conventional to diffuse ferroelectric phase transition behavior is observed. The end member  $\text{PbTiO}_3$  is representative of a large family of oxygen octahedra ferroelectrics that undergo a discontinuous phase change from a centrosymmetric cubic ( $m3m$ ) prototype to a tetragonal ( $4mm$ ) ferroelectric phase. The aliovalent substitution of  $\text{La(III)}$  for  $\text{Pb(II)}$  reduces the characteristic first-order discontinuity of the transition<sup>3</sup> and induces DPT behavior.<sup>4</sup>

The perovskites in this system may be envisioned as lying within a triangle formed by  $\text{PbTiO}_3$  and the two metastable defect compounds  $[\text{La}_{2/3}\square_{1/3}]\text{TiO}_3$  and  $\text{La}[\text{Ti}_{3/4}\square_{1/4}]\text{O}_3$ . These compositions have been described<sup>5-7</sup> by the general defect equation

$$\text{Pb} \frac{3(1-\alpha y)}{3+y(1.5-\alpha)} \text{La} \frac{3y}{3+y(1.5-\alpha)} \square \frac{y(2\alpha-1.5)}{3+y(1.5-\alpha)} \\ \times \left[ \text{Ti} \frac{3}{3+y(1.5-\alpha)} \square \frac{y(1.5-\alpha)}{3+y(1.5-\alpha)} \right] \text{O}_3,$$

where  $\square$  is a site vacancy and  $\alpha$  is the Pb elimination factor. In principle,  $\alpha$  may adopt values ranging from 1.5 (A-site vacancies only) to 0.75 (B-site vacancies only). However, although it is generally agreed that lanthanum resides exclusively on the A site of the perovskite structure, controversy exists regarding the ability of the structure to incorporate octahedral vacancies.<sup>8,9</sup> Nevertheless, for compositions with  $y < 0.3$ , it is found experimentally that for each value of  $y$  there exists a range  $0.9 < \alpha < 1.5$  for which the single-phase perovskite remains stable with respect to the pyrochlore  $\text{La}_2\text{Ti}_2\text{O}_7$ .<sup>6</sup>

For the perovskite-structured compositions with relatively low lanthanum concentrations ( $y < 0.05$ ), dielectric measurements<sup>4</sup> have shown that the anomalies associated with the transition to the ferroelectric phase are sharp and qualitatively consistent with what is expected at a conventional first-order ferroelectric phase change. As the lanthanum content is increased in the range of  $0.05 < y < 0.10$ , broadened transition anomalies and pronounced departures from Curie-Weiss behavior become evident. At still higher dopant levels ( $y > 0.20$ ), the character of the transition becomes markedly diffuse, but shows only weak frequency dispersion.

Although the dielectric properties of these materials have been studied in some detail,<sup>4,5,8,10-13</sup> their structural characteristics have not been thoroughly investigated. Recently, x-ray diffraction and transmission electron microscopy measurements<sup>14</sup> performed on a series of compositions ( $y = 0-0.15$ ) were used to investigate the structural changes associated with the breakdown of conventional ferroelectric phase transition behavior. The present contribution provides additional information regarding the structure and phase transition behavior of an intermediate A-site vacancy composition,  $[\text{Pb}_{0.85}\square_{0.05}\text{La}_{0.10}]\text{TiO}_3$ . The structure has been re-

fined from high resolution time-of-flight powder neutron diffraction data at 10, 200, and 300 K. In addition, the  $m3m \rightarrow 4mm$  transition has been investigated using specific heat and x-ray diffraction measurements in the temperature range 298–1023 K. The results are discussed in relation to the first-order character and diffuse nature of the transition.

## II. EXPERIMENT

### A. Powder neutron diffraction

A powder specimen of lanthanum-substituted lead titanate was prepared according to the A-site vacancy formula ( $[\text{Pb}_{1-1.5y}\text{La}_y]\text{TiO}_3$ ) using the conventional solid-state reaction method. Stoichiometric amounts of >99.99%  $\text{PbO}$ ,  $\text{La}_2\text{O}_3$ , and  $\text{TiO}_2$  required to make a composition with  $y=0.10$  were batched by weight accounting for the observed weight loss on ignition. The starting reagents were homogenized by ball milling for 24 h in isopropanol using high purity, high strength zirconia milling media. The powder was then dried at 353 K, precalcined in a closed alumina crucible at 1073 K (4 h), ground with a mortar and pestle, and calcined again at a higher temperature of 1323 K (8 h). The resulting powder was light yellow in color and the phase purity was verified by x-ray diffraction.

Powder diffraction data were collected using the high resolution time-of-flight neutron powder diffractometer (NPD) at the Los Alamos Neutron Scattering Center (LANSCE). The sample position on the NPD was 32 m from the source and standard collimation in the beam line produced a 5.0 by 1.0 cm beam at this location. Sufficient material ( $\approx 10$  g) to completely fill a 5  $\text{cm}^3$  vanadium specimen canister at tap density was sealed in place under helium. The canister was mounted in a closed-cycle refrigerator contained within a stainless steel experiment chamber that was lowered into the beam line of the diffractometer. Data were collected at 10, 200, and 300 K and the collection time at each temperature was approximately 4 h. The data summed from two right angle detector banks ( $2\theta = \pm 90^\circ$ ) and two backscattering banks ( $2\theta = \pm 148^\circ$ ) were used in the refinements.

### B. High-temperature x-ray powder diffraction

X-ray powder diffraction patterns of the sample were recorded in the range of 300–1023 K using a Scintag  $\theta$ – $\theta$  powder diffractometer equipped with an Anton Paar hot stage. Prior to the measurements, the stage was aligned at room temperature relative to a  $\text{LaB}_6$  reference material (Standard Reference Material No. 760). The hot stage employed a platinum heating strip onto which the specimen was uniformly deposited from an ethanol suspension. A type-S thermocouple welded to the underside of the heating strip provided the temperature measurement. Diffraction data in the scan range of  $2\theta$  ( $\text{Cu K}\alpha$ ) =  $20^\circ$ – $70^\circ$  were collected in air as continuous scans using a scan rate of  $2^\circ/\text{min}$ . The positions of the Bragg reflections appearing in this range were assigned using a peak locating algorithm based on a second derivative test. Lattice parameters were determined from the peak positions using a standard least-squares refinement routine. In addition, x-ray line broadening measurements were performed. The full widths at half-maximum (FWHM) for

selected  $hkl$  reflections were determined by fitting the diffraction profiles to a constrained pseudo-Voigt profile function. These data were used to qualitatively assess the temperature dependence of the diffraction profile broadening.

### C. Specific heat measurements

Heat capacity measurements were made using a Setaram TG-DSC 111 scanning calorimeter (DSC) operated in the horizontal configuration. The Setaram DSC is a microcalorimeter of the twin Calvet design. The temperature calibration of the instrument was determined by measuring the melting points of high purity In, Pb, Zn, and Al (Johnson Matthey, >99.999%) using graphite-lined stainless steel crucibles that eliminated molten metal-crucible interactions. The calorimeter calibration was performed by measuring the specific heat of a high purity  $\alpha$ -alumina powder sample (Johnson Matthey, >99.99%) that was calcined at 1773 K prior to the experiments to ensure phase purity. The sensitivity polynomial for the calorimeter was then determined as the ratio of these data to the reference data<sup>15</sup> for a synthetic sapphire sample (Standard Reference Material No. 720).

The alumina calibration (108.17 mg) and sample (108.83 mg) materials were sealed in pressure tight stainless steel crucibles. The specific heat measurements were made in heating runs over the range of 298–973 K using a scan rate of 10 K/min. The data were collected at intervals corresponding to 3 points/K. In order to inhibit oxidation of the crucibles and to provide a uniform heat transfer environment, the measurements were made under a constant flow (nominally 28 ml/min) of dry argon. The heat capacity of the sample was determined by subtracting the average of three such scans for the empty crucible from the average of three scans for the crucible plus sample.

## III. STRUCTURE REFINEMENT

The refinement of the structure was carried out using a Rietveld profile least-squares program adapted for time-of-flight data that was contained within the General Structure Analysis System (GSAS) package.<sup>16</sup> The unit cell was defined by fixing the O(II) atom at the (0,1/2,1/2) position. From this point of reference, the (Pb,L a), Ti, and O(I) atoms in the ferroelectric tetragonal  $4mm$  form of the perovskite structure are displaced by an amount  $\delta z$  along the  $c$  axis from the (0,0,0), (1/2,1/2,1/2), and (1/2,1/2,0) positions, respectively. Consequently, the structural parameters to be refined were the tetragonal lattice constants  $a$  and  $c$ , the three atom displacements  $\delta z_{\text{Ti}}$ ,  $\delta z_{(\text{Pb,L a})}$ ,  $\delta z_{\text{O(I)}}$ , and the temperature factors. Both isotropic ( $U$ ) and anisotropic ( $u_{ij}$ ) temperature factors were refined. In each case, the refinement was initiated by setting the  $\delta z$  values equal to zero, except for  $\delta z_{\text{Ti}}$ , which was given a small positive value to define the positive direction of the  $c$  axis.

The crystal structure parameters were refined along with a scale factor, a zero point correction, and six profile coefficients for each of the histograms generated by the four detector banks. The background function for each histogram was represented by a Fourier cosine series having six refined coefficients. Because this material exhibited an appreciable

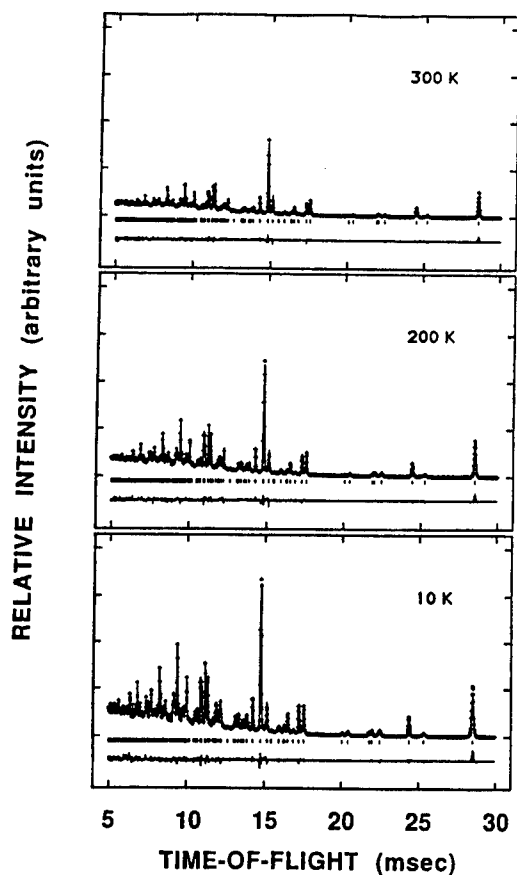


FIG. 1. Time-of-flight powder neutron diffraction patterns of the defect perovskite  $[\text{Pb}_{0.85}\square_{0.05}\text{La}_{0.10}]\text{TiO}_3$  collected at 10, 200, and 300 K.

degree of predominantly Lorentzian profile broadening (see the discussion below), the most appropriate profile function of those installed in GSAS consisted of a convolution of a pseudo-Voigt function with a pair of back-to-back exponentials. In applying this function, an anisotropic broadening axis was defined along the  $[001]$  direction. Using the refined profile coefficients, the anisotropic strain components parallel ( $S_p$ ) and normal ( $S_N$ ) to this axis were computed. Further details regarding the mathematical basis for the profile and background functions used can be found in the GSAS documentation<sup>16</sup> and in the references given there.

#### IV. RESULTS AND DISCUSSION

The observed, calculated, and difference neutron powder diffraction patterns as obtained from the  $2\theta = +90^\circ$  detector bank of the NPD are shown in Fig. 1. In Fig. 1, the observed data at each temperature are denoted by the crosses, and the corresponding calculated profiles are represented by the continuous lines. The tick marks below each histogram give the positions of all possible Bragg reflections. The difference between the calculated and observed data is plotted below the tick marks.

In spite of some difficulty in adequately modeling the broadened diffraction profiles, it is seen that, except at the

TABLE I. Refined structural parameters of  $[\text{Pb}_{0.85}\square_{0.05}\text{La}_{0.10}]\text{TiO}_3$ .

		10 K	200 K	300 K
Pb,La	$\delta z$ (Å)	0.406 (1)	0.365 (1)	0.331 (2)
	$u_{11}$ ( $10^{-2} \text{ Å}^2$ )	0.49 (2)	1.13 (3)	1.51 (3)
	$u_{33}$ ( $10^{-2} \text{ Å}^2$ )	0.83 (3)	1.11 (5)	1.43 (7)
Ti	$\delta z$ (Å)	0.281 (2)	0.255 (2)	0.234 (3)
	$u_{11}$ ( $10^{-2} \text{ Å}^2$ )	0.48 (3)	0.56 (4)	0.70 (4)
	$u_{33}$ ( $10^{-2} \text{ Å}^2$ )	1.30 (1)	1.60 (1)	1.43 (1)
O(I)	$\delta z$ (Å)	0.037 (1)	0.031 (2)	0.031 (2)
	$u_{11}$ ( $10^{-2} \text{ Å}^2$ )	1.00 (3)	1.17 (4)	1.52 (5)
	$u_{33}$ ( $10^{-2} \text{ Å}^2$ )	0.75 (4)	1.19 (6)	1.44 (8)
O(II)	$u_{11}$ ( $10^{-2} \text{ Å}^2$ )	0.73 (3)	1.13 (5)	1.38 (6)
	$u_{22}$ ( $10^{-2} \text{ Å}^2$ )	0.55 (3)	0.58 (4)	0.63 (5)
	$u_{33}$ ( $10^{-2} \text{ Å}^2$ )	1.27 (4)	1.76 (6)	2.24 (8)
$a$ (Å)	...	3.905	3.911	3.917
$c$ (Å)	...	4.057	4.043	4.031
$R_p$	...	0.065	0.068	0.074
$wR_p$	...	0.094	0.099	0.109
$\chi^2$	...	3.50	2.70	2.18

very lowest neutron energies, good agreement exists between the calculated and observed diffraction profiles. At the lowest temperature investigated (10 K), the data indicated that the sample retained its tetragonal symmetry. Observed Fourier maps generated from the histograms in Fig. 1 failed to reveal any additional information not contained in the original structural model. Consequently, although the substitution of lanthanum is effective at displacing the Curie temperature and in smearing the phase transition,<sup>4,12</sup> it apparently does not lead to any additional low temperature lattice instabilities.

The structural parameters refined at each temperature are summarized in Table I. As shown in Fig. 2, the values obtained for the isotropic temperature factors for all atoms were of the appropriate magnitude, and all exhibited a continuous decrease with decreasing temperature as expected. The re-

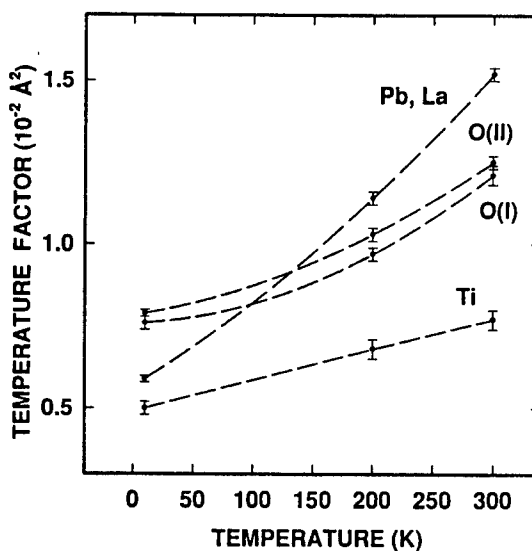


FIG. 2. Isotropic temperature factors for  $[\text{Pb}_{0.85}\square_{0.05}\text{La}_{0.10}]\text{TiO}_3$ .

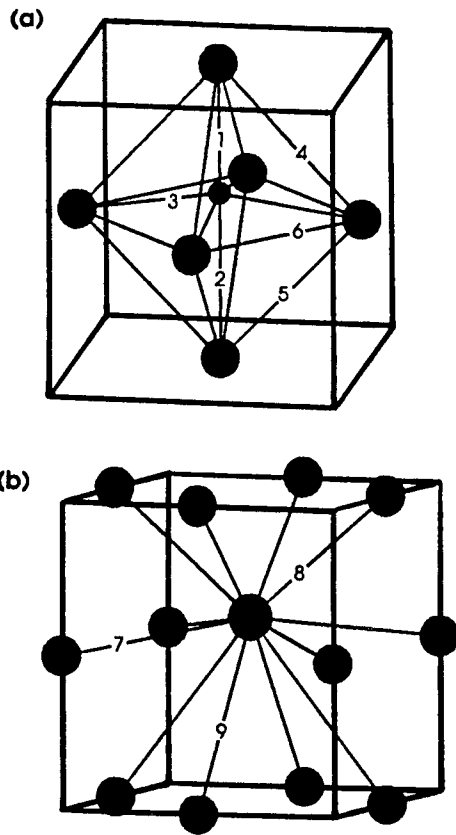


FIG. 3. Environment of (a) Ti and (b) Pb,La in the perovskite structure.

finement of anisotropic temperature factors was performed primarily to better determine the atomic positional parameters, although this did not appreciably influence the values of the  $R$  factors. Somewhat larger anisotropies for the Ti ( $u_{33} > u_{11}$ ) and O(II) ( $u_{33} > u_{11} > u_{22}$ ) atoms were observed relative to the (Pb,La) and O(I) atoms. Similar results have been obtained in single crystal neutron studies of the structure of unmodified lead titanate.<sup>17</sup> It appears, therefore, that any static disorder of the structure arising from the lanthanum/vacancies was not strongly reflected in the refined temperature factors.

Using the lattice parameter and atomic position data in Table I, the various bond distances depicted in Fig. 3 were computed. These are reported in Table II. Given the relatively large defect concentration in the sample and the wide range of temperature investigated, the average O(I)—O(I), O(I)—O(II), and O(II)—O(II) bond lengths were remarkably constant. As with unmodified lead titanate,<sup>18</sup> this result implies that the oxygen octahedral framework is very rigid. The ratio of the cation shifts on the (Pb,La) and Ti sites  $\delta z_{\text{(Pb,La)}}/\delta z_{\text{Ti}} = 1.43$  was also found to be independent of temperature, and was comparable to the value  $\delta z_{\text{Pb}}/\delta z_{\text{Ti}} = 1.50$  observed for lead titanate over a similar range of temperature (90–298 K).<sup>18</sup> These results indicate the average picture of the ferroelectric phase in  $[\text{Pb}_{0.85}\square_{0.05}\text{La}_{0.10}]\text{TiO}_3$  is not greatly different from that in pure lead titanate.

TABLE II. Summary of bond distances (Å) for  $[\text{Pb}_{0.85}\square_{0.05}\text{La}_{0.10}]\text{TiO}_3$ .

Bond <sup>a</sup>	Bond type	10 K	200 K	300 K
1	Ti—O(I)	1.78	1.80	1.81
2	Ti—O(I)	2.28	2.25	2.22
3	Ti—O(II)	1.97	1.97	1.97
4	O(I)—O(II)	2.84	2.84	2.83
5	O(I)—O(II)	2.79	2.79	2.79
6	O(II)—O(II)	2.76	2.77	2.77
7	(Pb,La)—O(I)	2.78	2.79	2.79
8	(Pb,La)—O(II)	2.54	2.56	2.58
9	(Pb,La)—O(II)	3.12	3.09	3.06

<sup>a</sup>The bonds (1)–(9) are depicted in Fig. 3.

Alternatively, information regarding the local disruption of the structure caused by the lanthanum and vacancies was contained in the shapes and breadths of the diffraction profiles. Upon closer examination, the profiles of the Bragg reflections in Fig. 1 showed an asymmetric broadening that increased with decreasing temperature over the range studied. The degree of the profile broadening and asymmetry exhibited an  $hkl$  dependence, and was most pronounced in reflections having high  $l$ -component indices. These observations suggested the existence of an inhomogeneous lattice strain connected primarily with a spatial variation of the tetragonal distortion. It should be mentioned that very similar results have also been obtained in high resolution x-ray diffraction experiments<sup>14</sup> performed on a series of chemically derived samples ( $y=0-0.15$ ). As the latter specimens were processed under conditions very different from those of the present sample, it is believed that this type of profile broadening is related to the defect structure and reflects an intrinsic microcrystalline characteristic of these materials, rather than being related to processing parameters such as chemical homogeneity, etc.

The degree of strain anisotropy associated with the observed profile broadening was quantified by calculating from the refined profile coefficients the nonuniform strain components perpendicular and parallel to the tetragonal  $c$  axis. As seen in Table III, it was found that the magnitude of the nonuniform strain calculated on this basis was quite large ( $\approx 10^{-3}$ ), and only about one order of magnitude smaller than the uniform tetragonal distortion ( $c/a-1$ ). The strain anisotropy was also very large, with the component of strain parallel to the  $c$  axis having a value that was about five times larger than the normal component. Both components of strain increased in magnitude as the temperature was lowered, with the parallel component increasing more strongly than the normal component.

TABLE III. Tetragonal distortion, effective coupling coefficient, and non-uniform strain for  $[\text{Pb}_{0.85}\square_{0.05}\text{La}_{0.10}]\text{TiO}_3$ .

Temp. (K)	$(c/a-1)$	$q^{\text{eff}}$ (Å <sup>-2</sup> )	$S_p$ (10 <sup>-3</sup> )	$S_N$ (10 <sup>-3</sup> )
10	0.039	$0.494 \pm 0.007$	$3.11 \pm 0.16$	$0.57 \pm 0.13$
200	0.034	$0.523 \pm 0.008$	$2.62 \pm 0.17$	$0.55 \pm 0.06$
300	0.029	$0.530 \pm 0.014$	$2.29 \pm 0.20$	$0.47 \pm 0.04$

The temperature-dependent component of the diffraction profile broadening can be qualitatively explained in the following way. In the tetragonal perovskite ferroelectrics, the uniform components of strain ( $x_i$ ) couple electrostrictively to the square of the spontaneous polarization ( $P_3$ ) in accordance with the relations (in Voigt notation)

$$x_1 = Q_{12} P_3^2, \quad (1)$$

$$x_3 = Q_{11} P_3^2. \quad (2)$$

From Eqs. (1) and (2), it is clear that any spatial variation in the spontaneous polarization, such as that arising from local La(III)/vacancy defect fields, will result in an inhomogeneous component of the electrostrictive strain. Because the magnitude of the spontaneous polarization increases continuously below the  $m3m \rightarrow 4mm$  transition, the degree of the nonuniform strain also increases with decreasing temperature. This in turn results in a temperature-dependent profile broadening in addition to any broadening caused by particle size effects, etc., which, if present, would also be observed in the nonpolar phase and would not be strongly temperature dependent. Further, because  $Q_{11}$  and  $Q_{12}$  differ in magnitude and are opposite in sign ( $Q_{11}/Q_{12} = -3.45$  for  $\text{PbTiO}_3$ ),<sup>19</sup> the degree of profile broadening and asymmetry exhibits an  $hkl$  dependence.

The spontaneous polarization is in turn directly related to the displacement of Ti along the polar axis.<sup>20</sup> It was of interest, therefore, to determine to what degree the local variation of the polarization, as reflected in the profile coefficients, may alter the effective coupling constant  $q^{\text{eff}}$  relating the uniform tetragonal deformation ( $c/a - 1$ ) and  $\delta z_{\text{Ti}}$ ,

$$(c/a - 1) \propto q P_3^2 \propto q^{\text{eff}} (\delta z_{\text{Ti}})^2. \quad (3)$$

The results, which are also summarized in Table III, showed that as the degree of the nonuniform strain increased, the effective electrostrictive coupling strength decreased. Furthermore, the magnitude of  $q^{\text{eff}}$  at room temperature was only about 85% of the value calculated using the published neutron diffraction results for pure  $\text{PbTiO}_3$ .<sup>18,21</sup>

An analysis of the thermodynamic equation of state for  $\text{PbTiO}_3$  within the quasihomogeneous approximation of the Landau theory of phase transitions<sup>22</sup> has suggested that only a small softening in the elastic/electrostrictive properties of the lattice is required to substantially alter the first-order character of the ferroelectric transition.<sup>23</sup> Indeed, dielectric measurements on single crystal specimens have shown that a dramatic reduction in the discontinuity of the reciprocal permittivity at the transition occurs at dopant levels as low as  $y = 0.002$ .<sup>24</sup> For compositions with  $0 < y < 0.05$ , it has been observed in diffraction and calorimetric experiments that the transition appears progressively more continuous as it becomes diffuse.<sup>14</sup> Similar results have also been obtained in x-ray scattering experiments on defect-doped barium titanate.<sup>25,26</sup>

With this in mind, the nature of the ferroelectric phase transition in the sample was investigated using specific heat and high-temperature x-ray diffraction measurements. The specific heat anomaly associated with the  $m3m \rightarrow 4mm$  transition is shown in Fig. 4(a). As expected, the anomaly was

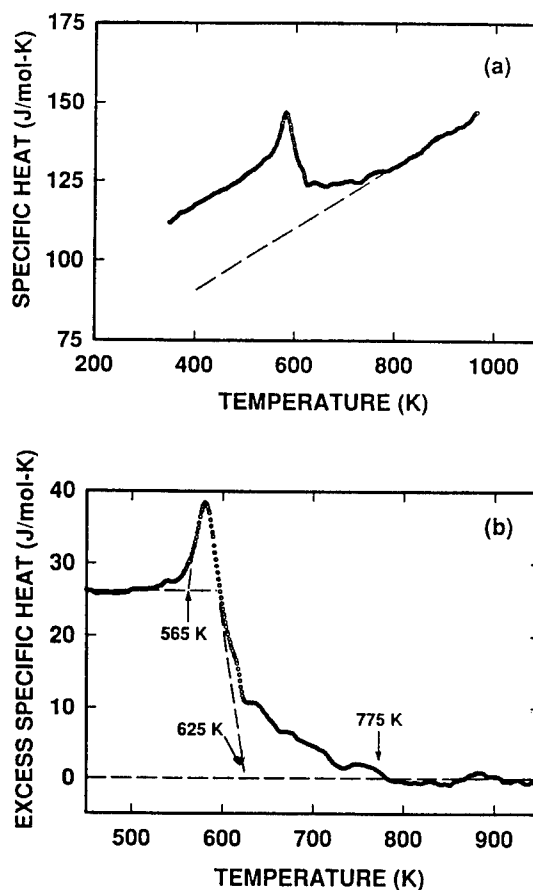


FIG. 4. (a) Specific heat anomaly at the  $m3m \rightarrow 4mm$  transition in  $[\text{Pb}_{0.85}\square_{0.05}\text{La}_{0.10}]\text{TiO}_3$ . (b) Excess specific heat relative to the linear extrapolation of the data above 850 K.

small, very broad, and was not characteristic of a first-order ferroelectric phase change. Because of the large difference in heat capacity for the two phases, it was difficult to accurately determine the transition energy. However, the value was certainly not greater than  $\approx 1$  kJ/mol.

At high temperatures, the variation of the specific heat with temperature was approximately linear over the range studied, with a slope that was nearly the same as that observed below the transition. In Fig. 4(b), the excess specific heat relative to that extrapolated from high temperature ( $T > 850$  K) is shown. It is clear from these data that the onset of the transition occurred close to 565 K, and that the anomaly was spread over an interval extending to about 625 K. Above 625 K, however, there appeared to be a "tail" to the excess heat capacity-temperature curve that did not return to the baseline until a much higher temperature in the vicinity of 775 K.

Figure 5 shows the temperature evolution of the unit cell parameters close to the  $m3m \rightarrow 4mm$  transition. Above 573 K, the structure was macroscopically cubic, and showed linear thermal expansion behavior over the range studied (573–1023 K). Using the thermal expansion data, the components of uniform spontaneous strain were computed from the relations



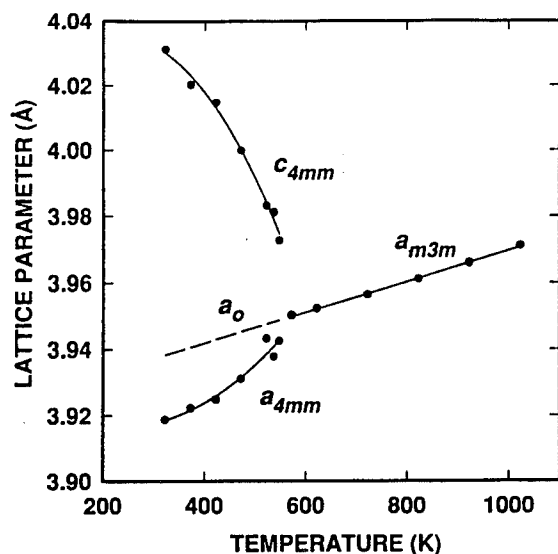


FIG. 5. Temperature variation of the lattice parameters of  $[\text{Pb}_{0.85}\square_{0.05}\text{La}_{0.10}]\text{TiO}_3$  near the ferroelectric  $m3m \rightarrow 4mm$  transition.

$$x_1 = \frac{a \sin \gamma}{a_0 \sin \gamma_0} - 1 = (a - a_0)/a_0, \quad (4)$$

$$x_3 = \frac{c \sin \alpha \sin \beta^*}{c_0 \sin \alpha_0 \sin \beta_0^*} - 1 = (c - a_0)/a_0, \quad (5)$$

where  $\alpha$ ,  $\gamma$ ,  $\beta$ ,  $\beta^*$  represent the interaxial angles in real and reciprocal (denoted by the asterisk) space and  $a_0$  is the equivalent lattice constant of the higher-temperature cubic phase extrapolated to the same thermodynamic conditions for which  $a$  and  $c$  are measured.<sup>27</sup>

Near the crossover from a discontinuous to a continuous ferroelectric phase transition (i.e., a tricritical instability), the spontaneous strain is expected to vary with temperature as<sup>27</sup>

$$x \sim P^2 \sim |T - T_c|^{1/2}. \quad (6)$$

As demonstrated in Fig. 6, Eq. (6) could be approximately satisfied over the range of temperature studied by choosing  $T_c = 565$  K (plots of  $\ln x_3$  vs  $\ln |T - T_c|$  yielded a straight line with slope  $m = 0.52$ ). This result agreed well with the transition temperature expected based on dielectric measurements,<sup>12</sup> where it was found that the temperature of the permittivity maximum varied linearly with the lanthanum concentration as  $T_c(y) = T_c(0) - 1950y$ , with  $T_c(0) = 765$  K. Based on these observations, it appears that the macroscopic symmetry changes at 565 K and that the transition is close to tricritical.

Inspection of the x-ray diffraction profiles, however, gave some indication that the structure was not truly cubic even at much higher temperatures. This local nature of the structure was reflected in a temperature-dependent broadening of the x-ray diffraction profiles similar to that observed in the neutron experiments. The observed temperature variation of the FWHM is illustrated by the data for the 211 reflection, shown in Fig. 7. Although there was some scatter in the data, a strongly temperature-dependent component of profile

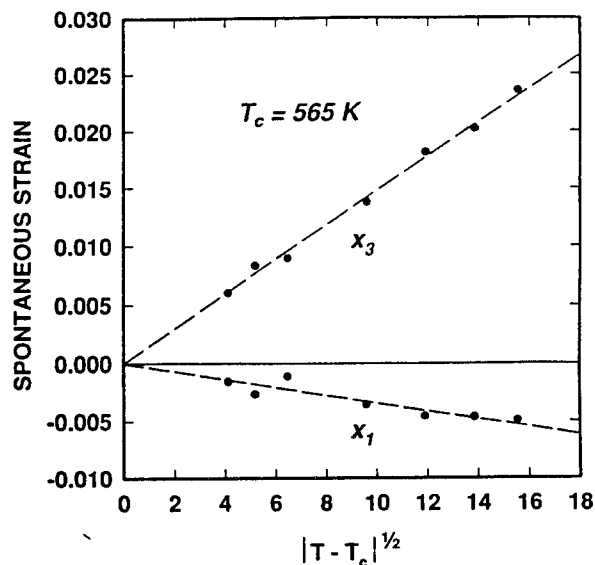


FIG. 6. Plot of the uniform spontaneous strain components ( $x_1$ ,  $x_3$ ) against  $|T - T_c|^{1/2}$  for  $[\text{Pb}_{0.85}\square_{0.05}\text{La}_{0.10}]\text{TiO}_3$ . The dashed lines represent the best linear least-squares fit of the data taking  $T_c = 565$  K and constraining the fit to pass through the origin.

broadening was evident below 565 K. The temperature dependence remained pronounced up to about 625 K, and there was some suggestion that a weaker temperature dependence may have persisted to as high as  $\approx 775$  K. Similar results were obtained in an independent experiment where the 100 reflection was examined, and in which the diffraction data were acquired in step scans and were collected at various

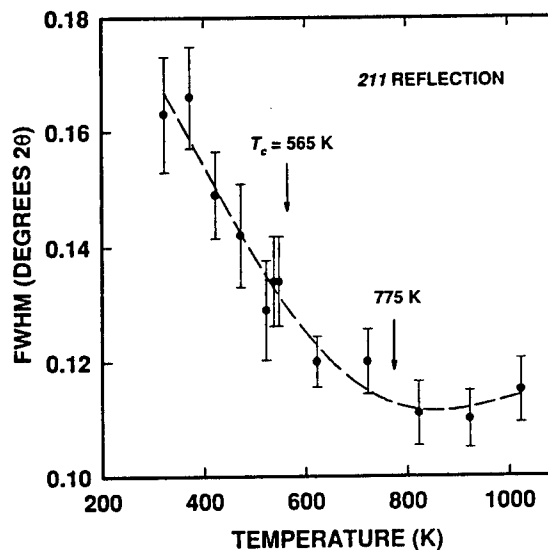


FIG. 7. Temperature variation of the FWHM of the 211 reflection for  $[\text{Pb}_{0.85}\square_{0.05}\text{La}_{0.10}]\text{TiO}_3$  determined by fitting the x-ray diffraction profiles to a pseudo-Voigt profile function. The dashed line is intended as a guide to the eye.

temperatures arrived at by random heating and cooling. It is believed that the broadening of the diffraction profiles reflects the local tetragonal distortion of the structure, and that this is responsible for the tail of the excess specific heat-temperature curve observed above the transition anomaly.

In summary, the results of powder neutron and x-ray diffraction and specific heat measurements at temperatures in the range of 10–1023 K support the notion that the origin of the diffuse ferroelectric transition in  $[\text{Pb}_{0.85}\square_{0.05}\text{La}_{0.10}]\text{TiO}_3$  is connected primarily with a spatial variation in the spontaneous polarization. Electrostrictive coupling to the local polarization produces a large nonuniform strain. The effective coupling between uniform strain and polarization is disrupted, causing the transition to appear more continuous as it becomes diffuse. Despite this, the oxygen octahedral framework is not severely distorted, and the relative displacements of the cations along the polar axis remain similar to those as observed for the host compound. At temperatures as low as 10 K, the structure retains its tetragonal symmetry.

As with the more strongly frequency dispersive lanthanum-modified lead zirconate-titanates,<sup>28–30</sup> the results of specific heat and x-ray line broadening measurements indicated that the temperature at which the local distortion of the structure first occurred was close to that of the Curie point of pure  $\text{PbTiO}_3$  ( $T_c \approx 765$  K). High resolution x-ray profile broadening experiments or optical birefringence measurements performed on dense ceramic samples would be required to confirm this behavior and to determine this temperature more precisely.

#### ACKNOWLEDGMENTS

This work was initiated at the Pennsylvania State University and was supported in part by contracts administered through the Office of Naval Research. Research carried out at Princeton University was supported by NSF Grant No. DMR 92-15802. The work has benefited from the use of facilities at the Manuel Lujan, Jr. Neutron Scattering Center, a national user facility funded as such by the Department of

Energy/Office of Basic Energy Sciences. One of us (G.A.R.) would like to thank Dr. Joyce Goldstone of the Los Alamos National Laboratory for her assistance with the experiments conducted using the neutron powder diffractometer.

- <sup>1</sup>G. A. Smolensky, *J. Phys. Soc. Jpn.* **28S**, 26 (1970).
- <sup>2</sup>L. Benguigui, *Solid State Commun.* **14**, 669 (1974).
- <sup>3</sup>K. Keizer and A. J. Burggraaf, *Phys. Status Solidi A* **26**, 561 (1974).
- <sup>4</sup>K. Keizer, G. J. Lansink, and A. J. Burggraaf, *J. Phys. Chem. Solids* **39**, 59 (1978).
- <sup>5</sup>D. Hennings and K. H. Härdtl, *Phys. Status Solidi A* **3**, 465 (1970).
- <sup>6</sup>D. Hennings, *Mater. Res. Bull.* **6**, 329 (1971).
- <sup>7</sup>D. Hennings and G. Rosenstein, *Mater. Res. Bull.* **7**, 1505 (1972).
- <sup>8</sup>K. Keizer, J. Bouwma, and A. J. Burggraaf, *Ferroelectrics* **7**, 341 (1974).
- <sup>9</sup>J. Bouwma, K. J. de Vries, and A. J. Burggraaf, *Phys. Status Solidi A* **35**, 281 (1976).
- <sup>10</sup>G. Burns and B. A. Scott, *Solid State Commun.* **13**, 417 (1973).
- <sup>11</sup>A. J. Burggraaf and K. Keizer, *Mater. Res. Bull.* **10**, 521 (1975).
- <sup>12</sup>K. Keizer and A. J. Burggraaf, *Ferroelectrics* **14**, 671 (1976).
- <sup>13</sup>M. Kuwabara, K. Goda, and K. Oshima, *Phys. Rev. B* **42**, 10012 (1990).
- <sup>14</sup>G. A. Rossetti, Jr., L. E. Cross, and J. P. Cline, *J. Mater. Sci.* (to be published).
- <sup>15</sup>D. A. Ditmars and T. B. Douglas, *J. Res. Natl. Bur. Stand.* **75A**, 401 (1971).
- <sup>16</sup>A. C. Larsen and R. B. Von Dreele, Los Alamos National Laboratory Report LA-UR-748, 1994.
- <sup>17</sup>R. J. Nelmes, R. O. Piltz, W. F. Kuhs, Z. Tun, and R. Restori, *Ferroelectrics* **108**, 165 (1990).
- <sup>18</sup>A. M. Glazer and S. A. Mabud, *Acta Crystallogr. Sect. B* **34**, 1065 (1978).
- <sup>19</sup>M. J. Haun, E. Furman, S. J. Jang, H. A. McKinstry, and L. E. Cross, *J. Appl. Phys.* **62**, 3331 (1987).
- <sup>20</sup>S. C. Abrahams, S. K. Kurtz, and P. B. Jamieson, *Phys. Rev.* **172**, 551 (1968).
- <sup>21</sup>G. Shirane, R. Pepinsky, and B. C. Frazer, *Acta Crystallogr.* **9**, 13 (1956).
- <sup>22</sup>L. Benguigui, *Phys. Status Solidi B* **60**, 835 (1973).
- <sup>23</sup>G. A. Rossetti, Jr., *Ferroelectrics* **133**, 103 (1992).
- <sup>24</sup>K. Wojcik, *Ferroelectrics* **99**, 5 (1989).
- <sup>25</sup>C. N. W. Darlington and R. J. Cernik, *J. Phys.: Condens. Matter* **3**, 4555 (1991).
- <sup>26</sup>C. N. W. Darlington and R. J. Cernik, *J. Phys.: Condens. Matter* **4**, 4387 (1992).
- <sup>27</sup>E. K. H. Salje, *Acta Crystallogr. Sect. A* **47**, 453 (1991).
- <sup>28</sup>G. Burns and F. H. Dacol, *Phys. Rev. B* **28**, 2527 (1983).
- <sup>29</sup>C. N. W. Darlington, *Phys. Status Solidi A* **113**, 63 (1989).
- <sup>30</sup>G. A. Rossetti, Jr., T. Nishimura, and L. E. Cross, *J. Appl. Phys.* **70**, 1630 (1991).

# APPENDIX 11

# Direct evaluation of domain-wall and intrinsic contributions to the dielectric and piezoelectric response and their temperature dependence on lead zirconate-titanate ceramics

Q. M. Zhang, H. Wang, N. Kim, and L. E. Cross

Materials Research Laboratory, The Pennsylvania State University, University Park, Pennsylvania 16802

(Received 12 July 1993; accepted for publication 17 September 1993)

By making use of the fact that domain-wall motions do not produce volumetric changes, an experimental method is introduced to directly and quantitatively determine the domain-wall and intrinsic contributions to the piezoelectric and dielectric responses of a ferroelectric material. Utilizing this method, the contributions from the domain walls and intrinsic part as well as their temperature dependence for lead zirconate-titanate (PZT) 52/48 and PZT-500 ceramics are evaluated. The data show that at temperatures below 300 K, the large change in the dielectric and piezoelectric constants with temperature is due to the change in the domain-wall activities in the materials. The results confirm that most of the dielectric and piezoelectric responses at room temperature for the materials studied is from the domain-wall contributions. The data also indicate that in PZT-500, both 180° wall and non-180° walls are possibly active under a weak external driving field.

## I. INTRODUCTION

For most ferroelectric materials, the existence of domain structures or domain walls makes a significant influence on the material properties. For example, in lead zirconate-titanate (PZT) solid solution system, the material properties can be modified over a wide range by using different dopants or by different processing conditions.<sup>1</sup> Such changes in the material properties are believed to be the result of changes in the domain-wall response in the materials.<sup>2,3</sup> From the Landau-Devonshire phenomenological theory, it has been proposed that for PZT at compositions near the morphotropic phase boundary, the domain-wall contribution accounts for more than half of the room-temperature dielectric and piezoelectric responses.<sup>4</sup>

In the literature, the material properties from a single-domain material are denoted as the intrinsic properties (or volume contribution) of the material, while the contributions from the other parts of the material, mainly from domain walls, are lumped as extrinsic properties of the material. Under this convention, the dielectric constant  $\epsilon$ , piezoelectric constant  $d$ , and elastic compliance  $s$ , can be written as a summation of two terms,<sup>5</sup>

$$\begin{aligned}\epsilon &= \epsilon_{\text{ex}} + \epsilon_{\text{in}}, \\ d &= d_{\text{ex}} + d_{\text{in}}, \\ s &= s_{\text{ex}} + s_{\text{in}},\end{aligned}\tag{1}$$

where the subscripts ex and in denote the extrinsic and intrinsic contributions, respectively.

To understand how domain structures and domain-wall motions are influenced by different processing conditions and dopants so that the material properties can be better tailored, one needs to quantitatively describe the changes of  $\epsilon_{\text{ex}}$ ,  $\epsilon_{\text{in}}$ ,  $d_{\text{ex}}$ ,  $d_{\text{in}}$ ,  $s_{\text{ex}}$ ,  $s_{\text{in}}$  with the processing conditions and dopants. That is, to distinguish the intrinsic

and extrinsic contributions from the experimental data which usually contain both parts. Currently, two methods are commonly used in separating the extrinsic properties and intrinsic properties in ceramics: One is based on the frequency dispersion characteristics of the dielectric constant and the other is based on the properties measured at near 0 K temperature.<sup>3,6-8</sup> Since dielectric dispersion only describes the dielectric property of a material, it cannot provide information on the piezoelectric responses from different parts and the difference between 180° domain-wall response and non-180° domain-wall response. While the results derived from the second method are only related to the material properties at near 0 K and may not be directly related to the material properties at higher temperatures.

In this article, we introduce a new experimental methodology which can directly and quantitatively determine the domain-wall and intrinsic contributions to the material properties and their temperature dependence. Using this method, the piezoelectric and dielectric responses from both the intrinsic and domain-wall contributions were investigated for both doped and pure PZT ceramics near the morphotropic phase boundary in the temperature range from 10 to 300 K. The basic principle of this method is that in contrast to the intrinsic response where any polarization change will be accompanied by a change in the unit-cell volume, the polarization change induced by domain-wall motion will not cause volume changes. As a consequence, the domain-wall motion will not contribute to the hydrostatic response of a material and the change in the piezoelectric hydrostatic coefficient  $d_h$  will not be related to the response from domain walls; therefore,  $d_h$  provides a very sensitive means to separate the intrinsic and extrinsic material responses. By combining these results with the data measured near 0 K, we can get the temperature dependence of the extrinsic response and intrinsic response of

tric and piezoelectric responses, one is able to gain information on the change of domain-wall responses of 180° type and non-180° type as the processing conditions or dopants are varied.

## II. EXPERIMENTS

The piezoelectric constants  $d_{33}$  and  $d_{31}$ , dielectric constant  $\epsilon_{33}$ , and remanent polarization  $P_r$  were characterized for pure PZT at the composition near the morphotropic phase boundary (PZT 52/48), and a soft PZT in the temperature range from 10 to 300 K. The PZT 52/48 ceramic samples were made through the standard solid-state processing.<sup>9</sup> The samples were poled at an electric field of 50 kV/cm and a temperature of 375 K for 5 min. All the samples were aged for more than 1 week at room temperature before any measurement. The soft PZT ceramic samples (PZT-500) were purchased from Piezo Kinetics, Inc. (Bellefonte, PA 16823) and were poled by the manufacturer.

The piezoelectric constants  $d_{33}$  and  $d_{31}$  were acquired through the resonance technique using a IIP impedance analyzer (IIP 4194A) for bar-shaped samples and the resonance frequencies were around 150 kHz. These constants were also measured at room temperature by a laser dilatometer.<sup>10</sup> The results from the two measurements were in good agreement. The temperature regulation for the resonance experiment was provided by a helium closed-cycle refrigerator (APD Cryogenics, Model IIC-2).

The dielectric constant measurement was carried out using a IIP multifrequency RLC meter (HP 4274A) and the temperature dependence of the remanent polarization  $P_r$  was obtained by combining the data acquired using the Byer-Roundy technique and from polarization hysteresis loop measurements. Since the ferroelectric-paraelectric transition temperature (Curie temperature) for these samples is far above the upper operation temperature for the setup which is at 500 K, the Byer-Roundy technique cannot provide the absolute value of the remanent polarization of the samples. To establish the absolute scale of the remanent polarization, the polarization hysteresis loop was measured at room temperature using a modified Sawyer-Tower circuit. A homemade temperature chamber was used to regulate the temperature for the polarization measurement. The temperature range of the measurement was from 100 to 470 K for PZT-500 and 100 to 340 K for PZT 52/48. In all experiments, the sample thickness was about 1 mm and the sample area was about  $5 \times 5 \text{ mm}^2$ . The electrodes were made by sputtering gold on both surfaces of the samples.

## III. RESULTS AND DISCUSSION

### A. Temperature dependence of the piezoelectric constants

Shown in Figs. 1(a) and 1(b) is the temperature dependence of the piezoelectric constants  $d_{33}$  and  $d_{31}$  for PZT 52/48 and PZT-500 samples, respectively. For PZT 52/48,

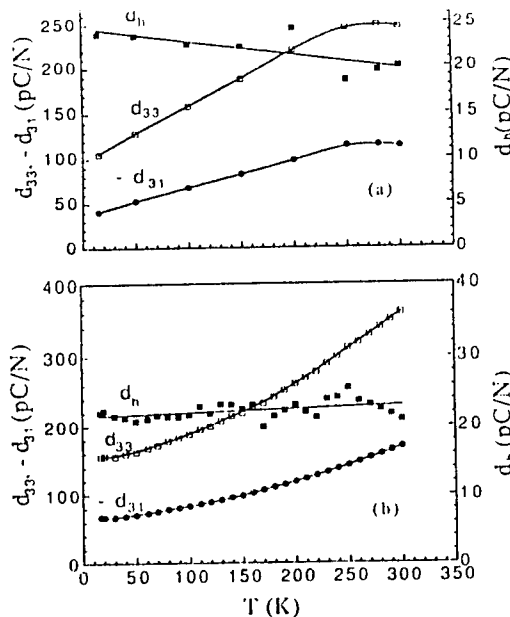


FIG. 1. The temperature dependence of piezoelectric constants  $d_{33}$ ,  $d_{31}$ , and  $d_h$  for (a) PZT 52/48 and (b) PZT-500 ceramics.

as the temperature increases from 10 K to room temperature (300 K),  $d_{33}$  increases about two and a half times (from about 105 to 245 pC/N). In the same temperature range,  $-d_{31}$  has about a threefold increase (from about 40 to 114 pC/N). From the relation  $d_h = d_{33} + 2d_{31}$ ,  $d_h$  can be determined in the same temperature range and clearly, unlike  $d_{33}$  and  $d_{31}$ ,  $d_h$  does not increase with temperature. Instead, from low temperature to room temperature,  $d_h$  exhibits a slight decrease from about 24 to 20 pC/N, which is shown in Fig. 1(a). The data for  $d_h$  in Fig. 1(a) also shows larger scattering than those of  $d_{33}$  and  $d_{31}$ . This is understandable since both  $d_{33}$  and  $d_{31}$  are much larger than  $d_h$ , any small data scattering in  $d_{33}$  and  $d_{31}$  will induce a relative large scattering in  $d_h$  when it is obtained by the difference between  $d_{31}$  and  $d_{33}$ . In spite of that, the data clearly shows that  $d_h$  has a much smaller temperature variation compared with both  $d_{33}$  and  $d_{31}$ .

Similarly, for PZT-500, in the temperature range from 15 K to room temperature,  $d_{33}$  increases from about 132 to 360 pC/N and  $-d_{31}$  from 54 to 170 pC/N, while  $d_h$  stays almost a constant around 23 pC/N in the same temperature range, as shown in Fig. 2. By relating this behavior to the discussions above, one can immediately draw the conclusion that in both pure and doped PZT ceramics, the large change in the piezoelectric activity ( $d_{33}$  and  $d_{31}$ ) in this temperature range is caused by the extrinsic contribution, most likely by the non-180° domain-wall motions.

### B. Temperature dependence of the dielectric constant and remanent polarization

In Fig. 2, the temperature dependence of  $\epsilon_{33}$  for both PZT 52/48 and PZT-500 is plotted from 15 to 300 K. For

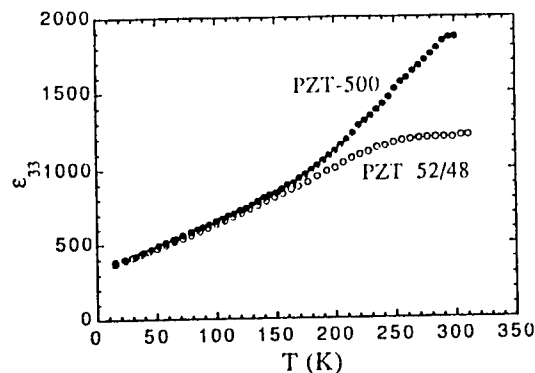


FIG. 2. The dielectric constant  $\epsilon_{33}$  for PZT-500 (●) and PZT 52/48 (○) poled samples measured at 1 kHz.

PZT 52/48, except for a broad anomaly at a temperature near 260 K,  $\epsilon_{33}$  shows a large increase, from about 370 at 15 K to near 1200 at room temperature, which is a more than threefold increase. For PZT-500,  $\epsilon_{33}$  is 375 at 15 K and increases to 1800 at room temperature. Therefore, the dielectric constants of the two PZT materials are almost the same at temperatures near 0 K. This is consistent with an earlier experimental result in which all the dielectric constants measured from PZTs with different dopants converged to a common value as the temperature approached to 0 K.<sup>3</sup> In contrast, at a temperature near 0 K, the piezoelectric constants for the two materials are not the same, which is probably caused by different degree of poling and different distribution of polarization about the poling direction in the materials. As is shown later, the remanent polarization of PZT-500 is higher than that of PZT 52/48. Apparently, dopants in PZT-500 facilitate the domain-wall movement and increase the degree of poling.

The piezoelectric response in a single-domain material can be viewed as polarization-biased electrostriction. Hence, the intrinsic piezoelectric and dielectric response are related through the electrostrictive coefficient  $Q_{ij}$  and the remanent polarization  $P_r$ ,<sup>11</sup>

$$d_{33} = 2\epsilon_{33}\epsilon_0 Q_{11} P_r, \quad (2a)$$

$$d_{31} = 2\epsilon_{33}\epsilon_0 Q_{12} P_r, \quad (2b)$$

and

$$d_h = 2\epsilon_{33}\epsilon_0 Q_h P_r, \quad (2c)$$

where  $\epsilon_0$  is the vacuum permittivity. These relations are derived from single-domain materials and should be valid for ceramics where the quantities in Eq. (2) are the averaged ones. Although the piezoelectric constants  $d_{ij}$  vary widely as the composition or temperature changes, the polarization-related electrostrictive coefficients  $Q_{ij}$  hardly change with composition and temperature in PZT ceramics.<sup>4</sup> Therefore, once the temperature dependence of  $P_r$  is determined, the temperature dependence of the intrinsic dielectric response can be evaluated through Eq. (2c). Similarly,  $d_{33}$  and  $d_{31}$  from the intrinsic contribution can also be determined from Eqs. (2a) and (2b).

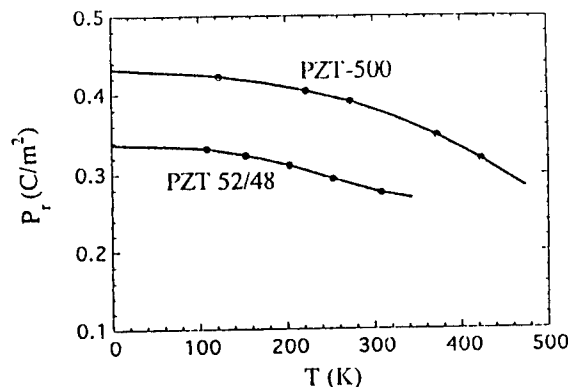


FIG. 3. The remanent polarization for PZT-500 and PZT 52/48 as a function of temperature. The curves at temperatures below 100 K are calculated from the fitting to the higher-temperature data.

For the two PZTs, the remanent polarization  $P_r$  as a function of temperature is shown in Fig. 3. Since the lowest temperature measured for the  $P_r$  was at 100 K, the data were fitted using a polynomial and the low-temperature (0 K)  $P_r$  was extrapolated from the fitting. As can be seen from Fig. 3, the  $P_r$  is a smooth function of temperature and from the theoretical consideration, one does not expect any irregular changes in  $P_r$  as the temperature is lowered, which justifies the extrapolation.<sup>4,11</sup> At temperatures near and above room temperature, there is a small irregular change in the  $P_r$  for PZT 52/48. This is likely caused by the internal stress field in the material, which increasingly realigns the domain as the temperature is raised. Hence, for PZT 52/48 the higher-temperature data are not plotted here.

### C. Discussion

From the results presented in Secs. III A, and III B, the temperature dependence of the piezoelectric and dielectric constants from both the intrinsic and domain-wall contributions can be determined. Assuming at 0 K,  $d_{ij}$  and  $\epsilon_{33}$  are from the intrinsic contribution,  $Q_{11}$ ,  $Q_{12}$  and  $Q_h$  for the PZT ceramics are calculated using Eq. (2), and the results (listed in Table I) are close to those of an earlier experimental result.<sup>4</sup> In the calculation, the data of  $d_{ij}$  and  $\epsilon_{33}$  at 0 K are extrapolated from the higher-temperature data and are very close to those measured at 15 K. Making use of Eq. (2), the temperature dependence of the dielectric constant  $\epsilon_{33}$  and piezoelectric constants  $d_{33}$  and  $d_{31}$  from the intrinsic contribution are calculated and they are shown in Figs. 4 and 5 for the dielectric constant and the piezoelectric constants, respectively. In all these calculations we as-

TABLE I. The electrostrictive coefficients for PZT-500 and PZT 52/48 ceramics used in this experiment.

	$Q_h$ ( $\text{m}^4\text{C}^{-2}$ )	$Q_{11}$ ( $\text{m}^4\text{C}^{-2}$ )	$Q_{12}$ ( $\text{m}^4\text{C}^{-2}$ )
PZT-500	0.0091	0.0505	-0.0207
PZT 52/48	0.012	0.046	-0.017

Zhang et al.

pendent of temperature. Clearly, in the temperature range studied, there is very little increase in the intrinsic dielectric activity. For PZT 52/48, it stays at about 350 in this temperature range and for PZT-500, it increases slightly with temperature from 350 at 0 K to 430 at 300 K. This is consistent with the experimental results from Bottger and Arlt<sup>7</sup> and from Kersten and Schmidt<sup>6</sup> on PZT ceramics, in which the low-frequency dielectric constant  $\epsilon_{33}$  showed a large change with temperature, while at frequencies above the dielectric relaxation peak (near 1 GHz)  $\epsilon_{33}$  was nearly a constant of about 400 at temperatures below 300 K for PZT 52/48. Since the dielectric relaxation at frequency near 1 GHz is believed to be due to the relaxation from domain walls, at frequencies above that one expects that the domain-wall contribution will die out and the major contribution to the dielectric response will only be the intrinsic part. In addition,  $\epsilon_{33}$  value of about 400 is almost the same as what we observed here at temperatures near 0 K. Therefore, in spite of different techniques used, the two sets of measurements yield almost the identical results. Besides that, the dielectric constants measured from single-crystal samples of PZT also stayed almost constant at low temperatures.<sup>12</sup>

The results presented here provide direct evidence that at room temperature, domain walls make major contributions to the dielectric and piezoelectric responses of PZT materials. This is consistent with the theoretical prediction using Landau-Devonshire theory.<sup>4</sup> At room temperature the intrinsic dielectric and piezoelectric contributions are less than 25% and about 37% of the total responses for PZT-500, and 30% and  $\frac{1}{3}$  for PZT 52/48.

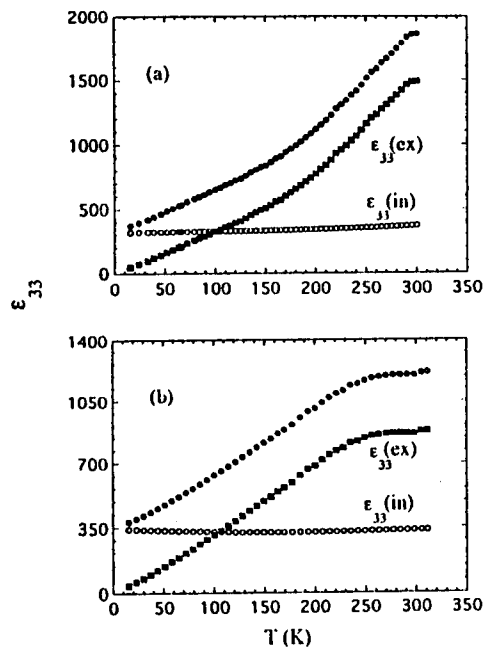


FIG. 4. The calculated intrinsic (○) and extrinsic (■) dielectric constant for (a) PZT-500 and (b) PZT 52/48. For the comparison, the total dielectric constant (●) measured is also presented.

wall and non-180° wall. A major difference between these two groups of walls is that 180° walls are not ferroelastic active, while non-180° walls are ferroelastic active. As a result, 180° wall motion will affect only the dielectric property and non-180° wall will affect both dielectric and piezoelectric properties. Hence, when one discusses domain-wall contributions to the material responses, it is important to know which kind of wall is active under weak driving field because by enhancing only the non-180° wall activity one can greatly improve the electromechanical coupling factor of the material, and on the other hand, by enhancing only the 180° wall activity, the dielectric response of the material can be improved significantly without introducing large dielectric losses, which are mostly caused by non-180° wall motions.<sup>13</sup> Currently, it seems to be widely believed that for PZT and other ferroelectrics with perovskite structure, under weak external driving fields, the major part of the domain-wall response is from non-180° walls and 180° walls are almost idle. The reason is that 180° wall width is much narrower (probably on the order of one unit cell) in comparison with non-180° walls,<sup>14,15</sup> which implies that there is a much steeper potential well for 180° walls; therefore, a weak external field may not be able to induce substantial changes in the 180° wall structure. Experimentally, there was no direct evidence to prove or disprove this; however, the results presented here may not be consistent with the idea that 180° walls in PZT ceramics are idle. From the results presented above, at room temperature, the extrinsic contribution to the dielectric constant is larger than that to the piezoelectric constant for PZT-500, while

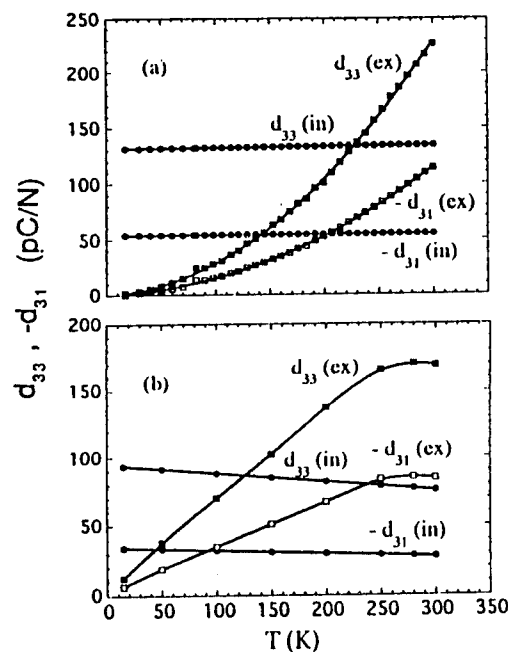


FIG. 5. The calculated intrinsic and extrinsic piezoelectric constants for (a) PZT-500, and (b) PZT 52/48: open circles are intrinsic  $d_{31}$ , solid circles intrinsic  $d_{33}$ , open squares extrinsic  $d_{31}$ , and solid squares extrinsic  $d_{33}$ .

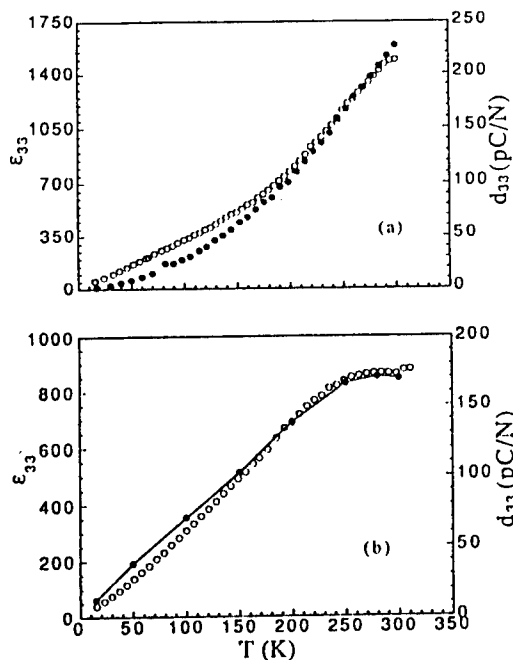


FIG. 6. The calculated extrinsic piezoelectric and dielectric constants for (a) PZT-500 and (b) PZT 52/48; solid circles are extrinsic  $d_{33}$ , open circles extrinsic  $\epsilon_{33}$ .

for PZT 52/48 they are almost the same (the ratio  $d_{33}^{\text{ex}}/d_{33}$  and  $\epsilon_{33}^{\text{ex}}/\epsilon_{33}$ ). That is, increased domain-wall activities in PZT-500 raise the dielectric constant more than the piezoelectric constant. The large increase in  $d_{\text{ex}}$  is apparently due to the increased activity in non-180° walls in PZT-500; however, the disproportionate increase in  $\epsilon_{\text{ex}}$  may reflect the fact that there are substantial increases in the 180° wall activity, too. In addition, as illustrated in Fig. 6, the extrinsic piezoelectric and dielectric contributions show a similar temperature dependence for both PZT-500 and PZT 52/48; however the ratio of  $d_{\text{ex}}$  to  $\epsilon_{\text{ex}}$  ( $d_{\text{ex}}/\epsilon_{\text{ex}}$ ) for the two materials is quite different. At room temperature, this ratio is 0.2 pC/N for PZT 52/48 and less than 0.15 pC/N for PZT-500. In other words, on average, corresponding to the same polarization change, the domain-wall motions will produce much less piezoelectric response in PZT-500 than in PZT 52/48 even though the poling level in PZT-500 is higher. From the analysis by Haun,<sup>4</sup> Arlt, Dederichs, and Herbiet,<sup>16</sup> Zhang *et al.*<sup>17</sup> and the earlier experimental results, which showed that as the poling level increases this ratio should increase if there are only non-180° domain walls active, the phenomenon observed here strongly suggests that there is a substantial increase in 180° wall activity in PZT-500, which raises the dielectric constant of the material while keeping the piezoelectric constant unchanged; therefore, both the non-180° wall and 180° wall should be active in PZT-500.

We would like to emphasize that the notion introduced here that the domain-wall motions do not contribute to the volume change may not be applicable when the wall motions are related to the polarization switch, which may introduce significant local stress and result in some volume change. This kind of volume change may provide informa-

tion on the local stress distribution and themselves deserve detailed studies. In addition, for ceramic materials, there exist pores which could change the local stress pattern and cause volume changes as the wall moves. However, for well-fabricated materials, this probability is very small and should not significantly alter the conclusions presented in this article. The consistency between the results here and earlier experimental results confirms this point.

#### IV. SUMMARY

In this article, we presented a new experimental method, based on the notion that domain-wall motions induced by weak external fields will not contribute to the hydrostatic piezoelectric response, to directly evaluate the intrinsic and domain-wall contributions in a piezoelectric ceramic sample. Using this method, the domain-wall and intrinsic contributions to the piezoelectric and dielectric responses and their temperature dependence for PZT 52/48 and PZT-500 ceramics are evaluated directly and quantitatively. The data show that at temperatures below 300 K the large change in the dielectric and piezoelectric properties with temperature is from the domain-wall contribution. The results confirm that most of dielectric and piezoelectric responses at room temperature for the materials studied are from the domain-wall contributions. The data also show that in PZT-500, both 180° wall and non-180° wall are most likely active under weak external driving fields.

The experimental methods presented in this article can be extended to a wide range of materials and to a wide temperature range to study how various external parameters change the extrinsic and intrinsic contributions and their temperature-dependence behavior. In combination with the analysis similar to that employed by Arlt and co-workers<sup>16</sup> and the information of the polarization distribution in a material, one can quantitatively determine how the 180° wall and non-180° wall activities change as one varies various conditions.

#### ACKNOWLEDGMENTS

The authors wish to thank Dr. R. E. Newnham, Dr. C. A. Randall, and Dr. Wenwu Cao for critical reading of the manuscript and suggestions concerning this article. This work was supported by the Office of Naval Research.

<sup>1</sup>B. Jaffe, W. J. Cook, and H. Jaffe, *Piezoelectric Ceramics* (Academic, London, 1971).

<sup>2</sup>G. Arlt, *Ferroelectrics* 104, 217 (1990).

<sup>3</sup>X. L. Zhang, Z. X. Chen, L. E. Cross, and W. A. Schulze, *J. Mater. Sci.* 18, 968 (1983).

<sup>4</sup>M. J. Haun, Ph.D. thesis, The Pennsylvania State University, 1988.

<sup>5</sup>R. Herbiet, U. Robels, H. Dederichs, and G. Arlt, *Ferroelectrics* 98, 107 (1989).

<sup>6</sup>O. Kersten and G. Schmidt, *Ferroelectrics* 67, 191 (1986).

<sup>7</sup>U. Bottger and G. Arlt, *Ferroelectrics* 127, 95 (1992).

<sup>8</sup>W. Kleemann and H. Schremmer, *Phys. Rev. B* 40, 7428 (1989).



- \*Namchul Kim, Ph.D. thesis, The Pennsylvania State University, 1993.
- <sup>10</sup>Q. M. Zhang, S. J. Jang, and L. E. Cross, J. Appl. Phys. **65**, 2807 (1989).
- <sup>11</sup>A. F. Devonshire, Philos. Mag. **42** 1065 (1951).
- <sup>12</sup>K. Tsuzuki, K. Sakata, and M. Wada, Ferroelectrics **8**, 501 (1974).
- <sup>13</sup>G. Arlt and H. Dederichs, Ferroelectrics **29**, 47 (1980).
- <sup>14</sup>F. Jona and G. Shirane, *Ferroelectric Crystals* (Dover, New York, 1993).
- <sup>15</sup>Wenwu Cao and L. E. Cross, Phys. Rev. B **44**, 5 (1991).
- <sup>16</sup>G. Arlt, H. Dederichs, and R. Herbiel, Ferroelectrics **74**, 37 (1987).
- <sup>17</sup>Q. M. Zhang, W. Y. Pan, S. J. Jang, and L. E. Cross, J. Appl. Phys. **64**, 6445 (1988).

# APPENDIX 12

# 90° domain reversal in $\text{Pb}(\text{Zr}_x\text{Ti}_{1-x})\text{O}_3$ ceramics

SHAOPING LI\*, A. S. BHALLA, R. E. NEWNHAM, L. E. CROSS

*Materials Research Laboratory, The Pennsylvania State University, University Park, PA 16802, USA*

CHI-YUEN HUANG

*Department of Mineral Engineering, National Cheng Kung University, Tainan, Taiwan 70101*

A simple and direct method has been proposed, which may be used for quantitatively distinguishing the mechanisms of domain reorientation processes in polycrystalline materials. Using this method, the 90° domain reorientation in the  $\text{Pb}(\text{Zr}_x\text{Ti}_{1-x})\text{O}_3$  ceramic under an electric field was examined through the X-ray diffraction analysis. It was found that polarization switching in the PZT ceramic with a composition near the morphotropic phase boundary, is predominantly controlled by the two successive 90° domain processes rather than only the 180° domain reversal process. Experimental results also indicate that the coercive field of ferroelectric ceramics is related to the cooperative deformation associated with each grain. This cooperative deformation arises from the 90° domain-reversal process.

## 1. Introduction

The interrelationship between the dynamic behaviour and the microstructures (intrinsic domain structures) of ferroelectric ceramics is of great significance. The investigation of polarization reversal in ferroelectric ceramics is of both theoretical and practical interest. Recently, much effort has been directed into developing polycrystalline ferroelectric thin films as non-volatile memory devices using the capability of switching the direction of remnant polarization under the influence of an electric impulse. In fact, the polarization reorientation processes are intimately associated with the basic dynamic memory capability and the switching threshold of polycrystalline thin-film memory devices, as well as the basic fatigue and degradation behaviour of thin-film devices. With regard to this, the mechanisms of the domain reversals in PZT polycrystalline systems have a special and important aspect.

Early investigations of the dynamic behaviour of 90°-type domain walls (90° in tetragonal, 71° and 109° in the rhombohedral phase) and 180° domain walls in PZT ceramics have been carried out over the last three decades [1-7]. Based on the bias-dependence measurements of dielectric constants, polarization, and spontaneous strain in certain PLZT ceramic systems, it has been suggested that the processes of polarization reversal may be characterized by two successive 90°-type domain processes rather than by the direct 180° domain switching processes. Apparently, all previous research results seemed to be adequate; however, they are by no means quantitatively conclusive, because no direct experimental methods could distinguish the mechanisms of the polarization reversal processes in the polycrystalline materials. In gen-

eral, the mechanism of polarization reversal processes in single crystals is explained by the nucleation and growth of new antiparallel domains. Ferroelectric ceramics consist of many randomly orientated grains. Therefore, the polarization reversal mechanism and switching behaviour in ferroelectric polycrystalline material is rather complicated and depends upon many conditions [8]. Usually, the polarization reversal processes in ferroelectric polycrystalline materials are substantially different from those in single crystals. In this work, a simple and direct method has been proposed, which can be used for quantitatively distinguishing the mechanisms of domain reorientation processes in polycrystalline materials. It has been directly confirmed that the polarization switching processes in PZT ceramic with the composition within the morphotropic phase boundary is predominantly dependent upon two successive 90° domain reversal processes.

## 2. Experimental procedure

The specimens used here are of chemical composition  $\text{Pb}(\text{Zr}_{0.52}\text{Ti}_{0.48})\text{O}_3 + 0.5 \text{ wt } \% \text{ Nb}_2\text{O}_5$ , which is within the morphotropic phase boundary. The ceramics were prepared by the conventional mixed-oxide process. The final sintering temperature is 1180-1250°C for 2-3 h. The scanning electron micrographs (Fig. 1) show the average grain size of the ceramic to be 3-3.5 µm. The domain structures can be clearly observed through the environmental scanning electron microscope without coating the samples [8]. Samples were cut in the dimensions 8 mm × 8 mm × 0.5-0.8 mm, and electroded with gold

\* Present address: 115 Sachem Village, West Lebanon, NH 03784, USA.

ited silver electrodes were used on the faces exposed to the X-rays in order to reduce the extra diffraction of the electrodes. Before making silver electrodes, the surfaces of the samples were polished and etched. X-ray diffraction measurements were performed on an automatic X-ray diffractometer using  $\text{CuK}_\alpha$  radiation ( $\lambda = 1.5418 \text{ nm}$ ). The experimental data were processed with the software developed by the Materials Research Laboratory at Pennsylvania State. The X-ray patterns were recorded at a scan rate of  $2\theta = 0.3^\circ \text{ min}^{-1}$ . The low scanning rate was chosen in order to enhance the intensity of the diffraction. The ceramic specimens were initially poled in two different ways in accordance with the sample shape, as shown in Fig. 2. The depth of X-ray penetration in this PZT system is estimated to be  $1\text{--}2 \mu\text{m}$ .

### 3. Results and discussions

#### 3.1. Principle of X-ray analysis

It is well known that PZT ceramics contain many  $90^\circ$  and  $180^\circ$  domains. The electric field will force them to

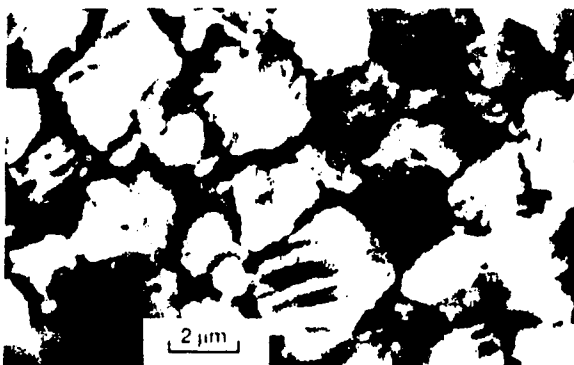


Figure 1 Scanning electron micrograph of PZT ceramic with composition near the morphotropic phase boundary.

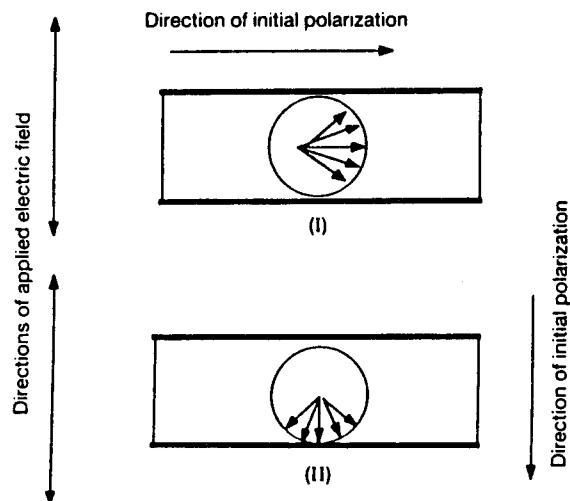


Figure 2 Shape and initial polarization orientation of specimens for two different cases: (a) the initial direction of remnant polarization parallel to the surface of the plate sample; (b) the initial direction of remnant polarization perpendicular to the surface of the plate sample.

of  $180^\circ$  domains during the polarization process could not be detected by the X-ray diffraction method. Therefore, it is believed that the change of ratio  $I_{(002)}/I_{(200)}$  is caused by the switching of the  $90^\circ$  domain alone [9, 10]. In general, the intensity of any  $(h, k, l)$  reflection, relative to that from a random specimen, is proportional to the volume fraction of domains having their  $(h, k, l)$  planes parallel to the plate surface. Regarding this study, the intensity of the  $I_{(002)}$  reflection is proportional to the volume fraction of the domain having the polarization direction parallel to the normal of the surface of plate specimens. Based on the general principle of X-ray diffraction, the diffractive intensity,  $I(h, k, l)$ , for the  $(h, k, l)$  plane can be usually expressed by [10]

$$I_{(hkl)} = CAI_0L|F_{(hkl)}|^2 N_{(hkl)} \rho_{(hkl)} \quad (1a)$$

where  $I_0$  is the incident X-ray diffraction,  $L$  the Lorentz angle factor,  $F_{(hkl)}$  a structure factor for the  $(h, k, l)$  plane,  $N_{(hkl)}$ , the multiplicity factor,  $A$  the absorption factor, and  $C$  is known as measuring system constant. Once the measuring conditions and specimens are defined,  $C$  can be calculated.  $\rho_{(hkl)}$  is the crystal plane orientation density which is defined as the volume fraction of the crystal grains with  $(h, k, l)$  plane parallel to specimen surface.

Obviously, for a specimen with the preferred orientation of the  $(h, k, l)$  plane, its  $\rho_{(hkl)}$  should be constant and can be taken as 1, therefore, one has

$$I_{p(hkl)} = CAI_0L|F_{(hkl)}|^2 N_{(hkl)} \quad (1b)$$

From the definition of diffraction intensity, it easily follows that the diffraction intensity for the  $(h, k, l)$  planes should be proportional to the volume fraction of domains (both  $90^\circ$  and  $180^\circ$  domains) in which the  $(h, k, l)$  planes are parallel to the surface of the plate specimens. Because there may be two possible kinds of domain reversal processes during the polarization switching, the measured  $I_{(002)}$  and  $I_{(200)}$  should contain the contributions of the planes  $(002)$  and  $(200)$  within both  $90^\circ$  reversal domains and  $180^\circ$  reversal domains, respectively, that is

$$I_{(002)} = n_1[90^\circ]I_{p(002)} + n_2[180^\circ]I_{p(002)} \quad (2)$$

$$I_{(200)} = g_1[90^\circ]I_{p(200)} + g_2[180^\circ]I_{p(200)} \quad (3)$$

and

$$n_1 + n_2 + g_1 + g_2 = 1$$

Here,  $n_1$  and  $n_2$  are the  $90^\circ$  and  $180^\circ$  domain volume fractions, respectively, which have the  $(002)$  plane parallel to the surface of the plate specimens.  $g_1$  and  $g_2$  are the  $90^\circ$  and  $180^\circ$  domain volume fractions, respectively, which have the  $(200)$  plane parallel to the surface of the plate specimens. It should be noted that  $n_1$  and  $g_1$  are functions of the applied electric field, whereas  $n_2$  and  $g_2$  are always constants during domain reversal processes because the reversal of  $180^\circ$  domains could not be detected by the X-ray diffraction method. The domain volume ratio between the domains with the polarization direction perpendicular

to the surface and those having the direction of their polarizations parallel to the surface of the plate specimen could be expressed as

$$R' = K \frac{I_{(0\ 0\ 2)}}{I_{(2\ 0\ 0)}} \quad (4)$$

where,  $K$  is a special coefficient. Because the change in diffraction intensities is only caused by  $90^\circ$  domains, the X-ray intensities of  $I_{(0\ 0\ 2)}/I_{(2\ 0\ 0)}$  under the influence of the electric field could represent the characteristics of  $90^\circ$  domain reversal. The changing rate of  $I_{(0\ 0\ 2)}/I_{(2\ 0\ 0)}$  may reveal some information about the mechanism of the domain reorientations. In the following, we shall discuss two different cases of polarization reorientation to distinguish the polarization reorientation processes between  $90^\circ$  domain reversal and  $180^\circ$  domain reversal processes. It should be noted that, in reality, the domains can never be perfectly aligned. The distribution of polarization directions always obey the certain axial distribution, as shown in Fig. 3. The  $I_{(0\ 0\ 2)}$  and  $I_{(2\ 0\ 0)}$  are measured by their average values.

### 3.1.1. Case 1

For case I of Fig. 2, the initial directions of polarization in most domains are parallel to the surface of the plate specimen. If an electric field is applied to the direction normal to the surface of the plate specimen, the polarization reversal process will be expected to be following the model in Fig. 3. As the applied electric field increases, the direction of polarization will gradually be changed. With a sufficiently strong electric field, the polarization directions in the ceramic will change their distribution direction. Eventually, all polarization directions will be lined up nearly parallel to the plus direction shown at point C via the  $90^\circ$  domain wall reversal process. The intriguing feature is that in this process only  $90^\circ$  domain reorientation is

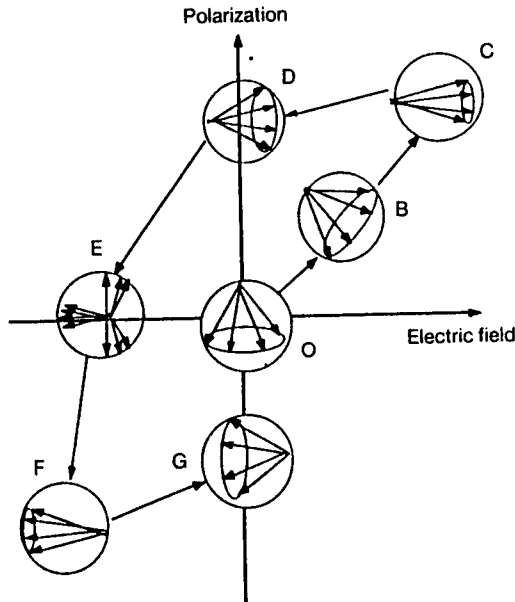


Figure 3 Two-dimensional representation of the vector model showing the spatial distribution of domains at different stages of the polarization reversal.

involved and no  $180^\circ$  domain wall reversal process occurs because the initial direction of polarization is perpendicular to the applied electric field. From equations 3 and 4, one obtains

$$R|_{O-C} = K \frac{I_{(0\ 0\ 2)}}{I_{(2\ 0\ 0)}} = K \frac{n_1[90^\circ] I_{p(0\ 0\ 2)}}{g_1[90^\circ] I_{p(2\ 0\ 0)}} \quad (5)$$

where  $n_1 + g_2 = 1$ , and  $n_2 = g_2 = 0$ . Equation 5 means that the diffraction intensity ratio  $I_{(0\ 0\ 2)}/I_{(2\ 0\ 0)}$  is equal to the diffraction intensity ratio  $\{n_1[90^\circ] I_{p(0\ 0\ 2)}/g_1[90^\circ] I_{p(2\ 0\ 0)}\}$  within the unit volume of  $90^\circ$  domain. In this case, the number of  $90^\circ$  domains per unit volume is equal to the number of domains per unit volume because only  $90^\circ$  domain reorientation is involved in this process. It should be noted that, in general, the number of  $90^\circ$  domains per unit volume is not necessarily equal to the number of domains per unit volume, when considering the coexistence of both  $90^\circ$  and  $180^\circ$  domains. We will explain this later. From Equation 5, the rate of changing  $R$  as a function of electric field can be expressed as

$$\frac{dR}{dE}|_{O-C} = \frac{d(K n_1[90^\circ] I_{p(0\ 0\ 2)}/g_1[90^\circ] I_{p(2\ 0\ 0)})}{dE} \quad (6)$$

where  $R$  is the measured value of the ratio  $I_{(0\ 0\ 2)}/I_{(2\ 0\ 0)}$ .  $dR/dE$ , the rate of change of  $I_{(0\ 0\ 2)}/I_{(2\ 0\ 0)}$  from point O to point C reflects only the feature of  $90^\circ$  domain wall reorientation.

### 3.1.2. Case 2

When the intensity of the electric field is decreased from the point C to point D, the domain polarization turns back to the nearest easy direction in favour of lowering the internal energy. If the applied electric field is increased further in the negative direction from point D to point F, the domain polarizations pointing in the positive direction are reversed. This process may involve both the  $90^\circ$  and  $180^\circ$  domain switching processes. Therefore, from Equations 2 and 3, we have

$$R|_{D-F} = K \frac{I_{(0\ 0\ 2)}}{I_{(2\ 0\ 0)}} = K \frac{n_1[90^\circ] I_{p(0\ 0\ 2)} + n_2[180^\circ] I_{p(2\ 0\ 0)}}{g_1[90^\circ] I_{p(2\ 0\ 0)}} \quad (7)$$

where  $n_1 + n_2 + g_1 = 1$ , and  $g_2 = 0$ . It should be noted that no  $180^\circ$  domain reversal occurs in the direction perpendicular to the applied field. Therefore, Equation 7 can be expressed as

$$R|_{D-F} = K \frac{I_{(0\ 0\ 2)}}{I_{(2\ 0\ 0)}} = K \frac{n_1[90^\circ] I_{p(0\ 0\ 2)} + n_2[180^\circ] I_{p(0\ 0\ 2)}}{g_1[90^\circ] I_{(2\ 0\ 0)}} \quad (8) = (n_1 + g_1)[90^\circ] K \alpha$$

where

$$\alpha = \frac{\{n_1[90^\circ] I_{p(0\ 0\ 2)} + n_2[180^\circ] I_{p(0\ 0\ 2)}\}}{g_1[90^\circ] I_{p(2\ 0\ 0)}(n_1 + g_1)}$$

diffractive intensity per unit volume of 90° domain, which reflects the feature of 90° domain reversal.  $\alpha$  is also a function of electric field and dependent upon the entire domain polarization reversal process. Precisely speaking, because only the  $(n_1 + g_1)$  portion of 90° domains contribute to the diffraction intensity of  $R$  [or  $I_{(002)}/I_{(200)}$ ] in Equation 8, thus, the contribution of 90° domains to  $R$  in the process from point D to point F should not be exactly the same as that of the intensity  $R$  in the process from point O to point C. In order to compare the features of these two domain reversal processes, we can define the changing rate of diffraction intensity as the same within the unit volume of 90° domains with respect to these two domain switching processes. Therefore, from Equation 8, one should have

$$\begin{aligned} \left. \frac{dR}{dE} \right|_{D-F} &= (n_1 + g_1)[90^\circ] K \frac{d\alpha}{dE} \\ &= (n_1 + g_1)[90^\circ] \left. \frac{dR}{dE} \right|_{O-C} \quad (9) \end{aligned}$$

Naturally, unlike Equation 6, Equation 9 describes a pure 90° domain wall reorientation process. From Equation 9, it can be found that the changing rate of  $R$  as a function of the electric field will also be affected by  $(n_1 + g_1)$ . Obviously, if  $(n_1 + g_1)$  is equal to 1, the polarization reversal process will be a pure type of 90° domain reversal process. Thus, Equation 9 should

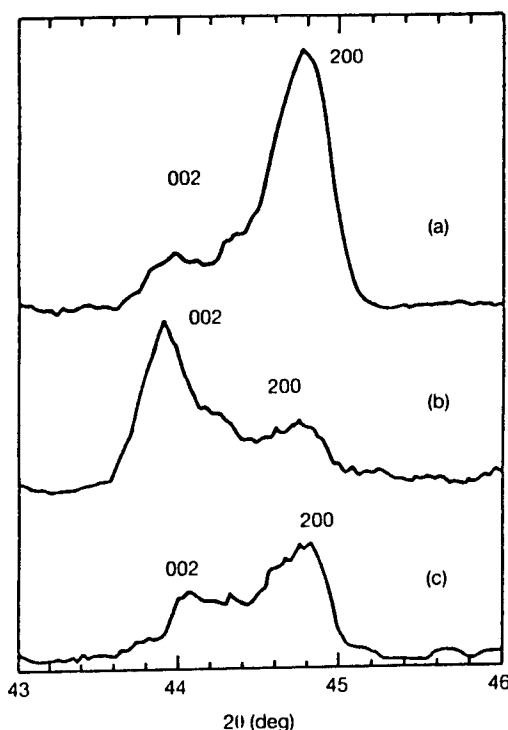


Figure 4 The XRD profiles of (002) and (200) peaks for plate PZT samples of different orientation of polarization. (a) X-ray intensity profile of a poled ceramic plate sample with its normal direction perpendicular to the poling direction. (b) X-ray intensity profile of a poled ceramic plate sample with its normal direction parallel to the poling direction. (c) X-ray intensity profile of an unpoled ceramic sample.

domain reversal will occur, and no X-ray information can be obtained. Equation 9 is an approximate expression which is precisely valid only if large amounts of 90° domains are involved in the polarization switching processes. Detailed discussions can be found elsewhere [8]. Compared to Equations 9 and 6, it could be asserted that if 90° domain wall reorientation is the main process in the polarization reversal from point D to point F, the changing rate of the measured ratio  $dR/dE$  would be slightly less than those from point O to point C according to Equation (9). In other words, the feature of domain reversal process from point D to point F is most likely a pure type of 90° domain reorientation process. Conversely, if 180° domains are predominantly involving the polarization reversal process from point D to point F, the measured changing rate,  $dR/dE$ , would be much smaller than that from point O to point C because  $(n_1 + g_1)$  is small in this case. Here, we assume the internal energy states at points O and D to be the same. This assumption means that the polarization distributions of ceramics are the same at both points O and D, which is almost fulfilled in reality. In short, Equation 9 could be used as the criterion for qualitatively evaluating the characteristics of the dynamic behaviour of domain reorientation processes in ceramics in terms of X-ray analysis techniques.

### 3.2. Results and conclusions

In practice, in order to sort out the mechanisms of domain reorientation in the ceramic specimens, we have to examine both the dependence of  $I_{(hkl)}$  as a function of applied electric fields and the changing rate of  $I_{(002)}/I_{(200)}$  as a function of the applied electric field (or  $d\{I_{(002)}/I_{(200)}\}/dE$ ) in some details. Fig. 4 shows the XRD profiles of (002) and (200) peaks for plate PZT samples in the case of different polarization orientations. It can be seen from Fig. 4a that when the normal direction of the plate is perpendicular to the polarization direction, the (200) peak is much higher than the (002) peak of the sample. Conversely, for samples with the normal direction of the plate parallel to the poling direction, as shown in Fig. 4b, the (002) peak is much higher than (200) peak. Fig. 4c is the case of an unpoled sample. Because no preferred orientation exists, the intensity of the (200) peak is about twice that of the (002) peak. Fig. 5 presents the ratio  $I_{(002)}/I_{(200)}$  as a function of the applied electric field in case II of Fig. 2. In Fig. 5, the magnitude of the applied electric field at points D and D' are almost exactly equal to the coercive fields of the P-E (polarization-electric field) hysteresis loop and S-E (strain-electric field) hysteresis loop measured at ultra-low frequency. Because the ratio  $I_{(002)}/I_{(200)}$  represents the characteristics of 90° domain reversal, it indicates that the coercive field of polarization switching is closely related to the 90° domain reversal in this ceramic sample. Fig. 6 presents the ratio of  $I_{(002)}/I_{(200)}$  as a function of the applied electric field from point O to point D' for Case I of Fig. 2. As

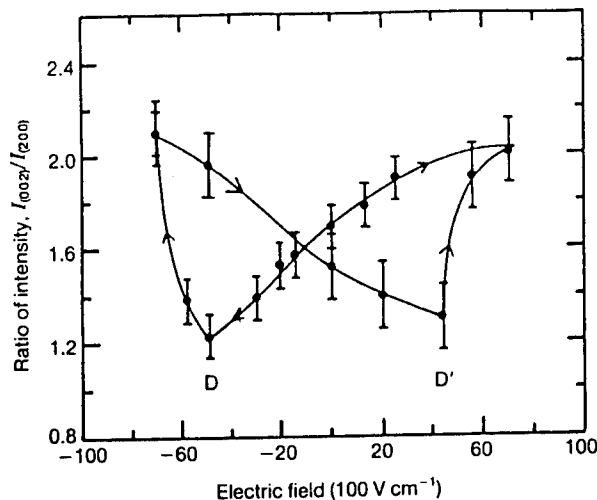


Figure 5 The ratio of  $I_{1002}/I_{2000}$  as a function of the applied electric field for Case II of Fig. 2.

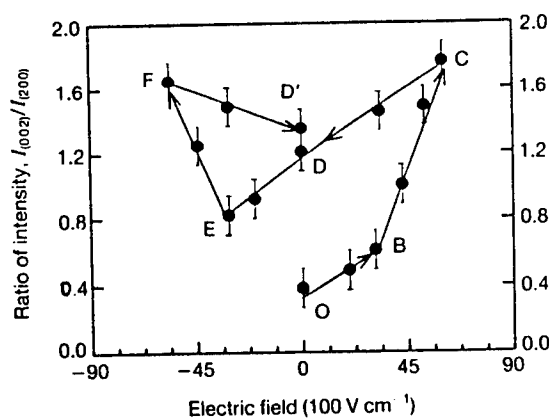


Figure 6 The ratio of  $I_{1002}/I_{2000}$  as a function of the applied electric field for Case I of Fig. 2.

discussed above, from point O to point C, the domain reorientation is a pure  $90^\circ$  domain type. If polarization reorientations involving both the  $180^\circ$  and  $90^\circ$  domain reversal processes from point D to point F, then the slopes of  $I_{1002}/I_{2000}$  as a function of electric fields from point D to point F should be substantially smaller than those from point O to point C. The slopes of  $dR/dE$  in Fig. 6 are listed in Table I, from which it can be clearly found that there is no substantial difference in the absolute values of the slopes between the

TABLE I Changing rate of  $I_{1002}/I_{2000}$  with applied electric field for the cases in Fig. 6

Lines	Slopes
O-B	$(0.95 \pm 0.2) \times 10^{-2} (100 \text{ V cm}^{-1})^{-1}$
B-C	$(4.2 \pm 0.3) \times 10^{-2} (100 \text{ V cm}^{-1})^{-1}$
D-E	$(1.1 \pm 0.2) \times 10^{-2} (100 \text{ V cm}^{-1})^{-1}$
E-F	$(3.2 \pm 0.3) \times 10^{-2} (100 \text{ V cm}^{-1})^{-1}$

O-B line and the D-E line or between the B-C line and the E-F line. This argument strongly suggests that the entire polarization reorientation process from point O to point F is predominantly controlled by the  $90^\circ$  domain reversal process. In other words, Equation 9 could be approximately satisfied by the experimental data. The estimated value ( $n_1 + g_1$ ) is around 0.7–0.8 from comparing the slopes between the line B-C and the line E-F in Table I. This result indicates that in PZT ceramics, 80% domains within total reversal domains are  $90^\circ$  domains. Therefore, it can be concluded that the  $90^\circ$  domain reorientation plays a major role in terms of the polarization switching in the PZT bulk ceramic with the composition within the morphotropic phase boundary.

### Acknowledgement

This research has been supported in full by the Office of Naval Research.

### Reference

1. N. B. CHAIM, M. BRUNSTEIN, J. GRUNBERG and A. SEIDMAN, *Ferroelectrics* **6** (1974) 299.
2. *Idem*, *J. Appl. Phys.* **45** (1974) 2398.
3. N. A. SCHMIDT, *Ferroelectrics* **312** (1981) 105.
4. P. GERTHSEN and G. KRUGER, *Ferroelectrics* **11** (1976) 489.
5. G. KRUGER, *Ferroelectrics* **11** (1976) 417.
6. N. UCHIDA and T. IKEDA, *Jpn J. Appl. Phys.* **4** (1965) 867.
7. Y. MASUDA and A. BABA, *Jpn. J. Appl. Phys.* **24** (1985) 113.
8. SHAOPIING LI, PhD thesis, Pennsylvania State University (1992).
9. J. MENDIOLA and L. PARDO, *Ferroelectrics* **54** (1984) 199.
10. Y. W. ZENG, W. R. XUE and G. F. FU, *J. Mater. Sci.* **22** (1991) 4294.

Received 15 February  
and accepted 26 August 1993

# **APPENDIX 13**



# Modified Lumped Parameter Method for Measurements of Dielectric Susceptibility in Ferroelectrics

Shaoping LI\*, Jyh SHEEN, Sei-Joo JANG, Amar S. BHALLA, Robert E. NEWNHAM and L. Eric CROSS

Materials Research Laboratory, The Pennsylvania State University, University Park, PA 16802, U.S.A

(Received February 21, 1993; accepted for publication August 21, 1993)

The transmission techniques for dielectric measurements can be classified into two categories; one belongs to the lumped capacitance method and the other is related to the distributed parameter method. In reality, however, the dielectric dispersion for high dielectric constant materials in the frequency range 1 MHz–5 GHz could not be made accurately by using the transmission techniques. In this work, a modified lumped parameter method has been discussed. We call this modified method as the quasi lumped parameter method which is especially suitable for the microwave measurements of dielectric dispersion for high dielectric materials in a particular frequency region. The proposed method combines some features of both the lumped parameter method and the distributed parameter method. By using this measurement method, the measurements of dielectric dispersions are presented for several ferroelectric materials, such as  $\text{Pb}(\text{Zr}_{1-x}\text{Ti}_x)\text{O}_3$ , and  $\text{BaTiO}_3$  in the frequency domain from 1 MHz to 1 GHz.

**KEYWORDS:** dielectric dispersion, microwave measurement

## 1. Introduction

Dielectric dispersions of materials with high susceptibility are of great importance in many applications. Particularly, dielectric dispersion in ferroelectric materials has been measured and discussed by many authors.<sup>1–6)</sup> In practice, however, it is often hard to make an accurate measurement of relative dielectric constant ( $\epsilon$ ) and loss tangent ( $\tan \delta$ ) in ferroelectric materials at microwave frequencies because of the large dielectric constant and loss tangents exhibited by these materials.

Generally, microwave measurement techniques for dielectrics are mainly divided into two sections. (1) the transmission techniques, and (2) the resonant techniques, among which only the transmission techniques have the swept frequency capability. In other words, the dielectric dispersion can only be accurately measured through the transmission methods. Meanwhile, the transmission techniques for microwave measurements on dielectric samples can be also classified into two categories. One is the lumped capacitance method and the other is the distributed parameter method. Nevertheless, in practice, the microwave measurements for high dielectric materials in the frequency range 100 MHz–5 GHz can not be made accurately by either of these two methods, even though the microwave equipments have been improved significantly in the past few decades.

## 2. Lumped Capacitance Methods

Basically a dielectric sample is considered as a capacitor in the language of the equivalent circuit in the lumped capacitance method. The dielectric sample is placed on the end of a shorted coaxial line and the complex reflection coefficient was measured by the time domain reflectometer through the vector-voltage ratio of the reflected wave to the incident wave from the

sample<sup>7–10)</sup>

$$\Gamma = \frac{V_{\text{ref}}}{V_{\text{inc}}} = \Gamma_x + j\Gamma_y = |\Gamma| e^{-j\theta} \quad (1)$$

where  $V_{\text{ref}}$  is the voltage of the reflected wave and  $V_{\text{inc}}$  represents the voltage of the incident wave. The complex reflection coefficient is a function of the complex permittivity, and thus, the real and imaginary parts of the relative permittivity can be expressed as<sup>7,11)</sup>

$$\epsilon' = \frac{2|\Gamma| \sin \theta}{\omega C_0 Z_0 \{|\Gamma|^2 + 2|\Gamma| \cos \theta + 1\}} \quad (2)$$

$$\epsilon'' = \frac{1 - |\Gamma|^2}{\omega C_0 Z_0 \{|\Gamma|^2 + 2|\Gamma| \cos \theta + 1\}} \quad (3)$$

where  $C_0$  is the capacitance of the test capacitor and  $Z_0$  is the characteristic impedance of the network analyzer. The basic assumption for the lumped capacitance method is that the electric field is uniform throughout the sample. In other words, this means that the measured reflection coefficient is equal to the intrinsic reflection coefficient of samples, which is caused by the complex permittivity of the sample. If this basic requirement could not be satisfied, the accurate results would not be obtained by using the lumped capacitance method.

At higher frequencies, the lumped capacitance method breaks down in several respects: (1) the measured capacitance of the sample cannot be simply related to the real dielectric constant of the sample because of the non-uniform variation of the electric field throughout the sample. In this sense, due to the wave compression, the basic assumption for the lumped impedance technique loses validity at the high frequency with respect to high dielectric constant materials. It is, therefore, required that the thickness of the sample should be around the order of a few percent of a wavelength at the highest frequency of interest in order to obtain rather accurate experimental data. If the material has a dielectric constant at about 1000 at the frequency of 1 GHz, the corresponding thickness of the

\*Present address: Max-Planck-Institute of Microstructure Physics, Halle/Saale, Germany.

sample should be of the order of  $100\ \mu\text{m}$ . The other dimensions of specimens should also be much less than the wavelength of light; (2) the fringe field effects<sup>12)</sup> and the inability of the measurement equipment also affect the accuracy of measured experimental data severely. At high frequencies, usually, the fringing fields are no longer negligible, thus, in some equipment, the maximum readable capacitance value within 5% accuracy is limited at higher frequencies. The samples of smaller cross section decreases the fringe field, however, the sample machining becomes difficult. On the other hand, it is well known that the distributed transmission method does not require the uniform field assumption. In this method, however, the wave guide is the primary medium of microwave propagation. If the cutoff frequency is around 300 MHz, the wave guide dimensions should be around the order of 0.5 m, which is apparently not reasonable in practical cases.

### 3. The Principle of the Proposed Method

From above discussions, we find that at the high frequency, due to the influence of fringing fields and the difficulty of sample machining, it is difficult to satisfy the requirement of the critical thickness which is imposed by the assumption of the lumped impedance technique. In other words, since the electric field is no longer uniform in the sample at the high frequency, and then the lumped capacitance method can not be used because the sample could not be considered as a capacitor in this case.

The question, therefore, arises as to whether or not the lumped impedance method can be modified in order to extend the scope of its applications. Virtually, in the high frequency region, the dimension of the sample does not fulfill the critical requirement of the sample dimension in terms of the basic assumption of the lumped parameter method. Therefore, the measured reflection coefficient is not exactly equal to the intrinsic reflection coefficient of the sample. Obviously, in this situation, the measured reflection coefficient is not solely related to the complex permittivity, which is also affected by the losses and the phase shift of the measuring signal during the electromagnetic wave passing through the sample.

In order to overcome these difficulties and to obtain accurate dielectric dispersion, we have to describe the measurement situation accurately, and to make the measurement practical. We here consider the measured sample as a "quasi-transmission" line since the sample could not be simply considered as a capacitor in this case. We assume that the measured sample is equal to a capacitor plus a two port network. The two-port network here is a black box. However, we can obtain some necessary information about this two-port network by using the theory of the distributed method. We will discuss this later.

Precisely speaking, in this situation, we try to visualize the measured sample comprising of two parts, as shown in Fig. 1. Part I is a very thin layer, which is thin enough to be equivalent to an ideal lumped capacitance system. The reflection coefficient of this part

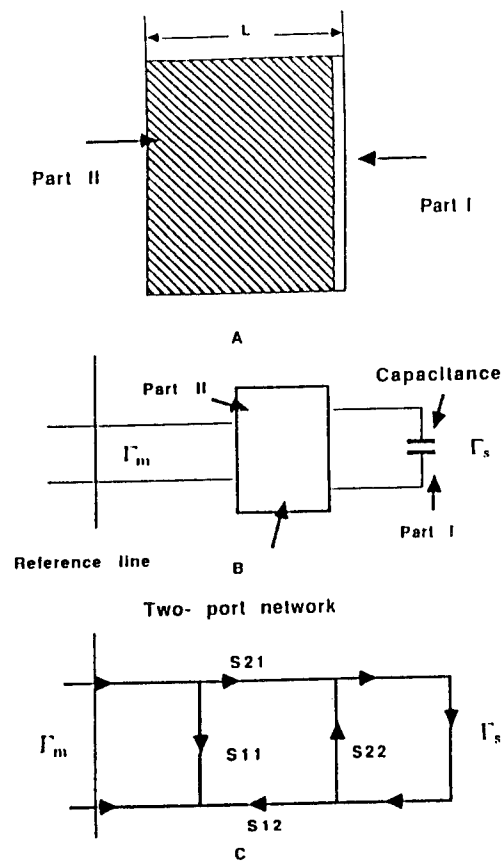


Fig. 1. (a) Schematic drawing of the sample imaged as the two parts of a "lossy quasi-lumped transmission line". (b) Equivalent circuit of the real sample. (c) Terminated two-port network with the  $S_{ij}$  parameters to describe the nature of the measured sample.

represents the intrinsic properties of the measured material. Part II is the rest of the sample (the shadowed area), which is a "lossy transmission line" or a distributed component, and could be described by a simple two-port network, as shown in Fig. 1(c). The equivalent circuits of the specimen are also shown in Figs. 1(b) and 1(c). According to this equivalent circuit, the relationship between the measured reflection coefficient and intrinsic reflection coefficient can be expressed as<sup>13)</sup>

$$\Gamma_s = \frac{1}{\left[ \frac{S_{12}S_{21}}{\Gamma_m - S_{11}} + S_{22} \right]}. \quad (4)$$

In reality, if the thickness of the measured samples does not fulfill the critical requirement of lumped parameter method, we have to consider that the part II exists in the measured sample, which will cause attenuation of the signal amplitude and the phase shift of the measured signal when the measured signal goes through the sample. Therefore, with the help of eq. (4), intrinsic reflection coefficients of the sample can be retrieved and obtained from the measured reflection coefficient provided the  $S_{ij}$  parameters are known. More precisely, if we can obtain the  $S_{11}$  and  $S_{21}$  from the theoretical calculation based on the theory of dis-

distributed parameter method, we can use these parameters to trim the measured reflection coefficient  $\Gamma_m$ , and then get the reflection coefficient  $\Gamma_s$  of the intrinsic sample.

In a simplified case (here we assume  $S_{11}=S_{22}$ ,  $S_{12}=S_{21}$ ), according to the theory of the distributed parameter method,<sup>5,14)</sup>  $S_{11}$  and  $S_{12}$  can be expressed in terms of the sum of reflected and transmitted waves and can be numerically evaluated by<sup>14)</sup>

$$S_{11} = \rho \frac{1 - \exp(-2\gamma L)}{1 - \rho^2 \exp(-2\gamma L)}; \quad (5)$$

$$S_{12} = \frac{[1 - \rho^2] \exp(-2\gamma L)}{1 - \rho^2 \exp(-2\gamma L)}, \quad (6)$$

where

$$\rho = \frac{1 - (\epsilon^*)^{1/2}}{1 + (\epsilon^*)^{1/2}}; \quad \gamma = \alpha + j\beta = j\omega(\mu^* \epsilon^*)^{1/2}$$

$L$  is the thickness of measured sample, and  $\epsilon^*$  is the relative complex permittivity. Figure 2 presents the theoretical calculations of  $S_{11}$  and  $S_{12}$  as a function of frequencies.

On the one hand, according to eqs. (5) and (6), it is very obvious that when the measuring frequency is very low,  $S_{11}$  approaches to zero and  $S_{12}$  is equal to 1. Thus, from eq. (4),  $\Gamma_m$  is equal to  $\Gamma_s$  in this case. This is the exact case in which an ideal lumped parameter method is valid and the measured sample is a capacitor in this situation.

On the other hand, as discussed above, if the measured frequency becomes very high in the real measurements,  $\Gamma_s$  will be strongly affected by the electromagnetic wave absorption and phase shift inside the part II of the sample. However, in principle, as long as the

influence of part II on the sample is not very strong, there is such a case in which this influence can be considered as a small perturbation term in terms of  $\Gamma_s$  (this condition can be easily fulfilled in practice). Therefore, we can obtain the intrinsic reflection coefficient of the sample ( $\Gamma_s$ ) by retrieving the measured reflection coefficients ( $\Gamma_m$ ) from eq. (4) through the numerically evaluating  $S_{ij}$  parameters based on eqs. (5) and (6) in an iterative process.

Finally, the complex dielectric dispersion ( $\epsilon^* = \epsilon' - j\epsilon''$ ) can be obtained from the intrinsic reflection coefficient of the sample  $\Gamma_s$  by

$$\epsilon^* = \frac{(1 - \Gamma_s)}{\{(1 + \Gamma_s)2\pi j f C_0 Z_0\}} \quad (7)$$

where  $Z_0$  is the characteristic impedance of the impedance analyzer  $C_0 = \epsilon_0 a/d$ .

The real retrieving procedure of an iterative process can be carried out by following steps: (a) initially we assumed  $\Gamma_m = \Gamma_s$ ,  $S_{12} = S_{21} = 1$ , and  $S_{11} = S_{22} = 0$  at the lowest measuring frequency, i.e., the lumped parameter method is valid in this case; (b) and then we use the measured dielectric coefficients of every preceding frequency spot to evaluate  $S_{ij}$  parameters according to eqs. (5) and (6); (c) thus we can retrieve the complex reflection coefficient of next neighbor higher frequency spot through eq. (4); (d) finally, we can obtain the frequency dependence of complex dielectric constants from eq. (7).

#### 4. Measurement Results and Discussions

$\text{Pb}(\text{Zr}_{1-x}\text{Ti}_x)\text{O}_3$ ,  $\text{BaTiO}_3$  and  $\text{Ba}_{0.5}\text{Sr}_{0.5}\text{TiO}_3$  ceramics were prepared by the conventional mixed-oxide process. The samples were cut to approximately the plate shape. Their dimensions were much smaller than the wavelength of light. Before making the electrodes, the surfaces of specimens were polished, etched and annealed in order to keep the contributions of surface layer low. The complex reflection coefficient of the sample was recorded with HP 4191A impedance analyzer, with a test frequency range from 1 MHz to 1 GHz. The frequency dependence of dielectric constants and their losses for PZT ceramics are shown in Fig. 3. These

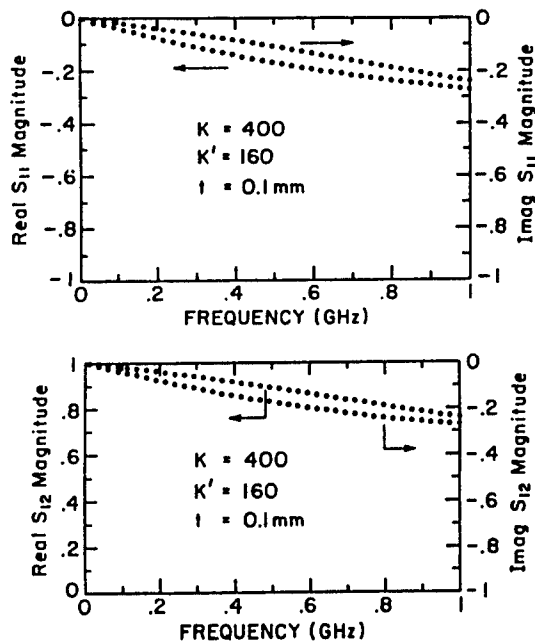


Fig. 2. Theoretical calculations of the real and imaginary parts of the  $S_{ij}$  parameters vs frequency. (a) Theoretical calculated real and imaginary magnitudes of  $S_{12}$ . (b) The  $S_{11}$  vs frequency in the range 1 Hz-1 GHz.

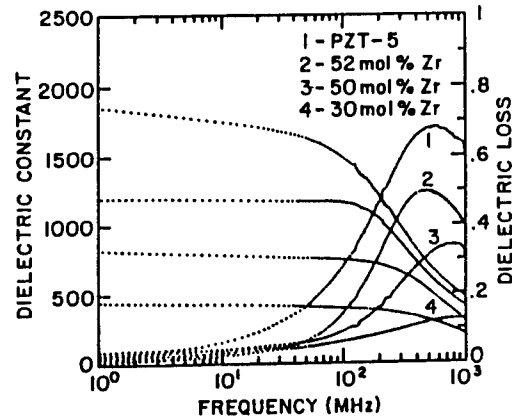


Fig. 3. Dielectric constants and losses (i.e.,  $\epsilon'$  and  $\tan \delta$ ) vs frequencies in the PZT system.

results are similar to those of previous investigations.<sup>11</sup> From our results, however, it can be found that the minimum relaxation frequency (or the resonance frequency of domain wall motions) occurs in the ceramic with the composition near the morphotropic phase boundary. These experimental data are useful for estimating the effective mass of domain wall motions.<sup>17)</sup>

Figure 4 shows the dielectric dispersions of both poled and unpoled PZT ceramic samples. The observed piezoelectric resonance peaks due to the sample dimension at very high frequency (around 100 MHz) indirectly implies the measured data are reliable. The dielectric dispersion in PZT, BaTiO<sub>3</sub> and Ba<sub>0.5</sub>Sr<sub>0.5</sub>TiO<sub>3</sub> have been presented in Figs. (5) and (6). It can be found that there is no appreciable relaxation in the dielectric dispersion of Ba<sub>0.5</sub>Sr<sub>0.5</sub>TiO<sub>3</sub> within measured frequency span, which is mainly consistent with previous studies.<sup>5,12,13</sup> It should be noted that since the  $S_{ij}$  parameter was estimated by the initially assumed dielectric constants, and the measurement instruments have some limitations, the measurement error is still rather significant regarding materials with ultra low loss tangents. In fact, at the frequency of 1 GHz, the measured dielectric losses (0.017–0.04) are almost one order of magnitude larger than the true values.<sup>5,15,16</sup> Figure 7 presents a Cole-Cole plot of the complex dielectric constants of the PZT system.

In summary, in the present work, a modified lumped

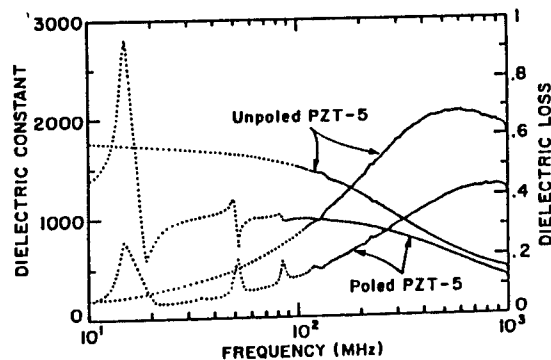


Fig. 4. The dielectric dispersions (including  $\epsilon'$  and  $\tan \delta$ ) of both the poled and unpoled PZT ceramics.

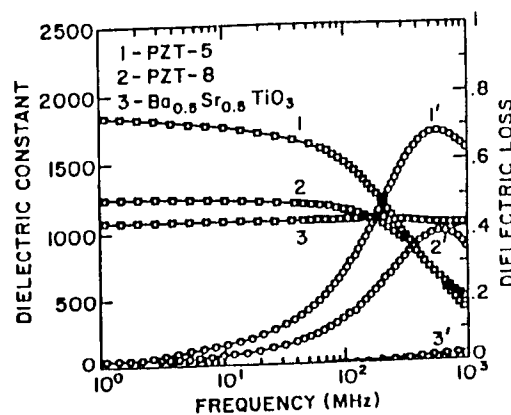
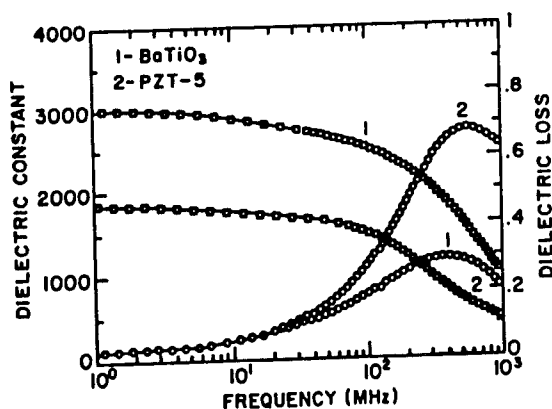


Fig. 6. The dielectric dispersions (including  $\epsilon'$  and  $\tan \delta$ ) of the soft PZT, hard PZT, and Ba<sub>0.5</sub>Sr<sub>0.5</sub>TiO<sub>3</sub> ceramics.

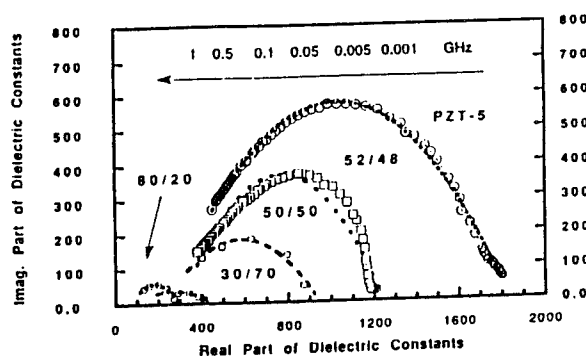


Fig. 7. Cole-Cole plot of the complex dielectric constants of PZT ceramics with different Ti concentration.

parameter method has been proposed and developed, which is especially suitable for microwave measurements of high dielectric materials in the frequency region 1 MHz–2 GHz. It combines some of the features of both the lumped parameter method and the distributed parameter method. The experimental results very well agree with the general trend of other experimental observations from other measurement techniques.

This proposed measurement technique seems to be very simple, however, it has successfully solved a measurement problem which has not been solved for last few decades, which provides a unique way to accurately study the dielectric dispersion of materials within the frequency region 1 MHz–2 GHz.

#### Acknowledgment

This research was supported by the Office of Naval Research.

- 1) O. Kersten and G. Schmidt: *Ferroelectrics* **67** (1986) 191.
- 2) A. V. Turik, K. R. Chernshov and V. D. Komarov: *Ferroelectrics* **6** (1973) 45.
- 3) M. M. Maglione, R. Bohmer, A. Loidl and U. T. Hochli: *Phys. Rev. B* **40** (16) (1989) 11441.
- 4) Y. M. Poplavk, V. G. Tsykalov and V. I. Molchanov: *Sov. Phys. Solid State* **16** (1974) 177.

- sity, U.S.A. 1987.
- 6) A. R. Von Hippel: Rev. Mod. Phys. **22** (1950) 221.
- 7) S. S. Stuchly, M. A. Rzepecka and M. F. Iskander: IEEE Trans. Instrum. Meas. **IM-23** (1974) 56.
- 8) S. S. Stuchly: IEEE Trans. Instrum. Meas. **IM-27** (1978) 285.
- 9) M. A. Rzepecka and S. S. Stuchly: IEEE Trans. Instrum. Meas. **IM-24** (1975) 27.
- 10) M. F. Iskander and S. S. Stuchly: IEEE Trans. Instrum. Meas. **IM-21** (1972) 425.
- 11) T. Ichino, H. Ohkawara and N. Sugihara: J. Hewlett-Packard (1980) 22.
- 12) M. F. Iskander and S. S. Stuchly: IEEE Trans. Instrum. Meas. **IM-27** (1978) 107.
- 13) S. F. Adams: *Microwave Theory and Applications* (Prentice-Hall, Engle-Wood Cliffs, 1969).
- 14) M. J. C. Van. Gemert: Phillips Res. Rep. **28** (1973) 530.
- 15) J. B. Horton and G. A. Burdick: IEEE Trans Microwave Theory Tech. **23** (1968) 873.
- 16) U. Syamaprasad, R. K. Gargali and B. C. Mohanty: Mater. Lett. **7** (1988) 197.
- 17) S. Li: Ph.D. Thesis, The Pennsylvania State University, U.S.A. 1992.

# APPENDIX 14

## Modified Lead Calcium Titanate Ceramics with a Relatively Large Dielectric Constant for Hydrophone Applications

Louis M. Troilo,\*\* Dragan Damjanovic,<sup>†</sup> and Robert E. Newnham\*

Materials Research Laboratory, The Pennsylvania State University, University Park, Pennsylvania 16802

Modified lead titanate of the base composition  $(\text{Pb,Ca})\text{Ti}(\text{Co,W})\text{O}_3 + 0.01 \text{ mol\% MnO}$  was doped with 2 to 6 mol% strontium and barium to increase the dielectric constant,  $K$ , while preserving a high piezoelectric anisotropy ( $d_{33}/d_{31}$ ).  $K$  was increased above 500 and a  $d_{33}/d_{31}$  ratio of 34/1 was achieved when the composition  $\text{Pb}_{0.65}\text{Ca}_{0.31}\text{Sr}_{0.04}\text{Ti}_{0.94}(\text{Co}_{0.5}\text{W}_{0.5})_{0.06}\text{O}_3 + 0.01 \text{ mol\% MnO}$  was fabricated. The large  $d_{33}/d_{31}$  resulted in an impressive hydrostatic piezoelectric coefficient ( $d_h = 81 \times 10^{-12} \text{ m}^2/\text{V}$ ). The relatively low transition temperature ( $T_c = 120^\circ\text{C}$ ) did not result in an increased aging rate when samples were tested at  $40^\circ\text{C}$  and 99% humidity for 120 h after poling. A small tetragonality ratio (1.008) enabled saturation of ceramic properties at poling fields as low as 30 kV/cm at  $100^\circ\text{C}$ .

### I. Introduction

MODIFIED lead calcium titanates are of considerable interest because of their highly anisotropic piezoelectric properties. The large longitudinal piezoelectric coefficient  $d_{33}$  and small transverse coefficient  $d_{31}$  result in reduced coupling between thickness and lateral vibrational modes and decreased cross talk between adjacent elements in an array transducer. As a result, lead titanate-based ceramics have been examined for use in low-frequency hydrophone applications.<sup>1</sup> At sufficiently low frequencies, the wavelengths of acoustic waves underwater are much larger than the dimensions of the hydrophone, and the effective stress may be considered hydrostatic. The corresponding piezoelectric (or charge) coefficient,  $d_h$ , is given by

$$d_h = d_{33} + 2d_{31} \quad (1)$$

Most piezoelectric ceramics, such as lead zirconate titanate (PZT), have  $d_{33} > 0$ ,  $d_{31} < 0$ , and a low anisotropy of piezoelectric properties ( $d_{33} \approx 2d_{31}$ ). Therefore, the resulting hydrostatic coefficient is very low. However, in modified lead titanate ceramics, even though  $d_{33}$  is several times smaller than in most PZT compositions, a very small or even positive  $d_{31}$ <sup>2</sup> gives a large  $d_h$ .

In addition, modified lead titanates exhibit dielectric constant,  $K$ , values much lower than most PZT materials. This is necessary for achieving a large value in voltage sensitivity, an important property for evaluating materials for sonar applications. Voltage sensitivity,  $g_h$ , is defined as

$$g_h = \frac{d_h}{K\epsilon_0} \quad (2)$$

where  $\epsilon_0$  is the dielectric permittivity of free space. However, too small of a  $K$  value is not preferred from a device viewpoint. The capacitance of the device should be large enough to prevent interference from stray capacitance associated with long hydrophone cables as well as provide acceptable impedance matching. The relatively small  $K$  value in modified lead titanate ceramics has been an important disadvantage for low-frequency hydrophone applications and is the impetus for increasing  $K$  in this investigation.

It was demonstrated that  $K$  values above 400 can be achieved by doping lead titanate with a high concentration of calcium (up to 34 mol%).<sup>3</sup> The increase in  $K$  was mainly accomplished by bringing the paraelectric-to-ferroelectric transition temperature ( $T_c = 120^\circ$ ) closer to room temperature. Further increases in calcium concentration led to a significantly lower piezoelectric anisotropy. Compositions with such a low  $T_c$  might have been expected to exhibit higher dielectric losses and considerable aging due to high mobility of domain walls at temperatures approaching  $T_c$ . However, no studies on aging of modified lead titanate with low  $T_c$  have been reported to date. Therefore, the goals of this investigation are to examine possible compositional modifications of modified lead titanate ceramics which would increase their dielectric constant above previously reported values of 400 while preserving the high anisotropy of piezoelectric properties, and to investigate the aging of prepared ceramics under conditions of high humidity and increased temperature.

### II. Experimental Procedure

#### (1) Choice of Materials

The ternary system  $(1 - x - y)\text{PbTiO}_3 \cdot y\text{Pb}(\text{Co}_{1/2}\text{W}_{1/2})\text{O}_3 \cdot x\text{CaTiO}_3$  was chosen as the starting material for this investigation. Previous studies showed that the dielectric constant in this system increased with  $x$ , but the piezoelectric anisotropy decreased abruptly for  $x \geq 0.36$ .<sup>3</sup>

Lead titanate ( $\text{PbTiO}_3$ ) is a typical perovskite ferroelectric with  $T_c = 490^\circ\text{C}$ . Additions of antiferroelectric  $\text{Pb}(\text{Co}_{1/2}\text{W}_{1/2})\text{O}_3$  and nonferroelectric calcium titanate ( $\text{CaTiO}_3$ ) decrease the transition temperature of lead titanate and, thus, effectively increase its  $K$  value at room temperature. To increase the dielectric constant without increasing the concentration of calcium, which is detrimental to piezoelectric properties, the above system was further modified with strontium titanate ( $\text{SrTiO}_3$ ) and barium titanate ( $\text{BaTiO}_3$ ). Barium titanate is ferroelectric at room temperature, and strontium titanate is an incipient ferroelectric with its dielectric permittivity following Curie-Weiss behavior below room temperature. It is reasonable to expect that even small additions in place of calcium of those two cations which support occurrence of ferroelectricity will increase  $K$  of the solid solution without significantly affecting the high piezoelectric anisotropy. Thus, in the present work, the above system was modified as follows:

W. Huebner—contributing editor

Manuscript No. 195713. Received May 11, 1992; approved December 14, 1993.

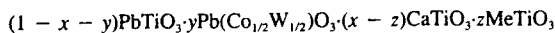
Based in part on the thesis submitted by L. M. Troilo for the degree in Solid State Science, The Pennsylvania State University, University Park, PA, 1991.

Supported by the Ben Franklin Partnership Program and Piezokinetics, Inc., Bellefonte, PA.

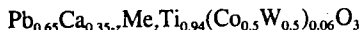
\*Member, American Ceramic Society.

<sup>†</sup>Current address: Naval Research Laboratory, Washington, DC 20375.

<sup>‡</sup>Current address: Ecole Polytechnique Fédérale, Laboratoire de Céramique, Lausanne, Switzerland.



where Me is Sr or Ba. Values for  $x$  and  $y$  are set at  $x = 0.35$  and  $y = 0.06$ , while  $z$  is varied from 0.02 to 0.06. Therefore, the general formula of the prepared composition is



## (2) Sample Preparation

The mixed, high-purity oxides (Alpha Products, Morton Thiokol, Inc., Danvers, MA) were milled for 24 h using a zirconia media. To decrease the dissipation factor, approximately 0.01 mol% of MnO was added to the mixture before milling. The  $\text{Mn}^{2+}$  ion, which substitutes into the B position of  $\text{ABO}_3$  perovskite structure,<sup>4</sup> also raises electrical resistivity and, thus, facilitates in poling of the sample.

The postmilled mixture was dried at 80°C and calcined for 2 h at 950°C. To ensure formation of the perovskite structure, a diffraction pattern was taken of the calcined powder using a diffractometer (Model Pad-V, Scintag, Santa Clara, CA). The diffraction pattern showed no zirconia impurities which could have resulted from the long milling step.

The calcined powder was crushed and put through a 150- $\mu\text{m}$  sieve. The powder was then mixed with 3 to 4 wt% binder (5200, DuPont, Wilmington, DE) and pressed under a pressure of  $1 \times 10^8 \text{ N/m}^2$  (100 MPa) into green disks with a diameter of 1.9 cm. All samples were fired on a platinum sheet in a closed alumina crucible at 1100°C for 20 h. In anticipation of lead evaporation during the calcination and sintering steps, an extra 2 mol% PbO was added to the initial composition. A radial shrinkage of 15% occurred during sintering, and all samples showed a dark-gray appearance with an average density of 6.61  $\text{g/cm}^3$  (94% of theoretical). Theoretical density ( $\rho_T = 7.03 \text{ g/cm}^3$ ) was calculated from the equation,

$$\rho_T = \frac{ZM}{N_0 a^2 c} \quad (3)$$

where  $Z$  is the number of molecules in a unit cell (one for perovskites),  $N_0$  the Avogadro number ( $6.02 \times 10^{23}$  atoms/mol),  $M$  the composition weight, and  $a$  and  $c$  the lattice constants calculated from the plane spacing equation for a tetragonal system.

After the disks were polished with 0.3- $\mu\text{m}$  alumina, gold electrodes were sputtered on each face. Samples were then poled in heated silicone oil (100°C) at fields ranging from 10 to 60 kV/cm for 10 min. Because samples poled relatively easily, it was not necessary to pole while cooling through  $T_c$ .

## (3) Piezoelectric and Dielectric Measurements

The longitudinal piezoelectric coefficient,  $d_{33}$ , was measured quasistatically using a Berlincourt  $d_{33}$  meter (Channel Products, Inc., Chagrin Falls, OH). The driving frequency was around 150 Hz. Transverse piezoelectric coefficients,  $d_{31}$ , and elastic constants were calculated using a modified resonance technique.<sup>5</sup> Impedance measurements were made using an impedance analyzer (Model HP 4192, Hewlett-Packard, Palo Alto, CA).  $K$  was calculated from the capacitance of a sample which was measured with an LCR meter at frequencies ranging from 100 Hz to 100 kHz (Model HP 4274A, Hewlett-Packard). To determine  $T_c$ , temperature-dependent capacitance measurements were made as samples were cooled from 200° to -50°C at -3°C/min. Dissipation factor and capacitance were also measured as a function of frequency (100 Hz to 100 kHz) at room temperature.

The hydrostatic charge coefficient,  $d_h$ , was measured by applying a hydrostatic pressure to the sample, thus producing a charge in the poled direction. A hydraulic oil bath was used as a sonic medium for transmission of pressure at 200 Hz. The source of the sound wave was either a speaker or a piezoelectric multilayer actuator. Two PZT standards were positioned on adjacent sides of the measured sample to ensure accurate measurements. The equation determining the hydrostatic coefficient is given by

$$D = \frac{Q}{A} = d_h P \quad (4)$$

where  $D$  is the electric displacement,  $Q$  the charge,  $A$  the area of the sample, and  $P$  the pressure. The charge produced by the sample and standards was converted via a charge amplifier into voltages,  $V_s$  and  $V_{st}$ , respectively, and was measured using a spectrum analyzer (Model HP 3585B, Hewlett-Packard). Because the hydrostatic charge coefficient of the standard,  $d_{hs}$ , was known, the hydrostatic charge of the sample,  $d_h$ , was calculated using the relationship derived from Eq. (4):

$$d_h = d_{hs} \frac{V_s A_{st}}{V_{st} A_s} \quad (5)$$

where  $A_s$  and  $A_{st}$  are the electrode areas of the sample and standard, respectively.  $d_h$  was also calculated using Eq. (1) and measured values for  $d_{33}$  and  $d_{31}$ . The measured and calculated values agreed well.

## III. Results and Discussion

### (1) Piezoelectric and Dielectric Properties

Table I summarizes the average results of dielectric and piezoelectric measurements taken on five samples of each composition. As stated previously, a goal of this work was to increase  $K$  from the current values reported for similar materials (up to 400) to the 500 range. Permittivity is within that range for strontium-doped samples but significantly lower for barium-doped samples. Lower permittivity in addition to higher  $\tan \delta$  values associated with barium-doped samples are limiting factors for their use in hydrophone applications.

A microstructural evaluation of these samples revealed strontium- and barium-doped samples to have similar grain sizes (6 to 9  $\mu\text{m}$ ) when sintered for 20 h. This is lower than reported values of 10  $\mu\text{m}$  when samples of the same, undoped composition were sintered for only 5 h.<sup>6</sup> It is likely that doping with strontium and barium inhibited grain growth. Emission diffraction spectroscopy on a scanning electron microscope did reveal a minor second phase in the 4 mol% strontium composition but only on extended sintering times (30 h). This phase was rich in the transition metals doped into the lead titanate: cobalt, tungsten, and manganese. Since the second phase was a minor phase, it was not noticed on X-ray diffraction patterns and was never apparent at sintering times less than 30 h.

This minor second phase, in addition to increased grain growth, may have caused decreased piezoelectric properties at sintering times longer than 20 h. Modified lead titanates were shown to sinter via a transient liquid phase at 30 h.<sup>6</sup> Duran *et al.*<sup>6</sup> used this sintering process to explain decreased density values with increased sintering times. Sintering times less than 20 h did result in slightly higher loss values and decreased piezoelectric anisotropy. As a result, 20 h appears to be the optimal sintering time.

The hydrostatic piezoelectric coefficient for strontium-doped samples increased with the concentration of dopant, reaching the maximum value of  $82 \times 10^{-12} \text{ C/N}$  for  $x = 0.06$ . The trend of  $d_h$  in barium-modified samples is opposite, decreasing  $d_h$  values with increasing barium amount. Compositions which contain strontium consistently exhibit a higher  $d_{33}/d_{31}$  ratio than barium-doped samples, with the 4 mol% strontium composition exhibiting the best overall properties. Large  $d_h$  ( $81 \times 10^{-12} \text{ C/N}$ ) and voltage sensitivity ( $g_h = 18 \times 10^{-3} \text{ mV/N}$ ) values result in a figure of merit of  $1458 \times 10^{-15} \text{ m}^2/\text{N}$ , which compares well with recently reported values.<sup>1</sup>

### (2) Aging Study

Lead titanate ceramics with small amounts of additives have long been known for a very low aging in dielectric and piezoelectric properties.<sup>7</sup> In addition to reduced motion of oxygen vacancies resulting from low defect concentrations, low aging is a function of the high tetragonality ratio ( $c/a = 1.06$ , where  $c$



# APPENDIX 15

**Table I.** Selected Dielectric and Piezoelectric Properties for  $\text{Pb}_{0.65}\text{Ca}_{0.35-z}\text{Me}_z\text{Ti}_{0.94}(\text{Co}_{0.5}\text{W}_{0.5})_{0.06}\text{O}_3$  Ceramics, where Me is Sr or Ba

Property	Composition, z (mol%)					
	Strontium			Barium		
	0.02	0.04	0.06	0.02	0.04	0.06
Dielectric constant, $K$	647	509	441	425	349	316
Dielectric loss, $\tan \delta$ (%)	1.6	1.3	1.4	2.2	2.3	2.6
Transition temperature, $T_c$ (°C)	106	120	132	135	158	178
Piezoelectric transverse coefficient, $d_{31}$ ( $10^{-12}$ C/N)	-1.7	-2.5	-3.0	-2.1	-2.1	-2.8
Piezoelectric longitudinal coefficient, $d_{33}$ ( $10^{-12}$ C/N)	70	86	88	77	65	63
Piezoelectric anisotropy, $d_{33}/d_{31}$	44/1	34/1	29/1	36/1	31/1	22/1
Hydrostatic charge coefficient, $d_h$ ( $10^{-12}$ C/N)	66	81	82	73	61	57
Hydrostatic voltage coefficient, $g_h$ ( $10^{-3}$ mV/N)	11	18	12	19	20	20
Figure of merit $d_h g_h$ ( $10^{-15}$ m <sup>2</sup> /N)	726	1458	1722	1387	1220	1140

and  $a$  are the tetragonal axes) of the unit cell. Aging experiments are usually performed at room temperature, which, in cases of lead titanate, is far from its  $T_c$ . Under such conditions, the mobility of the domain walls and, thus, aging, will be low.

A relatively low  $T_c$  (120°C) and low anisotropy of the unit cell in the 4 mol% strontium sample led to an investigation of the aging behavior of this sample. The tetragonality ratio, as measured from X-ray diffraction, was below 1% ( $c/a = 1.008$ ). To ensure accurate reproducibility of measurements, samples were fixed to a sample holder and placed in an atmospheric chamber set at 40°C and 99% humidity. Under experimental conditions, there was no significant deviation in piezoelectric coefficients, dielectric constant, or dissipation factor after 120 h. Figure 1 illustrates piezoelectric data from an aging experiment on the 4 mol% strontium composition.

### (3) Poling Study

Ease of polarization is another advantage of strontium-doped compositions over similar materials. Calcium-modified lead titanates were reported to require 50 kV/cm to give optimal properties,<sup>3</sup> whereas compositions modified with samarium needed a field of 60 kV/cm.<sup>1</sup> The 4 mol% composition showed no increase in piezoelectric coefficient or dielectric constant over 20 kV/cm at 100°C. Only the dissipation factor needed a field of 30 kV/cm to reach a minimum value. The need for a lower poling field is a result of the low  $T_c$  and small tetragonality which facilitated domain wall rearrangement.

## IV. Summary

This investigation demonstrates that it is possible to achieve dielectric constants over 500 while keeping the large anisotropy in piezoelectric properties for calcium-modified lead titanate by doping them with strontium. Because of a low tetragonality and a low transition temperature, the composition  $\text{Pb}_{0.65}\text{Ca}_{0.31}\text{Sr}_{0.04}\text{Ti}_{0.94}(\text{Co}_{0.5}\text{W}_{0.5})_{0.06}\text{O}_3$  requires low poling fields at moderate temperatures. The low transition temperature and tetragonality ratio did not increase the aging rate of the above composition.

**Acknowledgment:** The authors would like to thank Mr. Ron Turner and Mr. Roger Vandermark of Piezokinetics for their assistance. The work of Mr. Paul Moses and Mrs. Peg Klingler in the experimental setup for  $d_h$  measurements is also greatly appreciated.

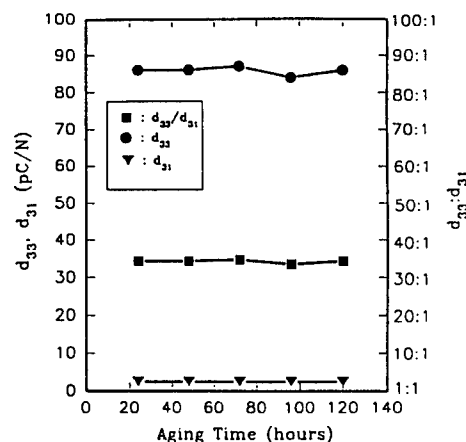


**Fig. 1.**  $d_{33}$ ,  $d_{31}$ , and  $d_{33}/d_{31}$  versus aging time for  $\text{Sr}_{0.04}$ —illustration of aging behavior for the best composition.

## References

- K. M. Rittenmyer and R. Y. Ting, "Piezoelectric and Dielectric Properties of Calcium- and Samarium-Modified Lead Titanate Ceramics for Hydroacoustic Applications," *Ferroelectric*, **110**, 171-82 (1990).
- D. Damjanovic, T. R. Gururaja, and L. E. Cross, "Anisotropy in Piezoelectric Properties of Modified Lead Titanate Ceramics," *Am. Ceram. Soc. Bull.*, **66** [4] 699-703 (1987).
- K. Takeuchi, D. Damjanovic, T. R. Gururaja, S. J. Jang, and L. E. Cross, "Electromechanical Properties of Calcium-Modified Lead Titanate Ceramics," pp. 402-405 in *Proceedings of the Sixth IEEE International Symposium on Applications of Ferroelectrics* (Lehigh University, Bethlehem, PA). Institute of Electrical and Electronic Engineers, New York, 1986.
- K. Takeuchi, "Electromechanical Properties of Modified Lead Titanate," Master's Thesis, Department of Electrical Engineering, The Pennsylvania State University, University Park, PA, 1986.
- D. J. Taylor, D. Damjanovic, A. S. Bhalla, and L. E. Cross, "Complex Piezoelectric, Elastic, and Dielectric Coefficients of La-Doped  $0.93\text{Pb}(\text{Mg}_{1/3}\text{Nb}_{2/3})\text{O}_3$ - $0.07\text{PbTiO}_3$  Under DC Bias," *Ferroelectric Lett.*, **11**, 1-9 (1990).
- P. Duran, J. F. Fernandez Lozano, F. Capel, and C. Moure, "Large Electromechanical Anisotropic Modified Lead Titanate Ceramics, Part 1, Processing," *J. Mater. Sci.*, **23**, 4463-69 (1988).
- I. Ueda and S. Ikegami, "Piezoelectric Properties of Modified  $\text{PbTiO}_3$  Ceramics," *Jpn. J. Appl. Phys.*, **7**, 236-42 (1968).

## DOMAIN SWITCHING AND MICROCRACKING DURING POLING OF LEAD ZIRCONATE TITANATE CERAMICS

E. C. SUBBARAO,† V. SRIKANTH, W. CAO and L. E. CROSS

*Materials Research Laboratory, The Pennsylvania State University,  
University Park, PA 16802-4800 USA*

*(Received December 17, 1992)*

The application of a DC electric field (poling) to a ferroelectric lead zirconate titanate (PZT) ceramic aligns domains in the field direction. The non 180°-domain switches involve mechanical deformations, which are detected as acoustic emission signals. Concurrent with AE signals, electrical current pulses arise from domain reorientations. When the poling field is large and domain switches are extensive, the resulting deformations, under the constraint of neighboring domains or grains, may exceed the elastic limit and cause microcracking. The onset and propagation of microcracking during poling of PZT is signalled by the appearance of continuous AE signals, unaccompanied by current pulses, in contrast to intermittent AE signals accompanied by corresponding current pulses during domain switching. The onset and extent of microcracking established by this method is confirmed by scanning electron micrographs and decrease in the value of piezoelectric coefficient ( $d_{33}$ ) and mechanical quality factor ( $Q_M$ ). The amplitude of AE signals due to domain switches are spread widely, while that of AE signals caused by microcracking occur in a narrow range around 50 db.

*Keywords: Acoustic emission, PZT, domain switching, microcracking*

### INTRODUCTION

The polar direction of ferroelectric crystals can be changed by an applied electric field. Due to the existence of many variants in the low temperature ferroelectric phase, a ceramic (polycrystalline) sample contains many randomly oriented regions of uniform polarization, called domains, upon transforming from the high temperature non-ferroelectric (paraelectric) phase, thus eliminating net polarization.<sup>1</sup> For many practical applications such as a piezoelectric device, the ceramic must be poled (i.e., subjected to a DC electric field) to align the polar axes as fully as possible in the field direction so that the ceramic acquires a net (non-zero) polarization. The fact that only partial alignment of domains is possible in a ceramic is reflected in the rounded D-E hysteresis loop compared to a square loop of a ferroelectric single crystal, and in a spontaneous polarization ( $P_s$ ) value of about 8  $\mu\text{C}/\text{cm}^2$  for a ceramic versus 26  $\mu\text{C}/\text{cm}^2$  for a single crystal of  $\text{BaTiO}_3$ .<sup>1</sup>

Associated with the spontaneous polarization ( $P_s$ ), there is a spontaneous strain ( $e_s$ ), which is proportional to  $P_s^2$ . This strain is a consequence of the fact that the polar axis is elongated compared to other crystallographic axes. When the ferroelectric domain switches by 180°, there is no strain change and hence does not affect its neighbors. On the other hand, domain reorientations by 90° cause max-

†Permanent address: Tata Research Development & Design Center, 1 Mangaldas Road, Pune 411001, India.

imum strain change, leading to intergranular stresses (Figure 1). Thus, domain switching during the poling process proceeds to minimize the total energy and accommodate the elastic deformation. For example, only 12% of the domains switch by  $90^\circ$  upon application of an electric field to ceramic  $\text{BaTiO}_3$  and half of them revert back on removal of the field.<sup>2,3</sup> This constraint by surrounding grains does not affect domain switches by  $180^\circ$ , since no strain is involved in this case.

Extensive studies on  $\text{BaTiO}_3$  single crystals have shown<sup>4-7</sup> that the domain switching is a nucleation and growth process. It starts with a wedge shaped domain of the new polarization state, proceed with a fast forward growth rate and slow sideways growth rate, finally the wedge taking the shape of a stripe across the grain or crystal. Ultimately the two  $180^\circ$  domain walls move sideways to widen the new polar region to complete the switching process.

Lead zirconate titanate (PZT) is a solid solution of ferroelectric lead titanate ( $\text{PbTiO}_3$ ) and antiferroelectric lead zirconate ( $\text{PbZrO}_3$ ). A composition at 48%  $\text{PbTiO}_3$ —52%  $\text{PbZrO}_3$  exhibits a morphotropic phase boundary (MPB), separating a tetragonal  $\text{PbTiO}_3$ -rich and a rhombohedral  $\text{PbZrO}_3$ -rich ferroelectric phases. Many properties (dielectric constant, piezoelectric coefficients, etc.) peak at this

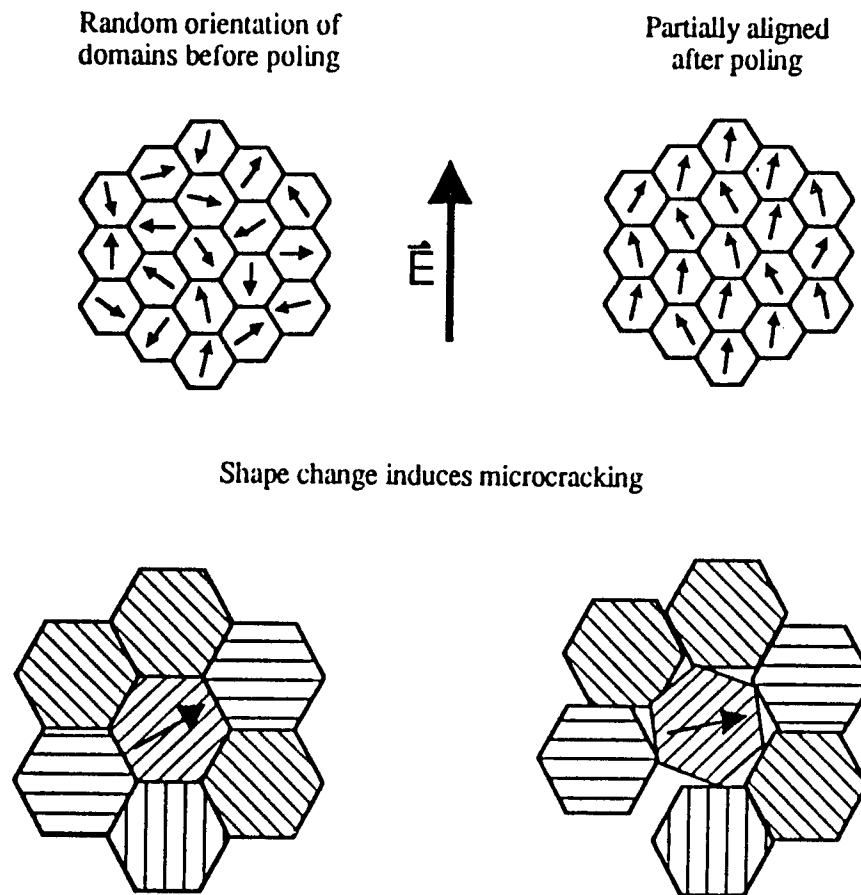


FIGURE 1 Schematic of domain structure of a ferroelectric ceramic before and after poling.

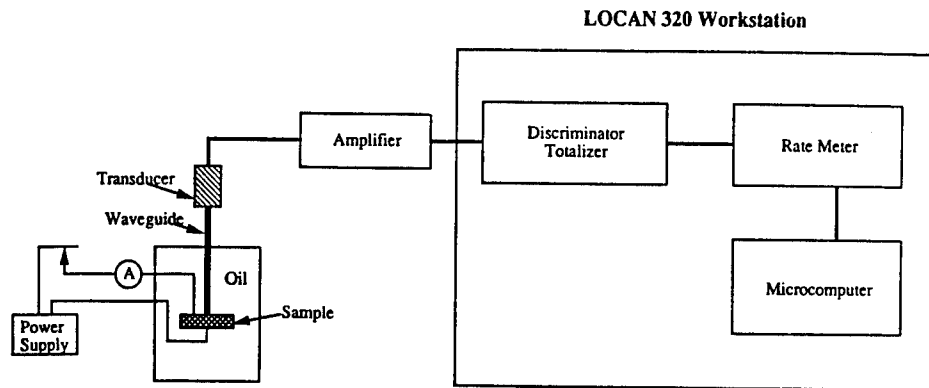


FIGURE 2 Schematic of experimental arrangement used for simultaneous detection of acoustic emission and current pulses during poling of a ferroelectric ceramic.

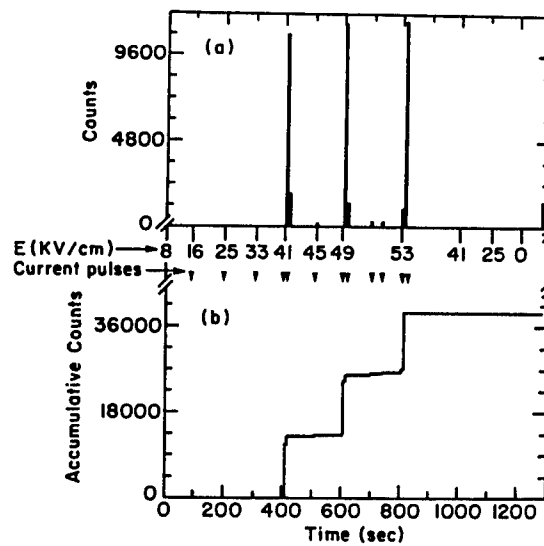


FIGURE 3 Acoustic emission count rate (a) and total AE counts (b) as a PZT ceramic (sample C) is poled to successively higher fields. The current pulses were observed at times indicated by triangles in this and succeeding figures (4 and 5).

TABLE I  
Microcracking and electrical properties of poled PZT

Sample	Extent of Poling and Microcracking	$d_{33}$ ( $10^{-12}$ C/N)	QM
C	Poled but no onset of microcracking	333	89
SS	Poled till microcracking barely starts	350	65
B	Poled till microcracking starts	200	49
E	Poled till extensive microcracking occurred	119	

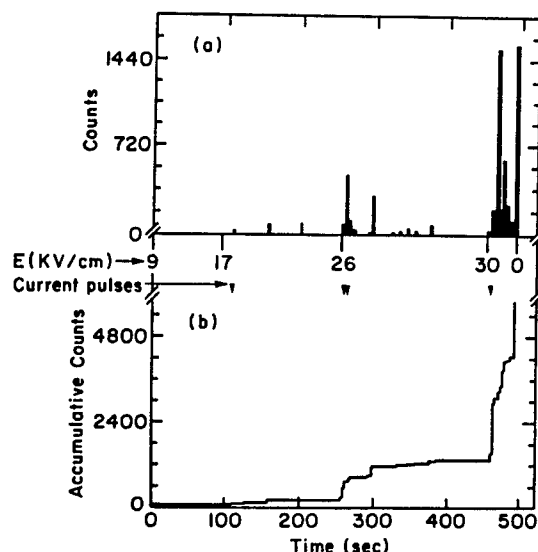


FIGURE 4 Similar data as in Figure 3 but for another sample B, poled till microcracking just starts.

composition, presumably due to the increase in the number of energetically degenerate states which makes the switching of domains easier under the influence of an electric field.<sup>8</sup> The higher Curie temperature (360°C vs 120°C), remanent polarization (47 vs 8  $\mu\text{C}/\text{cm}^2$ ) and piezoelectric coefficients make PZT far superior to  $\text{BaTiO}_3$  for piezoelectric applications. In fact, PZT is the leading electromechanical transducer material for over a quarter century and therefore is chosen for the present study.

The effect of electric field on the extent of domain reorientations in PZT is somewhat different in the tetragonal and rhombohedral phase regions. In tetragonal PZT, it is estimated that 66 $\frac{2}{3}$ % of all dipoles instead of the initial 16 $\frac{2}{3}$ % become aligned within the sextant around the poling direction.<sup>9</sup> On the other hand, dipoles switch by 71°, 109° and 180° in the rhombohedral phase. For PZT modified by  $\text{Nb}^{5+}$  ion addition, it is suggested that 74% of the dipoles are present in the octant around the poling direction.<sup>8</sup> The larger  $P_r$  value and the higher degree of domain orientation in PZT make the remanent polarization of PZT substantially higher than that of  $\text{BaTiO}_3$ . The improvement in planar coupling coefficient ( $k_p$ ) of PZT as a function of poling conditions (field, time and temperature) has been studied by Chiang *et al.*<sup>10</sup>

As already pointed out, the non-180° domain switches involve strain changes and hence demand the coordination of neighbor domains. The microdeformations arising from the domain wall movements, though small in magnitude, are detectable by sensitive acoustic emission methods.<sup>11,12</sup> The poling effects on acoustic velocity and attenuation in poled and unpoled PZT ceramics were studied as a function of temperature and frequency.<sup>14</sup> Application of a large electric field (or mechanical stress) can lead to microcracking, due to internal stresses.<sup>15</sup> Electrically induced microcracking in PZT has been shown to be dependent on grain size and tetragonality<sup>10,14,16-19</sup> and is detected by microscopy<sup>20</sup> and dielectric measurements. The external parameters influencing the extent of microcracking are the poling conditions (field, time and temperature).<sup>19,21</sup> Microcracking results in a deterio-

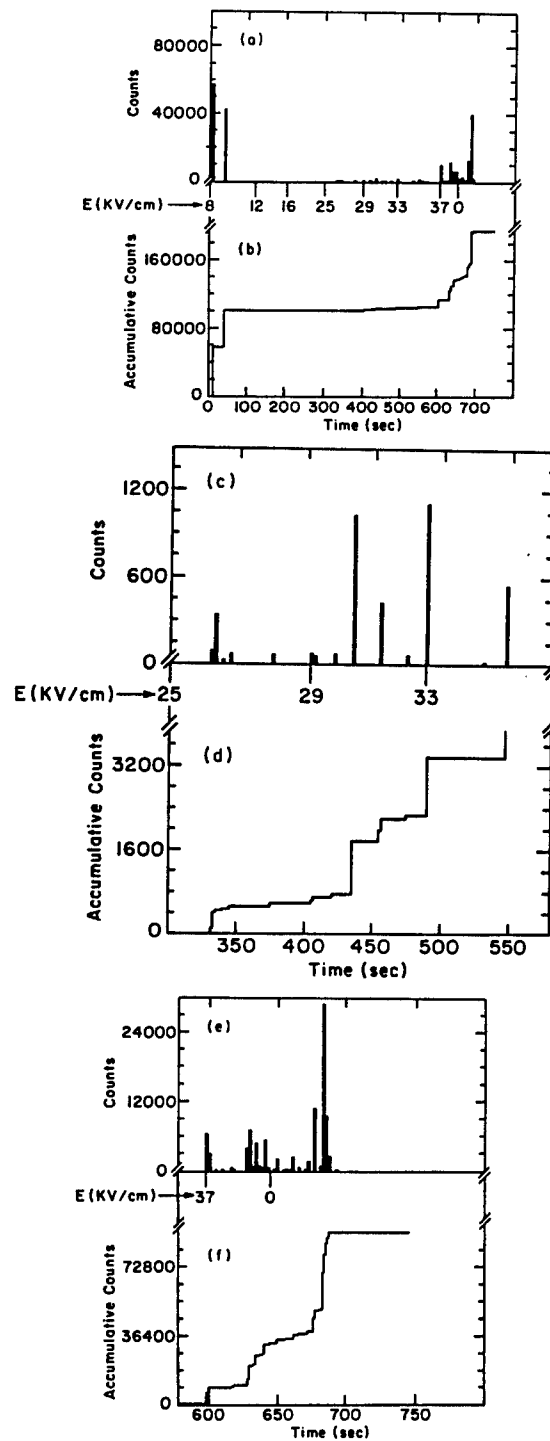


FIGURE 5 Same as in Figure 3 for sample SS but the electric field is maintained even after the onset of continuous AE counts, signifying beginning of microcracking. The regime just before [Figures (c) and (d)] and just after [Figures (e) and (f)] the onset of microcracking is shown in detail.

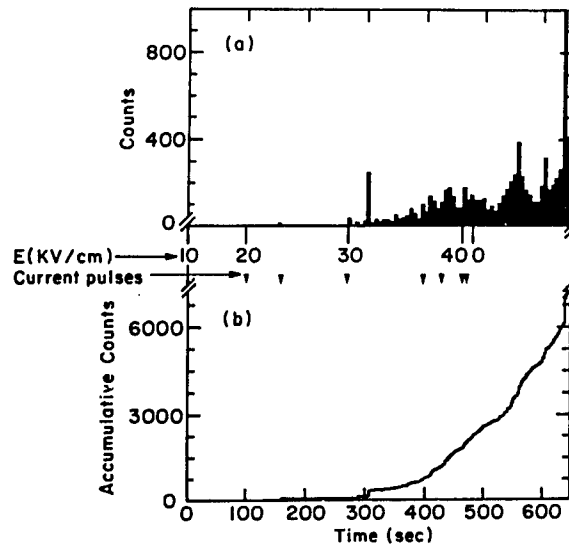


FIGURE 6 Same as in Figure 5 for sample *E* but the electric field is retained for extensive microcracking to occur, as indicated by continuous AE counts.

ration of electrical and mechanical properties of the ceramic<sup>21–23</sup> and hence should be minimized if not eliminated. Uchino *et al.* have studied AE signals in piezoelectric and electrostrictive actuators subjected to bipolar and unipolar electric fields and also after repeated cycles of thermal shocking.<sup>24</sup> They found that the unipolar field does not lead to acoustic emission, unless the samples have suffered mechanical damage as by thermal shocking.

The acoustic emission technique has recently been applied to the study of domain switching, as well as the occurrence and recombination of microcracks in ferroelectric  $\text{PbTiO}_3$  ceramics as it is heated and cooled.<sup>25</sup>

From the above discussion it is clear that poling is a critical process for achieving optimum piezoelectric properties of a ferroelectric ceramic. The domain reorientations which give rise to enhanced piezoelectric behavior also give rise to mechanical stresses, which can lead to microcracking, if the induced stresses exceed the elastic limit of the material. Therefore poling should be carried out to obtain maximum domain reorientation, but without the onset of the microcracking process, provided there is a simple, reliable means to distinguish the two deformation processes.

The purpose of the present study is to delineate the microdeformations accompanying domain switching from those due to microcracking during poling of PZT ceramics, as a contribution toward a better understanding and optimization of the poling process. Simultaneous detection of acoustic emission and electrical current pulses were employed in the study and the results are substantiated by scanning electron micrographs and electrical property measurements.

## EXPERIMENTAL

Ceramic lead zirconate titanate (PZT) composition (52%  $\text{PbZrO}_3$ , 48%  $\text{PbTiO}_3$ ) at the morphotropic phase boundary (MPB) was prepared by conventional method.



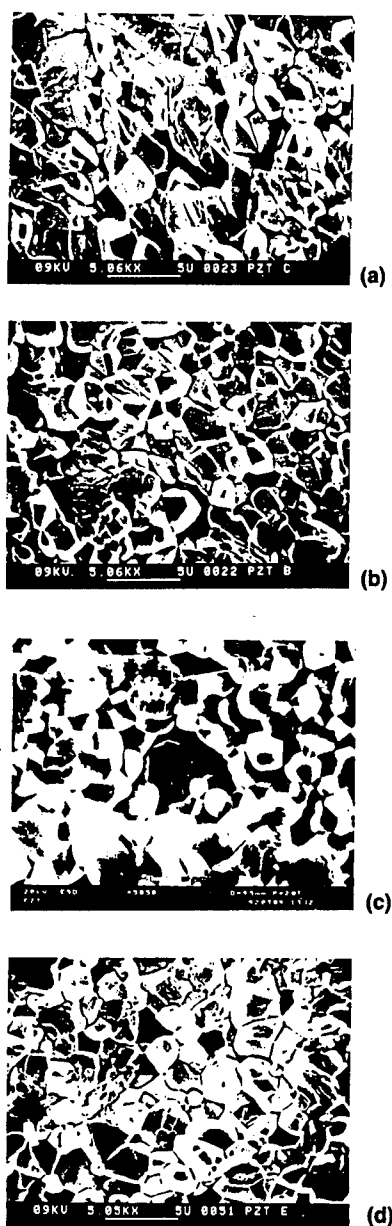


FIGURE 7 Scanning electron micrographs of PZT ceramic (a) as sintered; (b) poled, but not microcracked (sample C); (c) poled till microcracking started (sample B); (d) poled and extensively microcracked (sample E).

Stoichiometric proportions of reagent grade oxides (PbO from Hammond Lead Products, Potterstown, Pennsylvania,  $\text{ZrO}_2$  from Harshaw Chemical Co., Cleveland, Ohio, and  $\text{TiO}_2$  from J. T. Baker Chemical Co., Phillipsburg, New Jersey) were mixed in a polyethylene bottle for 12 hours using ethyl alcohol as wetting agent and  $\frac{1}{8}$ " diameter zirconia balls as grinding media. Excess lead oxide (0.5 wt%)

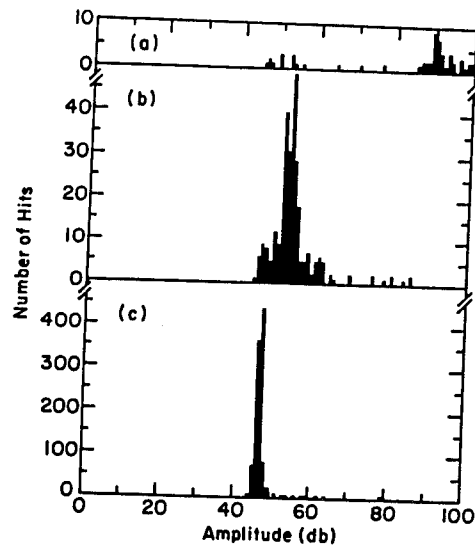


FIGURE 8 Number of AE hits vs amplitude for samples with (a) only domain reorientations (sample C), (b) both domain reorientations and initial microcracking (sample B) and (c) extensive microcracking (sample E). Note the scale change for (c) from (a) and (b).

was added to compensate for lead loss during calcination. The milled powder was dried at 80°C for 24 hours and calcined at 900°C for 24 hours. X-ray diffraction examination confirmed the formation of the perovskite phase. After mixing with 2% polyvinyl alcohol binder, the powder was pressed into pellets at 105 MPa. The binder was removed by heating at 350°C for three hours and 550°C for three hours. The pellets were sintered at 1250°C for five hours in closed crucibles in PbO atmosphere, at a rate of 5°C/min during heating and 3°C/min during cooling.

Sintered PZT ceramic discs were polished to obtain two parallel faces, which were then electroded with sputtered gold. The electroded disc is located in a suitable holder and immersed in a silicone oil bath at 50°C. High DC field is applied in a stepwise fashion from a power supply (Tred COR-A-TROL), while an alumina rod serving as a wave guide rests on the ceramic disc. A transducer is mounted at the other end of the wave guide. Acoustic emission signals are collected, filtered and analyzed by appropriate electronic circuitry and displayed as counts or count rate as a function of time (Locan 320 System from Physical Acoustics Corp.). The schematic of the experimental arrangement is shown in Figure 2. A microammeter is placed in the voltage input lead of the poling circuit, to detect current pulses arising from domain switching, superimposed on leakage current.

After various stages of poling, the samples were examined for piezoelectric coefficient,  $d_{33}$ , using a Berlincourt  $d_{33}$  meter, for mechanical quality factor,  $Q_M$ , using IRE standard method, and for microstructure and microcracks from scanning electron micrographs.

## RESULTS AND DISCUSSION

A PZT ceramic sample (C) was poled in successive steps of increasing DC field at intervals of 100 sec, while acoustic emission signals and current pulses were recorded

(Figure 3). No AE signals were detected until a poling field of 41 kv/cm was applied (though a few current pulses were observed as soon as poling field  $\geq 16$  kv/cm was applied). The current pulses (2–12 mA) were superimposed on a steady leakage current of 0.5 to 3 mA. It can be seen that a substantial number of AE signals occur as soon as the poling field is increased, though a smaller number of AE counts were recorded at irregular time intervals during the application of a fixed poling field, in agreement with earlier reports.<sup>12</sup> Everytime AE counts occurred, there were accompanying current pulses. Evidently both the AE and current pulses arise from domain reorientations. After 800 sec, the field was reduced in steps to zero at 1200 sec. While no AE counts were detected till the applied field was dropped to zero, AE counts were indeed recorded nearly 60 sec after removal of the field and these AE events may reflect domain reversals. The piezoelectric coefficient,  $d_{33}$ , of this sample was  $333 \pm 7 \times 10^{-12}$  C/N. The scanning electron micrograph of this sample [Figure 7(b)] is similar to that of a virgin sample [Figure 7(a)] and does not show clear microcracking, though grain boundaries become more obvious. The sample has a mechanical quality factor ( $Q_M$ ) of 89 (Table I).

An example of a sample (B) which was subjected to a stepwise increase of the poling field till microcracking just starts, as evidenced by continuous AE counts instead of intermittent AE signals, is shown in Figure 4. The field was quickly reduced to zero soon after the appearance of continuous AE counts. While current pulses were observed corresponding to the intermittent AE signals, no current pulses were observed during the continuous occurrence of AE counts. The  $d_{33}$  value of this sample is lower at  $\sim 200 \times 10^{-12}$  C/N and the scanning electron micrograph does not show any significant microcracking [Figure 7(c)].

These results were confirmed with another PZT ceramic sample (SS) which shows a large number of AE counts as soon as a poling field of 8 kv/cm is applied (poling temperature 50°C), but no further AE counts till the field applied was 25 kv/cm at 300 sec (Figure 5). There were intermittent AE signals as the poling field was increased stepwise from 25 kv/cm to about 37 kv/cm at 600 sec [Figures 5(c) and (d)]. In this regime AE counts were invariably accompanied by current pulses up to 60 mA. As soon as continuous AE counts started appearing at about 620 sec, the poling field was turned off. The AE counts continued which may indicate domain reversals [Figures 5(e) and (f)]. Since the microcracking process was quickly interrupted, the  $d_{33}$  was nearly unaffected (350).

The stepwise poling of another sample (E) was continued beyond the occurrence of intermittent AE signals accompanied by associated current pulses (of up to  $\sim 40$  mA) to the regime where AE counts occur continuously but no current pulses are detected (Figure 6). We believe that the onset of continuous AE counts must signify the beginning of microcracking due to excessive mechanical stresses generated by extensive domain switching. The poling field was reduced to zero at 480 sec but AE counts persisted for sometime (at least up to 640 sec) suggesting further microcracking or propagation of cracks till adequate stress relief is attained. Due to the extensive microcracking, the  $d_{33}$  value ( $119 \times 10^{-12}$  C/N) and  $Q_M$  were severely affected (Table I). The scanning electron micrograph of this sample [Figure 7(d)] shows extensive intergranular cracking.

The threshold amplitude for the AE experiments was set at 45 db. The distribution of the magnitude of the detected AE signals for three samples is given in

Figure 8. It can be seen that the number of hits increases and the amplitude spread decreases as the extent of microcracking changes from none to minor to extensive. When acoustic emission signals arise from domain reorientations, their amplitude reflects a wide range of accompanying microdeformations, depending upon the original domain orientations and the magnitude of the poling field [Figure 8(a)]. On the other hand, the initiation and propagation of microcracking is driven by stress concentrations in the ceramic and the corresponding AE signals occur in a narrow amplitude range [Figure 8(c)]. The case where domain reorientations and initial microcracking occur simultaneously represents an intermediate situation [Figure 8(b)]. This is in agreement with the observation of Pan and Cao,<sup>13</sup> who state that the AE signal amplitude is maximal at the polarization switching and minimal when the poling is established. Iwasaki and Izumi<sup>11</sup> also find that the peak of AE counts occurs at lower amplitude range and the spread of amplitude narrow as the poling field is increased.

## CONCLUSIONS

Application of a DC field to ferroelectric ceramics (poling) causes domain reorientations in the field direction. All but the 180° domain switches involve dimensional changes leading to mechanical stresses due to the constraint of the neighboring grains in a ceramic. When the stresses exceed the bonding strength between grains, the ceramic suffers microcracking, resulting in deterioration of electrical ( $d_{33}$ ,  $k_p$ ,  $e$ , etc.) and mechanical ( $Q_M$ , strength, etc.) properties. The present study established that concurrent AE counts and current pulses are observed when domain switches take place during poling. The onset and progress of microcracking is signalled by continuous AE counts but no accompanying current pulses. The delineation of domain switching from microcracking by this approach is corroborated by changes in electrical and mechanical properties and scanning electron micrographs and constitutes a simple, reliable, non-destructive in-situ means to control the poling process to achieve optimum piezoelectric properties in a ferroelectric ceramic.

## ACKNOWLEDGEMENT

The authors are grateful to the Office of Naval Research for financial support.

## REFERENCES

1. F. Jona and G. Shirane, *Ferroelectric Crystals*, McMillan, New York (1962).
2. E. C. Subbarao, M. C. McQuarrie and W. R. Buessem, *J. Appl. Phys.*, **28**, 1194 (1957).
3. H. G. Baerwald, *Phys. Rev.*, **105**, 480 (1957).
4. R. C. Miller and A. Savage, *Phys. Rev.*, **112**, 755 (1958).
5. W. J. Merz, *J. Appl. Phys.*, **27**, 938 (1956).
6. E. A. Little, *Phys. Rev.*, **98**, 978 (1955).
7. R. C. Bradt and G. S. Ansell, *J. Am. Ceram. Soc.*, **52**, 192 (1969).
8. B. Jaffe, W. R. Cook, Jr. and H. Jaffe, *Piezoelectric Ceramics*, Academic Press, New York (1971).
9. D. Berlincourt and H. H. A. Krueger, *J. Appl. Phys.*, **30**, 1804 (1959).
10. S. S. Chiang, R. M. Fulrath and J. A. Pask, *J. Am. Ceram. Soc.*, **64**, C-141 (1981).

11. H. Iwasaki and M. Izumi, *Ferroelectrics*, **37**, 563 (1981).
12. C. S. Wang, X. X. Yi, G. C. Xu, X. G. Zhu and J. P. Zhou, *Appl. Acoustics*, p. 39 (1984) in Chinese.
13. W. Pan and H. Cao, *Ferroelectrics*, **129**, 119 (1992).
14. C. K. Jen, C. J. Chung, G. Shapiro, J. R. Monchalin, P. Langlois and J. F. Bussiere, *J. Am. Ceram. Soc.*, **70**, C-256 (1987).
15. R. C. Pohanka, R. W. Rice and B. E. Walker, Jr., *J. Am. Ceram. Soc.*, **59**, 71 (1976).
16. H. T. Chung, B. C. Shin and H. G. Kim, *J. Am. Ceram. Soc.*, **72**, 327 (1989).
17. C. I. Cheon, S. J. Kin and H. G. Kim, *Ferroelectrics*, **115**, 35 (1991).
18. F. Kroupa, K. Nejezchleb, J. Rataj and I. Saxl, *Ferroelectrics*, **100**, 281 (1989).
19. B. C. Shin and H. G. Kim, *Ferroelectrics*, **100**, 209 (1989).
20. F. Kroupa, K. Nejezchleb and I. Saxl, *Ferroelectrics*, **88**, 123 (1988).
21. H. T. Chung and H. G. Kim, *Ferroelectrics*, **76**, 327 (1987).
22. K. Nejezchleb, F. Kroupa, M. Boudys and J. Zelenka, *Ferroelectrics* **81**, 339 (1988).
23. S. W. Freiman, *Proc. Sixth IEEE Intl. Symp. on Applications of Ferroelectrics*, Lehigh Univ., Bethlehem, p. 367 (1986).
24. K. Uchino, T. Hirose and A. M. Varaprasad, *Japan J. Appl. Phys.*, **26**, Suppl. 26-2, 167 (1987).
25. V. Srikanth and E. C. Subbarao, *Acta. Metall. Mater.*, **40**, 1091 (1992).

# APPENDIX 16

## DIELECTRIC PROPERTIES OF SINGLE GRAIN IN PLZT FERROELECTRIC CERAMICS

Q. Y. JIANG, E. C. SUBBARAO, L. E. CROSS  
Materials Research Laboratory, The Pennsylvania State University  
University Park, PA. 16802

(Received for Publication October 1, 1993)

**Abstract** The hot pressed and grain-grown transparent ceramics with maximum grain size 80~100  $\mu\text{m}$  provides the possibility of investigating the dielectric properties of single grain from ceramic specimens. The ion milling technique was employed to separate the grains. The dielectric permittivities of single grain of PLZT have been measured. It is found that the range of dielectric constant of single grains in unpoled state is larger than that of the bulk ceramic. Poling in both single grains and bulk ceramics reduces the dielectric constant in the poling direction, and increases it in the direction perpendicular to the poling field. The anisotropy of dielectric permittivity for PLZT 8/65/35 is calculated from the single grain data.

Lanthanum doped lead zirconate titanate (PLZT) ceramic system has been the subject of much interest due to their high optical transparency, excellent electro-optical characteristics, unusually high dielectric constant and piezoelectric constants, and square ferroelectric hysteresis loop with low coercive field.<sup>1,2</sup> PLZT ceramic is one of the best candidate materials for electro-optical devices and the non-volatile memory devices which have been developed rapidly in recent years.

Unfortunately, single crystal growth of PLZT is so difficult that it can only be made as a polycrystalline ceramic. Thus, there are no single crystal data available. However, the transparent PLZT polycrystalline ceramic with maximum grain size 30 to 100  $\mu\text{m}$  can be obtained from the hot pressed specimens by the grain-growth technique, which provides the possibility of investigation of the physical properties of the single grain from ceramic samples. In the present work, the dielectric constants of the PLZT single grain in unpoled and poled states and the temperature dependence of dielectric constant of single grain thick specimens were measured. The results are compared with the thick PLZT ceramic samples.

The composition of the PLZT is 8/65/35 (La/Zr/Ti, mole ratio) and this composition is located near the rhombohedral, tetragonal, and cubic phase boundary. PLZT 8/65/35 exhibits typical ferroelectric relaxor behavior.<sup>3,4</sup> Small discs with diameters ranging from 6  $\mu\text{m}$  to 100  $\mu\text{m}$  were obtained by the ion milling technique as follows. First the sample was polished, cleaned, and annealed at 600 °C for 1 hour, then one face of the sample was metallized with aluminium. After bonding to a thin glass

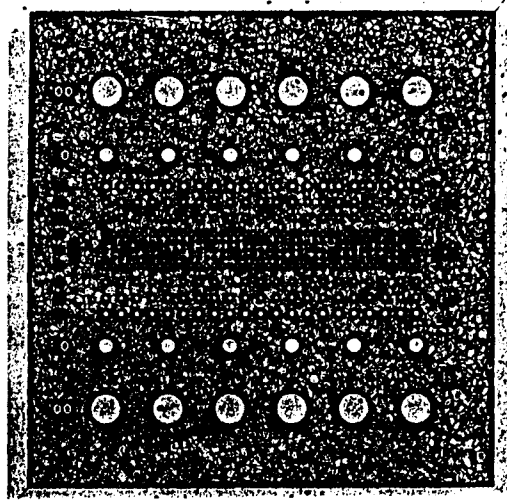


FIGURE 1. The top view of the ion milled PLZT sample (area 1). Figures on the left side are diameters of the dots (ranged from 6  $\mu\text{m}$  to 100  $\mu\text{m}$ ), and figures on the right side are the number of dots for each diameter.

slip, the sample was lapped to 8.9  $\mu\text{m}$  thickness. Then the top surface was also metallized with gold. After reticulation masking was applied to the top of the surface of the two regions, the edges of the dots were defined by ion milling. The milling depth was 2  $\mu\text{m}$  for one region (called area 1) and 7  $\mu\text{m}$  for another region (called area 2). The view of the well defined discs with diameters of 100  $\mu\text{m}$ , 50  $\mu\text{m}$ , 20  $\mu\text{m}$ , 15  $\mu\text{m}$ , 12  $\mu\text{m}$ , 10  $\mu\text{m}$ , 8  $\mu\text{m}$ , and 6  $\mu\text{m}$  for area 1 is shown in Figure 1. Area 2 which was ion milled to a depth of 7  $\mu\text{m}$  is not shown here.

The dielectric permittivity (constant) for each disc of different diameters was measured with General Radio 1621 Precision Capacitance Measurement System at 1 KHz. The contact between disc and measurement device was made possible by probes through the optical microscope.

The dielectric constant measured from the discs of all sizes in area 1 and area 2 at room temperature without prepoling are shown in Figure 2(a) and (b), respectively. For each diameter the measurements were carried out on at least five discs, and for some diameters on more than 30 discs. The dielectric constants of discs with different size ranged from 3800 to 8000 for area 1, and 4200 to 9000 for area 2. A dispersion of the dielectric constants of the discs with same diameter was observed (Fig. 2), and the effect was larger as the diameter of the disc decreased. The change of the dielectric constant ranged from 12% for 100  $\mu\text{m}$  diameter to 47% for 6  $\mu\text{m}$  diameter (Fig. 2(a)). From Figure 2 one can see that the average dielectric constant of area 2 is larger than that of area 1. This can be more clearly seen in Figure 3, in which the temperature dependence of dielectric constant of 100  $\mu\text{m}$  and 50  $\mu\text{m}$  discs in area 1 and area 2 are shown. The different mechanical boundary conditions between two areas due to the different milling depth (2  $\mu\text{m}$  and 7  $\mu\text{m}$  for area 1 and 2, respectively) are responsible for this difference. 78% of the disc edge in area 2 was free and 22% of the edge was clamped, compared with 22% free and 78% clamped in area 1.

The grain boundaries in area 1 are clearly visible under the optical microscope, and the discs with only single grains in them (including 8, 10, 12, and 15  $\mu\text{m}$  diameters)



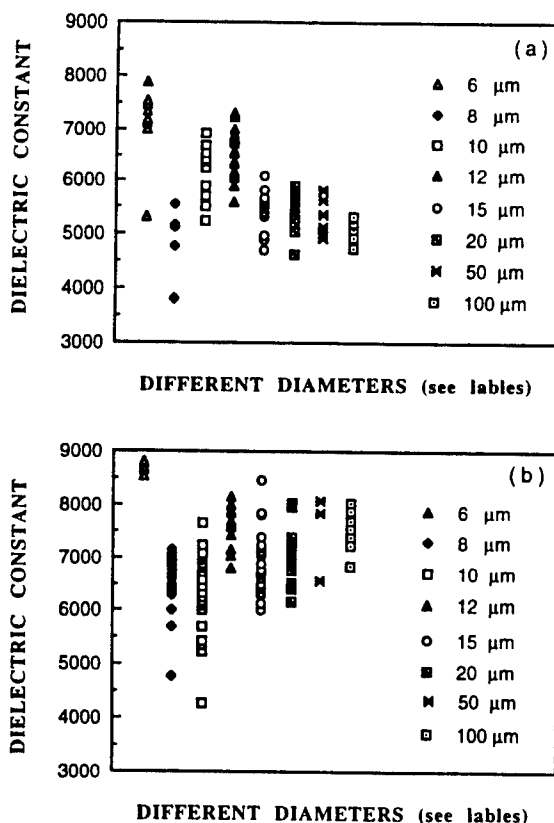


FIGURE 2. The dispersion of the dielectric constant of different diameters for discs of all sizes in (a) area 1 and (b) area 2 at 1 kHz without prepoling.

could be distinguished from those with multigrains (contained 1 to 3 grain boundaries). The dielectric constants of these single grains in unpoled states are shown in Figure 4(a) together with those of multigrains of same diameters (Figure 4(b)). There are no dramatic changes of the dielectric constants in single grains and multigrains. This can be understood by the fact that the polarization in an unpoled single grain is not aligned along one direction, and many microdomains existed within a grain. Therefore, both the multigrain discs and the single grain discs are assemblies of multidomains, except that the multigrain discs contained grain boundaries also. The results in Figure 4 also indicate that the grain boundaries connected parallel to grains do not significantly affect dielectric permittivity.

Anisotropy of the dielectric permittivity in PLZT single grains could be studied by poling the single grain discs under DC field (20 Kv/cm) larger than the coercive field (5 Kv/cm). The dielectric constants measured before and after poling are shown in Figure 5 and Table 1. The poled dielectric constants are smaller than the unpoled ones, which is in agreement with the dielectric data obtained from bulk PLZT ceramics by us. This can be explained by the formation of macrodomains from microdomains under high DC field<sup>5</sup>. The contribution to the weak field properties by microdomains is greatly reduced. The extent of the decrease of the dielectric constant was not always same for all single grain

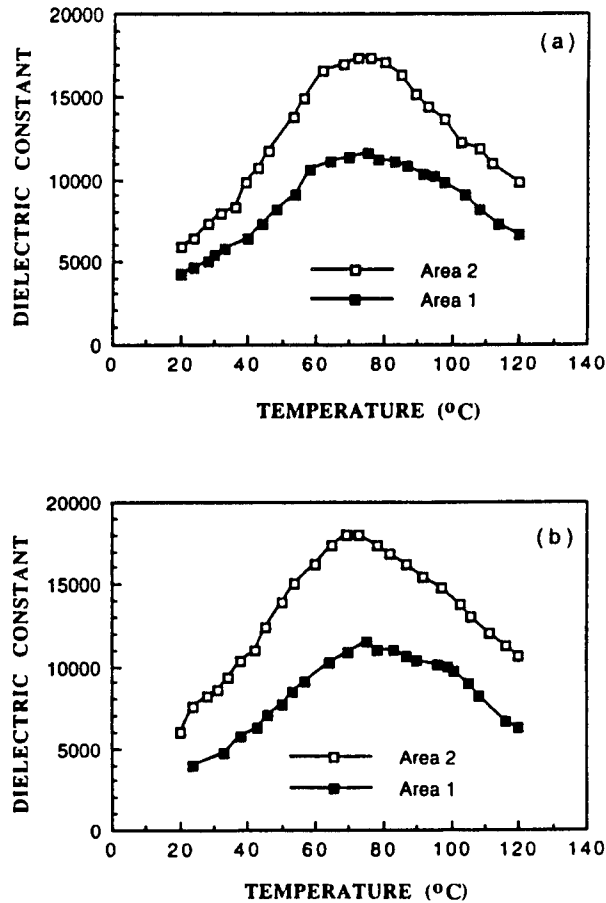


FIGURE 3. Temperature dependence of the dielectric constant of ion milled PLZT sample with disc diameter (a) 50  $\mu\text{m}$  and (b) 100  $\mu\text{m}$ .

TABLE 1 The Measured Dielectric Constant for Both Single Grains and bulk Ceramic of PLZT 8/65/35.

	Dielectric Constant	
	Single grains	Bulk ceramic
Unpoled	5000 ~ 7000	4500 ~ 5000
Prepoled	3000 ~ 6000	4100 ( $K_{33}$ ) 5900 ( $K_{11}$ )

discs both with different diameters and same diameter, and the decrease ranged from 8% to 30%. Since the crystallographic axes of the single grains are not always aligned in the same direction, the angle between the measured direction and crystallographic axis after poling is a function of individual grains, ranging from  $0^\circ$  to  $\pm 30^\circ$  for orthorhombic phase,  $0^\circ$  to  $\pm 35.5^\circ$  for rhombohedral phase, or  $0$  to  $\pm 45^\circ$  for tetragonal phase, provided that the poling is complete. The poled phase of PLZT 8/65/35 is orthorhombic.<sup>6, 7</sup> If we take the

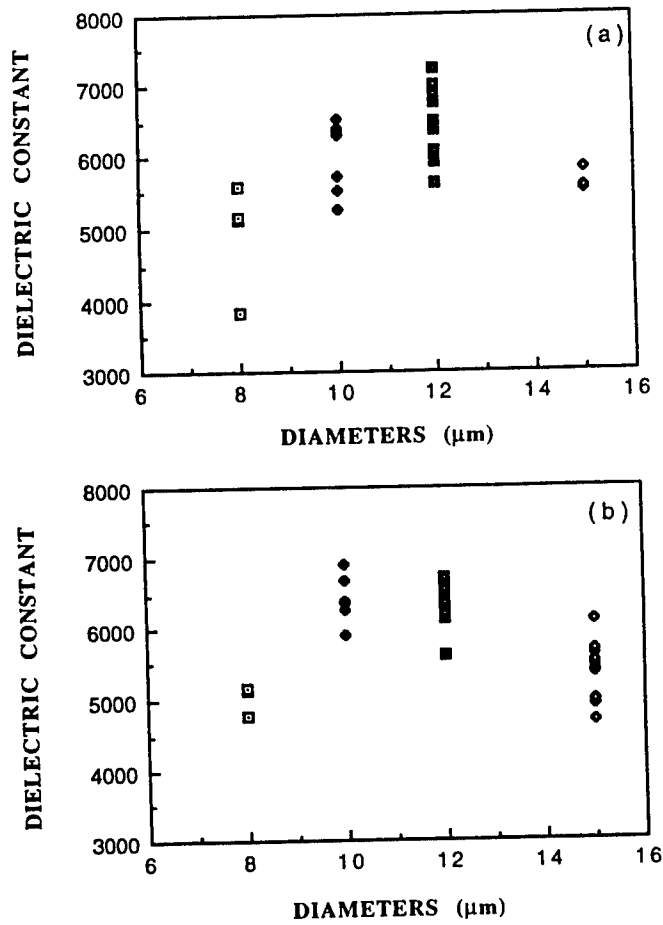


FIGURE 4. The dispersion of the dielectric constant of (a) single grains and (b) multigrains for four diameters at 1 kHz without prepoling.

minimum of the measured single grain dielectric constant as the  $K_{33}^T$  which is 3000, and the maximum 6000 as  $K^T$  along the direction of  $30^\circ$  away from the  $c$  axis (Table 1). The relationship among  $K_{11}^T$ ,  $K_{33}^T$ , and  $K^T$  for single grain is

$$K^T = (1 - (\cos 30^\circ)^2) K_{11}^T + (\cos 30^\circ)^2 K_{33}^T, \quad (1)$$

where it is assumed that  $K_{22}^T \sim K_{11}^T$ , since the lattice parameters  $a$  (5.777Å) and  $b$  (5.794Å) are very close in 8/65/35 composition.<sup>6</sup> After replacing  $K_{33}^T$  and  $K^T$  by 3000 and 6000 in equation (1), we have

$$K_{11}^T = 15000.$$

The calculated  $K_{11}^T$  is larger than  $K_{pole}^T$  (3000 ~ 6000) and  $K_{unpole}^T$  (5000 ~ 7000) in single grains, which is consistent with the results of the bulk PLZT 8/65/35 samples in which the measured  $K_{11}^T$  (perpendicular to the poling direction) is 5900, and  $K_{33}^T$  (parallel to the poling direction) is 4100, and  $K_{unpole}^T$  is 5000 (Table 1).

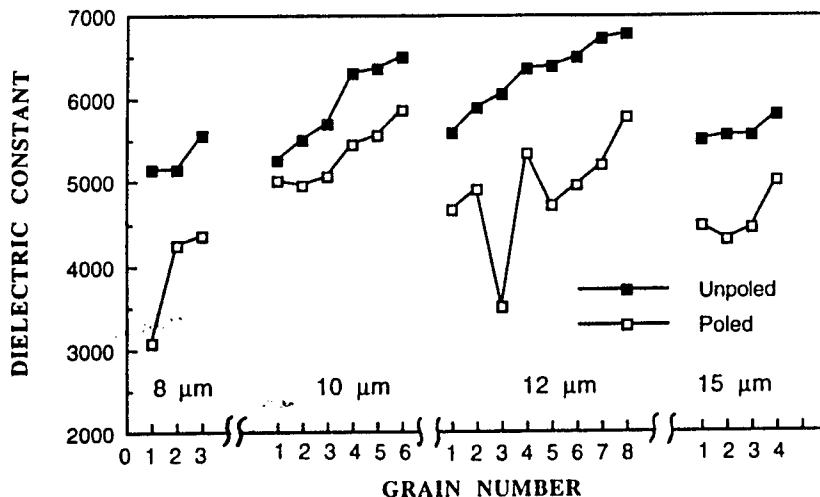


FIGURE 5. The dielectric constant of single grains measured before and after poling for four diameters.

In conclusion, the anisotropy of dielectric permittivity for PLZT 8/65/35 has been derived from the data measured from the single grains. The dielectric constant in c direction is  $\leq 3000$ , and in a or b direction  $\geq 15000$ . The range of dielectric constant (5000 ~ 7000) of single grains in unpoled state is larger than that of the unpoled bulk ceramic (4500 ~ 5000). The parallel grain boundaries do not severely affect the dielectric property of PLZT, but the mechanical boundary condition can influence the dielectric measurement. It is found that both in single grains and bulk ceramics poling process reduces the dielectric constant along the direction parallel to the poling field, and increases it along the direction perpendicular to the poling field, which is different from the PZT normal ferroelectric ceramics.

ACKNOWLEDGEMENT: The authors wish to thank Shanghai Institute of Ceramics in China for providing PLZT samples, and D. J. Pedder and R. A. C. Bache in Plessey Company for helping preparing samples by ion milling.

#### REFERENCES:

1. G. H. Heartling and C. E. Land, *J. Am. Cer. Soc.*, **54**, 1 (1971).
2. C. E. Land, P. D. Thacher, and G. H. Heartling, *Appl. Solid State*, **4**, 137 (1974).
3. M. Yokosuka and M. Marutake, *Jap. J. Appl. Phys.*, **25**, 981 (1986).
4. Fan Shemin, He Jiawen, and Xi Yao, *Ferroelectrics*, **77**, 181 (1988).
5. Yao Xi, Chen Zhili, and L. E. Cross, *J. Appl. Phys.*, **54**, 3399 (1983).
6. E. T. Keve and K. L. Bye, *J. Appl. Phys.*, **46**, 810 (1975).
7. E. T. Keve, *Ferroelectrics*, **10**, 169 (1976).

# APPENDIX 17

## SOFT PIEZOELECTRIC $(1-x)\text{Pb}(\text{Sc}_{1/2}\text{Ta}_{1/2})\text{O}_3$ - $(x)\text{PbTiO}_3$ CERAMICS WITH HIGH COUPLING FACTORS AND LOW $Q_M$

J.F. Wang, J.R. Giniewicz, and A.S. Bhalla  
Materials Research Laboratory  
The Pennsylvania State University  
University Park, PA USA

(Received for Publication July 15, 1993)

**ABSTRACT:** The piezoelectric behavior of materials from the  $(1-x)\text{Pb}(\text{Sc}_{1/2}\text{Ta}_{1/2})\text{O}_3$ - $(x)\text{PbTiO}_3$  solid solution system has been investigated. The  $[x=0.45]$  composition in particular has exhibited an outstanding piezoelectric response [ $d_{33}=650$  (pC/N),  $k_t=0.5$ ,  $k_p=0.61$ ,  $k_{33}=0.73$ ] and a low mechanical quality factor [ $Q_M \approx 30$ ]. These features make it a promising candidate for a variety of piezoelectric sensor applications. The difficulties involved in effectively poling a bar sample and a means to avoid these problems are also addressed.

### INTRODUCTION

Piezoelectric ceramics have found wide application as both sensing and actuating devices due in large part to their considerable efficiency in converting mechanical energy to electrical energy and vice versa and the relative ease of manufacturing as compared with the growth of single crystals. The early work on the  $\text{Pb}(\text{Zr}_{1-x}\text{Ti}_x)\text{O}_3$  [PZT] solid solution system by Jaffe et al.<sup>1</sup>, which showed the markedly enhanced piezoelectric performance of the morphotropic phase boundary compositions, has been followed by investigations of a number of other so-called morphotropic phase boundaries [MPB] occurring in binary, ternary, and quaternary system around which enhanced piezoelectric responses are observed. It should be noted that the "morphotropic phase boundaries" identified for many of these systems show some curvature at high temperatures and, therefore, strictly speaking, are not truly temperature independent as the name suggests; the boundary between crystalline phases is hence identified as a MPB in the sense that it is a boundary separating phases whose structure-type depends largely on composition, especially at low temperatures.

The solid solution of interest in this investigation is  $(1-x)\text{Pb}(\text{Sc}_{1/2}\text{Ta}_{1/2})\text{O}_3$ - $(x)\text{PbTiO}_3$  [PSTT] in which such a MPB occurs between rhombohedral and tetragonal phases over a narrow range of compositions  $[x=0.4-0.45]$  as pictured in Figure 1.<sup>2</sup> The focus of this study was to evaluate the piezoelectric response of ceramics prepared from this composition range by means of a resonance method.

Communicated by Dr. George W. Taylor

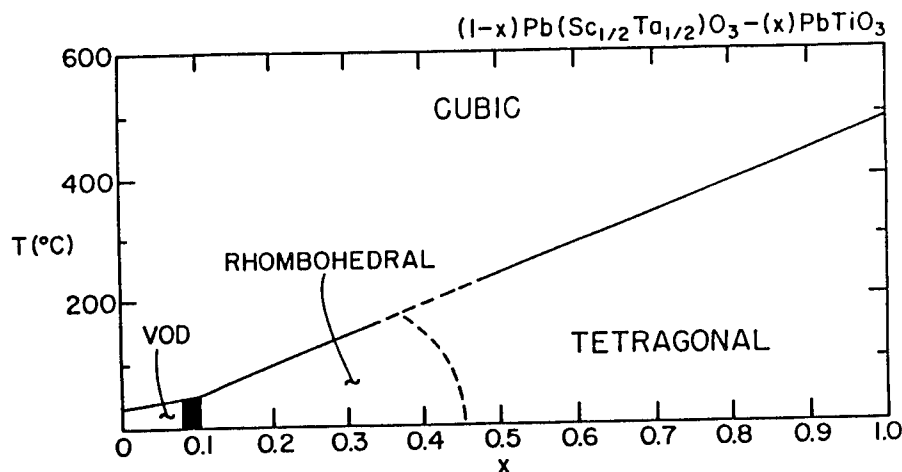


Figure 1: A preliminary depiction of the  $(1-x)\text{Pb}(\text{Sc}_{1/2}\text{Ta}_{1/2})\text{O}_3-(x)\text{PbTiO}_3$  system highlighting the proposed MPB region.

#### SAMPLE PREPARATION

The  $(1-x)\text{Pb}(\text{Sc}_{1/2}\text{Ta}_{1/2})\text{O}_3-(x)\text{PbTiO}_3$  ceramics were produced by a conventional mixed-oxide method involving the use of high purity starting compounds, a precursor-phase formulation, and controlled lead atmosphere sintering. The compositions of interest were initially prepared as powders employing a wolframite  $\text{ScTaO}_4$ <sup>3</sup> precursor method<sup>4</sup> in order to reduce the occurrence of undesirable pyrochlore phases. Starting oxides  $\text{Sc}_2\text{O}_3^\dagger$  and  $\text{Ta}_2\text{O}_5^\dagger$  were batched and calcined at  $1400^\circ\text{C}$  for 6-8 hours to form the  $\text{ScTaO}_4$  precursor. The compositions of interest were then formulated from  $\text{PbO}^\dagger$ ,  $\text{TiO}_2^\dagger$ , and the precursor phase. Each composition was calcined at  $900^\circ\text{C}$  for 4 hours and at  $1000^\circ\text{C}$  for 1 hour with an intermediate comminution step. Compacted specimens were then fired at  $1400^\circ\text{C}$  for one hour within sealed alumina crucibles containing  $\text{Pb}(\text{Sc}_{1/2}\text{Ta}_{1/2})\text{O}_3/\text{PbZrO}_3$  source powders.

Three sample geometries were required to evaluate the piezoelectric coefficients and coupling factors: (a) **Disks**: 0.06 (cm) in thickness and 1.0-1.2 (cm) in diameter, (b) **Bars**: 1.0-1.2 (cm) in length and with 0.04-0.0625 (cm<sup>2</sup>) cross-sectional areas, and (c) **Rectangular Blocks**: 0.06-0.08 (cm) in thickness and 0.8-1.0 (cm) on edge. Sputtered gold electrodes were applied to all specimens.

## EXPERIMENTAL PROCEDURE

The samples were poled in a stirred oil bath under a poling field of 20 (kV/cm), held at a temperature in the vicinity of the transition temperature for about 20 minutes, and then cooled slowly with the field to  $-50^\circ\text{C}$ . The poling field was then removed.

The dielectric constant was determined for disk-shaped specimens from capacitance data collected by means of an impedance analyzer [Hewlett-Packard HP-4192A]. The electromechanical coupling factors,  $k_p$  and  $k_{31}$ , were also determined for disk-shaped samples from the series and parallel resonance frequencies associated with the radial mode vibration of the specimen as measured by means of either a spectrum analyzer [Hewlett-Packard HP-3585A] or a network analyzer [Hewlett-Packard HP-3577A]. The mechanical quality factor,  $Q_M$ , may then be calculated utilizing the series and parallel resonance frequencies and the series resistance,  $R_1$ , (measured at the series resonance frequency of the radial vibration) using the impedance analyzer. The longitudinal thickness (laterally clamped) electromechanical coupling coefficient,  $k_t$ , was derived from the series and parallel resonance frequencies of the thickness vibrational mode of the disk-shaped or rectangular specimen and the longitudinal coupling factor,  $k_{33}$ , was similarly derived for bar-shaped specimens in the extensional vibration mode. The longitudinal piezoelectric strain coefficient,  $d_{33}$ , was measured directly making use of a Berlincourt  $d_{33}$  meter [Model CPDT-3300, Channel Products, Inc.] while the measurement of the hydrostatic piezoelectric coefficient,  $d_h$ , was conducted according to a conventional procedure.<sup>5</sup> The corresponding piezoelectric voltage coefficients,  $g_{33}$  and  $g_h$ , were subsequently calculated according to the relationship  $[g_{ij}=d_{ij}/\epsilon_{ij}]$ .

## RESULTS AND DISCUSSION

The elastic, dielectric, and piezoelectric properties of the MPB compositions [ $x=0.4$  and  $x=0.45$ ] are recorded in Table I along with those of two of the more sensitive, low  $Q_M$  PZT-based<sup>6</sup> ceramics. The higher piezoelectric and dielectric responses and lower mechanical quality factor ( $Q_M$ ) were observed for the [ $x=0.45$ ] PSTT composition, comparable with those of the PZT materials, which, together with the high elastic

---

† PbO [Johnson Matthey - Materials Technology UK - Grade A1];  $\text{Sc}_2\text{O}_3$  [Boulder Scientific Co. - 99.99%];  $\text{Ta}_2\text{O}_5$  [Hermann C. Starck (Berlin) - Stand. Opt. Grade];  $\text{TiO}_2$  [Aesar (Johnson Matthey Inc.) - 99.999%]



**Table I:** Elastic, dielectric, and piezoelectric properties of MPB compositions [x=0.4] and [x=0.45].

	PSTT [x=0.40]	PSTT [x=0.45]	PZT-5A <sup>ε</sup>	PZT-5H <sup>ε</sup>
$\rho$ (g/cc)	8.1	8.2	7.75	7.5
$\epsilon_3/\epsilon_c$	1205	3510	1700	3400
$T_d$ (°C)	185	205	365	193
$\sigma$	0.32	0.43	0.35	0.29
$s_{11}^E [10^{-12} \text{ m}^2/\text{N}]$	12.4	16.8	16.4	16.5
$Q_{11}$	97	30	75	65
$d_{31}$ [pC/N]	-76	-306	-171	-274
$d_{33}$ [pC/N]	182	655	374	593
$g_{33}$ [mV.m/N]	17	21	25	20
$d_{11}$ [pC/N]	30	43	32	45
$g_{11}$ [mV.m/N]	2.8	1.4	2.1	1.5
$k_t$	0.49	0.50	0.49	0.505
$k_f$	0.36	0.61	0.60	0.65
$k_{31}$	0.21	0.30	0.34	0.39
$k_{33}$	0.58	0.73	0.705	0.75

compliance of the material, make it particularly well-suited for sensor applications. Although the origin of the exceptionally large Poisson's ratio for this composition is not yet fully understood, it is a noteworthy characteristic of the material warranting a more thorough investigation.

Bar-shaped samples [x=0.45], with dimensions as described previously, poled individually for determination of the longitudinal coupling factor,  $k_{33}$  were consistently found to exhibit lower values of  $d_{33}$  [~580-600 (pC/N)] and  $k_{33}$  [~0.71] than what was obtained for a disk-shaped sample poled under identical conditions, indicative of insufficient poling. It is suggested that, in addition to the difficulties in maintaining proper electrical contact to the specimen under these poling conditions, there likely occurs, due to the considerable side surface area of the bar-shaped sample,

a much more pronounced fringing of the poling field around the specimen as compared with that occurring for the thinner disk-shaped sample. In order to inhibit this detrimental effect, four bar samples were bound together with twine and poled together under the same poling conditions originally applied to the individual bar specimens. All specimens from the bundle achieved higher, near optimum values of  $d_{33}$  and  $k_{33}$  [ $d_{33}=630-650$  (pC/N);  $k_{33}=0.73$ ]. Clearly, this is an effective means of avoiding the difficulties of poling bar-shaped specimens; the bundle configuration pictured in Figure 2, where the elements surrounding the specimen to be poled, placed at the center, may be "dummy" pieces of any other suitable material, is proposed as a convenient arrangement for optimizing the field concentration on the piezoelectric bar and hence the degree of poling achieved.

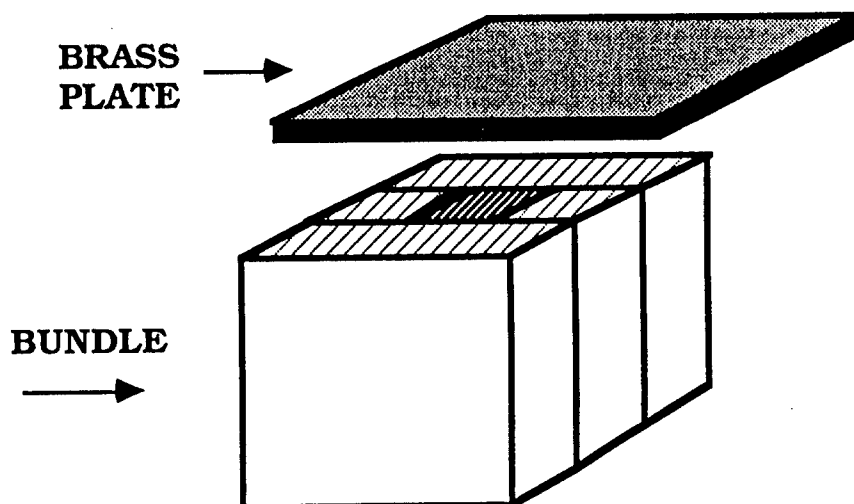


**Figure 2:** Suggested "bundle" configuration for poling bar-shaped piezoelectric specimens. The piezoelectric element is placed at the center of the bundle.

## SUMMARY

The results of this investigation of the piezoelectric response of the MPB compositions  $[x=0.4]$  and  $[x=0.45]$  from the  $(1-x)\text{Pb}(\text{Sc}_{1/2}\text{Ta}_{1/2})\text{O}_3$ - $(x)\text{PbTiO}_3$  solid solution system are summarized below.

(1) The higher piezoelectric response [ $d_{33}=650$  (pC/N),  $k_t=0.5$ ,  $k_p=0.61$ ,  $k_{33}=0.73$ ] and lower mechanical quality factor [ $Q_M=30$ ] were observed for the  $[x=0.45]$  composition distinguishing it as a viable candidate for use as a hydrophone pick-up and various other receiver-type transducer applications.

(2) A notable characteristic of the  $[x=0.45]$  composition is its exceptionally high Poisson's ratio [ $\sigma=0.43$ ]; further investigation is currently underway to better understand the origin and nature of this feature.

(3) An alternative "bundle" method for poling bar-shaped specimens has been suggested which both improves electrode contact and minimizes the detrimental effects of excessive "fringing" of the poling field about the sample. Near-optimum poling was achieved by these means leading to a more accurate measurement of the longitudinal coupling factor,  $k_{33}$ .

## REFERENCES

- [1] B. Jaffe, R.S. Roth, and S. Marzullo, J. Appl. Phys. **25**, 809 (1954).
- [2] J.R. Giniewicz, A.S. Bhalla, and L.E. Cross, Mater. Res. Lett. (submitted).
- [3] JCPDS #24-1017 [ $\text{ScTaO}_4$ ].
- [4] T.R. Shrout and A. Halliyal, Am. Ceram. Soc. Bull. **66**(4), 704 (1987).
- [5] A. Halliyal, A. Safari, A.S. Bhalla, R.E. Newnham, and L.E. Cross, J. Am. Ceram. Soc. **67**(5), (1984).
- [6] Landolt-Börnstein, Group III-Crystal and Solid State Physics (1979).

# APPENDIX 18

## THE COMPLEX PIEZOELECTRIC, ELASTIC, AND DIELECTRIC COEFFICIENTS FOR A LEAD ZIRCONATE-BASED CERAMIC UNDER ELECTRICAL BIAS

E. F. Alberta and A. S. Bhalla  
*Materials Research Laboratory, The Pennsylvania State University,  
University Park, Pennsylvania, 16802 USA*

T. Takenaka  
*Faculty of Science and Technology, Science University of Tokyo,  
Noda, Chiba-ken, 278 JAPAN*

(Received August 9, 1993)

**Abstract** Various material parameters for hot pressed ceramics in the solid solution system (x)  $\text{PbZrO}_3$  - (y)  $\text{Pb}(\text{Zn}_{1/3}\text{Nb}_{2/3})\text{O}_3$  - (z)  $\text{PbTiO}_3$  (PZNT) have been studied. Previous work within this system has shown a morphotropic phase boundary separating the antiferroelectric ( $A_\alpha$ ) and the high temperature rhombohedral ( $F_\alpha$ ) phases. This paper will further explore the electrical field dependence of the complex elastic constants ( $s'_{11}^E$  and  $s''_{11}^E$ ), complex piezoelectric coefficients ( $d'_{31}$  and  $d''_{31}$ ), and dielectric constant ( $K_{33}$ ) near this phase boundary. In addition, these parameters will be compared to those obtained for PZT-5A at room temperature.

### INTRODUCTION

Solid solutions containing PZ have been widely studied in the past due to the antiferroelectric to ferroelectric phase transition and the existence of morphotropic phase boundaries. PZNT is such a system. It is a ternary system composed of the end-members: (x) $\text{PbZrO}_3$  - (1-x) $\text{Pb}(\text{Zn}_{1/3}\text{Nb}_{2/3})\text{O}_3$  [PZZN] and (x) $\text{PbZrO}_3$  - (1-x) $\text{PbTiO}_3$  [PZT]. Previous work has shown that this system contains a room temperature orthorhombic (antiferroelectric) to rhombohedral (ferroelectric) phase boundary. This transition has been located between x=93% PZ in the PZZN end-member and x=94% PZ in PZT end-member.<sup>1</sup>

This paper will explore the complex dielectric, piezoelectric, and elastic properties of the PZNT system. Two compositions, located near the room temperature orthorhombic to rhombohedral phase boundary, have been selected for discussion. They are PZZN (93.2) and PZT (95.0). For comparison, similar measurements have been made on a hot pressed PZT-5 ceramic.

## EXPERIMENTAL PROCEDURES

Hot pressed ceramic samples were prepared by normal ceramic mixed oxide techniques. The samples were thinned and then polished to a 1- $\mu\text{m}$  Diamond finish. Finally, the samples were gold sputtered using a dc magnetron sputtering system.

Room temperature polarization versus electric field hysteresis loops were observed using a computer controlled polarization measurement system. This consisted of a modified Sawyer-Tower circuit interfaced to an IBM-PC and a Trek high-voltage supply. The frequency at which the hysteresis loops were made was 10 Hz and the samples were placed in a silicone oil bath to prevent electrical breakdown at high fields.

The temperature dependence of the dielectric constant was measured at various frequencies in a temperature range from -150°C to 250°C using a computer controlled measurement system. This system consisted of a multifrequency LCR meter (HP4274A, Hewlett Packard Co.), a desktop computer (HP9816, Hewlett Packard Co.), a nitrogen fed furnace (Model-2300, Delta Design Inc.), and a high-voltage power supply (Kiethly-240A). For measurements requiring a higher temperature range, up to 1200°C, a Kanthol wound tube furnace was substituted.

Piezoelectric measurements were made using a modified resonance technique with samples prepared as long thin bars with typical dimensions of 20 x 2 x 0.2 mm. Once poled, fine silver lead wires were attached to the samples using a conducting silver epoxy (E-Solder-3021, Insulating Materials Inc.). Next, the admittance of the specimen near resonance was measured using an impedance analyzer (HP-4192A, Hewlett Packard Co.). To calculate the real and complex compliance,  $s_{11}^E$ , piezoelectric coefficient,  $d_{31}$ , dielectric constant,  $\epsilon_{33}$ , and coupling coefficient,  $k_{31}$ , the equation for the admittance of a bar resonator was used:

$$Y = i \frac{\omega l w}{t} \left( \epsilon_{33}^x - \frac{d_{31}^2}{s_{11}^E} \right) + i \frac{2 w d_{31}^2}{s_{11}^E t (\sqrt{\rho s_{11}^E})} \tan \left( \frac{\omega l \sqrt{\rho s_{11}^E}}{2} \right) \quad (1)$$

Where:  $w$  = width,  $\rho$  = density,  $t$  = thickness,  $\omega$  = frequency, and  $l$  = length. This equation applies to only an ideal resonator; therefore, the piezoelectric coefficients must be assumed to be complex quantities. After introducing the complex nature of  $d_{31}$ ,  $s_{11}^E$ , and  $\epsilon_{33}$  the resulting complex admittance equation is solved by the method described by Damjanovic.<sup>2</sup> This method involves an iterative calculation using an initial guess of the elastic constant and three values of the admittance near the sample's resonant frequency. These calculations are then repeated up to 30 times for statistical purposes.

## RESULTS

### (1) Dielectric Properties:

Using the previously described hysteresis system, the P-E hysteresis behavior of the samples was observed at room temperature. Figure 1(a) shows the resulting hysteresis loop for PZT-5. By applying a maximum electric field of  $\pm 33.0$  kV/cm one finds a coercive field of  $\pm 12.31$  kV/cm and a remnant polarization of  $\pm 33.9$   $\mu\text{C}/\text{cm}^2$ .

The composition PZNT (92.8/0.0), i.e. PZZN (92.8), was also studied. It is on the ferroelectric side of the room temperature antiferroelectric to ferroelectric phase boundary and is therefore in the high temperature rhombohedral (R3m) phase. This composition exhibits a hysteresis loop (figure 1(b)) with a remnant polarization of  $\pm 28.0$   $\mu\text{C}/\text{cm}^2$  and a coercive field of  $\pm 15.9$  kV/cm.

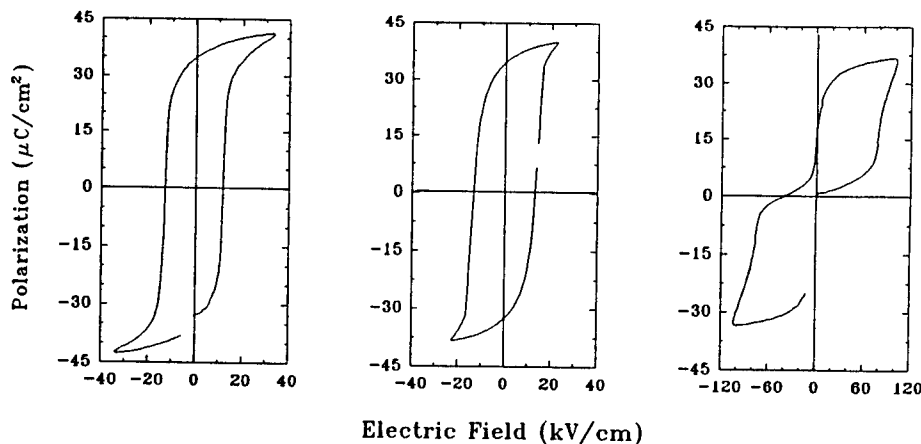


Figure 1. Room temperature hysteresis loops taken at 10 Hz for: (a) PZT-5, (b) PZZN (92.8), and (c) PZT (95.0).

The antiferroelectric case is shown in figure 1(c). This composition is PZNT (95.0/5.0), i.e. PZT (95.0), and shows a relatively linear hysteresis loop until the critical field of  $\pm 79.0$  kV/cm is exceeded. Once the critical field is surpassed the antiferroelectric loop opens up to yield a maximum polarization of  $\pm 35.5$   $\mu\text{C}/\text{cm}^2$  with an applied field of  $\pm 105$  kV/cm.

The dielectric constant of these compositions can be found in figure 2 and also figure 3(c). The temperature and frequency dependence of the PZT-5 sample is shown in figure 2(a). This shows one phase transition,  $T_c$ , at  $268^\circ\text{C}$ . Figure 3(c) shows, as predicted by Takagi<sup>3</sup>, that the dielectric constant decreases with increasing dc bias for ferroelectric phases.

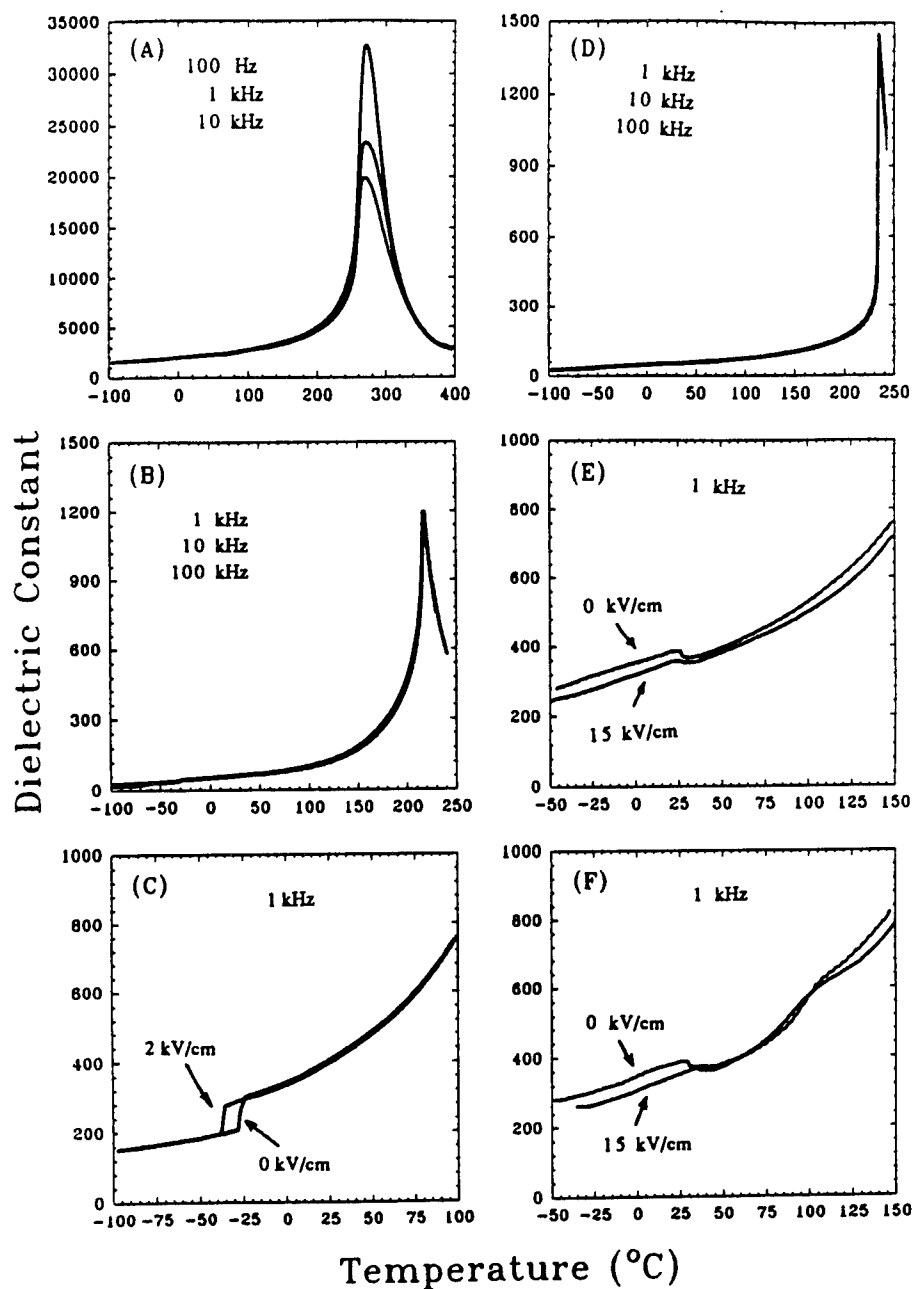


Figure 2. Temperature dependence of the dielectric constant,  $K'_{33}$ , measured during heating and cooling at  $5^{\circ}\text{C}/\text{min}$ . (a) PZT-5 during cooling with no bias. (b) PZZN (92.8) during cooling with no bias. (c) PZZN (92.8) during cooling with 0 kV/cm and 2 kV/cm. (d) PZT (95.0) during cooling with no bias. (e) PZT (95.0) during cooling with 0 kV/cm and 15 kV/cm. (f) PZT (95.0) during heating with 0 kV/cm and 15 kV/cm.



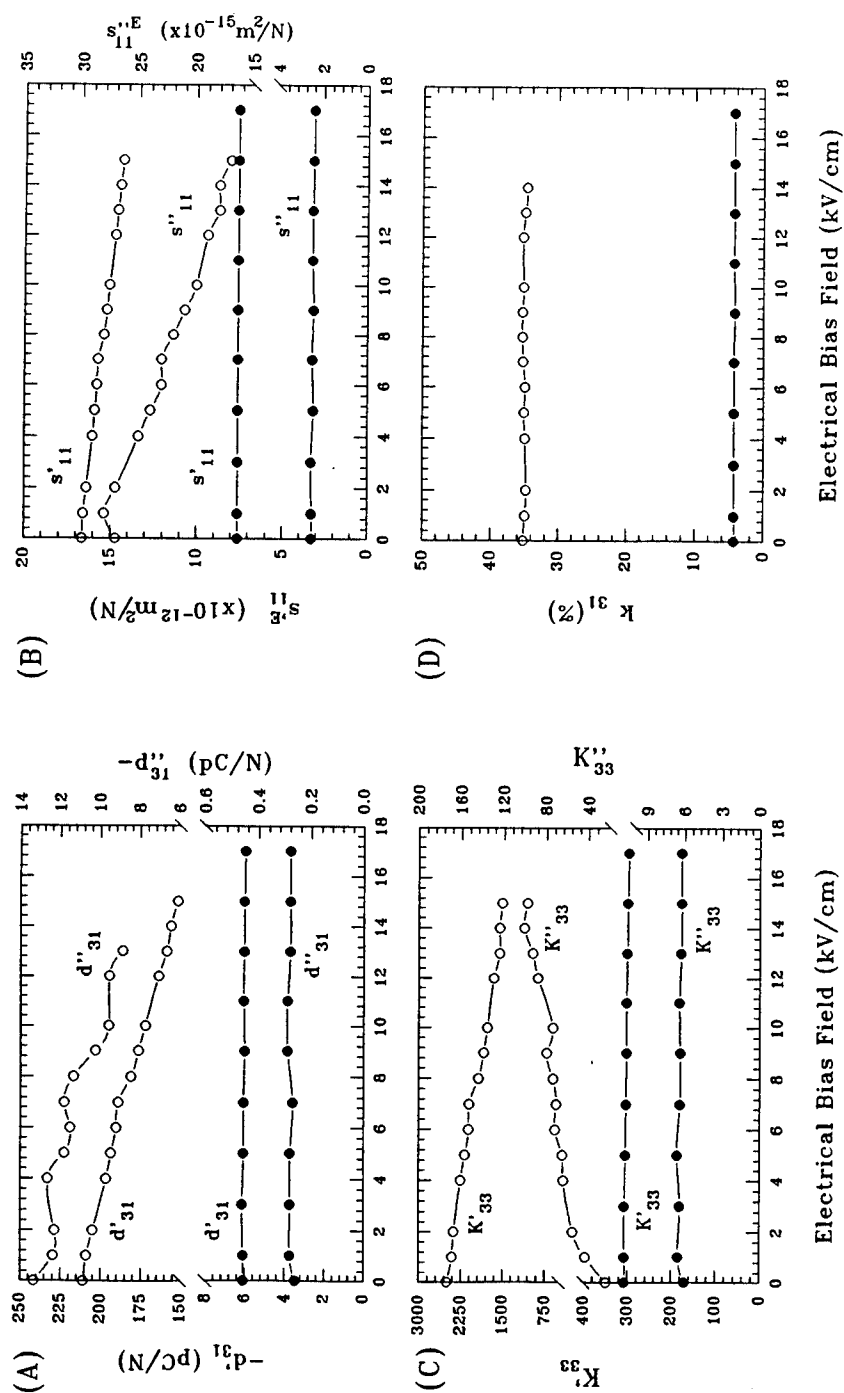


Figure 3. Room temperature properties for PZT-5  $\circ$  and PZNN (92.8)  $\bullet$ . (a) Real ( $d'_{31}$ ) and imaginary ( $d''_{31}$ ) piezoelectric coefficients. (b) Real ( $s'_{11}E$ ) and imag. ( $s''_{11}E$ ) elastic compliance. (c) Real ( $K'_{33}$ ) and imag. ( $K''_{33}$ ) dielectric constants. (d) coupling coefficient ( $k_{31}$ ).

PZZN (92.8) shows slightly more interesting behavior. From figure 2(b) one can first notice the decreased frequency dispersion in this compositions. Next the existence of two phase transition can be found. The Curie temperature has been reduced to 220°C in this composition, and an additional transition is found to occur at -35°C. This second anomaly is due to the high to low temperature rhombohedral phase boundary.

Finally, figure 2(d-f) shows the behavior of the dielectric constant for PZT (95.0). This room temperature antiferroelectric composition shows three phase changes at 26°C, 110°C, and 240°C which correspond to the  $F_{R_{LT}}-A_O$ ,  $A_O-F_{R_{HT}}$ , and  $F_{R_{HT}}-P_C$  transitions. It is also interesting to notice the large thermal hysteresis in the two lower temperature transitions. Finally, dc bias was found to increase the temperature of the ferroelectric to paraelectric and antiferroelectric transitions and decrease that for the ferroelectric to ferroelectric transitions.

#### (b) Piezoelectric and Elastic Properties.

Measurements were taken with the modified resonance technique described earlier. Figures 3(a-d) show the room temperature results for both PZZN (92.8) and PZT-5. No data for PZT (95.0) is given here due to the lack of resonance behavior in this room temperature antiferroelectric composition.

The behavior of PZZN (92.8) is typical of the ferroelectric PZZN and PZNT ceramics near the room temperature antiferroelectric - ferroelectric phase boundary. For this composition all seven measured parameters have been found to be independent of dc bias. At zero field these values are:  $-d_{31} = (6.10 + i 0.26)$  pC/N,  $s_{11}^E = (7.60 + i 0.025) \times 10^{-12}$  m<sup>2</sup>/N,  $K_{33} = (307.45 + i 6.00)$ , and  $k_{31} = 4.24\%$ . In addition,  $d_{33}$  was found using a Berlincourt  $d_{33}$  meter, to be 53 pC/N. Finally, the hydrostatic piezoelectric coefficient,  $d_h$ , has been calculated to be 41 pC/N.

PZT-5 shows much different behavior. Initially, at zero field the measured values are:  $-d_{31} = (210.81 + i 13.32)$  pC/N,  $s_{11}^E = (16.63 + i 0.27) \times 10^{-12}$  m<sup>2</sup>/N,  $K_{33} = (2500 + i 30)$ , and  $k_{31} = 34.75\%$ . With increasing bias these parameters (with the exception of  $k_{31}$ ) show strong field dependence. After increasing the field to 15 kV/cm the values are changed to:  $-d_{31} = (151.66 + i 10.61)$  pC/N,  $s_{11}^E = (14.33 + i 0.17) \times 10^{-12}$  m<sup>2</sup>/N,  $K_{33} = (1516 + i 120)$ , and  $k_{31} = 34.63\%$ . The zero field value of  $d_{33}$  was found to be 495 pC/N and  $d_h$  was then calculated to be 75 pC/N.

#### REFERENCES

1. E.F. Alberta, A.S. Bhalla, T. Takenaka, *Proc. of ISAF92*, IEEE, Piscataway (1990).
2. D. Damjanovic, *Ph.D Thesis*, Pennsylvania State University, University Park (1987).
3. Y. Takagi, *Phys. Rev.*, **85** [2] 315 (1952).